Design, analysis and evaluation of sigma-delta based beamformers for medical ultrasound imaging applications

Altinok, G.

DESIGN, ANALYSIS AND EVALUATION OF SIGMA-DELTA BASED BEAMFORMERS FOR MEDICAL ULTRASOUND IMAGING APPLICATIONS

by

Gunes Damla Engindeniz

A Thesis Submitted in Partial Fulfilment of the Requirements of the University of Westminster for the Degree of Doctor of Philosophy

The Department of Electronics Engineering, Faculty of Science and Technology
University of Westminster

2016

Abstract

The inherent analogue nature of medical ultrasound signals in conjunction with the abundant merits provided by digital image acquisition, together with the increasing use of relatively simple front-end circuitries, have created considerable demand for single-bit Σ–Δ beamformers in digital ultrasound imaging systems. Furthermore, the increasing need to design lightweight ultrasound systems with low power consumption and low noise, provide ample justification for development and innovation in the use of single-bit Σ–Δ beamformers in ultrasound imaging systems. The overall aim of this research program is to investigate, establish, develop and confirm through a combination of theoretical analysis and detailed simulations, that utilize raw phantom data sets, suitable techniques for the design of simple-to-implement hardware efficient Σ–Δ digital ultrasound beamformers to address the requirements for 3D scanners with large channel counts, as well as portable and lightweight ultrasound scanners for point-of-care applications and intravascular imaging systems.

In addition, the stability boundaries of higher-order High-Pass (HP) and Band-Pass (BP) Σ–Δ modulators for single- and dual- sinusoidal inputs are determined using quasi-linear modeling together with the describing-function method, to more accurately model the Σ–Δ modulator quantizer. The theoretical results are shown to be in good agreement with the simulation results for a variety of input amplitudes, bandwidths, and modulator orders. The proposed mathematical models of the quantizer will immensely help speed up the design of higher order HP and BP Σ–Δ modulators to be applicable for digital ultrasound beamformers.

Finally, a user friendly design and performance evaluation tool for LP, BP and HP Σ–Δ modulators is developed. This toolbox, which uses various design methodologies and covers an assortment of Σ–Δ modulators topologies, is intended to accelerate the design process and evaluation of Σ–Δ modulators. This design tool is further developed to enable the design, analysis and evaluation of Σ–Δ beamformer structures including the noise analyses of the final B-scan images. Thus, this tool will allow researchers and practitioners to design and verify different reconstruction filters and analyze the results directly on the B-scan ultrasound images thereby saving considerable time and effort.

Table of Contents

List of Figures

List of Tables

Abbreviations

2D	Two-Dimension
3D	Three-Dimension
A/D	Analogue to Digital
ADC	Analogue to Digital Converter
AMP	Amplifier
B-mode	Brightness Mode
BP	Band-Pass
CDF	Cumulative Density Function
CNR	Contrast to Noise Ratio
CT	Computed Tomography
D/A	Digital to Analogue
DAC	Digital to Analogue Converter
DEMUX	De-multiplexer
DF	Describing Function
DR	Dynamic Range
DSP	Digital Signal Processing
ECG	Electrocardiogram
EEG	Electroencephalogram
FFT	Fast Fourier Transform
FIR	Finite Impulse Response
GNSS	Global Navigation Satellite System
GUI	Graphical User Interface
HP	High-Pass
HV	High Voltage
I	Intensity
IC	Integrated Circuit
IIR	Infinite Impulse Response
LNA	Low-Noise Amplifier
LP	Low-Pass
LP -> BP	Low-Pass to Band-Pass
LP -> HP	Low-Pass to High-Pass
LPF	Low-Pass Filter

MASH	Multistage Noise-Shaping
MRI	Magnetic Resonance Imaging
MSA	Maximum Stable Amplitude
MUX	Multiplexer
NTF	Noise Transfer Function
OS/UI	Operating System/User Interface
OSR	Oversampling Ratio
PDF	Probability Density Function
PGA	Programmable-Gain Amplifier
PSD	Power Spectral Density
PSF	Point Spread Function
PET	Positron Emission Tomography
RO	Rank-ordered
RV	Random Variable
S/H	Sample-and-Hold
SNR	Signal to Noise Ratio
SQNR	Signal to Quantization Noise Ratio
STF	Signal Transfer Function
T/R	Transmit/Receive
VCA	Variable-Gain Amplifier
VLSI	Very Large Scale Integration

Symbols

α	All-Pass filter coefficients of low-pass polyphase filters
β	All-Pass filter coefficients band-pass polyphase filters
Δ	Quantizer step size
$e_n(k)$	Noise related quantizer input
$e_x(k)$	Input related quantizer input
η	Ultrasound array element indices
λ	Wavelength of the sound signal
μ_{in}	Mean values inside the cyst image
μ_{out}	Mean values outside the cyst image
ρ	Ratio of input signal variance to noise signal variance at quantizer input
ρ_a	Ratio of the power of the input signal of an amplitude a to noise power at the quantizer input (dual sinusoidl input)
ρ_b	Ratio of the power of the input signal of an amplitude b to noise power at the quantizer input (dual sinusoidal input)
$\sigma_{e_n}^2$	Variance of the noise related quantizer input signal
$\sigma_{e_x}^2$	Variance of the signal related quantizer input signal
σ_q^2	Quantization noise variance
σ_{out}	Standard deviation outside cyst
$\sigma_{q_{ab}}^2$	Quantization noise power related to dual input signals
σ_{qb}^2	In-band quantization noise variance
σ_x^2	Input signal variance
Σ–Δ	Sigma-Delta

υ	Normalized frequency
ω_t	Transition band
τ	Propagation time of ultrasound echo signals
$\tau_\eta^{'}$	Propagation time difference of echo signals to η th array element
τ_0	Propagation time of ultrasound signals to the center of the array element
θ	Angle
θ_0	Angle to the horizontal axis of the focal point
ω_n	Stop-band bandwidth
a	Amplitude of the first input signal of the dual sinusoidal input signal, $x_a(k)$
a_x	Amplitude of the input signal for single sinusoidal input x(k)
$a_0(t)$	Gaussian envelope of sound wave p(t)
A_p	Attenuation term of the sound waves
A(K)	Noise amplification curve
$A_{\min}$	Minimum of noise amplification curve
$A(z)$	Transfer function of all-pass filter
b	Amplitude of the second input signal of the dual sinusoidal input signal, $x_b(k)$
c	Speed of sound wave
d	Space between array elements
D(z)	Denominator of loop-filter in z-domain
e(k)	Input signal to the quantizer
$e_{x_a}(k)$, $e_{x_b}(k)$	Quantizer input signals related to dual sinusoidal input signals $x_a(k)$ and $x_b(k)$
f_B	Signal bandwidth
f_s	Sample frequency
f_0	Center frequency

F(x)	Cummulative density function
$H_{HB}(z)$	Half-band filter composed of all-pass subsections
H(z)	Loop-filter in z-domain
i	indices for filter coefficients
in	indices (order) of cascaded of all-pass filters
k	Sample of signal
K	Quantizer gain
K_a , K_b	Quantizer gains related to dual sinusoidal input signals
$K_{\min}$	Minimum quantizer gain value
$K_{\max}$	Maximum quantizer gain value
K_n	Quantizer gain for noise model
K_x	Quantizer gain for signal model
k_s	Gaussian test coefficient
L(z)	Overall loop-filter in summation of feedforward/feedback coefficients modulator topologies
m	Number of bits
N	Number of filter order
N_1	Order of the first modulator in MASH Σ–Δ modulator architecture
N_2	Order of the second modulator in MASH Σ–Δ modulator architecture
p	feedback coefficients of the Σ–Δ modulator topologies
p(t)	beam summation localized at focus point
P	Focus point
$p_\eta(t)$	ultrasound signal at η th array element
$P_q(f)$	PSD of quantization noise
r	Depth
$r_{\max}$	Maximum imaging depth

r_0	Depth of focal point to the center of the ultrasound array
r_η	Distance of the focal point to the η th array element
R_s	Stop-band attenuation
S	Number of ultrasound array elements
T_s	Sample time interval
u	iteration number for all-pass subsection of polyphase filters
Q	Quantization level
q(k)	Quantization noise
Q(z)	Quantization noise signal in z-domain
w_N	Feedforward coefficients of weighted feedforward summation topology
$x_a(k), x_b(k)$	Dual sinusoidal input signals
x(k)	Discrete-input signal
x(t)	Continuous-time input signal
X(z)	Input signal in z-domain
y(k)	discrete-time output signal
$y_x(k)$	Output signal of signal model
Y(z)	Output signal in z-domain
Y(z)	Output signal in z-domain
2w	Ultrasound transducer size

Acknowledgements

I would like to express my thanks to all my supervisors. I especially thank Prof. Izzet Kale. His guidance helped me in all the time of research and writing of this thesis. I would like to thank him for his advice throughout my Ph.D studies with his detailed knowledge and experience about sigma-delta modulators. And during the most difficult times when writing this thesis, he gave me the moral support and the guidance I needed to move on.

I would like to express my sincere gratitude to my Director of Studies Dr Mohammed Al-Janabi for his continuous support of my Ph.D study and research, for his patience, motivation, enthusiasm, and immense knowledge. I have been extremely lucky to have a supervisor who cared so much about my work, and who responded to my questions and queries so promptly. I could not have imagined having a better advisor and mentor for my Ph.D study.

I express my special thanks to my parents, who always believed in me and encouraged me to do these studies in the first place. Their patience and continuous support, especially at the end, was invaluable.

I would like to thank my husband, Ihsan Engindeniz, for all his support and encouragements he gave me to finish my studies.

Declaration

I declare that all the material contained in this thesis is my own work.

Chapter 1

Introduction

The sigma-delta (Σ-Δ) analogue-to-digital (A/D) converter architecture of Inose and coworkers [Ino62], [Ino63] emerged as a modification of 'delta' modulation, which was first invented at the ITT Laboratories in France by E. M. Deloraine, S. Van Mierlo, and B. Derjavitch in 1946 [Del46], [Del53]. The idea behind delta-modulation was to transmit the changes (delta) in sample values rather than the values themselves. The Cutler patent [Cut52], [Cut60] introduced the oversampling technique with the noise-shaping concept by describing first- and second-order noise-shaping loops. Later in 1965, Brahm's patent [Bra65] described the second-order multi-bit oversampling noise-shaping A/D converter. However, the name 'delta-sigma' modulation to describe the Cutler's noise-shaping oversampling architecture was first introduced by Inose, Yasuda and Murakami in the early 1960s [Ino62], [Ino63]. The basic principle behind Σ-Δ modulation is to use a feedback loop to track the input signal by the coarse fed-back quantization error [Che98], [Nor97]. The work described until the mid 1960s was related to the transmission of oversampled digitized signals rather than the actual implementation of Nyquist A/D converters. The first design of using digital filters and decimators following the Σ–Δ modulators was first published by Goodman at Bell Labs in 1969 [Goo69]. This was then further extended to multi-bit Σ–Δ modulators by Candy in 1974 [Can74]. Extensive discussions of the most commonly used Σ–Δ modulator architectures and the key milestones of the history of Σ–Δ modulators are well detailed in [Hau91], [Kes08a].

Even though the concepts of Σ–Δ modulation were first presented in the middle of the last century, they were not widely used until the 1980s due to improvements in integrated circuit (IC) technology [Can92], [Eyn91], [Fer91], [Nor97]. Advances in very-large-scale-integration (VLSI) technology have made oversampling A/D converters more attractive in digital processing applications [Azi96], [Gai89], [Can92], [Nor97]. Because of their relative simplicity and ease of integration into other processing elements, Σ–Δ A/D converters have been widely used in applications such as instrumentation, voice-band, data telecommunications, high-fidelty audio and speech, metering applications, data-acquisition, telecom, radar and sonar [Ada86], [Adl98], [Can92], [Hou03], [Hau91], [Lia14], [Par05], [Rib94], [Rus03], [Sch02], [Sir15], [Sun03]. Also, there are several applications of Band-Pass (BP) Σ–Δ data converters such as in digital radio systems [Bry94], [Hag02], [Nak01], [Par14], [Qia15], [Tro93], [Vun05], [Yan14], receivers for digital mobile cellular telephony [Erg99], [Gau94], [Hen01], high-speed modems [Baz95], satellite communication services [Chu97] as well as in GNSS front-end applications [Kim07]. The Σ–Δ modulators are also used in sensor systems to shape out the noise from the sensor itself and its environment [Sap08]. In addition, Σ–Δ modulators are widely used in biomedical imaging systems such as ultrasound imaging systems [Tex13], [Bil10], [Fre99],[Koz01],[Nor96],[Tex10], Electroencephalogram (EEG) and Electrocardiogram (ECG) [Chi15], [Tex10], [Shu06], Magnetic Resonance Imaging (MRI) [Tex10][Tex13], Computed Tomography (CT), [Tex13], Positron Emission Tomography (PET) [Lai15]. Examples of commercial Σ–Δ modulator products (ADS1605,ADS1610, ADS1258, ADS1278) used in medical applications are given in Table 1-1.

Product	ADS1605	ADS1610	ADS1258	ADS1278
Bandwidth	2.45 MHz	5MHz	61 kHz	62kHz
Sampling Rate	5 MSPS	10 MSPS	125 kSPS	144 kSPS
Bit-Resolution	16-bit	16-bit	24-bit	24-bit
Application	Ultrasound, MRI	Ultrasound, MRI	ECG,EEG	ECG, EEG

Table 1-1 Σ–Δ modulator product examples used in biomedical applications [Tex10], [Tex13]

As shown in Table 1-1, high sampling rate with high bit-rates required by ultrasound imaging- and MRI systems can be achieved with state-of –art Σ–Δ modulators (ADS1605, ADS1610). On the other hand, ECG- and EEG systems require lower sampling frequency with higher bit-resolution (ADS1258, ADS1278).

Ultrasound imaging compared to the other medical imaging techniques (x-ray, MRI, CT), provides high-resolution images without the use of ionizing radiation. This makes them perfectly safe and thus popular to use especially for regular scans [Tex10], [Ali08].

Ultrasound is defined as acoustic waves with frequencies above those which can be detected by the ear, from about 20 kHz to several hundred MHz [Wel69]. Ultrasound for medical applications typically uses only the portion of the ultrasound spectrum from 1 MHz to 50 MHz, which is used to produce images of the exposed part of the body including the heart, vessels, kidney, liver, developing fetuses and other soft tissues [Hav79], [Wel69]. The ultrasound waves are generated by a transducer which is held against the body as shown in Figure 1-1. The piezoelectric crystal elements in the transducer start to vibrate and produce high-frequency sound waves when a high voltage is applied across the transducer. Ultrasound waves are generated by converting a radio frequency (RF) electrical signal into mechanical vibration via a piezoelectric transducer. Through their propagation, sound-waves are partially reflected and refracted depending on the tissue they are exposed to. When two mediums with different densities are located next to each other, an acoustic impedance mismatch is created and sound waves are reflected by this mismatch. Therefore, the ultrasound imaging technique is based on processing these echo signals [Sho88]. The processed echo signals are then reconstructed and displayed on a monitor as gray-scaled, called B-mode, which allows obtaining information about the structure and nature of tissues and organs of the body. In the B-mode (brightness mode) in ultrasound, the transducer simultaneously scans a plane through the body that can be viewed as a two-dimensional image on screen. This is composed of bright dots representing the ultrasound echoes. The brightness of each dot is determined by the amplitude of the returned echo signal.

In ultrasound scanning systems, in order to scan a sufficiently wide far field, the ultrasound signals have to diverge from virtually the same point. In other words, ultrasound signals should be originated from the same point, which is called beam focusing or beamforming [Joh93]. Beam focusing can be performed mechanically by placing acoustic lenses on the surface of the transducer. However, the common process is beam focusing electronically using phased arrays, as used in this PhD study. Transducer arrays can be

explained as a single transducer element divided into S-elements, and each element transmits and receives ultrasound pulses differently. During the transmit- and receive-process, focusing can be performed electronically using phased arrays. The differences in propagation time from a focus point to each array element are compensated by time delays in order to maintain a coherent summation. Therefore, beamforming is defined as the summation of phase-shifted signals that are generated from a common source, but received at different times. The echo signals are delayed dynamically by an appropriate amount and added together to form a beam [Ald07], [Joh93], [Tho96]. By adjusting the time delays across the array, a region of interest can be scanned over predetermined directions and depth. The echoes are processed by a digital beamformer and in the B-mode the brightness of each pixel in the image is adjusted as a function of the amplitude of the reflected signals. A simplified block diagram of an ultrasound system is given in Figure 1-1.

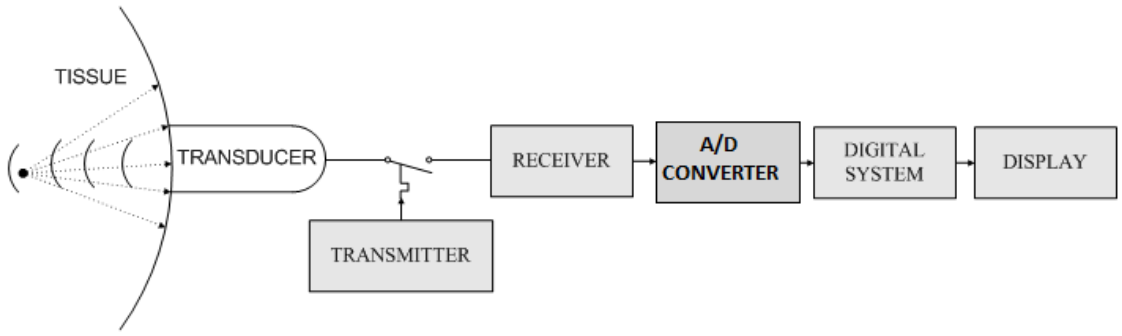

Figure 1-1 Simplified block diagram of the ultrasound system

Ultrasound systems are signal processing intensive and thus the performance of digital ultrasound imaging systems is strongly dependent on the front-end-components. The front-end components are the bottleneck to system's performance; once noise and distortion have been introduced, it is essentially impossible to remove them. At this stage, the precision of the A/D conversion becomes critically important. Therefore, on-going research is focusing in two main areas:

- Increasing the image quality [Ali08], [Tex13],
- Decreasing the power consumption and size in order to design more portable, accessible and affordable ultrasound systems [Hem15], [Wag12], [Tex13].

1.1 Motivation

The typical channel count number of an ultrasound system can vary from 8 for ultra-portable systems to 512 for high-end devices, whereas for 3-dimension (3D) systems this number can be even higher [Tex13]. As a result, the major challenge in ultrasound imaging systems is to simplify the front-end hardware especially for economical scanners with large channel count beamformers.

In the 1990s, 'system-on-chip'- design and manufacturing made Σ–Δ modulators even more popular especially in mixed signal ICs which combined the ADC, DAC and DSP functions on to a single chip [Kes08b]. Σ–Δ modulators can employ a digital ultrasound beamformer to simplify the array front-end and beamforming to handle the data acquisition and signal processing. This is seen to critically affect the overall cost and performance of the ultrasound system [Bil10], [Sea02]. State-of-the-art ultrasound imaging systems are moving in the directions of using full-scale real-time 3D imaging [Sav03]. These consist of 2D arrays with thousands of elements, and micro devices such as portable and lightweight scanners as well as intravascular imaging systems [Bil10], [Deg06], [Gill07], [Ora03], [Sal07], [Sav03], [Tex13]. As a result, reducing the cost, size, and power consumption of the front-end by deploying Σ–Δ modulators is crucial for the design of low-cost and 'on-chip' design compact beamformers.

Besides the reduced hardware- and signal processing complexity of the front-end, the use of Σ–Δ beamformers introduces severe image artefacts in the final image, thus significantly reducing the image quality [Fre99]. The repeated/omitted samples during beamforming degrade the synchronization between the modulator and demodulator, which leads to elevated noise floor in the reconstructed signal. As a result, the increased in-band noise level reduces the image resolution causing significant image artefacts which appear as a snowy background. Therefore, to reduce the artefacts many studies were investigated in the open literature [Bil02], [Bil10], [Bru02], [Che08a], [Che08b], [Fre99], [Han02], [Hem15], [Koz01], [Nil08], [Nor96], [Tom05],[Tho96]. However, the improvements were achieved by modifying the beamforming processes or Σ–Δ beamformer structures at the expense of either increased hardware- or signal processing complexity of the array front-end. Therefore, the main motivation of this PhD project is to design, analyse and evaluate hardware efficient structures for enhancing the image resolution for ultrasound Σ–Δ beamformers.

1.2 Objectives

The principles and the performance limitations including stability analysis of the Σ–Δ modulators are given followed by an overview of the present architectures of Σ–Δ ultrasound beamformers. A new reconstruction architecture is introduced, which has the potential of achieving high image quality without compromising the basic structure of Σ–Δ modulators. In order to analyze the principles and design methodologies of Σ–Δ ultrasound bemformers, the first objective is to give a comprehensive coverage of the design principles of the Σ–Δ modulators and to determine the stability boundaries of higher-order low-Pass (LP), band-pass (BP) and high-pass (HP) Σ–Δ modulators.

The second objective is to develop techniques for improving image resolution for digital ultrasound systems that utilize Σ–Δ modulator based beamformers by significantly simplifying the hardware complexity of the ultrasound system front-end.

The third objective is to develop a user friendly design and performance evaluation tool for LP, BP and HP Σ–Δ modulators, which is further modified to enable the performance analysis for digital ultrasound Σ–Δ beamformers.

1.3 Contributions by the Author

The contributions resulting from this thesis can be summarized in two categories. The first category is the original contributions covering novel propositions, which to the author's best knowledge have not been reported elsewhere in the open literature. The second category refers to the extensions or developments of existing works.

1.3.1 Novel Contributions

- Novel techniques are developed to suppress the image artefacts and improve image resolution for digital ultrasound systems that utilize Σ–Δ modulator based beamformers. Different from the existing approaches, the image artefacts that are produced by Σ–Δ beamformers are proposed to be eliminated in the reconstruction stage after the beam summation by post-processing techniques. Moreover, the proposed techniques result in greatly simplified hardware complexity. This to the author's best knowledge has not been proposed in the literature.

- The typical element number of an ultrasound phased array system can vary from 128 to 512, which results between 128-512 beamformers in the frond-end. Therefore any increase in the beamformer complexity affects the overall complexity of the front-end dramatically. The existing artefact reduction methods in the literature modify either the structures of Σ–Δ modulators or the align-and-sum processes in each of the 128-beamformers, which significantly increase the hardware complexity of the front-end components. On the other hand, the proposed method eliminates the artefacts in the reconstruction stage and does not need any modification in the conventional single-bit beamforming processes or the Σ–Δ modulator structures. In addition, since the proposed post-processing filters are applied after the beam summation, only one such filter is required per beam sum. Therefore, the hardware simplicity of the conventional single-bit Σ–Δ beamformer structures is completely preserved. As a result, the simplicity of the proposed hardware efficient reconstruction methods makes it suitable for cost-efficient, intra-vascular, portable, lightweight ultrasound scanners as well as 3D scanners with large channel counts.

- The conventional LP reconstruction filters are shown to be insufficient to eliminate the elevated noise floor at the low-frequencies due to the repeated/omitted samples in dynamic focusing. Therefore, novel BP reconstruction filters are proposed to suppress the low-frequency noise components [Alt11b].

- However, it has been shown that the noise elevation is changing dynamically due to the dynamic focusing. Therefore, novel adaptive rank-ordered filters with variable cut-off frequencies adaptive to the noise characteristics are developed to reduce the demodulation error [Alt11c].

- Further improvements in the resolution are proposed by employing the novel rank-ordered filters in combination with BP decimation filters. The performance of the proposed hardware efficient methods has been tested by means of emulations using RF data acquired from two different phantoms. It was verified through extensive simulation results that the proposed structures improve the image resolution and provide high quality B-scan images comparable to the ones obtained by multi-bit A/D beamformers.

- The hardware complexity of the LP- and BP-decimation filters are further simplified by proposing polyphase filters as cascaded all-pass filters, which to the author's best knowledge have not been reported elsewhere in the open literature.

- A novel Graphical User Interface (GUI) driven design and performance analysis tool for the reconstruction filters for the ultrasound Σ–Δ beamformers is created including the envelope detection and scan conversion stages. This tool will allow researchers and practitioners to design and verify different ultrasound reconstruction filters and analyse the results directly on the B-scan ultrasound images thereby saving considerable time and effort.

1.3.2 Development/Extended Contributions

- The non-linear quantizer in the feedback-loop complicates the stability analyses of higher-order Σ–Δ modulators [Ard97]. Therefore, time-consuming simulations are required to verify the stability. In order to derive the stability boundaries and stable amplitude limits, many publications are reported in the open literature [Aga83], [Ard87], [Lot07], [Lot13], [Ris94a], [Ris94b], [Sch97], [Zha00]. However, they are confined to certain modulator types or modulator-orders. Therefore, in this PhD project, a methodology that involves more accurate modelling of the quantizer for the design and evaluation of LP, BP and HP Σ–Δ modulators including more accurate stability analyses are presented.

- The prediction of the maximum stable amplitude limits for LP Σ–Δ modulators are detailed in [Lot07], [Lot08]. However the accuracy and the reliability of the existing quantizer model had not been previously verified for higher-order HP [Alt10b] and BP Σ–Δ modulators [Alt10a], [Alt11a]. Therefore, the validation of the existing stability curve analyses for the design of LP Σ–Δ modularors are extended in terms of a variety of Σ–Δ modulator specifications such as the bandwidth, modulator order and stop-band attenuation. The proposed mathematical models of the quantizer will immensely help speed up the design of higher-order HP and BP Σ–Δ modulators.

- MATLAB routines have been developed for the complete image acquisition systems for Nyquist A/D and conventional Σ–Δ ultrasound beamformers using real ultrasound data-sets. Routines are developed to simulate the entire beamforming stages followed by reconstruction stages for the final B-scan sector image display.

- Routines in MATLAB have been developed for various performance evaluation parameters for ultrasound images such as: Signal-to-Noise Ratio (SNR), contrast-to-noise ratio (CNR), Point Spread Function (PSF)-lateral, PSF-axial.

- A user-friendly design tool has been created in the MATLAB/Simulink environment to speed up the design, analysis and evaluation of single-stage and multistage sigma-delta (Σ–Δ) modulators. A variety of Simulink-based design topologies of LP, BP and HP Σ–Δ modulators are developed [Alt09]. The creation of a Graphical User Interface (GUI) driven design tool for HP Σ–Δ modulators has not been previously reported in the public domain to the best knowledge of the author.

1.4 Thesis Organization

Chapter 2 presents the fundamental concepts of LP, BP and HP Σ–Δ modulation, lists some of the fundamental modulator design choices; various design topologies and their design methodologies including modulator performance analyses. A comprehensive coverage of the fundamental design principles of Σ–Δ modulation are detailed and their characteristics are compared with those of Nyquist rate and conventional oversampling A/D converters. A detailed explanation of the operation of single-stage, multi-stage-, and distributed feedback Σ–Δ modulator topologies are provided. In addition, system-level description as well as the design and analysis of BP and HP Σ–Δ modulators are provided. The LP-to-BP $(LP \rightarrow BP)$ and LP-to-HP $(LP \rightarrow HP)$ frequency transformations are explained and analysed in order to design BP and HP loop-filters for arbitrary normalised centre frequencies and bandwidths.

Chapter 3 provides the non-linear stability analyses of higher-order HP and BP Σ–Δ modulators for single- and dual-sinusoidal inputs. The maximum stable amplitude limits for Butterworth filter- and Chebyshev Type-II filter-based Σ–Δ modulators are established by using a combination of the Describing Function (DF) method with quasi-linear modelling of the quantizer. Closed-form mathematical expressions are derived for the stability curves for different quantizer gain values. The stability prediction for the maximum stable input limits for higher-order inverse Chebyshev and Butterworth based HP and BP Σ–Δ modulators for different stopband attenuation and bandwidths are established. The theoretical results are

shown to be in good agreement with the simulation results for a variety of input amplitudes, bandwidths, and modulator orders.

In Chapter 4, the main features and constraints of ultrasound image reconstructions employing conventional 10-bit A/D and single-bit Σ–Δ beamformers are examined. A comprehensive coverage of the main factors that affect the image quality obtained by Σ–Δ beamformers is presented. The characteristics of the image artefacts caused by conventional single-bit Σ–Δ beamformers are examined qualitatively and quantitatively by means of emulations using RF data acquired from two different phantoms.

Chapter 5 presents the design analysis and evaluation of novel classes of Σ–Δ beamformer reconstruction techniques with reduced image artefacts and significantly increased image quality, in which the hardware simplicity of the array system is the key objective. First of all, the band-pass reconstruction technique is developed to eliminate the image artefacts at the low frequencies and improve the image quality for Σ–Δ beamformers. The second technique, which is absolutely novel, involves the use of adaptive LP- and BP-reconstruction filters, to suppress the dynamically changing noise components along the scan depth. The third reconstruction approach, which significantly reduces the hardware complexity, employs polyphase-filter structures in combination with adaptive rank ordered filters. Detailed models of these Σ–Δ beamformer reconstruction filters incorporating the simulations of the entire image acquisition steps of the digital ultrasound systems are evaluated at the final ultrasound images. Detailed guidelines for the choice of reconstruction filters as well as coefficient complexity are obtained and presented in tabular form. Graphs and charts are provided, which depict beamformer performances including signal-to-noise ratios, contrast-to-noise ratios as well as the quality of the final B-scan images.

Chapter 5 introduces a design tool for LP, HP and BP Σ–Δ modulators to speed up the design, analysis and evaluation of single- and multi-stage Σ–Δ modulators. The toolbox is further extended as an analysis tool for a variety of reconstruction filters designed for digital ultrasound Σ–Δ beamformers including the filter responses and noise analyses in terms of Signal-to-Quantization-Noise Ratio (SNQR) values.

Chapter 6 gives a summary of the research study highlighting the novelties resulted from this PhD study and suggestions for the future research directions.

1.5 Author's Publications

The key publications are listed as follows: The author's surname has changed to Engindeniz; please note that all the published papers are under the previous surname (Altinok)

- Altinok, G.D.; Al-Janabi, M.; Kale, I.; "A GUI Driven Σ–Δ Modulator Design, Evaluation and Measurement Tool with a View to Practical Implementation", *IEEE I2MTC*, Singapore, pp. 1022-1025, May 2009.

- Altinok, G.D.; Al-Janabi, M.; Kale, I.; "Stability Predictions for Higher-Order Band-Pass Σ–Δ Modulators for Dual Sinusoidal Inputs", *IEEE I2MTC*, Texas, pp. 541-545, 2010.

- Altinok, G.D.; Al-Janabi, M.; Kale, I.; "A Describing Function Based Method for Predicting the Stability of Higher-Order High-Pass Σ–Δ Modulators', *IEEE Prime Conference in Microelectronics & Electronics*, Berlin, pp. 1-4, Print ISBN: 978-1-4244-7905-4, Germany, July 2010.

- Altinok, G.D.; Al-Janabi, M.; Kale, I.;, "Improved Ultrasound Digital Beamforming Using Single-Bit Sigma-Delta Modulators with Band-Pass Decimation Filters", *IEEE International Symposium on Circuits and Systems*, Rio de Janeiro, Brazil, 15-18 May 2011.

- Altinok, G.D.; Al-Janabi, M.; Kale, I.; "Improved Sigma-Delta Ultrasound Beamformers with Adaptive Low-Pass Decimation Filters", *IEEE I2MTC*, Hangzhou, China, 10-12 May 2011.

- Altinok, G.D.; Al-Janabi, M.; Kale, I.; "Stability Analysis of Band-Pass Sigma-Delta Modulators for Single and Dual Tone Sinusoidal Inputs", *IEEE Transactions on Instrumentation and Measurement*, vol. 60, no. 5. pp. 1546-1554, May 2011.

Chapter 2

An Overview of Σ–Δ Modulators

In order to analyze the ultrasound applications based on the Σ–Δ modulators, the theory of sigma-delta converters is introduced with an overview of LP, BP and HP Σ–Δ modulators including a review of Nyquist rate A/D converters, the basic principles of Σ–Δ modulators, the Σ–Δ modulator topologies and their design methodologies as well as the basic metrics to analyze the Σ–Δ modulator performance. Section 2.1 describes conventional A/D conversion with a conventional Nyquist sampling rate. The simulation methods and the parameters to be used to analyze the performance of the converter are given in Sections 2.3 and 2.4 . This is followed by the basic principles of LP Σ–Δ converters and how they combine the advantages of oversampling techniques with the noise-shaping concepts. In Section 2.5 low- and higher-order LP Σ–Δ modulators are designed, examined and analyzed. Various single-loop and multi-stage Σ–Δ modulator analysis and simulations are introduced. The noise transfer function design methods by using differencers, Butterworth and inverse Chebyshev filters are introduced. In Sections 2.6 and 2.7 BP and HP Σ–Δ converter architectures are described in detail.

2.1 Nyquist-rate A/D Converters

A/D conversion is based on two separate operations: uniform sampling in time, and quantization in amplitude. The conventional A/D conversion process is shown in Figure 2-1. A Sample-and-Hold (S/H) circuit samples a continuous-time signal, $x(t)$, at uniformly spaced time interval T_s [Opp89], [Sha49], [Pro96] in order to have discrete-time signal $x(k)$ at samples of k.

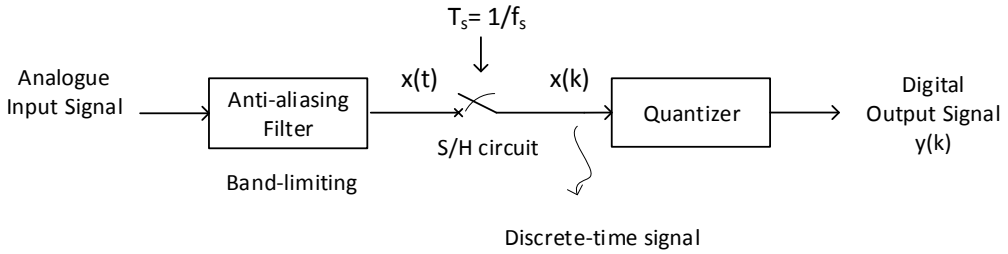

Figure 2-1 Block diagram of a conventional A/D converter

The discrete-time signal, x(k), can be represented as [Opp89]:

$$x(k) = x(kT_s) = \sum_{k=-\infty}^{\infty} x(t)\delta(t - kT_s) \tag{2.1}$$

The effect of the S/H process in the frequency domain results in the appearance of replicas of the original signal spectrum at integer multiples of the sampling frequency $f_{s=1/T_s}$ [Opp89]:

$$X_s(f) = \frac{1}{T_s} \sum_{l=-\infty}^{+\infty} X(f - lf_s) \tag{2.2}$$

where l represents discrete index in the frequency domain and $X_s(f)$ represents the spectrum of the sampled signal, and $X(f)$ is the spectrum of the original continuous-time

signal. Although the analogue input signal is continuously changing, the output of the S/H circuit must be constant between samples so that the signal can be quantized properly.

According to Shannon's sampling theorem [Sha49], if the sampling frequency f_s is less than twice the signal bandwidth f_B, the repeated versions of the signal will overlap resulting in signal distortion known as aliasing [Opp89]. To avoid aliasing, an anti-aliasing filter is used, which exhibits a flat response over the signal band of interest and attenuates the frequencies above the signal-band. As a result, the input signal is forced to be band-limited [Par98].

Once the signal is sampled, the amplitudes are quantized by mapping the sampled sequence into a finite set of predefined values. The quantization levels Q and the digital word length m, i.e. number of bits, can be expressed by the following relationship: $Q = 2^m$. For an A/D converter with Q quantization levels, only input values separated by at least the step size of the quantizer (Δ) can be distinguished or resolved to different output levels [Azi96]:

$$\Delta = \frac{2V}{Q-1} = \frac{2V}{2^m - 1} \tag{2.3}$$

The error of the quantizer, q(k), added to the system can be modelled as the difference between the output sequence $y(k)$ and the input sequence x(k), where q(k) can be considered as a random variable in the interval [$-\Delta/2$, $\Delta/2$] with equal probability. The quantization error can be considered as an independent additive white noise source [Can81]. By doing so, the quantization error signal is assumed to be:

- Uncorrelated to the quantizer input signal,
- Uniformly distributed within the interval [$-\Delta/2$, $\Delta/2$] and approximately equal to $1/\Delta$.

For zero mean q(k), the mean square quantization noise power is the variance of the quantization noise, σ_q^2, which can be written as in [Azi96]:

$$\sigma_q^2 = E[q^2] = \frac{1}{\Delta}\int_{(-\Delta)/2}^{\Delta/2} q^2 dq = \frac{\Delta^2}{12} \tag{2.4}$$

Consider an *m*-bit quantizer with $Q = 2^m$ quantization levels (2.3), so that (2.4) yields:

$$\sigma_q^2 = \frac{\Delta^2}{12} = \left(\frac{2V}{2^m - 1}\right)^2 /12 \cong \left(\frac{2V}{2^m}\right)^2 /12 \tag{2.5}$$

2.2 Σ–Δ A/D Converters

The A/D converter based on the Σ–Δ modulation, which is capable of providing a very high resolution for low-to-medium signal bandwidth applications such as those, used in the front-end components of the medical ultrasound systems [Chi15], [Fre97], [Hem15], [Jun13], [Kar00], [Koz01], [Kri13], [Nor96], [San13], [Tex13], [Tov04], [Tom13]. In contrast to Nyquist rate A/D converters, Σ–Δ modulators are based on two major processes: oversampling and noise-shaping [Ada94], [Aziz96], [Can85], [Nor97].

2.2.1 Oversampling

Oversampling is the process of sampling a signal with a sampling frequency that is significantly higher than the bandwidth of the highest frequency component of the sampled signal. Oversampling helps to reduce the in-band quantization noise, improves resolution and avoids aliasing [Ada98], [Nor97]. Since the input signal has equal probability to have any value between the step sizes $\pm\Delta$, the total power of the sampled signal and the total power of the original signal are exactly the same. On the other hand, the noise power produced is the same as that produced by a Nyquist rate converter, but its frequency distribution is different because of the OverSampling Ratio (OSR). The quantization noise is designated as white noise [Can85], [Gra90] with zero mean uniformly distributed between $[-f_s/2, f_s/2]$ and independent from the input signal. Therefore, the probability density function of the quantization noise is assumed to be uniform and in the oversampling case is spread over a bandwidth f_S which is much bigger than the signal bandwidth f_B. Therefore, as seen in Figure 2-3, a considerably smaller part of this total noise power falls in the

signal-band [- f_B, f_B]. As a result, the quantization-noise power has been reduced by the OSR, where $OSR = \frac{f_s}{2f_B}$.

The power spectral density of the quantization noise, $P_q(f)$, spread uniformly over the frequency range $[-f_s/2, f_s/2]$, can be therefore written as in [Ben48], [Can81]:

$$P_q(f) = \frac{\sigma_q^2}{f_s} \tag{2.6}$$

The in-band noise power σ_{qb}^2 for the oversampled A/D converter case is given by [Azi96]:

$$\sigma_{qb}^2 = \int_{-f_B}^{f_B} P_q(f)df = 2\int_0^{f_B} P_q(f)df = \int_0^{f_B} \frac{2\sigma_q^2}{f_s}df \tag{2.7}$$

As a result, the in-band quantization noise power is reduced by the OSR:

$$\sigma_{qb}^2 = \sigma_q^2\left(\frac{2f_B}{f_s}\right) = \sigma_q^2 \big/ OSR \tag{2.8}$$

Typical values of the OSR lie in the range of 8-512. The maximum f_S is restricted by technology limitations. Higher f_S imply higher clock rates, which increase the power consumption of the chip. On the other hand, smaller OSRs are constrained by the resolution specification of the modulator. Therefore, there is a trade-off between resolution and power consumption.

2.2.2 **Noise-shaping:**

The oversampling technique becomes more effective if used in combination with noise-shaping, resulting in a further reduction of the in-band quantization noise. Noise-shaping is a technique which alters this noise spectrum so that it is no longer uniform, but rather, is shaped such that most of the noise power is shifted to frequencies outside the signal band. As shown in Figure 2-2, a conventional Σ–Δ modulator as reported in [Azi96], [Nor97] consists of:

- A feedforward loop-filter, transfer function of $H(z)$, (accumulator)

- A 1-bit quantizer enclosed in a feedback loop.

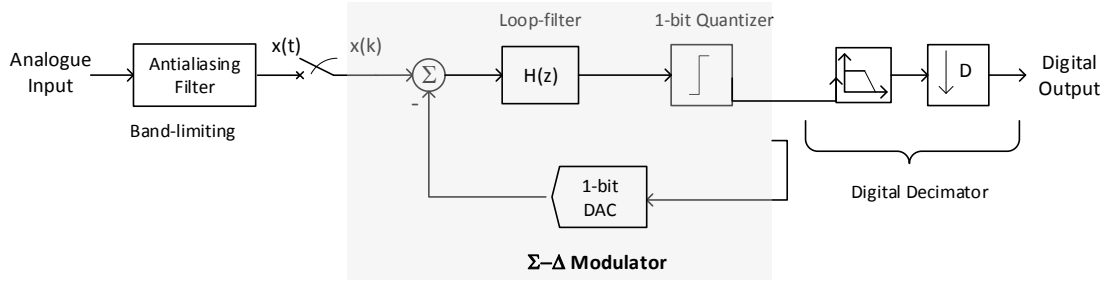

(a)

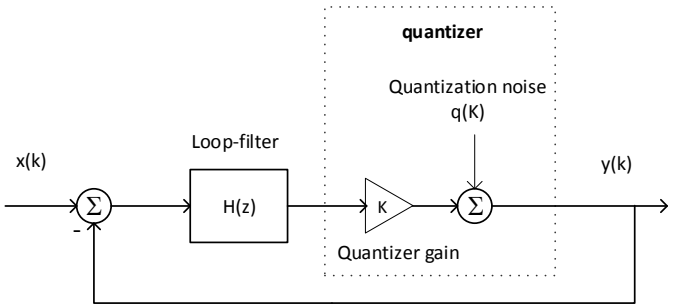

(b)

Figure 2-2 (a) Block diagram of Σ–Δ A/D converter, (b) Linear model representation of Σ–Δ modulator

As given in Figure 2-2-a, the Σ–Δ A/D converter consists of an anti-aliasing filter, a sampler, a Σ–Δ modulator and a digital decimator. The basic idea of Σ–Δ A/D converters is to exhange the resolution in amplitude for resolution in time. Therefore, the analogue input signal is modulated at a sampling rate much higher than the Nyquist sampling rate, and the shaped quantization noise is filtered by digital decimation filters [Nor97]. The feedback loop of an oversampling low-pass Σ–Δ modulator allows the input signal to pass essentially unfiltered through the converter, but high-pass filters the quantization noise [Can81], [Can85], [Can92]. Since the high frequency noise components can be removed by means of a digital decimation filter without affecting the input signal, high resolution at the output can be obtained [Nor97].

The 1-bit quantizer makes the Σ–Δ modulator a non-linear system which is highly difficult to analyse. Therefore an approximate linear model is used, where the quantizer is replaced with an additive white noise source q(k). This approach is straightforward to apply and widely used by many practitioners in the field for preliminary design analysis. Furthermore, the D/A converter is assumed to be ideal with a gain of unity, as shown in Figure 2-2b. Thus, the output of a Σ–Δ modulator can be written in the z-domain as follows:

$$Y(z) = \frac{K \cdot H(z)}{1 + K \cdot H(z)} X(z) + \frac{1}{1 + K \cdot H(z)} Q(z) \tag{2.9}$$

where $H(z)$ is the loop-filter and K is the quantizer gain. The output of the modulator is the superposition of the input signal filtered by an appropriate Signal Transfer Function (STF), and the added quantization noise shaped by the Noise Transfer Function (NTF). For this linear model, the quantizer gain is assumed to be 1 ($K = 1$) .

$$Y(z) = STF(z) \cdot X(z) + NTF(z) \cdot Q(z) \tag{2.10}$$

As a result, the loop-filter together with the feedback-loop, give rise to the desired in-band noise suppression and at the same time push most of this noise to outside the signal band [Azi96]. The gain of the STF is close to one in the signal band and close to zero outside that band [Can92], [Nor97].

The quantization noise power spectral density in the signal-band, $P_q(f)$ is given in Figure 2-3. The process of shifting most of the quantization noise out of the signal band is referred to as *noise-shaping*.

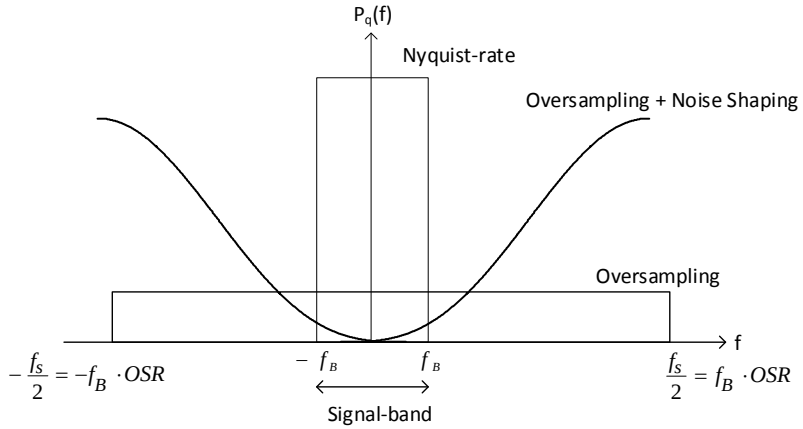

Figure 2-3 Comparison of Quantization noise power spectral density of Nyquist-rate-, oversampled- and Σ–Δ A/D converters

2.3 Simulation Approach

Behavioural level simulations help to validate the Σ–Δ modulator performance with relative ease prior to the actual circuit implementation. Therefore, all the Σ–Δ modulators in this thesis are modelled and simulated in a Matlab/Simulink based environment in order to evaluate the behaviour of Σ–Δ modulators in discrete-time using the actual 1-bit quantizer.

These simulations are conducted for an input block length of 42768. The first 10000 samples are excluded as transient points. The remaining 32768 (2^{15}) output samples use a Hanning-windowed Fast Fourier Transform (FFT). In order to speed up the simulation, the FFT length is chosen to be a power of 2.

2.4 Performance Computation Parameters

2.4.1 SNR

The SNR is defined as the ratio of the signal power to the in-band quantization noise power. The in-band quantization noise is computed by identifying the location and the number of bins that represent the input signal and removing them from the output spectrum [Alj00]. Therefore, 32768 samples are windowed by Hanning window and then the FFT operation is performed. As a result of the A/D conversion processes, the original input signal is not

fully represented due to the quantization process. Therefore this section presents the commonest evaluation criterion used by practitioners to assess the accuracy of Σ–Δ modulators. The SNR is the ratio of the input signal power to the in-band quantization noise power of the converter. It is usually expressed in decibels [Nor97].

$$SNR = 10\log\left(\frac{P_{signal}}{P_{noise}}\right) = 10\log\left(\frac{\sigma_x^2}{\sigma_q^2}\right) \tag{2.11}$$

Using (2.5), the signal to quantization noise ratio becomes:

$$SNR = 10\log\left(\sigma_x^2\right) + 10\log\left(\frac{12\cdot 2^{2m}}{2^2 V^2}\right) \tag{2.12}$$

$$SNR = 10\log\left(\frac{\sigma_x^2}{V^2}\right) + 4.77 + m\cdot 6.02dB \tag{2.13}$$

For each extra bit of resolution (m), there is an approximate 6 dB improvement in the SNR.

2.4.2 Tonality

In practice there are discrete tones appearing in the output spectrum because of the non-linearity of the negative feedback which can distort the signal by coupling to the baseband region [Fri88], [Nor97]. The periodic components and repetitive patterns in the system like sinusoidal input signals cause harmonic tones [Nor92]. These tones can cause serious problems if they occur in the signal-band. Since the human eye and ear are sensitive to these repetitive signals, tones can be distinguished by humans as audio or visual. Moreover, the pattern noise in the signal band degrades the SNR values by means of bumps and slope changes [Alj00]. Therefore, a white noise with a small amplitude compared to the input signal amplitude, which is called dither, can be injected at the quantizer to reduce tones in Σ–Δ modulators, in order to disturb the periodicity of the repetitive signals [Nor92].

2.5 Low-Pass Σ–Δ Modulators

For a LP Σ–Δ modulator, the STF should be a low-pass filter and the NTF a high-pass filter [Jan94], [Azi96].

2.5.1 **Single-stage Structures**

The number of the accumulators used around the loop actually determines the order of the Σ–Δ modulator. As shown in Figure 2-4, a first-order Σ–Δ modulator contains a single accumulator, I(z):

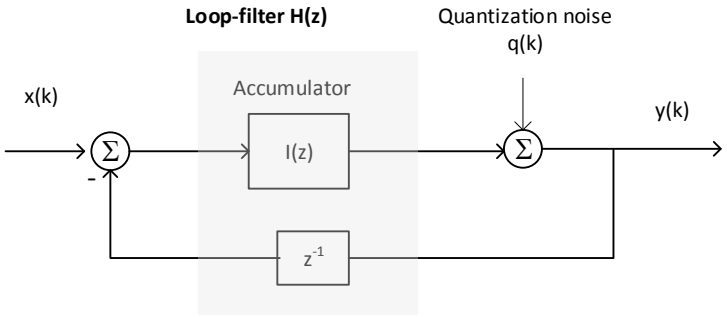

Figure 2-4 Block diagram for the first-order Σ–Δ modulator

The output $y(k)$ in z-domain, $Y(z)$ of a first-order Σ–Δ modulator is given by:

$$Y(z) = \frac{I(z)}{1 + I(z)z^{-1}} X(z) + \frac{1}{1 + I(z)z^{-1}} Q(z) \tag{2.14}$$

Where the accumulator is:

$$I(z) = \frac{1}{1 - z^{-1}} = \frac{z}{z - 1} \tag{2.15}$$

Therefore (2.14) becomes:

$$Y(z) = X(z) + \underbrace{(1 - z^{-1})}_{NTF} Q(z) \tag{2.16}$$

As seen in (2.16), the input signal remains unchanged while the quantization noise is shaped by the $NTF = (1 - z^{-1})$. The NTF is a high-pass filter with a zero at dc, so that it attenuates the quantization noise at very low frequencies. Using the definition of the z-domain: $z \to e^{j\omega t}$, the NTF can be rewritten in the frequency-domain as:

$$NTF = 1 - e^{-j2\pi fT} = 2je^{-j\pi fT} \sin(\pi fT) \tag{2.17}$$

The squared magnitude of the NTF results in the amplification of the quantization noise by 4, but due to the $sin^2(\pi fT)$ term, this results in huge attenuation at low-frequencies [Nor97]. Using (2.7):

$$\sigma_{qb}^2 = \int_{-f_B}^{f_B} P_{qb}(f)df = 2\int_0^{f_B} P_{qb}(f)df = 2\int_0^{f_B} (2\sin^2(\pi fT)P_q(f)df \tag{2.18}$$

Using the approximation $\sin(x) \cong x$, for $\pi f_B T << \pi / 2$ [Tho05] and $P_q(f) = \sigma_q^2 / f_s$ [Opp89], and $T_s = 1/f_s$, then (2.18) yields:

$$\sigma_{qb}^2 = 2\frac{\sigma_q^2}{f_s}\int_0^{f_B} 4\pi^2 \frac{1}{f_s^2} f^2 df = \sigma_q^2 8\frac{\pi^2}{3}\left(\frac{f_B}{f_s}\right)^3 \tag{2.19}$$

$$\sigma_{qb}^2 = \sigma_q^2 \frac{\pi^2}{3}\left(\frac{2f_B}{f_s}\right)^3 \tag{2.20}$$

Then the SNR for a first-order Σ–Δ modulator is mathematically given as:

$$SNR = 10\log\left(\frac{\sigma_x^2}{\sigma_{qb}^2}\right) = 10\log\left(\frac{\sigma_x^2}{\sigma_q^2}\right) - 5.17 + 30\log\left(\frac{f_s}{2f_B}\right)(dB) \tag{2.21}$$

As seen in (2.20), the in-band quantization noise power σ_{qb}^2 decreases as the OSR increases. Thus, as given in (2.21) for every doubling of the OSR, the SNR improves by 9.03 dB, or 1.5 bits of resolution [Azi96].

A standard second-order Σ–Δ modulator is constructed by adding another accumulator to the first-order Σ–Δ modulator as shown in Figure 2-5a, which consists of two accumulators in the feedforward path, a quantizer and a feedback loop. The output spectrum of the second-order Σ–Δ modulator with a normalized input frequency of 0.01 and an amplitude of 0.5 is given in Figure 2-5b, which shows that the quantization noise is shaped to outside the signal band. In order to achieve Nth-order Σ–Δ modulators, N-accumulators are added in the feedforward path as given in Figure 2-5c.

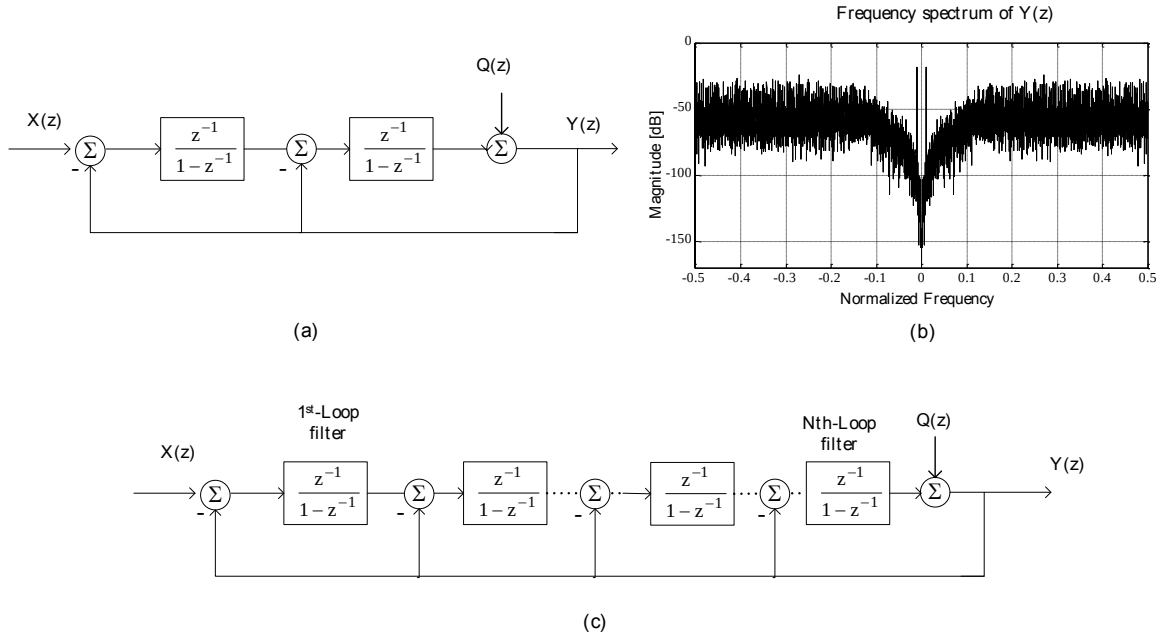

Figure 2-5 (a) Block diagram of second-order Σ–Δ modulator, (b) output frequency spectrum of the second-order Σ–Δ modulator, (c) block diagram of Nth-order Σ–Δ modulator

The output signal of the second-order Σ–Δ modulator is given by:

$$Y(z) = X(z) + \underbrace{(1-z^{-1})^2}_{NTF} Q(z) \tag{2.22}$$

This gives the NTF as $(1-z^{-1})^2$. The past two samples are cancelled in the NTF, which results in more attenuation at the low frequencies. The power of the output noise can be computed using the squared magnitude of the NTF as a function of frequency, in a similar way as calculated for first-order Σ–Δ modulators. Therefore, the noise power can be written as:

$$\sigma_{qb}^2 = \sigma_q^2 \frac{\pi^4}{5}\left(\frac{2f_B}{f_s}\right)^5 \tag{2.23}$$

Using (2.23), the SNR of a second-order Σ–Δ modulator is calculated as:

$$SNR = 10\log(\frac{\sigma_x^2}{\sigma_q^2}) - 1.29 + 50\log\left(\frac{f_s}{2f_B}\right)(dB) \tag{2.24}$$

Thus, for every doubling of OSR the SNR improves by 15.05 dB, or 2.5 bits of resolution. This is 1-bit better than that of a first-order Σ–Δ modulator.

The frequency spectra of first-, second- and third-order Σ–Δ modulators for a sinusoidal input signal amplitude of 0.5 and normalized frequency of 0.01 are shown and compared in Figure 2-6.

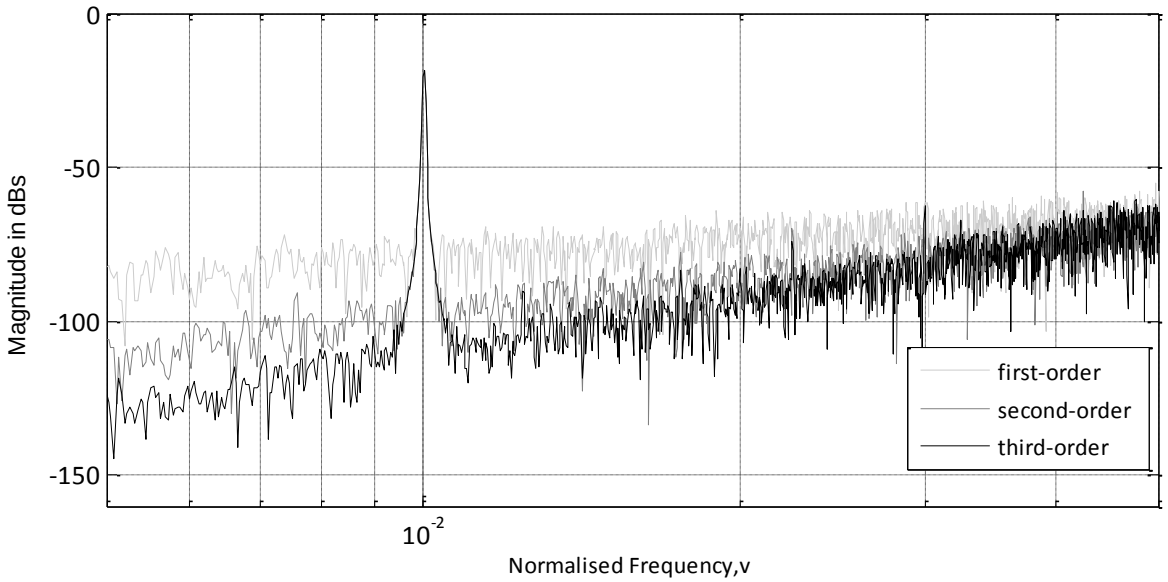

Figure 2-6 Frequency spectrum of first-, second- and third-order Σ–Δ modulator

As seen in Figure 2-6, the attenuation of the quantization noise in the signal-band increases as the order of the modulator increases.

As given in Figure 2-5b, higher-order Σ–Δ modulators are a straightforward extension of the first-order Σ–Δ modulator with extra accumulators added in the feedforward loop. As the order (N) of the modulator increases, the attenuation of the NTF at the lower frequencies becomes higher by pushing more noise power out of the signal band as demonstrated in Figure 2-7.

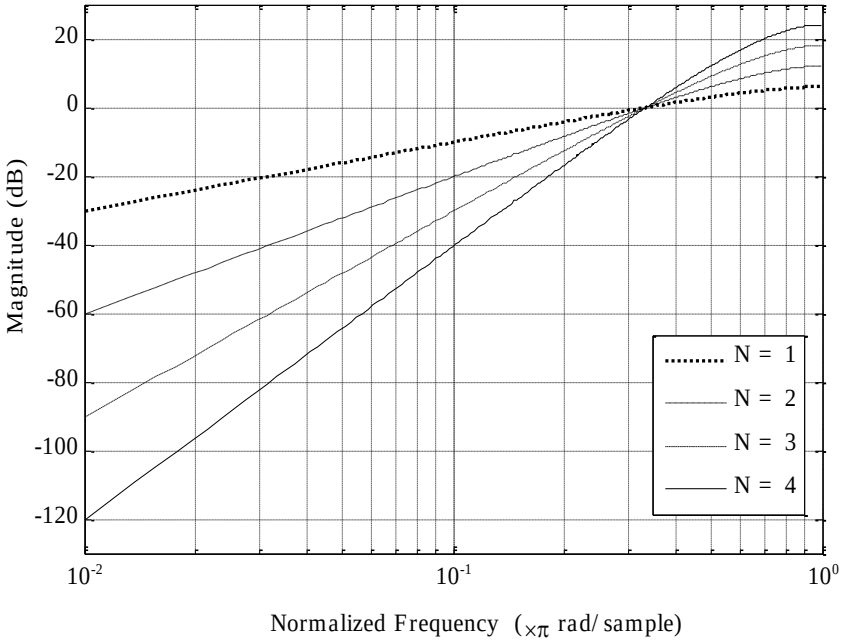

Figure 2-7 Frequency responses of the NTF of Σ–Δ Modulator of the Nth-order

The output signal in the z-domain of an Nth-order Σ–Δ modulator is given by:

$$Y(z) = X(z) + \underbrace{(1 - z^{-1})^N}_{NTF} Q(z) \tag{2.25}$$

Therefore the in-band SNR value can be computed in the same manner as in the case of first- and second-order Σ-Δ modulators [Azi96]:

$$SNR = 10\log(\frac{\sigma_x^2}{\sigma_q^2}) - 10\log\left(\frac{\pi^{2N}}{2N+1}\right) + 10(2N+1)\log\left(\frac{f_s}{2f_B}\right)(dB) \tag{2.26}$$

As seen in (2.26) for every doubling of the OSR, the SNR improves as much as (6N + 3) dB, or (N + 0.5) bits of resolution. The relationship of the SNR versus the OSR for first to fourth order Σ–Δ modulators is given in Figure 2-8.

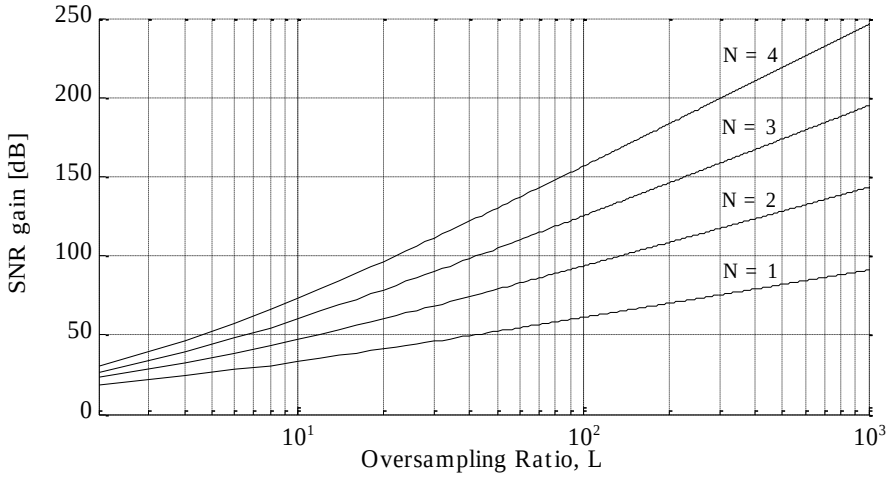

Figure 2-8 SNR gain of Σ–Δ modulators of order N=1,2,3,4 for increasing OSR values

The theoretical results which utilize the approximate linear model for the quantizer are shown in Figure 2-7 and Figure 2-8. In practice, they are different because of the non-linearity of the 1-bit quantizer [Lee87], [Nor97].

2.5.2 Higher-order Σ–Δ Modulators: Stability

Higher-order 1-bit Σ–Δ modulators (i.e. above second-order) are conditionally stable. Instability in Σ–Δ modulators occurs when the internal signal levels in the Σ–Δ modulators grow indefinitely. This uncontrollable growth causes the quantizer to overload permanently making the feedback ineffective. The Σ–Δ modulator output in the time-domain may exhibit an indefinite string of 1's or -1's. The Σ–Δ modulator will no longer be able to achieve noise-shaping, thus resulting in very low SNRs and poor resolution [Ada94], [Can81], [Leu92], [Nor97].

The stability of these Σ–Δ modulators depends on the modulator input amplitude, type of input signal, the total delay in the feedforward and/or feedback paths as well as the characteristics of the loop-filter [Agr83], [Ada91], [Can85], [Koz03], [Nor97], [Ris94], [San08].

Respectable SNRs for relatively low OSRs can be accomplished with higher-order 1-bit Σ–Δ modulators. These higher-order Σ–Δ modulators are generally less tonal than their lower-order counterparts [Azi96], [Alj00], [Nor97].

2.5.3 Multi-stage Σ–Δ Modulators

The cascaded structure can be used to design high-order Σ–Δ modulators to overcome the stability problems of single-stage Σ–Δ modulators and at the same time provide high resolution [Uch88]. The multi-stage noise-shaping (MASH) topology consists of cascaded low-order (first or second) single-stage Σ–Δ modulators [Mat89]. Each Σ–Δ modulator converts the quantization error from the previous modulator. The outputs of each stage are digitally combined with suitable digital filters so as to achieve quantization noise cancellation of the intermediate stages [Azi96], [Uch88]. Figure 2-9 gives the structure of a double-stage modulator.

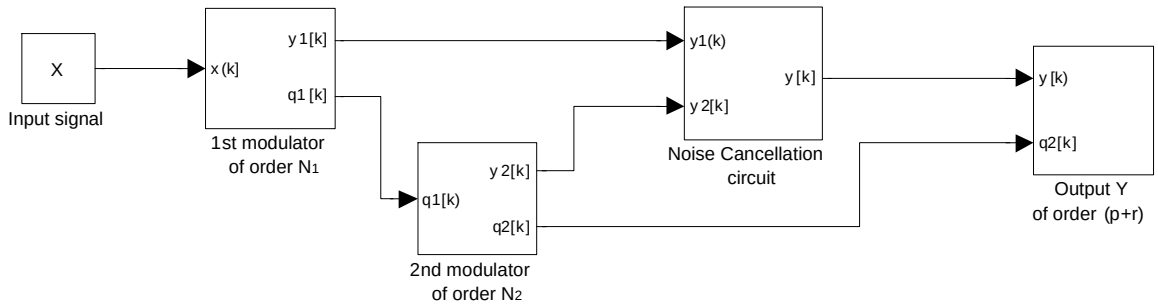

Figure 2-9 Block diagram of a cascaded Σ–Δ the modulator

As seen in Figure 2-9, the quantization noise of the 1st modulator $q_1(k)$ is the input of the 2nd modulator while the output of the second modulator $y_2(k)$ is combined with the output of the first modulator $y_1(k)$ via a noise cancellation circuit. As a result, the first stage quantization noise is cancelled digitally. The system can be analysed in the z-domain as follows:

$$Y_1(z) = STF_1 X(z) + NTF_1 Q_1(z) \tag{2.27}$$

$$Y_2(z) = STF_2 Q_1(z) + NTF_2 Q_2(z) \tag{2.28}$$

The noise transfer functions of the first and second modulators are $NTF_1 = (1 - z^{-1})^{N_1}$ and $NTF_2 = (1 - z^{-1})^{N_2}$ respectively, where N_1 and N_2 denote the order of the modulators. The corresponding STF's are; $STF_1 = (z^{-1})^{N_1}$, $STF_2 = (z^{-1})^{N_2}$ for the first and second modulator respectively. Then the outputs of the modulators become:

$$Y_1(z) = z^{-N_1} X(z) + (1 - z^{-1})^{N_1} Q_1(z) \tag{2.29}$$

$$Y_2(z) = z^{-N_2} Q_1(z) + (1 - z^{-1})^{N_2} Q_2(z) \tag{2.30}$$

The noise cancellation circuit removes the quantization error of the first modulator, $Q_1(z)$ by the following process in the digital domain:

$$Y(z) = STF_2 Y_1(z) - NTF_1 Y_2(z) \tag{2.31}$$

Using the explicit forms of the transfer function given in (2.29) and (2.30), the output becomes;

$$Y(z) = z^{-(N_1+N_2)} X(z) + (1 - z^{-1})^{N_1+N_2} Q_2(z) \tag{2.32}$$

As seen in (2.32), the first stage error is cancelled digitally by the signal processing of the cancellation circuit. Howover, the signal is just delayed at the output while the quantization error contributed from the second modulator is shaped by the NTF of order $N_1 + N_2$.

The overall Σ–Δ modulator is still stable because this multi-stage topology contains only feedforward paths and no feedbacks between the single-stage modulators [Azi96], [Nor97]. Using the advantage of the inherent stability of low-order Σ–Δ modulators, high order modulators of any order can be constructed. Beside the improvements in stability, the cascaded Σ–Δ modulators have fewer tones compared to a first- or second- order Σ–Δ modulators [Can92], [Gra90].

In practice, however, the error contribution from the first Σ–Δ modulator, $Q_1(z)$, does not completely cancel out because the NTF of the first modulator may not be exactly equal to $NTF_1 = (1 - z^{-1})^{N_1}$. The mismatch of the components and the non-idealities of the op-amps cause residual noise at the output. The noise leakage is [Mal07]:

$$Q_{1,out}(z) = (NTF_{expected} - NTF_{ideal}) Q_1(z) \tag{2.33}$$

The non-idealities cause a shift in the NTF by a small amount as much as δ so that the zero of the NTF is moved from $z = 1$ to $z = 1 - \delta$. When the case of the first order modulator is considered, then the residual noise term becomes:

$$Q_{1,out}(z) = [(1 - z^{-1}) - (1 - (1 - \delta)z^{-1})] \cdot Q_1(z) = \delta \cdot z^{-1} \cdot Q_1(z) \tag{2.34}$$

The quantization noise of the second Σ–Δ modulator, $Q_2(z)$, is attenuated by an order $N_1 + N_2$ as seen in (2.32) and the in-band quantization noise power of the residual noise $Q_{1,out}(z)$ is shaped by δ^2, which is lower than that of $Q_2(z)$.

$$\log(\frac{\delta^2}{OSR}) < \log\left(\frac{\pi^{2N}}{2N+1} \cdot \frac{1}{OSR^{2N+1}}\right) \tag{2.35}$$

Therefore the overall in-band SNR value given in (2.26) does not become worse. However, in practice the non-idealities become more significant for a MASH Σ–Δ modulator structure that has more than 3 stages [Lia14], [Mal07].

Figure 2-10 gives the output spectrums of third-order Σ–Δ modulators using single-stage structure and a 1-1-1 cascaded structure for an input signal amplitude of 0.5 and a normalized frequency of 0.01. The output frequency spectrum of the MASH structure has fewer tones and higher attenuation of the noise components in the signal-band, compared to the single-stage structure.

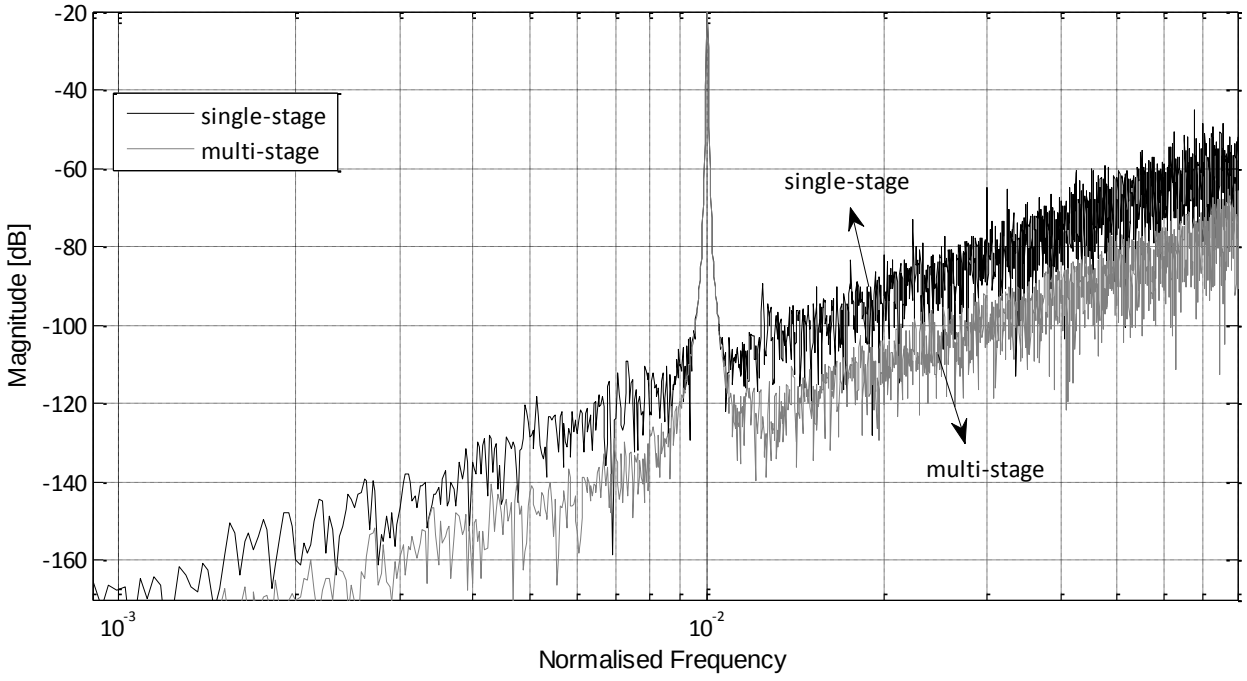

Figure 2-10 Third-order Σ–Δ modulator using single-stage and multi-stage structures

As a result of the MASH structure, a higher-order Σ–Δ modulator is obtained whose overall stability is guaranteed by the unconditional stable low-order Σ–Δ modulators. Higher-order structures are usually designed from first-order modulators or also using second-order modulators [Uch88], [Wil94], [Yin93].

The main features of single-stage (low- and higher-order) and multi-stage LP Σ–Δ modulators are given in Table 2-1 [Nor97].

MODULATOR STRUCTURE	Design complexity	SNR	Stability	Tonality
Single-stage (low-order)	Simple	Low	Unconditional stable	High
Single-stage (high-order)	Moderate	High	Conditional stable	Moderate
Multi-stage	Moderate	High	Stability guaranteed	Low

Table 2-1 Comparative features: the single-stage and multi-stage Σ–Δ modulators

2.5.4 Loop-Filter Topologies

There are many structures that can be used to design LP Σ–Δ modulators [Nor97]. These can be modified by adding extra feedback paths. The most frequently used structures are: the chain of accumulators with weighted feedforward summation and chain of accumulators with feedforward summation with local resonator feedbacks[Fer90], [Nor97], [Mou94], [Wel89].

2.5.5 Weighted Feedforward Summation

Using the *N*-th order pure differencer $H(z) = (1 - z^{-1})^N$ as the NTF causes instability for higher orders, as previously discussed. One solution to this problem is to introduce poles into the $H(z)$ so as to flatten the magnitude response at the higher frequencies [Ada94]:

$$H(z) = \frac{(z-1)^N}{D(z)} \tag{2.36}$$

As seen in Figure 2-11, the $H(z)$ has a flat response in the out-of-band region due to the $D(z)$ in the denominator.

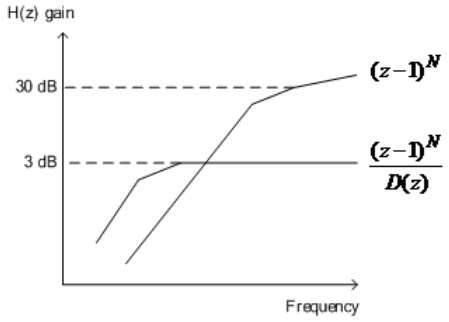

Figure 2-11 The comparison of the frequency responses of the $H(z)$ after modification [Nor97]

The poles can be chosen according to a Butterworth alignment so that the 3dB-gain rules as well as the causality rules are satisfied [Nor97].

The weighted feedforward topology consists of cascaded accumulators with the transfer functions $H(z) = z^{-1} / 1 - z^{-1}$, whose outputs are weighted and summed up to form the overall loop-filter, $L(z)$. The summation output is used as the input of the quantizer generating the feedback signal $Y(z)$[Nor97]. The Σ–Δ modulator loop should have a delay of at least one sample period to ensure the causality of the modulator [Erg99], as shown in Figure 2-12.

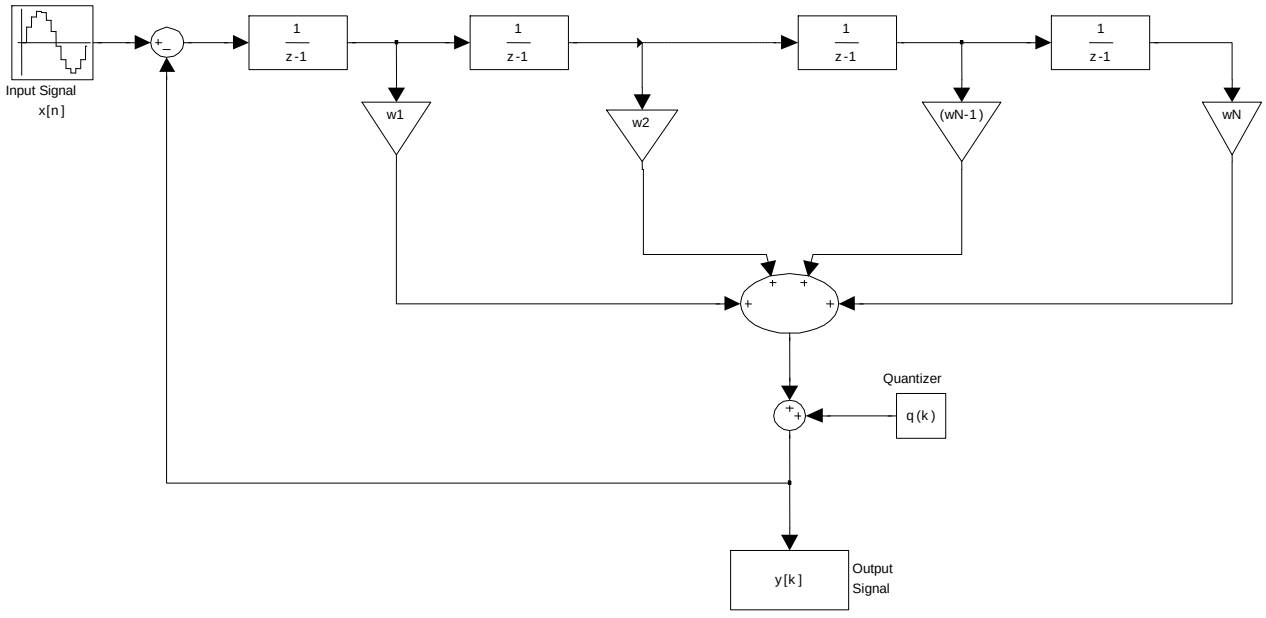

Figure 2-12 Chain of accumulators with weighted feedforward summation

For this topology, the transfer function of the loop-filter, L(z) is:

$$L(z) = \frac{1}{(z-1)} \cdot w_1 + \frac{1}{(z-1)^2} \cdot w_2 + \frac{1}{(z-1)^3} \cdot w_3 + ... + \frac{1}{(z-1)^N} \cdot w_N \qquad (2.37)$$

where, N is the order of the loop-filter, and the w's values are the feedforward coefficients which are a function of the loop-filter or NTF zeros. As seen in (2.37), all the poles of $L(z)$ are at dc, i.e. at $z = 1$. Therefore, a Butterworth high-pass filter can be used to obtain suitable coefficients that will ensure the stability of the Σ–Δ modulator. Once the NTF is obtained, the corresponding $L(z)$ can be computed from the relationship; $NTF = \frac{1}{1+L(z)}$. This is then equated to the Butterworth NTF to calculate the feedforward coefficients.

2.5.6 **Feedforward Summation with Local Feedbacks**

The Butterworth response can be modified so that the zeros are moved from dc to other frequencies (i.e. to the complex locations) on the unit-circle in the vicinity of dc (zero-splitting). As a result of these complex alignments, compared to the Butterworth case, more attenuation of the quantization noise in the in-band region is achieved resulting in improved SNR [Nor97]. In order to have complex zeros besides the real zeros, one should use inverse Chebyshev filters instead of Butterworth filters [Ada94], [Nor97], [Sch05], [Sno01]. The lower and upper frequencies of the NTF are selected so as to ensure that the input signal is positioned at the center of the signal bandwidth.

For relatively large signal bands, the zeros of the NTF do not need to be positioned at particular frequencies to reduce the noise at certain points. Instead, it is necessary to have an overall low noise level across the entire signal band [Mal07]. The distribution of the NTF zeros across the signal band will cause moderate attenuation, when compared with having all zeros concentrated at a single frequency. The corresponding Σ–Δ modulator structure to achieve this is shown in Figure 2-13, where negative feedback around pairs of accumulators is added, so that the zeros of the loop-filter are shifted away from $z = 1$ [Nor97]. As seen in Figure 2-13, the second accumulators of the pairs are delay-free.

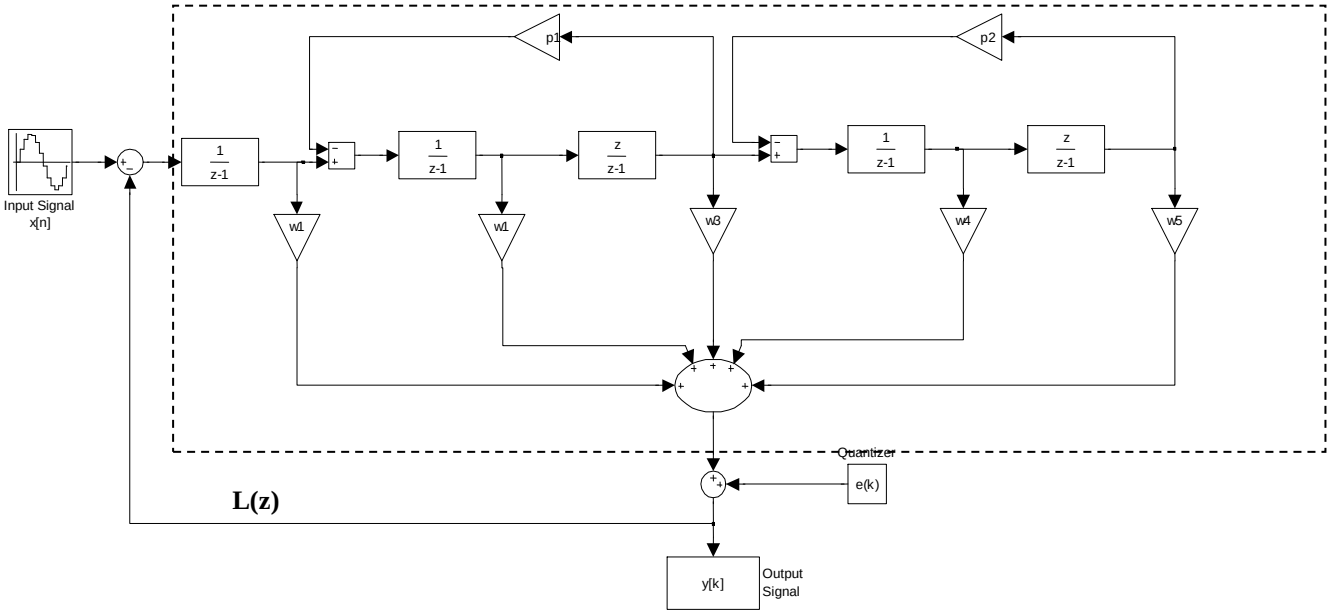

Figure 2-13 5th order Σ–Δ modulator using the chain of accumulators structure with local feedbacks

The w's, are the feedforward gains and the p's are the feedback coefficients around the accumulator pairs. For the case of one pair of the accumulators, the loop transfer function yields:

$$L(z) = \frac{z(w_1 + w_2) - w_1}{z^2 + z(p_1 - 2) + 1} \tag{2.38}$$

As seen in (2.38), the poles of the $L(z)$ are moved away from the real axis to complex positions on the unit-circle. Inverse Chebyshev based NTFs provide such flexibility and are well suited for such Σ–Δ modulator structures [Ada94], [Nor97]. The coefficients can be solved by equating $L(z)$, to the NTF of the Inverse Chebyshev filter [Ada94], [Nor97].

The poles of the transfer function of the loop-filter become the zeros of the corresponding NTF, therefore the local feedbacks actually determine the shift of zeros away from $z = 1$. These zeros can be used to have a flat transfer function in the signal band and prevent a high STF gain at higher frequencies so as to ensure stability and high resolution. The signal band may be extended but this will be at the cost of a lower SNR value [Alj00], [Sno01], [Mal07].

- The feedforward coefficients for a third-order Butterworth filter are calculated: $w_1 = 0.3138$, $w_2 = 0.0473$, $w_3 = 0.0033$.

- For a third-order inverse Chebyshev filter, the feedforward coefficients are: w_1 = 0.3648, w_2 = 0.0573, w_3 = 0.0012 and the feedback coefficient: p_1 = 0.0185.

Figure 2-14 compares the simulation results of the NTFs of third-order Σ–Δ modulators with (a) weighted feedback summation structure, that has all the zeros at $z = 1$, (b) weighted feedback summation with local resonators, that has one zero at $z = 1$ and others moved to complex conjugates on the unit-circle.

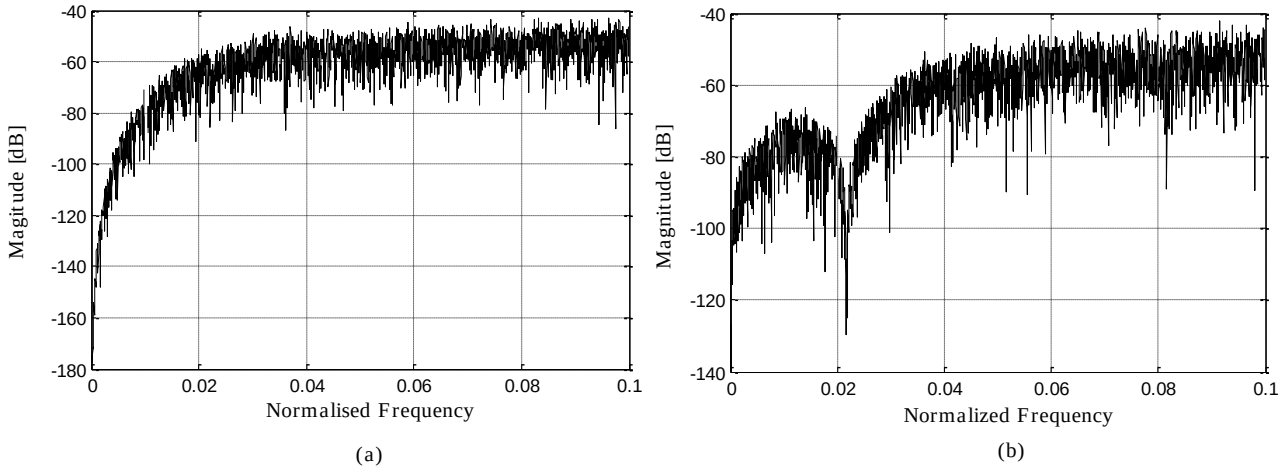

Figure 2-14 NTFs of a third order Σ–Δ modulator using chain of accumulators with (a) weighted feedforward summation, (b) weighted feedforward summation and local feedbacks

At low frequencies, there is higher noise suppression when all the zeros of the NTF are at $z = 1$, as shown in Figure 2-14. As a comparison; in (a) all the zeros are located at dc ($z=1$) and in (b) there are complex conjugate zeros. However, for a signal-band at the frequencies around $v = 0.02$, the second modulator with the complex zeros becomes more effective in terms of noise-shaping.

2.6 Band-Pass Σ–Δ Modulators

BP Σ–Δ modulators have been reported to be applied in the ultrasound front-end structures [Nor96]. According to the band-pass sampling theorem, BP Σ–Δ modulators have a sampling rate much greater than the signal bandwidth instead of the highest frequency in the input signal, $f_s >> f_B$ [Zri05].

The NTF of a BP Σ–Δ modulator is designed to have a very low gain in the signal band centred at f_0 in order to ensure minimum quantization noise in the in-band-region. [Sch89]. The corresponding block diagram and the frequency responses of the NTF and the STF are given in Figure 2-15. LP or BP Σ–Δ modulators, have a small amount of noise in the narrow band around the zeros of the NTF. Therefore, unlike the high-pass NTFs of the LP Σ–Δ modulators, that have zeros at around $z = 1$, the NTFs realized by the BP Σ–Δ modulators have zeros in the signal band around f_0, where the NTF is a band-stop filter. The loop-filter must have a very large gain in the signal region $[f_o \pm f_B/2]$ [Azi96], [Pau87].

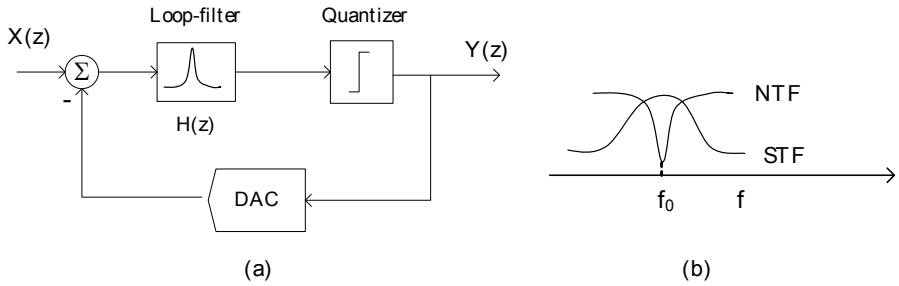

Figure 2-15 (a) Block diagram of a BP Σ–Δ modulator (b) Typical NTF and STF [Mal07]

Moving the zeros of the NTF from dc to complex conjugates on the unit-circle cause the gain of the NTF to be close to zero around the centre frequency, f_0 [Sch89]. As given in Section 2.5.1 the zeros of NTF become the poles of the loop-filter, $H(z)$, which directly defines the STF of the Σ–Δ modulator. Therefore, the minimum gain of the NTF in the in-band-region makes the gain of $H(z)$ a very large value. The STF becomes unity in the signal region, while away from f_0, the NTF pushes the quantization noise to the out-of-band region, as illustrated in Figure 2-15b.

2.6.1 **Loop-Filter Design**

The simplest and commonest way to design the loop-filter for a BP Σ–Δ modulator is to derive it from a LP Σ–Δ modulator via simple mathematical transformations as reported in [Sch89]. For this, a low-pass-to-band-pass ($LP \rightarrow BP$) transformation is applied to any

LP single- or multi-stage Σ–Δ modulator, so that from a LP Σ–Δ modulator of order N, a BP modulator of order $2N$ is obtained [Jan91], [Jan93], [Nor97], [Rib94].

The loop-filter transfer function can be obtained by applying a low-pass-to-band-pass transformation at the points $z = \pm e^{j2\pi\nu}$. By moving the zeros from $z = 1$ to complex conjugates, the NTF becomes:

$$NTF = \frac{(z - e^{j2\pi\nu}) \cdot (z - e^{-j2\pi\nu})}{z^2} \tag{2.39}$$

This results in:

$$NTF = \frac{z^2 - z \cdot (e^{j2\pi\nu} + e^{-j2\pi\nu}) + 1}{z^2} \tag{2.40}$$

Using the Euler identity [Tho05], the NTF is:

$$NTF = \frac{z^2 - z \cdot 2\cos 2\pi\nu + 1}{z^2} \tag{2.41}$$

This NTF can be expressed as:

$$NTF = 1 - (2\cos 2\pi\nu) \cdot z^{-1} + z^{-2} \tag{2.42}$$

Since $H(z) = \frac{1 - NTF}{NTF}$, the transfer function of the loop-filter becomes:

$$H(z) = \frac{2\cos 2\pi\nu \cdot z^{-1} - z^{-2}}{1 - 2\cos 2\pi\nu \cdot z^{-1} + z^{-2}} \tag{2.43}$$

The above generalised equation (2.43) is valid for any normalized frequency ν value. Some normalised centre frequencies such as when $\upsilon = 1/4$, $\upsilon = 1/3$ and $\upsilon = 1/6$ result in simpler hardware as they do not require any coefficients [Nor97]. For the case of $\nu = 0.25$, which implies that $2\pi\nu = \pi/2$ or $z = \pm e^{j2\pi\nu} = \pm j$, the loop-filter becomes:

$$H(z) = \frac{-z^{-2}}{1 + z^{-2}} \tag{2.44}$$

The transformation of $z \rightarrow -z^2$ for the LP loop-filter, doubles the order of the NTF and shifts the zeros of the NTF from dc to $\pm\pi/2$ i.e. from $z = 1$ to $z = \pm j$. The corresponding locations of the zeros of the LP and BP NTFs are given in Figure 2-16.

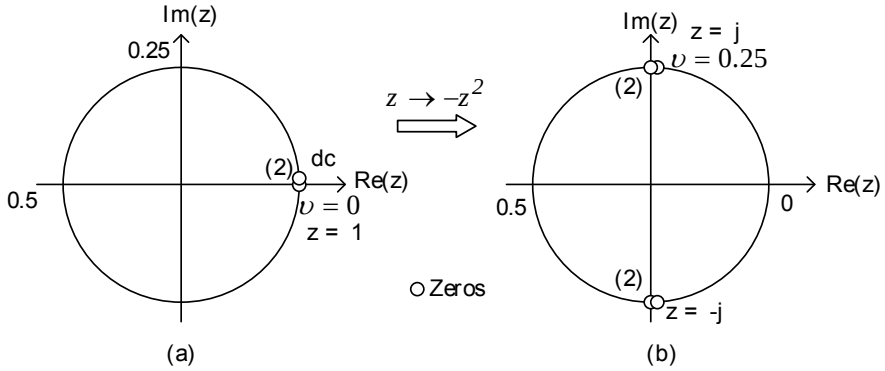

Figure 2-16 The zero alignments of the NTFs for (a) second-order low-pass (b) fourth-order band-pass Σ–Δ modulators

Figure 2-17 presents a transformed BP version of the second-order LP modulator given in Figure 2-5a. For the mid-band resonator, the stability as well as the noise properties of the original LP Σ–Δ modulator is preserved [Jan93], [Nor97], [Rib94].

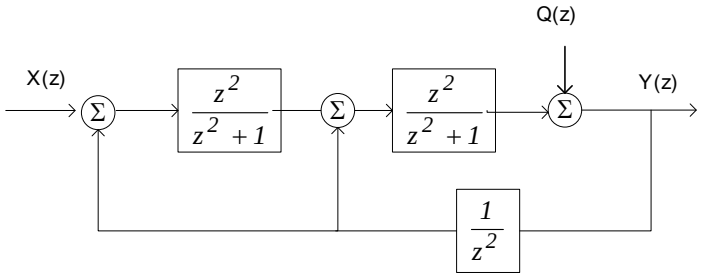

Figure 2-17 A fourth-order band-pass Σ–Δ modulator obtained with $LP \rightarrow BP$ transformation

Another case is $\nu = 0.125$, that gives $2\pi\nu = \pi/4$, so that the loop-filter becomes;

$$H(z) = \frac{z^{-1}\sqrt{2} - z^{-2}}{1 - z^{-1}\sqrt{2} + z^{-2}} \tag{2.45}$$

2.7 High-Pass Σ–Δ Modulators

The range of applications offered by HP Σ–Δ modulators together with their numerous advantages, are well detailed in the literature [Ish03], [Ral07]. HP Σ–Δ modulators have been used in very high frequency Class-S power amplifiers for wireless communication applications because they reduce the switching rate [Ral07]. Chopper-stabilized HP Σ–Δ modulators are well suited in micro-power A/D converters for low frequency small signal applications in order to reduce the low-frequency noise such as thermal drift, dc offset and 1/f noise [Nyg06], [Ish03]. In addition, a high-pass sigma delta modulator-based bio-signal processor can be applied for signal acquisition and digitization [Chi15], [Lee15].

For HP Σ–Δ modulators, the NTFs have minimum gains at the higher frequencies in order to attenuate the in-band quantization noise at high frequencies [Nyg06], [Ish03], [Ral07]. The locations of zeros of the NTF of HP Σ–Δ modulator are shown in Figure 2-18.

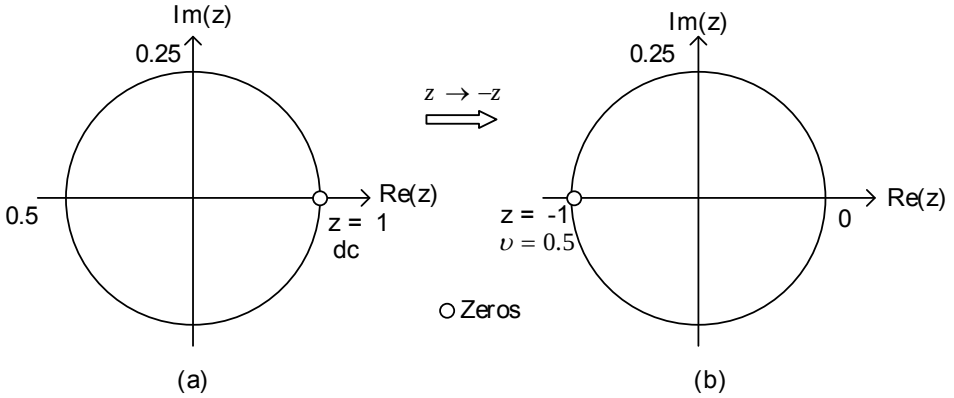

Figure 2-18 Zero locations of NTF of a first-order (a) LP Σ–Δ modulator, (b) HP Σ–Δ modulator

Thus, as seen in Figure 2-18, a $LP \rightarrow HP$ transformation in the z-domain is applied to LP Σ–Δ modulators to shift the zero locations from $z = 1$ to $z = -1$, i.e. the zeros of NTF are shifted from dc to $f_s/2$. Therefore, the transformation $z \rightarrow -z$ is applied to the STF and NTF of the LP Σ–Δ modulator:

$$STF\big|_{LP}(z) \rightarrow STF(-z) \tag{2.46}$$

$$NTF\,|_{LP}(z) \rightarrow NTF\,(-z) \tag{2.47}$$

Therefore, the loop-filter of a HP Σ–Δ modulator, $H(z)$ can be written as:

$$H(z) = \frac{-z^{-1}}{1+z^{-1}} \tag{2.48}$$

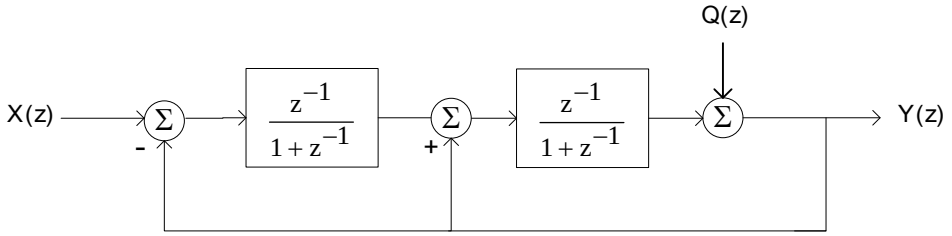

Figure 2-19 Block diagram of second-order HP Σ–Δ modulator

As seen in Figure 2-19, the output signal, Y(z) can be written as:

$$Y(z) = z^{-2}X(z) + (1+z^{-1})^2 Q(z) \tag{2.49}$$

2.8 Concluding Remarks

In this chapter, a comprehensive study to examine the design methodologies of Σ–Δ modulators was reviewed in order to analyze the limitations of Σ–Δ modulator based ultrasound beamformers. Σ–Δ modulators are based on oversampling and noise-shaping, which cause the quantization noise to spread over a region much larger than the signal bandwidth. Noise-shaping pushes most of the noise components to outside the signal band via error-feedback securing a significant attenuation of the quantization noise in the signal band. The SNR values of of 1-bit Σ–Δ modulators as a result of using the oversampling and noise-shaping techniques are much higher compared to the conventional Nyquist-rate converters. Using these advantages of 1-bit Σ–Δ converters over Nyquist-rate converters, Σ–Δ modulators are proposed to be used in the medical ultrasound system front-end instead of Nyquist A/D converters to digitize the incoming echo signals [Chi15], [Hem15], [Koz01], [Jun13]. It has been shown that the theoretical SNR values increase with the increased order of the Σ–Δ modulators. However, the Σ–Δ modulator based ultrasound

system applications are limited to low-order Σ–Δ modulators due to the stability problems of the higher-order Σ–Δ modulators. In order to ensure the stability of the modulators, the topologies such as the multi-stage, chain of accumulators with weighted feedforward summation and chain of accumulators with distributed feedback topologies are examined. The loop-filter design methodologies based on Butterworth- and Inverse Chebyshev filters responses were detailed. The performance analyses of the topologies were determined using the linear-model of the quantizer. However, this linear model does not adequately characterize the behavior of Σ–Δ modulators, because it assumes that the quantizer gain is independent of the Σ–Δ modulator input amplitude. Therefore, in the next chapter, a more accurate quasi-linear model of the quantizer is proposed in order to analyse the stability of the higher-order LP, BP and HP Σ–Δ modulators.

Chapter 3

Stability Analysis of HP and BP Σ–Δ Modulators

Higher-order Σ–Δ modulators provide high SNR values, however they may suffer from stability problems [Hei92], [Hei93],[Rei05]. The non-linearity of the 1-bit quantizer makes the prediction of the stable input amplitude limits for higher-order Σ–Δ modulators complicated [Rei08], [Ste94], [Wan93], [Wol88]. In this chapter, quasi-linear modeling of the quantizer in combination with the Describing Function (DF) method is used to determine the stability boundaries of higher-order Σ–Δ modulators. In Section 3.1 an overview of the stability analysis of Σ–Δ modulators is given. In Section 3.2 the principles of quasi-linear modeling of the quantizer are detailed. The quasi-linear stability analysis of Σ–Δ modulators based on the noise amplification curves for different quantizer gain values are described. In Section 3.3 the input- and quantization noise- variances at the input to the quantizer are established. The DF methods to derive the noise amplification curves for single- and dual sinusoidal inputs are explained. The theoretical results for stability boundaries for HP and BP Σ–Δ modulators are given in Section 3.4 The theoretical and simulated maximum-stable-amplitude (MSA) values are compared and discussed in Section 3.5 The accuracy of the proposed quantizer model is verified in terms of a variety of Σ–Δ modulator specifications such as the bandwidth, modulator order and stop-band attenuation. The effect of adding a dither signal to the Σ–Δ modulator is also evaluated.

3.1 An Overview of Stability Analysis of Σ–Δ Modulators

As discussed in Section 2.5.2 the stability of Σ–Δ modulators depends on the input signal, initial conditions, and the number of quantizer levels as well as the modulator order. The one-bit quantizer is the main source of the non-linearity. This directly affects the overall stability of the Σ–Δ modulator [Ard87], [Sch91]. As the order of the modulator increases, the internal signal amplitudes in the feedforward path continue to grow, which cause the input to the quantizer to significantly exceed the magnitude of the signal in the feedback path. As a result of this, the quantizer enters into unrecoverable oscillations resulting in Σ–Δ modulator instability. In addition, as the order of the modulator increases most of the quantization noise power is shifted towards the out-of-band region. Therefore, higher-order Σ–Δ modulators are more prone to instability compared to lower-order Σ–Δ modulators. The stability of higher Σ–Δ modulators can be more accurately examined by analysing the quantizer input signal as well as the order of the NTF.

Therefore, time consuming simulations are required for verifying stability. In order to establish the stability boundaries of LP Σ–Δ modulators, many different approaches were reported in the open literature [Agr83], [Ard87], [Cha90], [Chi09], [Far98], [Fra00], [Fra02], [Goo95], [Hei92], [Hon92], [Lot08], [Lot14],[Rei05], [Rei08], [Rit90], [Ris94a], [Ris94b], [Sab14], [Sch91], [Sch97], [Ste94], [Won03], [Zha03], [Zri05]. However, these techniques are limited to LP Σ–Δ modulators. In order to simplify the stability analysis, the input signal is assumed to be DC- or a single-tone sinusoidal signal. For dual inputs, i.e. two sinusoidal inputs, the stability analyses become even more complicated.

However, an extensive literature review has revealed the lack of detailed stability analysis of higher-order BP Σ–Δ modulators. Moreover and to the best knowledge of the author, there has not been any work reported in the open literature on the stability analysis of HP Σ–Δ modulators. A survey of the major publications on the stability analysis of Σ–Δ modulators reported in the open literature is given in Table 3-1.

Summary of Publications	Limitations	Ref
Finding invariant sets by iterating the initial region and enlarging it until an invariant region is found.	Computationally intensive and lacks a closed form mathematical model.	[Goo95] [Sch97] [Nor97]
A trapping region is found in which the integrator output of a second-order Σ–Δ modulator will never take on values outside that region.	Restricted to low-order Σ–Δ modulators.	[Far98]
An empirical stability criteria for a fourth-order Σ–Δ modulator is proposed	Dependent on simulations and the modulator order.	[Chi09]
Modeling the quantizer as a threshold function in the state equations.	Analytically complex, limited to first- and second-order Σ–Δ modulators	[Hon92] [Ste94]
Analysis of BP Σ–Δ modulators using non-linear dynamics for zero- and single-tone sinusoidal inputs	Lack of an analytical expression for stability boundaries	[Fee95] [Fee96] [Fee97]
Linear modelling of the quantizer as representing the quantizer as an additive white noise source with unity gain	Do not link the effect of the input signal to the modulator output spectrum	[Agr83] [Can85] [Sch91] [Sch97] [Hei92]
Quasi-linear modelling of the quantizer, wherein the quantizer is modelled as a additive white noise with a linear gain	Limited to DC- or a single-tone sinusoidal input signal, lack of analytical stability boundaries	[Ada91] [Ard87] [Cha90] [Nau87] [Sti88] [Wol88]
Extended quasi-linear model to more than one input using the DF method, where each input is represented by a separate equivalent gain.	Limited stability analysis depending on the order of the modulator	[Gel68] [Ard87]
Mathematical models for the stability boundaries by establishing noise amplification curves	Limited to DC signals	[Ris94a] [Ris94b]
Extended Quasi-linear model of the quantizer in conjunction with DF method using noise amplification factors	Derived for LP Σ–Δ modulators	[Lot07] [Lot08]
Non-linear feedback control analysis for multiple sinusoidals	Derived for LP Σ–Δ modulators	[Lot13] [Lot14]
Stability of various symmetric cross coupled Σ–Δ	Derived for LP Σ–Δ modulators,	[Sab14]

modulators by using the describing function theory	limited for low-orders	
Analytical root locus method to determine the stability criteria for continuous time Σ–Δ modulators	Derived for continuous-time Σ–Δ modulators	[Kan14] [Kan15]

Table 3-1 Survey of contributions for stability analysis of Σ–Δ Modulators

The commonest model of the quantizer, which is suitable for preliminary design analysis involves an additive white noise source with a unity gain. However, this model is inadequate for establishing the stability boundaries of Σ–Δ modulators, because it assumes that the quantizer gain is independent of the Σ–Δ modulator input amplitude. Since the gain of the quantizer correlates with the input signal, modelling the quantizer as an additive white noise source with a variable gain provides more accurate stability analysis especially for higher-order Σ–Δ modulators. Furthermore, in the linear model of the Σ–Δ modulator, the NTF changes as the loop-filter is scaled, whereas the actual modulator with a 1-bit quantizer is invariant to the scaling of the loop-filter. The use of the quasi-linear model of the quantizer with a variable gain enables the loop-filter scaling to be compensated with the reciprocal scaling of the quantizer gain so that the NTF maintains its invariance [Ris94a]. This quasi-linear approach can be extended to a more accurate quantizer model when combined with the DF method, where the input- and noise signals are represented by separate equivalent gains [Gel68] [Ard87]. However, DF analysis did not provide useful mathematical models to predict the stability boundaries in Σ–Δ modulators until the noise amplification factors were introduced by L. Risbo [Ris94a], [Ris94b]. Therefore, the quasi-linear model is further developed in conjunction with DF analysis and noise amplification factors [Lot08], [Lot14],[Sab14]. However, the accuracy of this method for HP and BP Σ–Δ modulators for different signal bandwidths, stop-band attenuations and modulator order has not been investigated by others to the best knowledge of the author.

Therefore, in this chapter, a variable gain quantizer model is used to obtain closed form mathematical expressions that define the stability boundaries of higher-order HP and BP Σ–Δ modulators [Alt10a], [Alt10b], [Alt11a]. The noise amplification curves as a function of the quantizer gain are established using the quasi-linear model. The noise amplification curves as a function of the signal- and noise-variances at the quantizer input are produced using the DF method. The stability boundaries of Σ–Δ modulators as a function of quantizer gain K, can be obtained by equating the mathematical expressions that define the two noise amplification curves. As a result, the MSA limits for different quantizer

gain values for single- and dual sinusoidal inputs are established from first principles using quasi-linear modelling in conjunction with the DF analysis. In addition, the stability boundaries are not restricted to a single Σ–Δ modulator structure and are in fact extended to the chain of loop-filters with weighted feedforward summation and chain of loop-filters with weighted feedforward summation and local feedback Σ–Δ modulator structures. The theoretical results obtained from the proposed model are validated using extensive simulations. The limitations of the model are established. The proposed mathematical models of the quantizer will immensely help speed up the design and evaluation of higher-order HP and BP Σ–Δ modulators.

3.2 Quasi-linear Stability Analysis of Σ–Δ Modulators

A Σ–Δ modulator contains a highly nonlinear component namely the 1-bit quantizer. The quantizer in a conventional Σ–Δ modulator can be modelled by a gain factor K followed by an additive white noise source with zero mean, $q(k)$ [Ris94a], [Ris94b] as given in Figure 3-1. Therefore, the non-linear modulator becomes a quasi-linear model with one output and two input signals: the first is the input to the modulator, $x(k)$ and the second is the quantization noise signal $q(k)$. Unlike the linear model representation given in Section 2.2 in the quasi-linear model, the quantization noise depends on both the value of K and the input signal amplitude. Thus the proposed model reflects the non-linear behavior of Σ–Δ modulators.

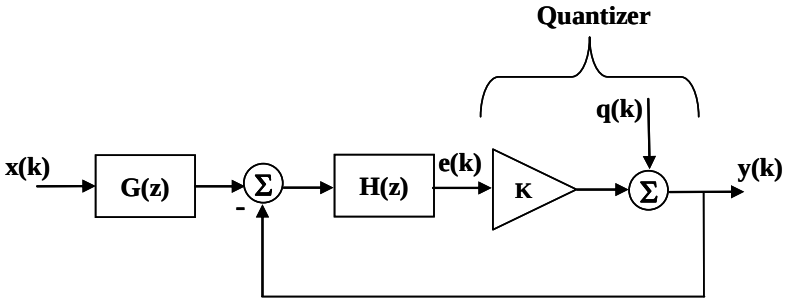

Figure 3-1 Quasi-linear model of Σ–Δ modulator

As discussed in Section 2.5 the output of the Σ–Δ modulator is:

$$Y(z) = STF_K(z) \cdot X(z) + NTF_K(z) \cdot Q(z) \tag{3.1}$$

The *K*-indices imply that both the STF and NTF are dependent on the *K* values. The NTF can be obtained from Figure 3-1.

$$NTF_K = \frac{1}{1 + K \cdot H(z)} \tag{3.2}$$

As known from linear system theory, the poles of a stable system must be inside the unit-circle. The modulator stability is therefore dependent on $H(z)$ and the K values, so that for a given $H(z)$, there will be a certain K interval $[K_{min}, K_{max}]$, which defines the Σ–Δ modulator stability [Sti88]. The quantization noise, $q(k)$, is assumed to be white noise with zero mean and variance σ_q^2. Since the NTF is the transfer function between the quantization noise and the output signal, the variance of the output signal is the result from the quantization noise filtered by the NTF. Therefore, as given in (3.3), the output noise variance can be defined in terms of the total noise power amplification factor, $A(K)$ [Ris94a], [Ris94b]:

$$Var\{y(k)\} = \sigma_q^2 \int_0^1 |NTF_K(e^{j\pi f})|^2 \, df = \sigma_q^2 \cdot A(K) \tag{3.3}$$

where $Var\{.\}$ denotes variance. Therefore, as seen in (3.3), the noise amplification factor is the ratio of the total output noise power to the quantization noise power. As a result, using Parseval's theorem, $A(K)$ yields the squared two norm of the $NTF_K(z)$, where $ntf_K(k)$ is the impulse response corresponding to $NTF_K(z)$ [Ris94a], [Ris94b]:

$$A(K) = \sum_{k=0}^{\infty} |ntf_K(k)|^2 \equiv \| NTF_K(z) \|_2^2 \tag{3.4}$$

Using (3.4), the $A(K)$ curve can be derived numerically, which is a function of K and NTF_K. The $A(K)$ curves are crucial for the design of stable Σ–Δ modulators, whose NTFs are given by: $NTF(z) = N(z)/D(z)$, where $N(z)$ and $D(z)$ are the N^{th} order polynomials in the z-domain. The corresponding loop-filter can be designed directly from the NTF-prototype by using:

$$H(z) = \frac{1}{K} \frac{D(z) - N(z)}{N(z)} \tag{3.5}$$

The $A(K)$ curve for a fifth-order Σ–Δ modulator with a stop-band attenuation, Rs of 85 dB is shown in Figure 3-2. This is an example to illustrate the behaviour of the $A(K)$ curves for variable K-values and there is no restriction for a modulator type, any NTF-prototype can be designed for HP- or BP Σ–Δ modulators according to the desired quantization noise attenuation. Therefore, different types of Butterworth- and Chebyshev Type II HP and BP loop-filers will be investigated in Section 3.4

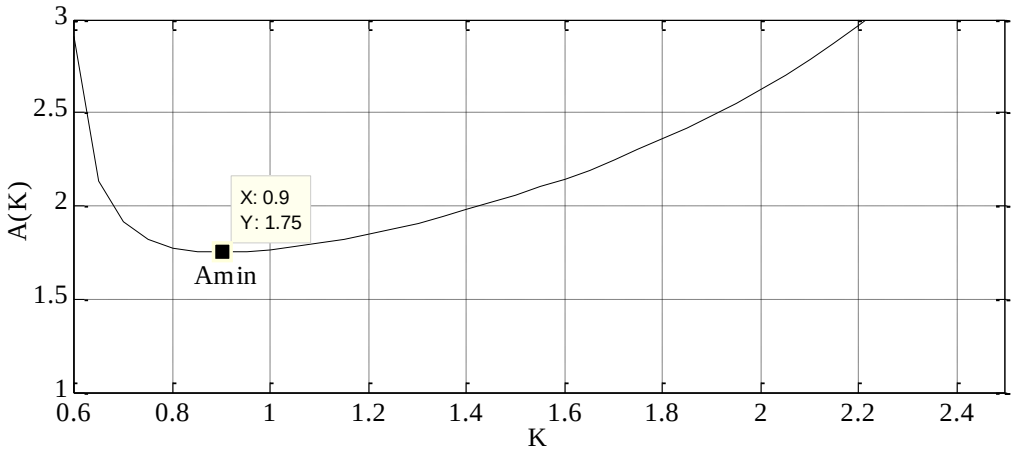

Figure 3-2 Noise amplification curve for fifth-order HP Σ–Δ modulator

As seen in Figure 3-2, the convex *A(K)* curve has global minima somewhere in the middle of the stable K intervals and becomes infinite at the endpoints of the K intervals. Higher K values increase the noise amplification factor *A(K)*, i.e. the circulating noise in the Σ–Δ modulator is increased. Since more noise is transferred to the quantizer input, the K values will tend to decrease. As a result, the Σ–Δ modulator is forced back to equilibrium. On the other hand, as the signal amplitude increases, the *A(K)* curve decreases which implies lower K values. The reduced loop gain perturbs the noise suppression of the loop and causes the in-band noise to increase. Therefore, in order to maintain the stability, the K values are forced to decrease, which forces the Σ–Δ modulator back to equilibrium. These decreasing and increasing *A(K)* values merge at one point, A_{min}. This global minimum of the curve, A_{min} depicts the onset of instability. At the A_{min} point, the Σ–Δ modulator operating state escapes to the left branch of the *A(K)* curve with a low quantizer gain value, K. The lower gain is more desirable in order to accommodate higher input signals before the Σ–Δ modulator becomes unstable. Thus the Σ–Δ modulator is stable for $A(K) \geq A_{min}$ [Ris94a], [Ris94b].

The stability of the Σ–Δ modulators can be established using *A(K)*-curves obtained by the quasi-linear analysis. However the quasi-linear model does not reflect the effects of the type of the input signal on the quantizer input. Therefore, the quasi-linear model is further modified using the DF method.

3.3 Modelling of the Non-linear Quantizer: DF Method

The quasi-linear analysis can be further developed using non-linear control analysis. The input signal to the quantizer consists of two parts, which are related to the modulator input signal and the quantization noise. Therefore, the quasi-linear model given in Figure 3-1 can be separated as a signal model with a linear gain K_x and a noise model with a linear gain K_n using the DF method [Ard87].

The following assumptions for the PDF of the signals have been made:

- $q(k)$, quantization noise signal: zero mean Gaussian distribution
- $e_n(k)$, noise-related-quantizer input: zero mean Gaussian distribution
- $x(k)$, input signal: a random variable (RV) with a phase having uniform distribution

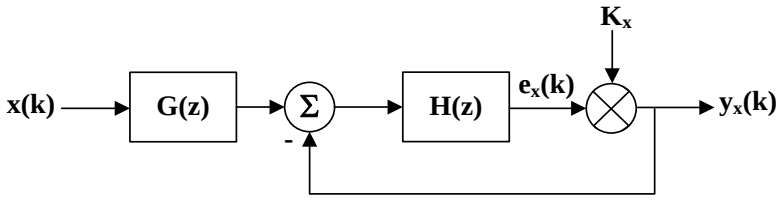

Figure 3-3 Equivalent Σ–Δ modulator model for sinusoidal input

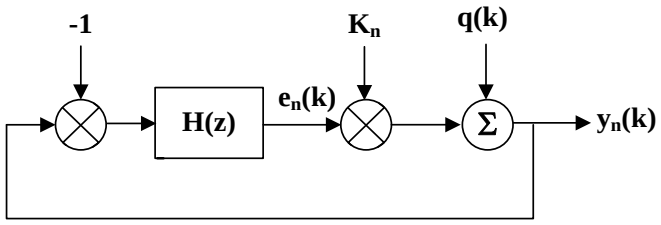

Figure 3-4 Equivalent Σ–Δ modulator model for quantization noise

As a result of the DF analysis, the noise amplification factors can be derived as a function of the ratio of signal- and noise variances at the quantizer input.

3.3.1 DF Analysis: Single-Tone Sinusoidal Input

The output signal, *y(k)* can be written as the superposition of the output signals of the signal- and noise models y_x, y_n as given in Figure 3-3 and Figure 3-4:

$$y(k) = y_x(k) + y_n(k) \tag{3.6}$$

From Figure 3-3 and Figure 3-4, the system analysis gives:

$$y(k) = e_x(k) \cdot K_x + e_n(k) \cdot K_n + q(k) \tag{3.7}$$

Where K_x, K_n are quantizer gain values of signal- and noise-model, respectively. The variance of the output signal yields [Ard87]:

$$Var\{y(k)\} = E\{y^2(k)\} - E^2\{y(k)\} \tag{3.8}$$

where E{.} denotes the expectation function. Since a zero mean Gaussian distribution with zero mean has been assumed for *q(k)* and $e_n(k)$ and the input signal is a random variable with a phase having uniform distribution :

$$E^2\{y(k)\} = 0 \tag{3.9}$$

Therefore (3.8) yields:

$$Var\{y(k)\} = E\{e_x^2(k) \cdot K_x^2\} + E\{e_n^2(k) \cdot K_n^2\} + E\{q^2(k)\} \tag{3.10}$$

$$Var\{y(k)\} = \sigma_{e_x}^2 \cdot K_x^2 + \sigma_{e_n}^2 \cdot K_n^2 + \sigma_q^2 \tag{3.11}$$

Since the Σ–Δ modulator is separated into a two interlocked linear system as given in Figure 3-3 and Figure 3-4, in one system the input forcing function is the sinusoid *x(k)* and in the other system, the forcing function is the additive noise source *q(k)* produced by quantization [Ard87]. Using the signal model in Figure 3-3, the system analysis in the z-domain gives:

$$\frac{E_x(z)}{X(z)} = \frac{G(z) \cdot H(z)}{1 + K_x \cdot H(z)} \tag{3.12}$$

A second-order Σ–Δ modulator can be implemented with two HP loop-filter transfer functions $H_1(z)$ and $H_2(z)$, where $H_2(z) = H_1(z)$. Thus, *G(z)* and *H(z)* in Figure 3-1 can be written as:

$$G(z) = \frac{H_1(z)}{1 + H_1(z)} \tag{3.13}$$

$$H(z) = [1 + H_1(z)] \cdot H_2(z) \tag{3.14}$$

As discussed in Section 2.7 for HP Σ–Δ modulators, the zeros of the NTF are located at $z = \pm e^{j2\pi\nu} = \pm e^{j2\pi 0.5} = -1$. Therefore this results in $H_1(z) = \frac{z}{z+1}$. Therefore in the feed-forward path $H(-1) \to \infty$ and the signal frequency is assumed to be large, $G(-1) \approx 1$ [Ard87]

For BP Σ–Δ modulators, as discussed in Section 2.6 the zeros of the NTF are located on the unit-circle in the *z*-domain depending on the normalized input signal frequency ν at $z = e^{j2\pi\nu}$, so that the NTF yields:

$$NTF = 1 - (2\cos 2\pi\nu) \cdot z^{-1} + z^{-2} \tag{3.15}$$

The transfer function of a resonator is written as:

$$H_1 = \frac{2 \cdot \cos(2\pi\nu) \cdot z^{-1} - z^{-2}}{1 - 2 \cdot \cos(2\pi\nu) \cdot z^{-1} + z^{-2}} \tag{3.16}$$

Any higher-order Σ–Δ modulator can be represented as in Figure 3-3 and Figure 3-4. Therefore, the NTFs of eighth- and tenth-order Σ–Δ modulators are composed of second-order building blocks as given in (3.16). Since the feedforward path includes a resonator and the signal frequency is assumed to be ν, $\left|H(e^{j2\pi\nu})\right| \to \infty$ and $\left|G(e^{j2\pi\nu})\right| \to 1$ for all ν [Ard87].

Since $|H(z)| \to \infty$ and $|G(z)| \to 1$, for higher-order HP and BP Σ–Δ modulators, (3.12) becomes:

$$\frac{E_x(z)}{X(z)} \to \frac{1}{K_x} \tag{3.17}$$

Therefore, the variance of the quantizer input signal $e_x(k)$ can be expressed in terms of the variance of the input signal to the Σ–Δ modulator.

$$\sigma_{e_x}^2 = \frac{1}{K_x^2}\sigma_x^2 \tag{3.18}$$

where the variance of the sinusoid with an amplitude of a_x is $\sigma_x^2 = a_x^2 / 2$.

Using (3.18), (3.11) becomes;

$$Var\ \{y(k)\} = \sigma_x^2 + \sigma_{e_n}^2 \cdot K_n^2 + \sigma_q^2 \tag{3.19}$$

The output-noise variance becomes;

$$Var_{noise}\ \{y(k)\} = \sigma_{e_n}^2 \cdot K_n^2 + \sigma_q^2 \tag{3.20}$$

For a 1-bit quantizer with an output of $\pm \Delta$, the linear gains K_x and K_n have been calculated by using the mean-square-error criterion as in [Ard87], [Ath82]:

$$K_x = \left(\frac{2}{\pi}\right)^{1/2} \left(\frac{\Delta}{\sigma_{e_n}}\right) M\left(\frac{1}{2}, 2, -\rho^2\right) \tag{3.21}$$

$$K_n = \left(\frac{2}{\pi}\right)^{1/2} \left(\frac{\Delta}{\sigma_{e_n}}\right) M\left(\frac{1}{2}, 1, -\rho^2\right) \tag{3.22}$$

where $\rho = \frac{a_x}{\sqrt{2}\sigma_{e_n}}$, is the square root of the ratio of the variance of the sinusoidal component to the Gaussian component at the quantizer input, (a_x is the amplitude of the sinusoidal component). Therefore, ρ denotes the effect of the input signal to the

quantization noise power at the quantizer input. The functions $M(\alpha_M, \gamma_M, \chi_M)$ are the confluent hypergeometric functions [Had75]:

$$\frac{\Gamma(\gamma_M - \alpha_M)\Gamma(\alpha_M)}{\Gamma(\gamma_M)} M(\alpha_M, \gamma_M, \chi_M) = \int_0^1 e^{\chi_M t} t^{\alpha_M - 1} (1-t)^{\gamma_M - \alpha_M - 1} dt \qquad (3.23)$$

For the constant output power (Δ^2), the noise variance has been solved in [Ard87] and is given by:

$$\sigma_q^2 = \Delta^2 [1 - \frac{a_x^2}{2\Delta^2} - \frac{2}{\pi} M^2(\frac{1}{2}, 1, -\rho^2)] \qquad (3.24)$$

$$\rho^2 M^2(\frac{1}{2}, 2, -\rho^2) = \frac{\pi}{4} \frac{a_x^2}{\Delta^2} \qquad (3.25)$$

The variation of the quantization noise variance σ_q^2 and the ρ values with respect to the input signal amplitude (3.24) and (3.25) are solved using the Newton-Raphson technique and plotted in Figure 3-5.

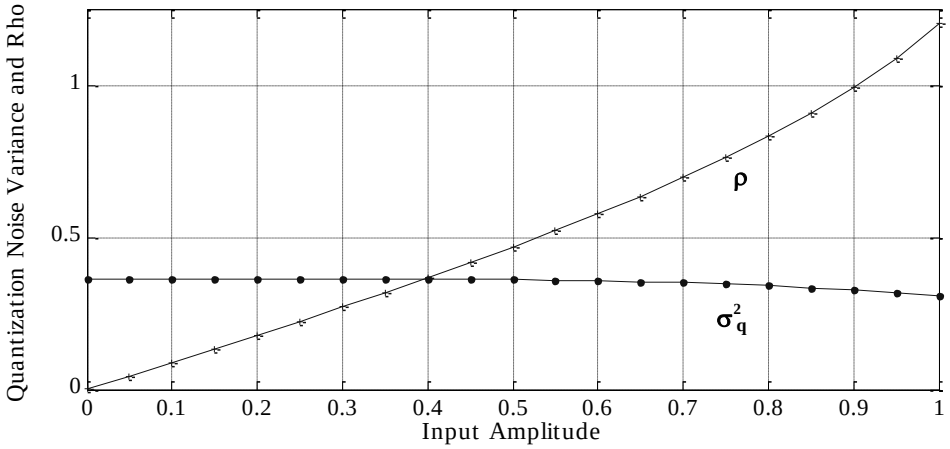

Figure 3-5 Noise variance (σ_q^2) and $\rho = \frac{a_x}{\sqrt{2}\sigma_{e_n}}$ for a sinusoidal signal

The quantization noise variance is almost constant around $\Delta^2/3$, where $\Delta = 1$. Therefore, the noise variance is close to this value as it has uniform distribution and decreases slightly when the input amplitude is close to 1. On the other hand, the ρ values

($\rho = a_x / \sqrt{2\sigma_{e_n}}$) are increasing as the input amplitude approaches the maximum range 1 (Δ). As a result, the ratio of the variance of the sinusoidal signal ($a_x^2/2$) to the variance of the quantization noise signal ($\sigma_{e_n}^2$) at the input to the quantizer becomes very large.

The noise amplification factor is the ratio between the total output noise variance and the quantization noise variance. Therefore, by combining (3.3), (3.20) and (3.21) the noise power amplification factor becomes:

$$A(K) = \frac{Var_{noise}\{y(k)\}}{\sigma_q^2} = \frac{\left(\frac{2}{\pi}\right) M^2(\frac{1}{2},1,-\rho^2) + \sigma_q^2}{\sigma_q^2} \tag{3.26}$$

3.3.2 DF Analysis: Dual-Tone Sinusoidal Inputs

If the inputs to the non-linear component are of different PDFs or of different magnitudes of similar waveforms, the output component from one of these inputs depends not only on the magnitude of this particular input but also on the magnitudes of all the other inputs [Ath82]. In order to derive the linear gains for two sinusoidal inputs, this modified linearity concept is used, where the non-linearity is modified in turn by each of the input signals.

The input signal *x(k)* can be represented as two sinusoids: $x_a(t) = a \cdot \cos(\omega_1(t) + \phi_1)$ and $x_b(t) = b \cdot \cos(\omega_2(t) + \phi_2)$. Figure 3-3 can be extended to the dual inputs case: $x_a(k)$ and $x_b(k)$, where each input is represented by separate equivalent gains, K_a and K_b respectively. Thus, the output signal can be obtained as:

$$y(k) = e_{x_a}(k) \cdot K_a + e_{x_b} K_b + e_n(k) \cdot K_b + e_n(k) \cdot K_n + q(k) \tag{3.27}$$

where *q(k)* and $e_n(k)$ are assumed to have zero mean Gaussian distributions.

Using the equivalent gains, K_a, K_b and K_n are obtained by the modified nonlinearities concept [Ath82], [Lot08]:

$$K_a = \left(\frac{2}{\pi}\right)^{5/2} \left(\frac{\Delta}{\sigma_q}\right) \left(\frac{b}{a}\right) \left(\frac{1}{1/2 - \rho_b^2}\right) \left\{ M\left(1, \frac{3}{2}, -\rho_a^2\right) + \Psi_a \right\} \tag{3.28}$$

$$K_b = \left(\frac{2}{\pi}\right)^{5/2}\left(\frac{\Delta}{\sigma_q}\right)\left(\frac{a}{b}\right)\left(\frac{1}{1/2-\rho_a^2}\right)\left\{M\left(1,\frac{3}{2},-\rho_b^2\right)+\Psi_b\right\} \tag{3.29}$$

$$K_n = \left(\frac{2}{\pi}\right)^{1/2}\left(\frac{\Delta}{\sigma_q}\right)\left\{e^{-\rho_a^2}e^{-\rho_b^2}\varphi\right\} \tag{3.30}$$

$$\sigma_{q_{ab}}^2 = \Delta^2\left[1-\frac{a^2}{2\Delta^2}-\frac{b^2}{2\Delta^2}-\frac{2}{\pi}[e^{-\rho_a^2}e^{-\rho_b^2}]^2\varphi^2\right] \tag{3.31}$$

where,

$$\varphi = 1+\rho_a^2\rho_b^2+\frac{\rho_a^4\rho_b^4}{4}+\frac{\rho_a^6\rho_b^6}{36}+\frac{\rho_a^8\rho_b^8}{576}+\cdots \tag{3.32}$$

and $\rho_a^2 = (1/2)\left(a^2/\sigma_q^2\right)$, $\rho_b^2 = (1/2)\left(b^2/\sigma_q^2\right)$. In order to get the ρ_a and ρ_b values, the two equations (3.33) and (3.34) have been solved simultaneously:

$$\left(\frac{2}{\pi}\right)^5\left(\frac{b^2}{a^2}\right)\left(\frac{\rho_a^2}{[1/2-\rho_b^2]^2}\right)\left[M(1,\frac{3}{2},-\rho_a^2)+\psi_a\right]^2 = \frac{a^2}{2} \tag{3.33}$$

$$\left(\frac{2}{\pi}\right)^5\left(\frac{a^2}{b^2}\right)\left(\frac{\rho_b^2}{[1/2-\rho_a^2]^2}\right)\left[M(1,\frac{3}{2},-\rho_b^2)+\psi_b\right]^2 = \frac{b^2}{2} \tag{3.34}$$

where,

$$\psi_b = \frac{4}{3}\rho_b^2-\frac{16}{45}\rho_b^4+\frac{16}{175}\rho_b^6-\frac{128}{6615}\rho_b^8+\cdots \tag{3.35}$$

$$\psi_a = \frac{4}{3}\rho_a^2-\frac{16}{45}\rho_a^4+\frac{16}{175}\rho_a^6-\frac{128}{6615}\rho_a^8+\cdots \tag{3.36}$$

The variation of σ_{qab}^2 and the ρ values with respect to the input amplitude b at $a = 0.2$ and $a = 0.6$ are shown in Figure 3-6.

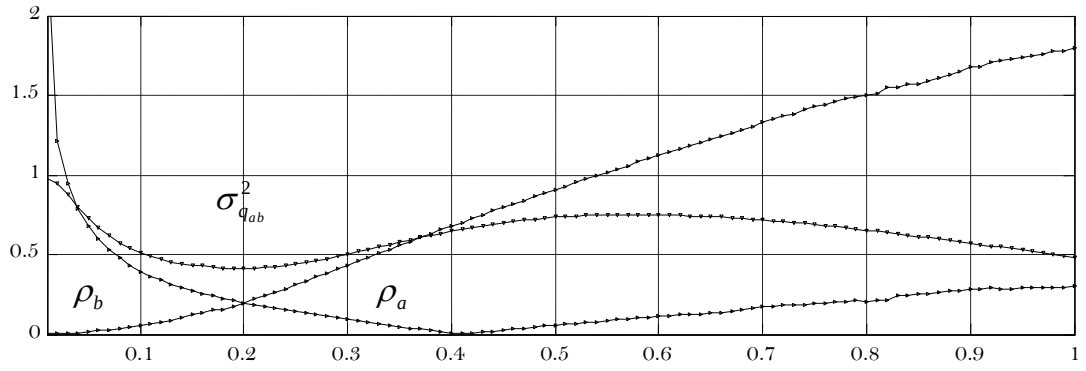

(a)

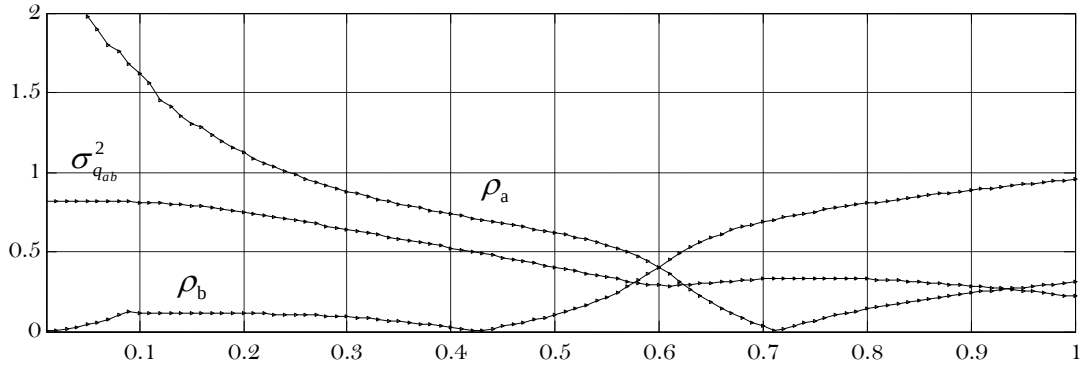

(b)

Figure 3-6 Variation of quantization noise variance ($\sigma^2_{q_{ab}}$), ρ_a and ρ_b values for different input values b with respect to the second input amplitude, (a) a = 0.2, (b) a = 0.6

The ρ_b values increase as the input amplitude b increases and have sharp increases when b is greater than a and approaches 1 (Δ). The variance of the sinusoidal component to the noise component at the quantizer input becomes very large, which causes the noise variance to decrease. Therefore, as a increases from 0.2 to 0.6, ρ_b attenuates. This causes the quantization noise variances to decrease more for a = 0.6. On the other hand, ρ_a decreases when b increases. Thus, for b values less than a, the ρ_b values increase, which cause the noise variance to decrease. Since the ρ_a values get bigger when the a-values are decreasing, the noise variance decreases further when a is increased from 0.2 to 0.6. The ρ_a and ρ_b values intersect each other at $a = b$, thus causing the noise variance curve to have local minima.

The noise amplification factor *A(K)* and the quantization noise variance σ^2_{qab} for a one-bit quantizer with an output of $\pm\Delta$ can be expressed as in [Lot08]:

$$A(K) = \frac{\frac{2}{\pi}[e^{-\rho_a^2} e^{-\rho_b^2}]\varphi^2 + \sigma^2_{q_{ab}}}{\sigma^2_{q_{ab}}} \tag{3.37}$$

Using (3.37), the *A*(*K*) curves with respect to the input signal amplitudes *b* are plotted in Figure 3-7.

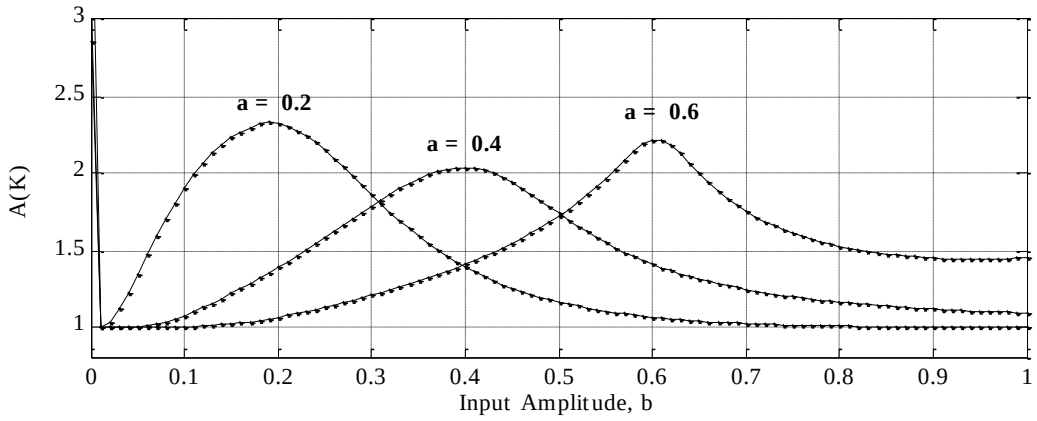

Figure 3-7 The noise amplification curves for values for dual input values *b* and *a*

The noise amplification curves *A(K)* reach their peaks at the local minima of the noise variances, where ρ_a and ρ_b values intersect each other at *a* = *b* (Figure 3-6).

3.4 Theoretical Results and Discussion

3.4.1 HP Σ–Δ Modulators: Theoretical Stability Boundaries

As discussed in Section 3.2 for a given loop-filter quasi-linear analysis, a relationship between the noise amplification factor and quantizer gain K is derived. The noise amplification curves obtained for the third-, fourth- and fifth-order HP Σ–Δ modulators based on Chebyshev Type-II filter response with a normalized frequency of $\nu = 63/64$ and with different stop-band attenuations are shown in Figure 3-8.

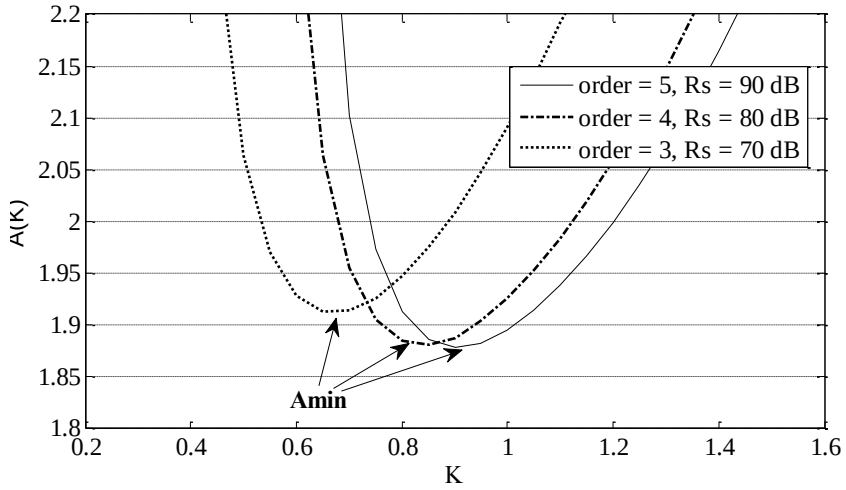

Figure 3-8 Noise amplification curves for the NTFs of HP Chebyshev Type-II filter based Σ–Δ modulator of the order = 3,4,5 with different stop-band attenuations

The $A(K)$-curves for fifth-order HP Σ–Δ modulators with increasing stop-band attenuation are illustrated in Figure 3-9.

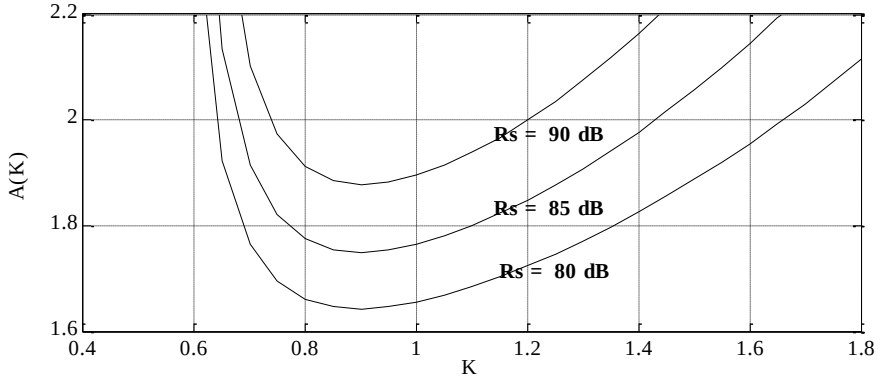

Figure 3-9 $A(K)$-curves for fifth-order HP Chebyshev Type-II with R_s = 80, 85, 90 dB

Figure 3-9 shows that the A_{min} values are increasing due to the increased stop-band attenuation, which cause the stable amplitude range to decrease. According to the NTF theorem stated in [Ger89], the average NTF magnitude must be zero or positive, i.e. in the plot of logarithmic magnitude of the NTF versus frequency, the area above and below the 0 dB line are equal [Ris94a], [Ger89]. This results in higher stop-band attenuation. The gain in the pass-band is increased in order to compensate for the high attenuation of the noise components in the signal-band. Therefore, the increased stop-band attenuation causes

the quantization noise to be elevated in the out-of-band region and the A_{min} values to increase. In other words, the dynamic range of the Σ–Δ modulator is reduced.

On the other hand, increasing the stop-band attenuation provides better noise suppression in the signal band. As a result, there is a trade-off between the stable amplitude limits and the SNR values.

In addition, the theoretical MSA values with respect to the stop-band attenuation for the third-, fourth- and fifth-order Chebyshev Type-II based HP Σ–Δ modulator for unity *K*-values are shown in Figure 3-10.

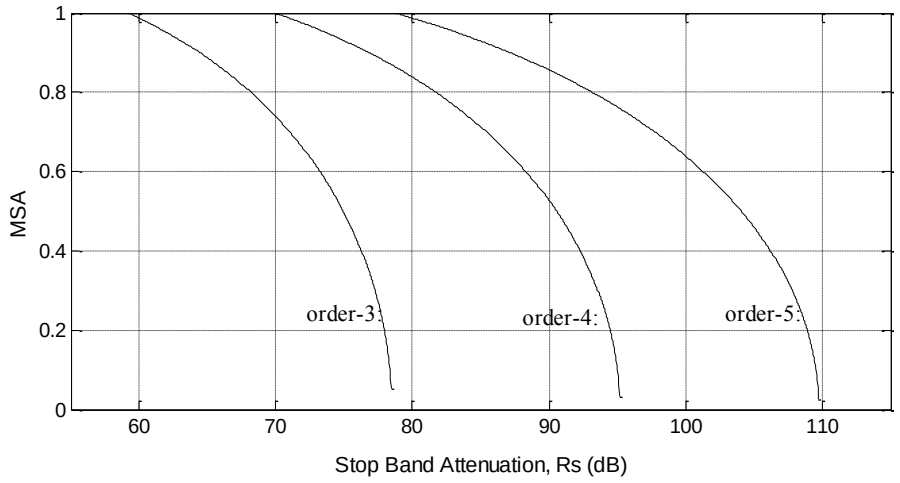

Figure 3-10 MSA limits for the NTFs of the Chebyshev Type-II based HP Σ–Δ modulators

Figure 3-10 shows that the MSA values are decreasing due to the increased stop-band attenuations. In addition, for the same stop-band attenuation, higher-order Σ–Δ modulators achieve higher MSA values. Consequently, it can be concluded that the dynamic range of a Σ–Δ modulator increases with the order of the Σ–Δ modulator. The stability curves should follow the stable branch of the theoretical A(K) curves obtained using quasi-linear analysis so that the equilibrium point will be on the *A(K)* curves obtained using the DF method as given in Section 3.3 Therefore, the stability boundaries for different *K* values can be obtained by solving (3.4) and (3.24) simultaneously.

The theoretical values for the MSA limit for the fourth- and fifth-order Chebyshev Type-II based HP Σ–Δ modulator for different *K* and R_s values are illustrated in Figure 3-11a and Figure 3-11c. As seen in Figure 3-11, the stability boundaries of Σ–Δ modulators

for different orders, stop-band attenuation sweeps and a range of *K*-values are displayed on one graph. The MSA values for a fixed stop-band attenuation (R_s = 80 dB) is given as a 2D plot as illustrated in Figure 3-11b.

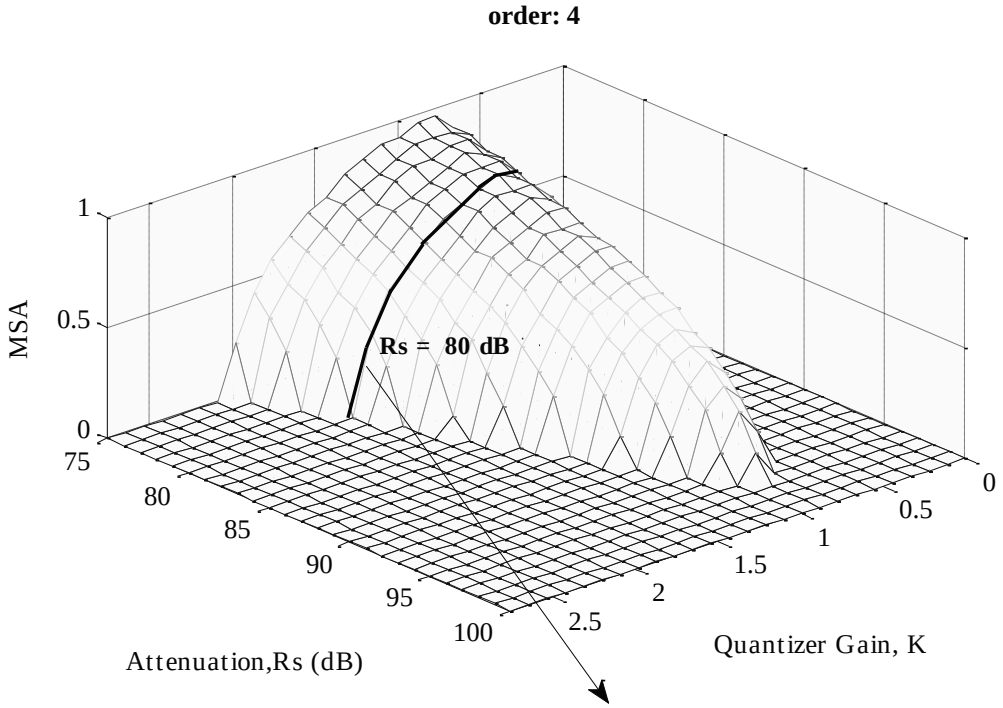

(a)

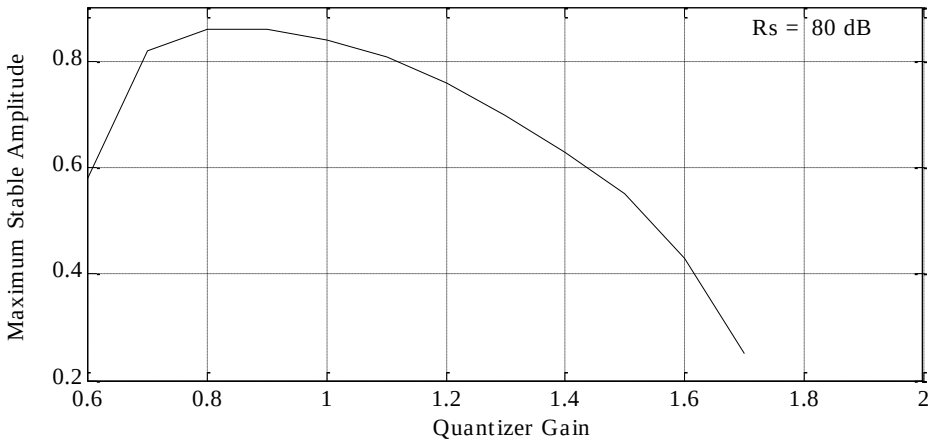

(b)

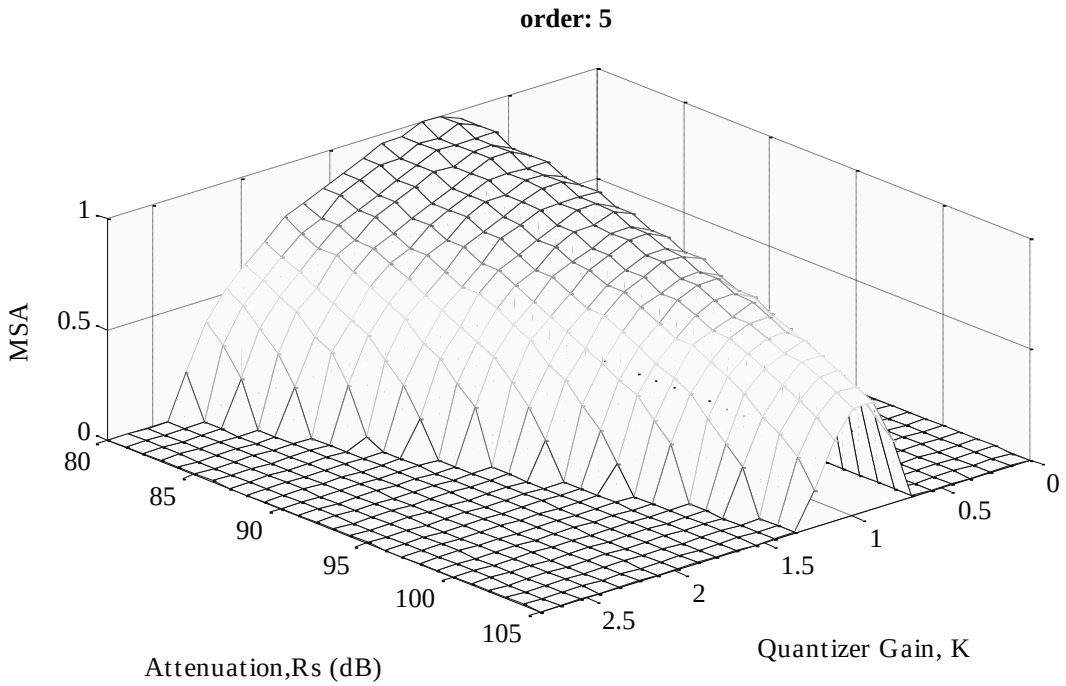

(c)

Figure 3-11 Theoretical MSA values for (a) fourth- order Chebyshev Type-II based HP Σ–Δ modulator, (b) for R_s = 80 dB, (c) fifth-order Chebyshev Type-II based HP Σ–Δ modulator

As seen in Figure 3-11, the theoretical results show that the stable range increases with the increased order. In addition, the stability curves exhibit a circle-like shape centred at *K*-values close to unity. The MSA curves reach their maximum value when the quantizer gain is close to unity, but not exactly unity. The *K*-values, where the MSA values reach their peak values correspond to the *K*-values, where the noise amplification curves obtained using quasi-linear analysis reach their minimum values, i.e. $A(K) = A_{min}$

3.4.2 BP Σ–Δ Modulators: Theoretical Stability Boundaries

The noise amplification curves obtained by employing quasi-linear stability analysis for the eighth- and tenth-order BP Chebyshev Type-II Σ–Δ modulators with a normalized band-width of $\omega_n = [0.495\ 0.505]$ are plotted in Figure 3-12.

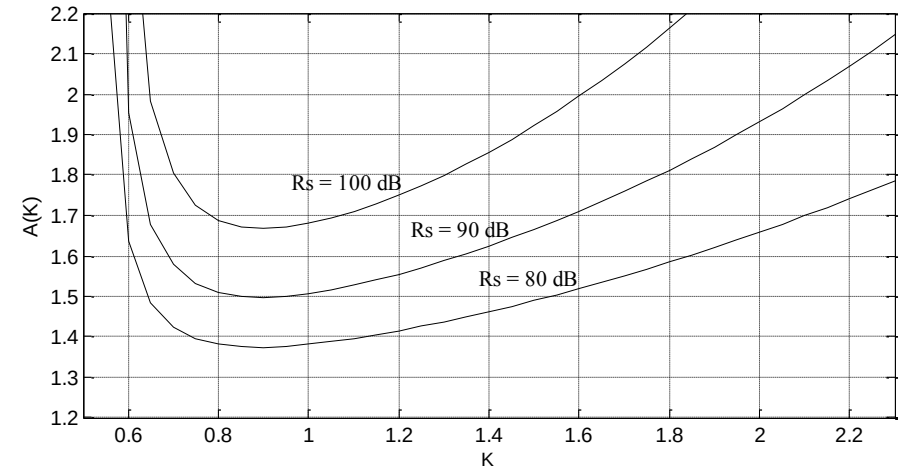

(a)

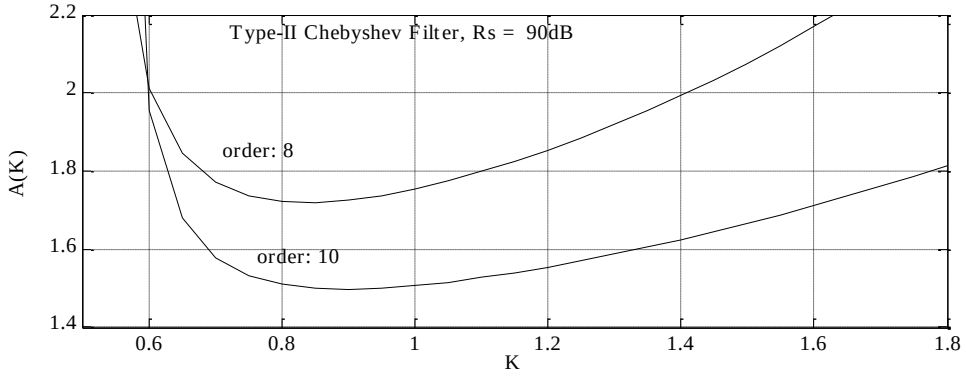

(b)

Figure 3-12 $A(K)$ curves for the NTFs of the Chebyshev Type-II with ω_n = [0.495 0.505], (a) tenth-order with increasing R_s, (b) eighth-, tenth-order for R_s = 90dB

As in the HP-case, the A_{min} values shown in Figure 3-12a, are increasing due to the higher stop-band attenuation, which causes the stable amplitude range to decrease. In addition, as seen in Figure 3-12b, increasing the order of the Σ–Δ modulator causes the A_{min} values to decrease. This increases the dynamic range of the Σ–Δ modulator. Also, the infinite ends of the $A(K)$ curves as seen in Figure 3-12, can be obtained by using root locus analysis of the Σ–Δ modulator. Thus, the root locus of an eighth-order Chebyshev Type-II based BP Σ–Δ modulator with a stop-band attenuation of 90 dB is given in Figure 3-13. The $NTF_K(z)$ root locus demonstrates that the Σ–Δ modulator is stable for K values greater than 0.5.

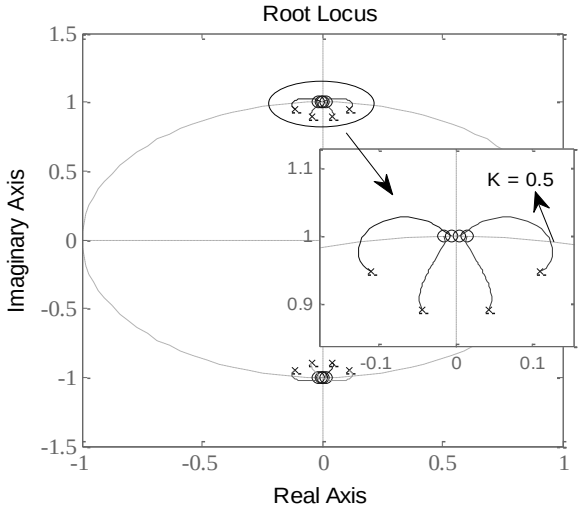

Figure 3-13 Eighth-order $NTF_K(z)$ root locus versus K (for R_s = 90dB)

As shown in Figure 3-13, the intersection of the unit-circle is when K = 0.5, which indicates the stability of the NTF. Moreover, for BP Σ–Δ modulators, the effect of widening the stop-band region on the Σ–Δ modulator stability response in terms of the A_{min} values is shown in Figure 3-14.

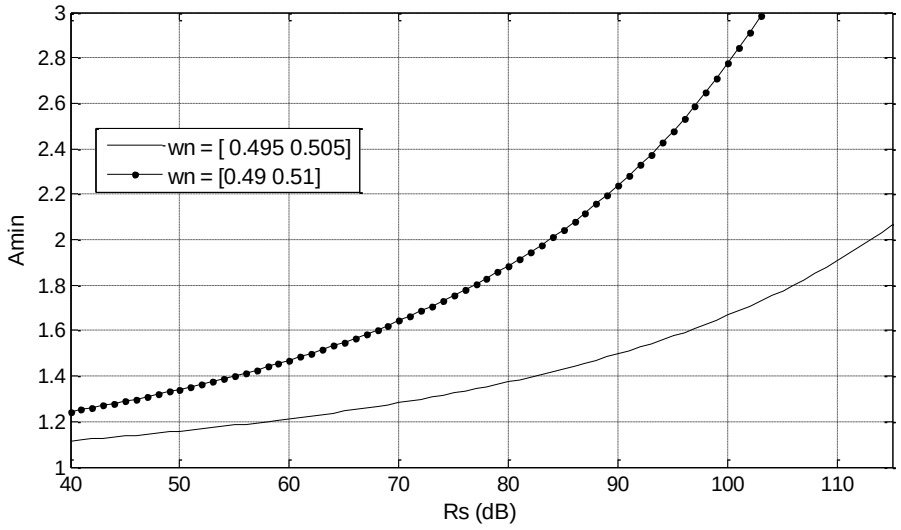

Figure 3-14 Variation of A_{min} values for different R_s and ω_n values

Since the NTF theorem stated that the average logarithm of the magnitude of the NTF must be zero with a wide transition band, the gain in the pass-band is increased in order to compensate for the wider stop-band region [Ger89], [Ris94a]. Therefore, the widened

stop-band causes the quantization noise to be elevated in the out-of-band region and the A_{min} values to increase. In other words, the dynamic range of the Σ–Δ modulator is reduced.

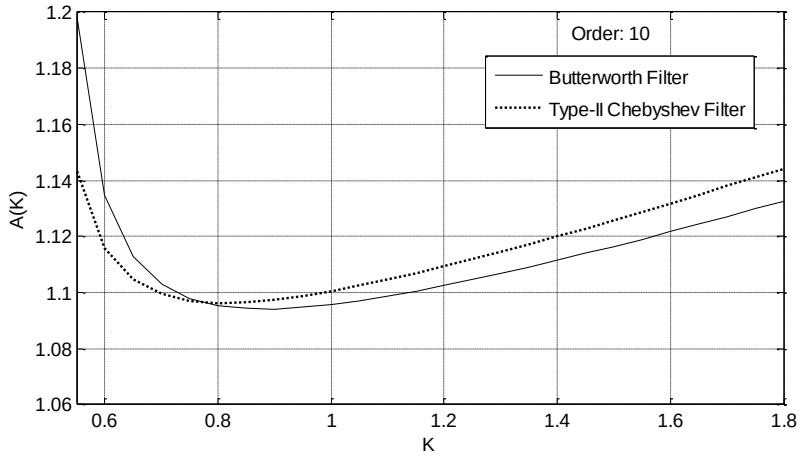

Figure 3-15 $A(K)$-curves for tenth-order BP Butterworth- and Chebyshev Type-II Filter

In addition, as seen in Figure 3-15, the A_{min} values of tenth-order Butterworth and tenth-order Chebyshev Type-II Σ–Δ modulators with R_s = 35 dB are the same. Therefore, Chebyshev Type-II based Σ–Δ modulators have greater stop-band attenuation resulting in better in-band SNRs compared with Butterworth based Σ–Δ modulators of the same order.

3.4.3 BP Σ–Δ Modulators Stability Boundaries: Single-Tone Sinusoidal Input

The stability boundaries for the eighth- and tenth-order Chebyshev Type-II filter based BP Σ–Δ modulator with $w_n = [0.49\ 0.51]$ for a single sinusoidal input with a normalized frequency of $\nu = 0.25$ are plotted in Figure 3-16.

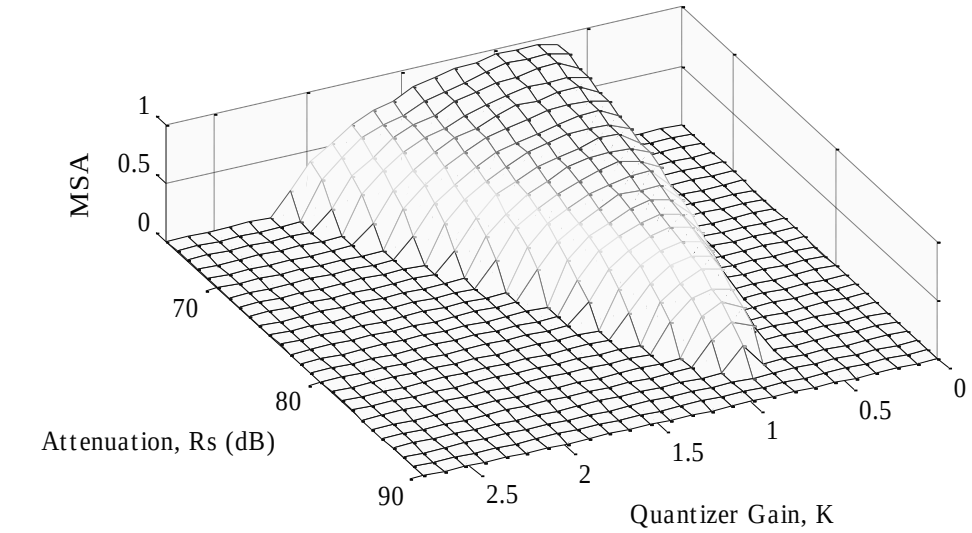

(a)

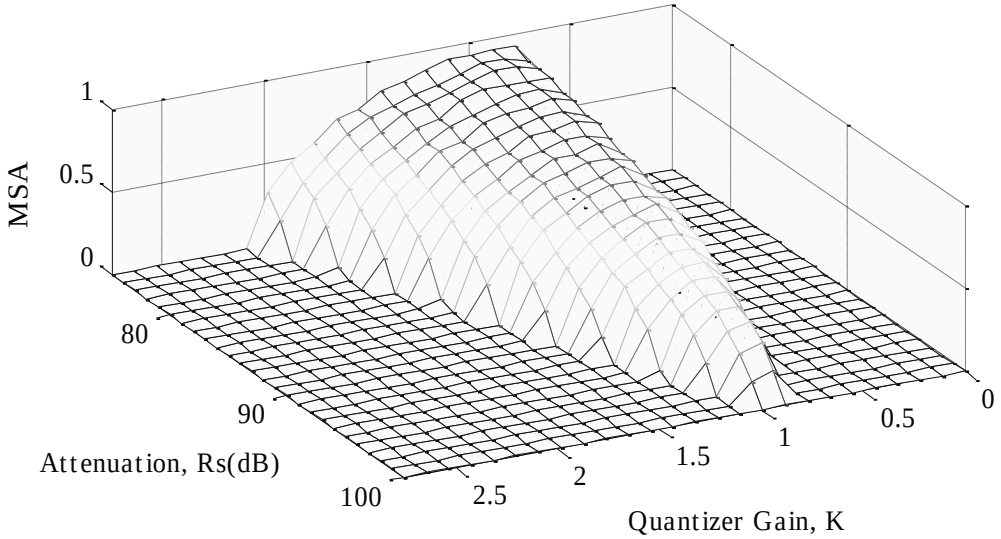

(b)

Figure 3-16 MSA limits for single input (a) eighth- (b) tenth-order

As obtained in the HP case, the stability curves are centred at K-values where the $A(K)$ curves reach their minimum values, (A_{min}) and also become narrower with increased stop-band attenuation.

3.4.4 BP Σ–Δ Modulators Stability Boundaries: Dual-Tone Sinusoidal Input

For dual sinusoidal inputs, the input to the quantizer is dependent on the variances of the two input signals as well as the quantization noise. This means that the stability boundaries for each input need to be plotted separately. Therefore, the MSA limits for the

first input signal are obtained while keeping the second input amplitude fixed. Thus, the stability boundaries for the eighth- Chebyshev Type-II based BP Σ–Δ modulators with $\omega_n = [0.495\ 0.505]$ for the input amplitudes a = 0.2 and 0.4 are plotted in Figure 3-17. Figure 3-18 shows the MSA values for the eighth- Chebyshev Type-II based BP Σ–Δ modulators with $\omega_n = [0.495\ 0.505]$ for the input amplitudes a = 0.4 and 0.6.

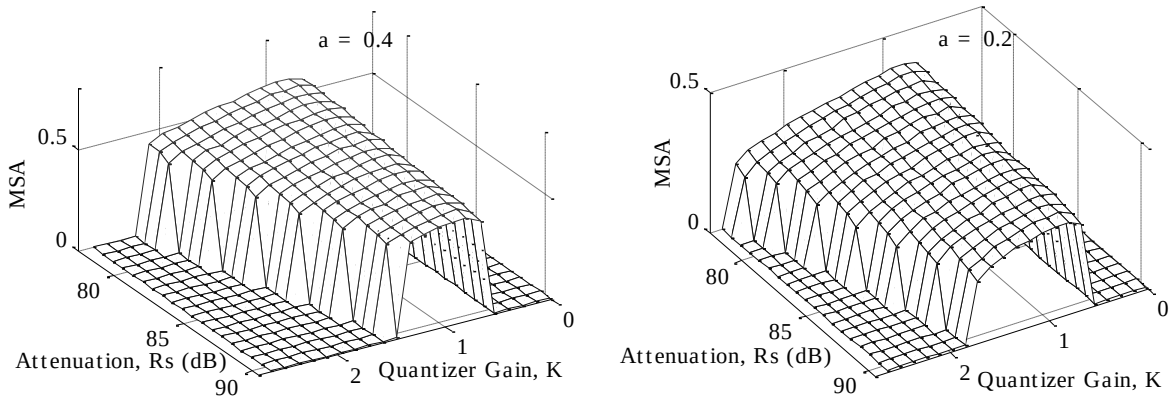

(a) (b)

Figure 3-17 MSA limits for eighth-order for (a) a = 0.4, (b) a = 0.2

As seen in Figure 3-17, the MSA values are decreasing for lower input amplitudes, i.e. MSA values for a = 0.4 are bigger than those obtained for a = 0.2. On the other hand, the decreased input amplitude causes the stability curves to spread to a wider range of K-intervals.

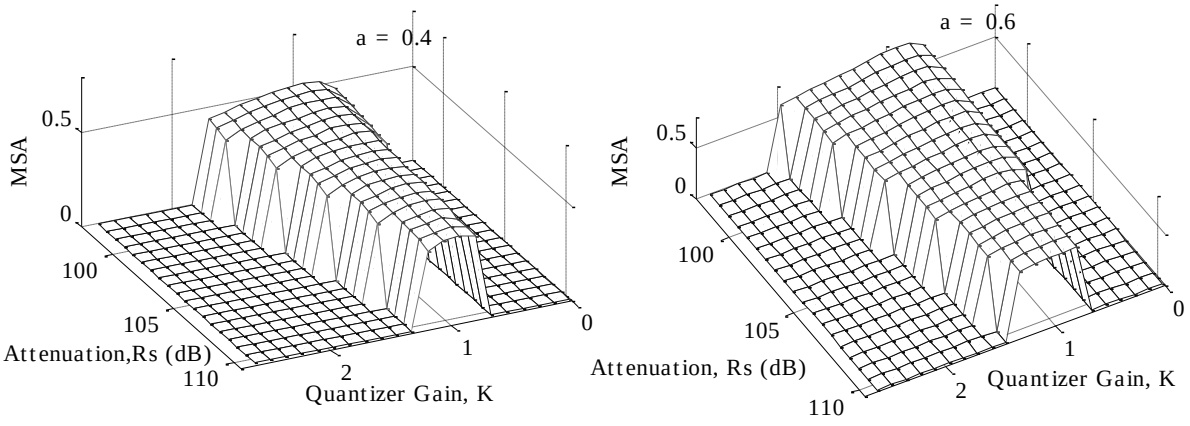

(a) (b)

Figure 3-18 MSA limits for tenth-order for (a) a = 0.4, (b) a = 0.6

3.5 Simulation Results and Discussion

The theoretical boundaries given in 3.4 are verified by extensive simulations of Chebyshev Type II and Butterworth based Σ–Δ modulators for single- and dual-tone sinusoidal inputs as given in Figure 3-19 and Figure 3-20.

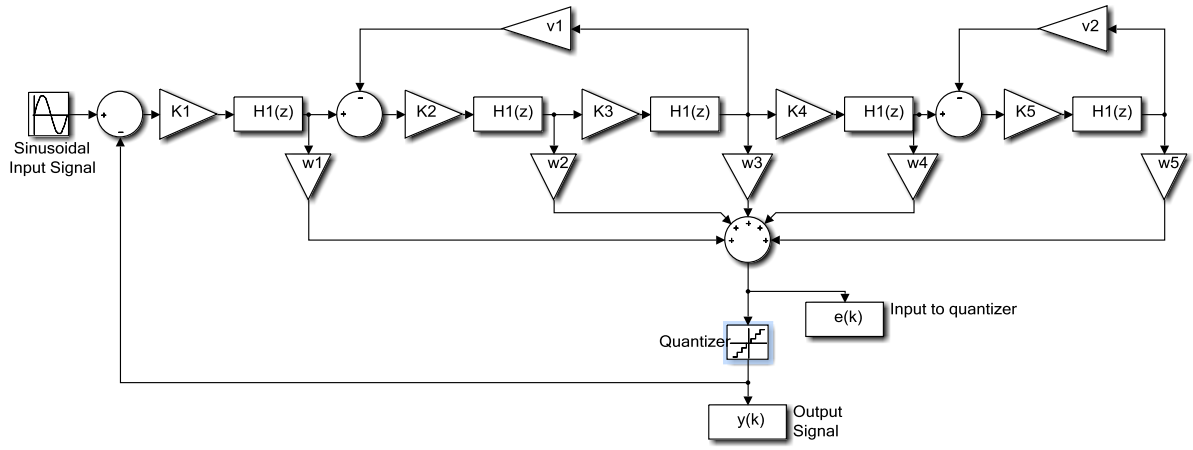

Figure 3-19 Chebyshev Type-II based Σ–Δ modulator topology

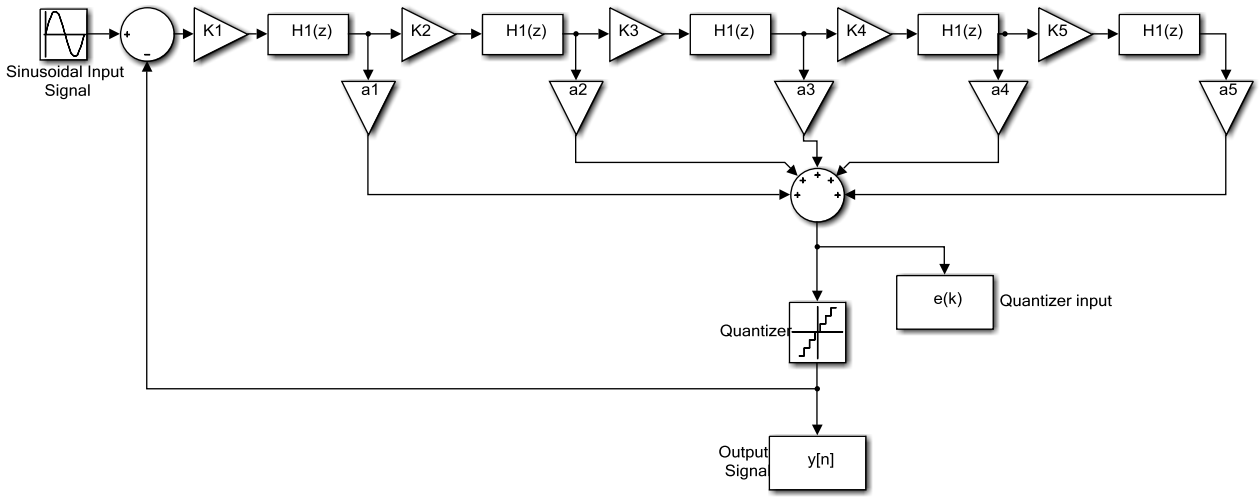

Figure 3-20 Butterworth based Σ–Δ modulator topology

The simulations were performed for 1638400 time samples with input amplitudes in increments of 0.01. The corresponding K values depending on the quantizer input signal are obtained as reported in [Ris94b]:

$$K = \frac{Covariance\{e(k), y(k)\}}{\sigma_e^2} \tag{3.38}$$

where *e(k)* corresponds to the input signal to the quantizer and *y(k)* is the output signal. As shown in Figure 3-19 and Figure 3-20, e(k) and y(k) are directly obtained from simulations using simulink building blocks, which are used to obtain the covariance of {*e(k)* , *y(k)*} and σ_e^2.

Using (3.3) and (3.11), the simulated $A(K)$ curve with respect to the quantizer input signal can be obtained as:

$$A(K) = \frac{Var\{y(k)\}}{Var\{y(k)\} - \sigma_e^2 \cdot K^2} \tag{3.39}$$

3.5.1 Simulation Results for HP Σ–Δ Modulators

Simulations were undertaken for third-, fourth- and fifth-order Chebyshev Type-II based HP Σ–Δ modulators using a normalized cut-off frequency of $\nu = 63/64$. Using (3.24) and (3.39), the comparison of the theoretical- and the simulated-$A(K)$ curves for a fifth-order Σ–Δ modulator with $R_S = 85.5$ dB is given in Figure 3-21.

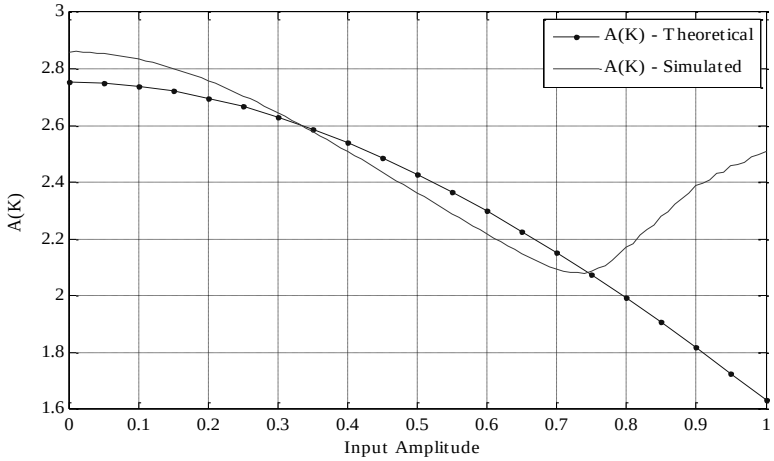

Figure 3-21 Theoretical- and simulated- noise amplification curves

In order to maintain the stable state in Figure 3-8, Figure 3-9, Figure 3-12, the *A(K)* curves in Figure 3-21 are expected to decrease with increasing input amplitudes. The simulation results agree reasonably well with the expected *A(K)* values. However, as seen in Figure 3-21 the simulated *A(K)* curves show that the actual modulator becomes unstable, when the input amplitude is greater than 0.75.

Figure 3-22 shows the noise amplification curve plotted versus the quantizer gain, *K*. The simulated results are in good agreement with the theoretical results. As expected, the modulator is stable for the increasing branch of the *A*(*K*)-curve [Ris94a].

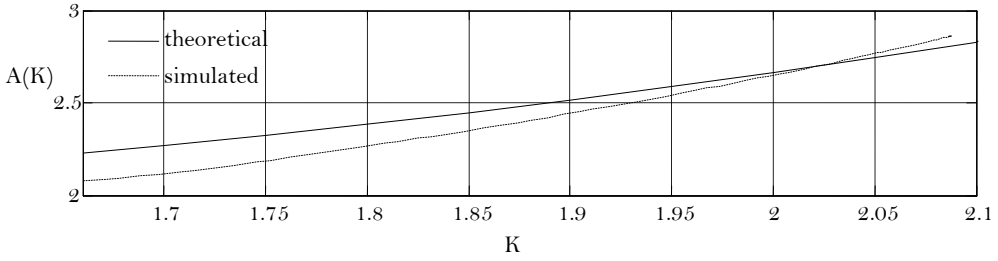

Figure 3-22 Simulated- and theoretical *A*(*K*)-curves

The theoretical MSA values are compared with the actual results obtained by the simulation of the fourth-order Chebyshev Type-II based HP Σ–Δ modulator with $R_S = 70$ dB as given in Figure 3-23 and Table 3-2.

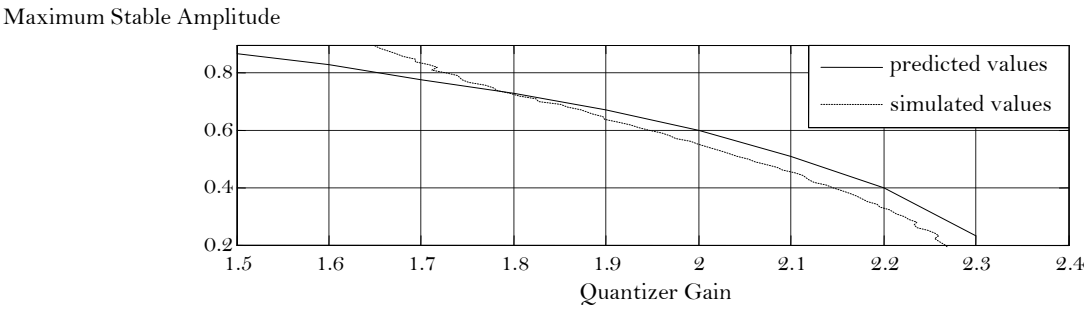

Figure 3-23 Theoretical and simulated MSA limits for the order of four

K-values	Theoretical MSA	Simulated MSA	Error (%)
1.7	0.78	0.83	6
1.8	0.72	0.72	0
1.9	0.67	0.64	4

Table 3-2 Simulation results for order four

The variations of the theoretical and simulated results for the fifth-order Chebyshev Type-II based HP Σ–Δ modulator with R_S = 80 dB are given in Figure 3-24 and Table 3-3.

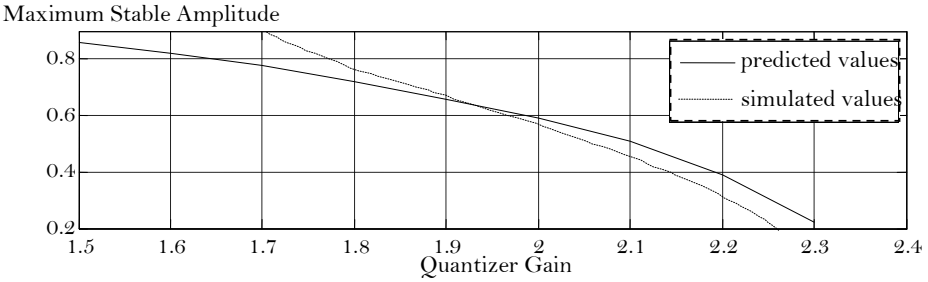

Figure 3-24 Theoretical and simulated MSA for the order of five

K-values	Theoretical MSA	Simulated MSA	Error (%)
1.7	0.78	0.91	14.2
1.8	0.72	0.76	5.2
1.9	0.66	0.67	1.4

Table 3-3 Simulation results for order five

It is seen in Figure 3-23 and Figure 3-24 that the modulator becomes unstable earlier compared to the theoretical results. As the order of the modulator is increased, the differences between the theoretical- and simulated results are decreased for higher *K*-values, because the stable range of the Σ–Δ modulator increases with the increased order.

In addition, the differences between the theoretical and simulated results are attributed to the fact that the quantization noise is not completely Gaussian. However, as the order of the Σ–Δ modulator increases, the quantizer input becomes more random thus resulting in a Gaussian-shaped probability density function (PDF) of the quantizer input. The randomisation effect of the order of the Σ–Δ modulator on the quantizer input can be analysed by using the Kolmogorov-Smirnov k_S Gaussian-Test [Mas51]:

$$k_s = \max(|F(x) - G(x)|) \tag{3.40}$$

where $G(x)$ is the Gaussian and $F(x)$ is the cumulative density function (CDF) of the input to the quantizer. According to this test, the lower the value of k_S, the closer is the PDF of the quantizer input to the Gaussian PDF.

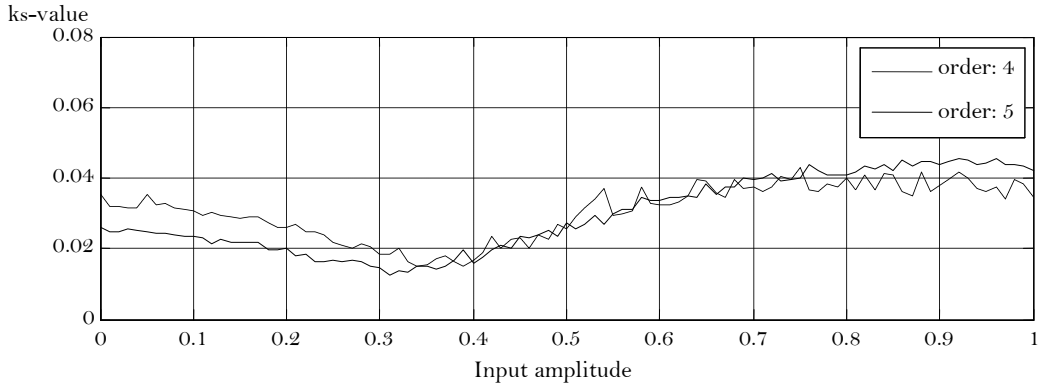

Figure 3-25 k_S test for fourth- and fifth-order HP Σ–Δ modulator

As seen in Figure 3-25, the k_S values decrease as the order of the modulator increases, thus the input to the quantizer becomes more random. The increase of the k_S values for input amplitude values bigger than 0.75 shows that the Σ–Δ modulator becomes unstable. The k_S values reach their minimum values when the input amplitude is in the middle range (0.3-0.4). This occurs when the Σ–Δ modulator is more stable and the input to the quantizer is more Gaussian.

3.5.2 Simulation Results for BP Σ–Δ Modulators: Single-Tone Sinusoidal Input

For BP Σ–Δ modulators of normalized bandwidths of [0.495 0.505] and [0.49 0.51], the frequency of the sinusoidal inputs were chosen as 0.25. For the bandwidth of [0.245 0.255], the corresponding input frequency was chosen as 0.125. The variations of the theoretical and simulated results for the eighth- and tenth order cases with ω_n = [0.49 0.51] and R_s = 70 dB are given in

Table 3-4.

Order	K-values	Theoretical MSA	Simulated MSA	Error (%)
8	1.4	0.70	0.71	1.4
	1.5	0.62	0.69	10.1
	1.7	0.45	0.59	23.7
10	1.4	0.85	0.75	13.3
	1.5	0.80	0.74	8.1
	1.7	0.75	0.74	1.3

Table 3-4 Simulation results, R_s =70 dB ω_n = [0.49 0.51]

The theoretical and simulated values for the MSA limits for the eighth-order BP Σ–Δ modulator with ω_n = [0.245 0.255] are given in Figure 3-26 and Table 3-5.

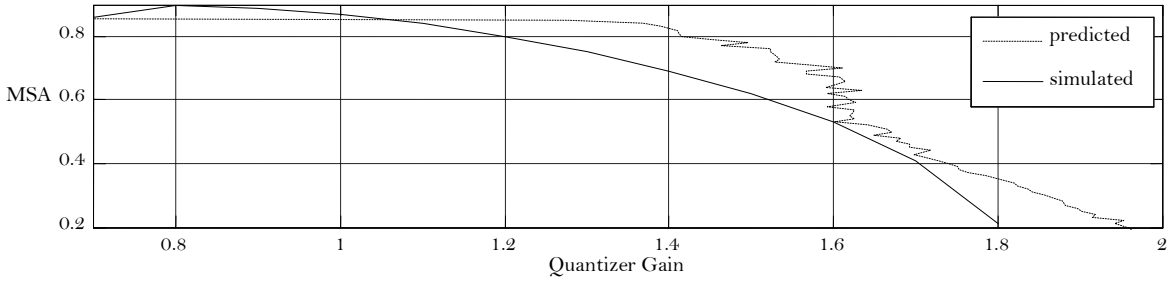

Figure 3-26 Theoretical- and simulated results, eighth-order BP Σ–Δ modulator, R_s =70 dB

ω_n = [0.24 0.26]

Order	K-values	Theoretical MSA	Simulated MSA	Error (%)
8	1.1	0.84	0.84	0
	1.4	0.69	0.8	13.7
	1.6	0.53	0.52	1.9
10	1.4	0.89	0.89	0
	1.8	0.72	0.88	18.1
	2	0.53	0.53	0

Table 3-5 Simulation results, R_s =70 dB ω_n = [0.24 0.26]

The sharp decrease of the MSA limits as the quantizer gain values increase shows that the Σ–Δ modulator becomes unstable. The results show that, as in the HP-case, when the order of the Σ–Δ modulator is increased, the differences between the theoretical- and simulated values are decreased for higher K values. Therefore for higher orders, the proposed quantizer model is closer to the actual non-linear quantizer especially at greater K values.

3.5.3 Simulation Results for BP Σ–Δ Modulators: Dual-Tone Sinusoidal Input

For BP Σ–Δ modulators of normalized bandwidths of $\omega_n = [0.495\ 0.505]$ and $\omega_n = [0.49\ 0.51]$, the normalized frequencies of the sinusoidal inputs were chosen as $\nu_1 = 0.25$ and $\nu_2 = 0.251$. For $\omega_n = [0.24\ 0.26]$ the corresponding input frequencies were chosen as $\nu_1 = 0.125$ and $\nu_2 = 0.126$.

The variations of the theoretical- and simulated results for $\omega_n = [0.495\ 0.505]$ for eighth- and tenth-order BP Σ–Δ modulators are shown in Figure 3-27.

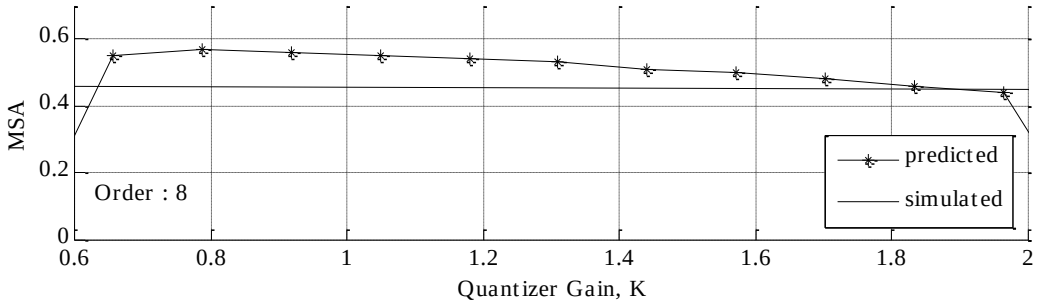

(a)

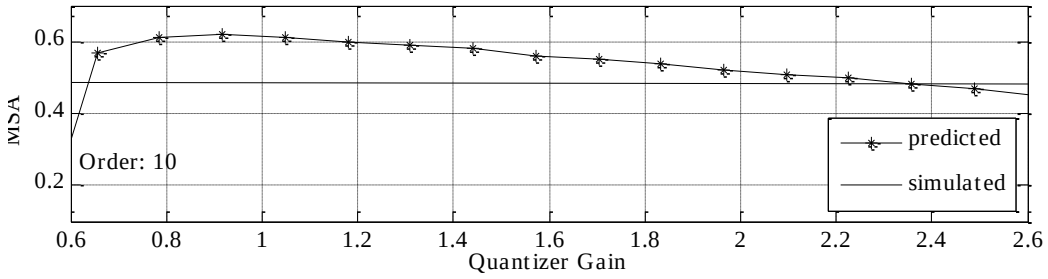

(b)

Figure 3-27 Theoretical and simulated MSA values for $a = 0.4$ and with $R_s = 80$dB for (a) eighth-, (b) tenth-order

As seen in Figure 3-27 and as expected, as the order of the Σ–Δ modulator increases, the quantizer input becomes more random, thus increasing the accuracy of the proposed quantizer model. Therefore, the differences between the theoretical and simulated results are decreased when the order of the Σ–Δ modulator is increased.

The variations of the theoretical and simulated results for different R_S values and different input amplitudes are given in Table 3-6, Table 3-7.

a	Theoretical MSA	Simulated MSA	Error (%)
0.2	0.37	0.60	38.3
0.4	0.53	0.41	29.2
0.6	0.46	0.21	119

Table 3-6 Simulation Results, Order: 8, R_S = 80dB, ω_n = [0.495 0.505]

A	Attenuation [dB]	Theoretical MSA	Simulated MSA	Error (%)
0.2	90	0.36	0.65	44.6
	100	0.34	0.58	41.3
	110	0.31	0.50	38.0
0.4	90	0.53	0.42	26.1
	100	0.51	0.38	34.2
	110	0.47	0.28	67.8

Table 3-7 Simulation Results, Order: 10, ω_n = [0.495 0.505]

As seen in Table 3-6 and Table 3-7, the differences between the theoretical- and simulated results for dual sinusoidal inputs are bigger than those obtained for a single-tone sinusoidal input. In the proposed quantizer model, the modified linearity concept is used to obtain the linear gains for two sinusoidal inputs, where the non-linearity is modified in turn by each of the input signals. However, the actual non-linearity of each input exists simultaneously. Therefore, the accuracy of the proposed model is expected to get worse when the number of the input signal increases.

In addition, according to the simulation results given in Table 3-6 and Table 3-7, the difference between the theoretical and simulated results are bigger when the input amplitude is too small (a = 0.2) or too big (a = 0.6).

According to the k_s-Gaussian test results given in Figure 3-28, the bigger the a input amplitudes become, the more the input to the quantizer exhibits the shape of a Gaussian function. Therefore, the differences between the simulation- and theoretical results get smaller when the input amplitude is increased from 0.2 to 0.4. The sharp increase in the k_s-values shows that the modulator becomes unstable.

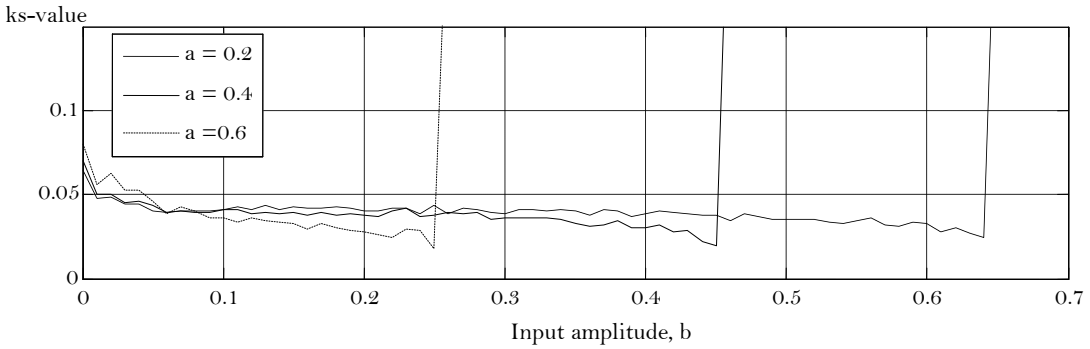

Figure 3-28 *k*-Gaussian test for eighth-order BP Σ–Δ modulator for input amplitude,*a* = 0.2, 0.4, 0.6

The input to the quantizer becomes more random as the input amplitude increases. On the other hand, as seen in the frequency spectrums of the same modulator with increasing input amplitudes shown in Figure 3-29, the bigger the *a* input amplitude is, the more the Σ–Δ modulator approaches its stability limits and the more spectral tones appear in the signal band. Therefore, the differences between the theoretical and simulated results become larger when the *a* values are bigger than 0.4.

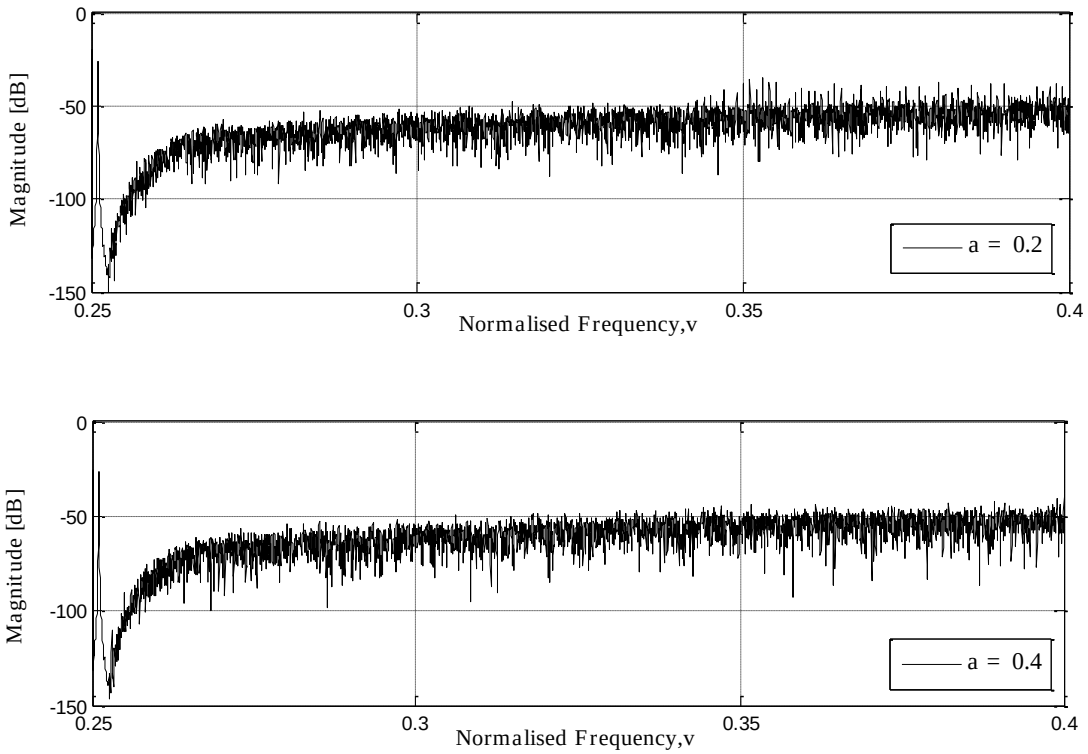

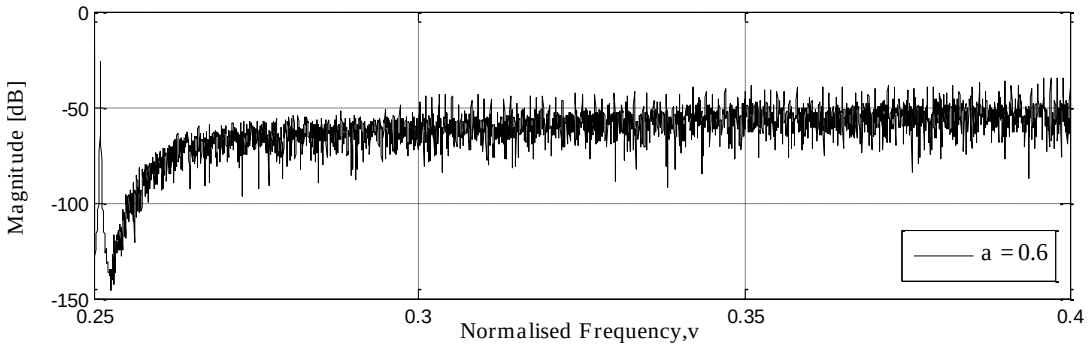

Figure 3-29 Frequency spectrum of BP Σ–Δ modulators for dual sinusoidal inputs for $b = 0.2$ and for $a = 0.2, 0.4, 0.6$

The effect of widening the stop-band on the Σ–Δ modulator stability boundaries in terms of the A_{min} values is shown in Figure 3-14. The dynamic range of the Σ–Δ modulator is reduced as expected. The simulations of the tenth-order Chebyshev Type-II based BP Σ–Δ modulator at $a = 0.4$, $\omega_n = [0.49\ 0.51]$ and $R_s = 60$, 70 dB are given in Table 3-8. The simulated MSA values are decreased compared to the MSA values of a Σ–Δ modulator that has a narrower bandwidth (Table 3-7), i.e. the Σ–Δ modulator becomes unstable for smaller input amplitudes. Also, as expected, the stable K intervals are narrowed and the stop-band attenuations are decreased by almost 20 dB.

Order	Attenuation [dB]	Theoretical MSA	Simulated MSA	Error (%)
8	60	0.51	0.42	21.4
	70	0.44	0.33	33.3
10	60	0.53	0.46	15.2
	70	0.45	0.38	18.4

Table 3-8 Simulation Results, $a = 0.4$ (Wider Stop-Band $\omega_n = [0.49\ 0.51]$

3.5.4 Effects of Dither on Simulation Results

As discussed in Section 2.5.2 dither can be injected at the quantizer input to reduce tones in Σ–Δ modulators. However, the addition of dither tends to reduce Σ–Δ modulator stability, resulting in a lower loop gain and increased in-band noise level [Ger89]. As a result, the MSA limits will be decreased compared to un-dithered Σ–Δ modulators.

In order to show the effect of the dither, as given in Figure 3-30, a fourth-order Chebyshev Type-II based HP Σ–Δ modulator (R_s = 75 dB) is simulated with a dither amplitude of 0.08. Figure 3-31 shows the simulation results for a fifth-order Chebyshev Type-II based HP Σ–Δ modulator (R_s = 85.5 dB) with a dither amplitude of 0.1. As seen in Figure 3-30 and Figure 3-31, the simulated MSA limits are reduced. Therefore, the differences between the theoretical and simulated results are reduced when dither is added at the input of the quantizer.

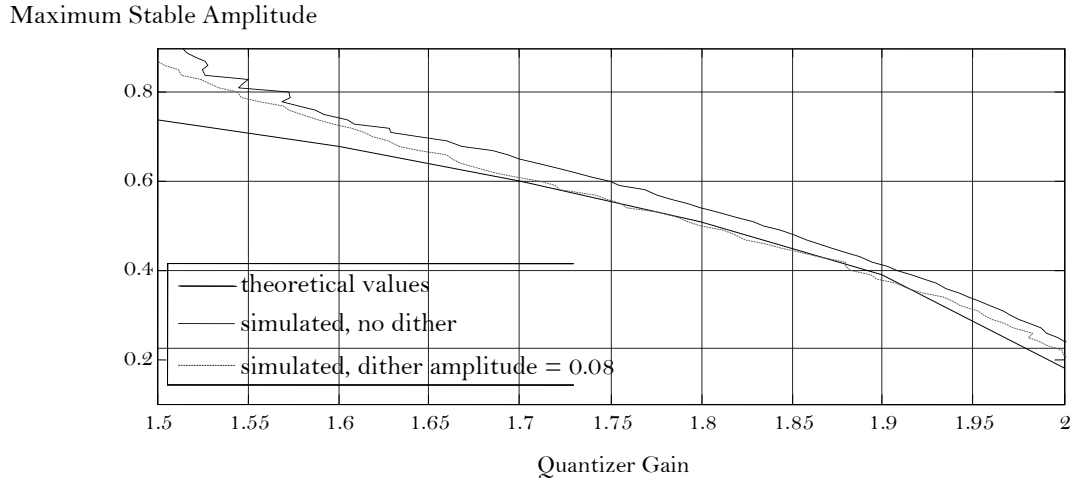

Figure 3-30 Comparison of theoretical MSA values with simulated results for dithered- and un-dithered fourth-order HP Σ–Δ modulators

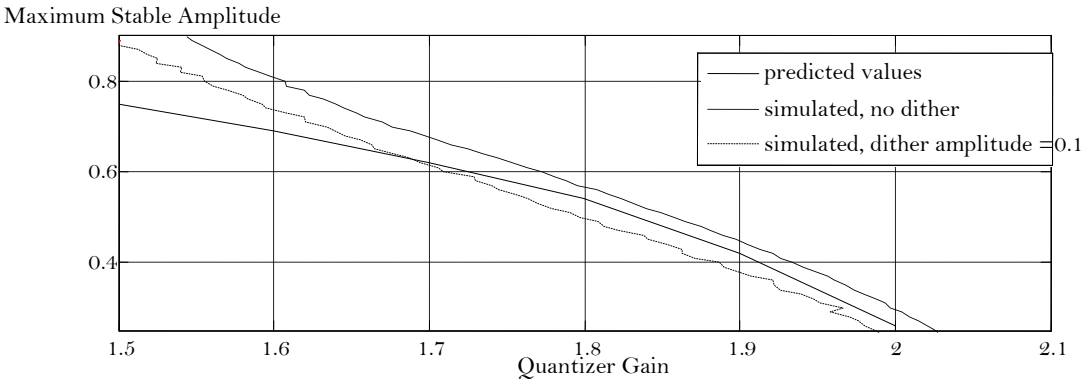

Figure 3-31 Comparison of theoretical MSA values with simulated results for dithered- and un-dithered fifth-order HP Σ–Δ modulators

The decreased k-values shown in Figure 3-32, prove that the quantizer input of the dithered Σ–Δ modulator tends to be more Gaussian-shaped compared to one of the un-dithered Σ–Δ modulator.

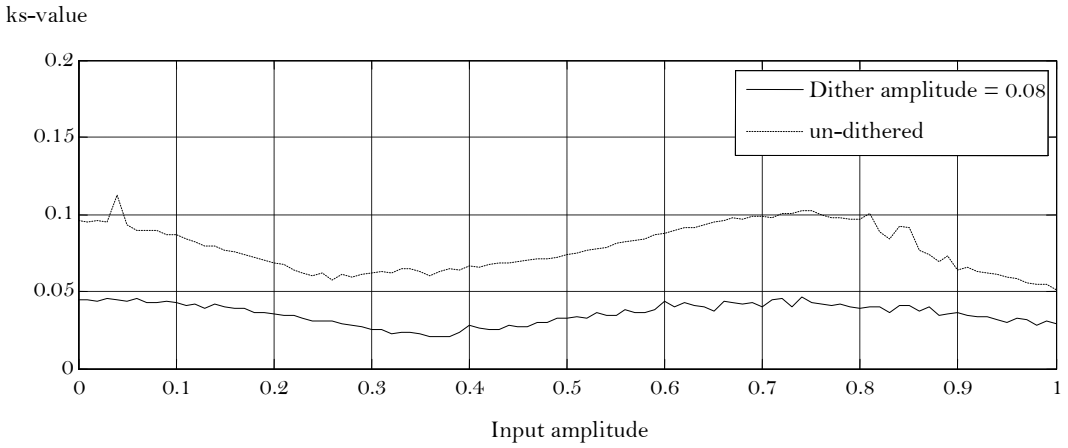

Figure 3-32 k-Gaussian test values for dithered- and un-dithered fourth-order HP Σ–Δ modulator

Since the proposed model assumes that the input to the quantizer has a Gaussian PDF, the randomization effect of the dither makes the proposed model more accurate.

3.6 Concluding Remarks

The stability boundaries for higher-order HP and BP Σ–Δ modulators were derived from the modified quasi-linear model in conjunction with the DF method. The quantization noise variances as well as the theoretical noise amplification curves for different input amplitudes, stop-band bandwidths and stop-band attenuations were also derived. Using these noise amplification curves, the maximum stable amplitude limits for different quantizer gain values depending on the input amplitudes were established.

The theoretical results showed that the increased stop-band attenuation caused the maximum stable amplitude limits to reduce. However, increasing the stop-band attenuation provided better noise suppression in the signal band so that better SNR values were achieved. As a result, there was a trade-off between the MSA limits and the resolution of the Σ–Δ modulator output.

In addition, theoretical results showed that the widening of the stop-band caused the noise amplification factor to increase, resulting in a reduction in the dynamic range of the Σ–Δ modulator, i.e. the MSA limits were reduced and the stable K-interval became narrower. Therefore, the Σ–Δ modulator is less stable compared to Σ–Δ modulators with narrower bandwidths or reduced stop-band attenuations. Moreover, the theoretical $A(K)$

curves showed that the Chebyshev Type II based Σ–Δ modulators achieved better in-band noise attenuation as compared with Butterworth based Σ–Δ modulators of the same order.

The theoretical results were shown to match reasonably well compared with their corresponding simulation results, especially for middle-range input amplitudes (a = 0.4) and higher-order Σ–Δ modulators. Because of the spectral tones introduced in the signal band, the difference between the theoretical and simulated results became higher as the input amplitude a increased. The differences in the results are attributed to the fact that the quantization noise is not completely Gaussian. In addition, the tonality of the Σ–Δ modulator output causes the simulated results to vary from the theoretical values. Furthermore, for a single sinusoidal input, the non-linear quantizer was modeled with linearized gains obtained by using the mean square error criterion, where the quantization noise power, σ_q^2, was minimized. However, in the dual sinusoidal case, the nonlinearity was modelled as three linearized gains, two for the input signals (K_a, K_b) and one for the noise component (K_n), which was assumed to have a Gaussian PDF. Therefore, the signal- and noise-model gains were obtained by the modified nonlinearities concept. The nonlinearity function model of each input was modified for the other remaining inputs in turn, starting with the nonlinearity function models for the sinusoidal inputs, and following on with those further modified for the quantization noise model. In reality, however, the non-linearity of each input exists simultaneously. Therefore, the differences in the results were comparatively larger for dual-tone sinusoidal inputs compared with single tone ones.

These stability curves resulting from this work would accelerate the design and evaluation of higher-order HP and BP Σ–Δ modulators with increased dynamic ranges for various applications that utilize single- and dual-tone input signals. The proposed novel mathematical expressions could be integrated with various design tools to more accurately and rapidly predict stability in HP and BP single-bit higher-order Σ–Δ modulators.

In addition, ultrasound signals are single-tone narrow-band BP damped sinusoidal signals. For future work, the analysis of higher-order BP Σ–Δ modulators as well as the determination of their stability boundaries for single- and dual sinusoidal inputs would enable researchers to design, evaluate and implement higher-order LP or BP Σ–Δ modulators in the ultrasound beamformer structure, thus saving considerable time.

Chapter 4

Digital Ultrasound Beamformers

In this chapter, the performance of 1-bit Σ–Δ beamformers, 10-bit A/D beamformers and their resulting image quality comparisons are examined through software simulations using experimental phantom data sets. First of all, the advantages of using Σ–Δ beamformers over Nyquist-rate multi-bit A/D beamformers are detailed in Section 4.1 In order to understand how Σ–Δ beamformers operate, the basic principles behind the ultrasound systems are briefly explained in Section 4.3 The signal processing aspects are divided into three parts: front-end-, mid-end-, and back-end-processing [Ali08]. The front-end processing is detailed in Section 4.4 by focusing on the digital beamforming process. Section 4.6 introduces the mid-end processing including envelope detection and log compression. The back-end processing is given in Section 4.7 which describes the scan conversion process. The experimental data sets and parameters to analyse the simulation results are given in Sections 4.5 and 4.8 In Sections 4.9 and 4.10 the performance of Σ–Δ beamformers are evaluated by means of computer simulations and compared with 10-bit A/D beamformers. In Section 4.11 the image artefacts caused by single-bit Σ–Δ beamformers are quantified and their effects on image resolution are discussed.

4.1 Σ–Δ Modulators in Ultrasound Imaging Systems

Ultrasound imaging is used in a variety of medical applications, including cardiology, obstetrics, genecology, general abdominal imaging, developing fetuses, vascular imaging and bone densitometers [Moo94], [Nel08], [Qui97], [Sza04], [Tex13], [Wel87]. Ultrasound imaging has been directly influenced by developments in microelectronics. In the late 1980s, electronic sector scanning using phased array systems became increasingly popular because of advances in A/D conversion [Hem15], [Mas85], [Odo90], [Wag12], [Zho14].

A typical simplified state-of-the-art ultrasound system can be broken down into three main parts: pulser, analog-front-end and digital-front end as given in Figure 4-1 [Tex13]. The transmit beamformer, HighVoltage (HV) pulser and HV multiplexer form the transmit path that is responsible for the pulse-excitation of the transducer elements. The main function of the Transmitter/Receiver (T/R) switches is to prevent high-voltage pulses from damaging the receive electronics. The echoes are then amplified properly and converted from analogue to digital in order to be processed in the digital front-end part. The main function of the digital front end in an ultrasound system is to focus at a given depth and direction [Tex13]. Ultrasound systems are signal processing intensive. The performance of digital ultrasound imaging systems is strongly dependent on the transducers and front-end-components. At this stage, the precision of the A/D conversion becomes critically important.

Generally, ultrasound beamformers are designed to suppress the side lobes by more than 60 dB, which correspond to at least a 10-bit amplitude quantization requirement [Che09a]. Therefore, conventional digital ultrasound beamformers use typically 10- and 12-bit A/D converters to digitize echo signals from each transducer element [Fre99], [Jen13], [Tex13], [Wag12], [Zho14]. However, the complexity of digital beamforming using 10-bit A/D converters makes the design of phased array systems with a large channel count difficult [Mas85], [Jeo07], [Odo90], [Pet84], [Pri79], [Ran04]. Therefore, the major challenge in ultrasound imaging systems is to simplify the front-end hardware of the ultrasound system especially for scanners with large channel count beamformers. Σ–Δ beamformers have been proposed to reduce hardware complexity of the phased array front-end circuitry in digital ultrasound imaging systems. Σ–Δ A/D converters trade digital signal processing complexity for relaxed requirements on the analogue components

compared to Nyquist-rate A/D converters. Σ–Δ A/D converters combine both oversampling and noise shaping making it possible to effectively convert an electrical analogue signal into its digital, discrete-time representation using modern digital CMOS technology. The use of such converters in ultrasound beamformers offers the following advantages: integration of beamforming logic and A/D converters, as these can be manufactured using the same semiconductor technology, small area per converter, making it possible to accommodate a large number of A/D converters on a single chip at a relatively low price.

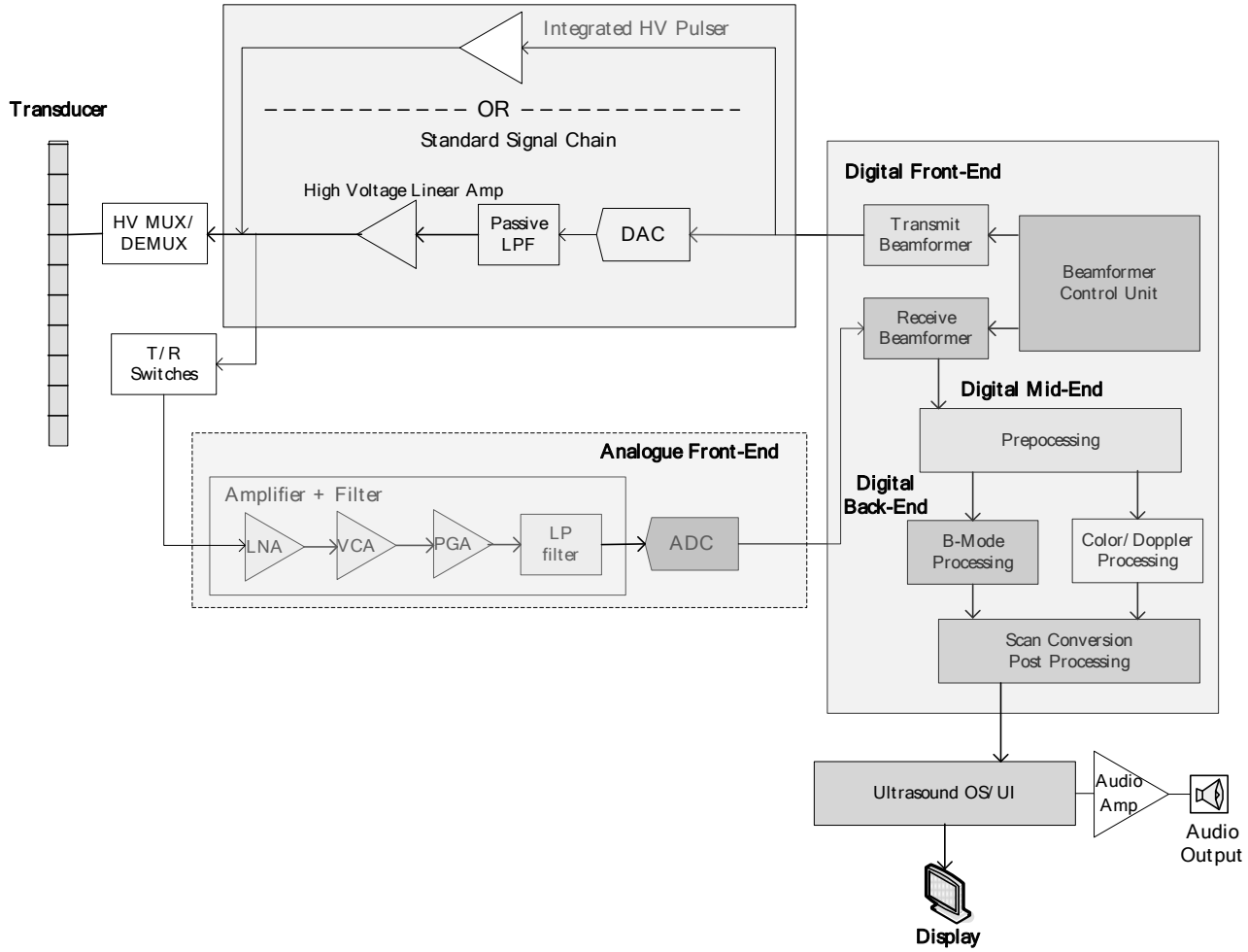

Figure 4-1 Ultrasound system block diagram [Tex13]

4.2 Advantages of Σ–Δ Beamformers over Nyquist-rate Beamformers

Advances in VLSI technology have made oversampling A/D converters more attractive in digital processing applications [Can92], [Nor97]. Because of their relative simplicity and ease of integration into other processing elements, digital beamformers using 1-bit Σ–Δ modulators have crucial advantages over traditional multi-bit Nyquist-rate A/D beamformers [Fre98], [Liu09], [Nou93], [Rig02], [Ste01], [Ste96], [Zie98] as outlined below:

1. In ultrasound systems, for accurate focusing, a delay resolution of 1/32 of the wavelength of the ultrasound transmit signal is needed [Lip94], [Nou93]. Therefore, traditional Nyquist-rate A/D converters at a sampling rate of 4 times the ultrasound operating frequency are not sufficient to achieve accurate delays to properly form a focus. For example, for an ultrasound signal with an operating frequency of 3.5 MHz, a delay resolution of 9 nanoseconds is required. However, a Nyquist-rate A/D converter at a sampling rate of 14 MHz, which corresponds to a delay resolution of 72 nanoseconds, does not provide accurate delay resolution. As a result, many complicated processing techniques are required to ensure sufficient delay accuracy, which increase the cost and complexity of the circuit dramatically. On the other hand, the inherently high sampling rate of Σ–Δ modulators ensures sufficient delay resolution by manipulating the samples taken with a high sampling rate. For example, Σ–Δ modulators at a sampling rate of 222 MHz, have delay resolution of 4 nanoseconds. As a result, the complicated interpolating/decimating- or baseband-rotate circuits of traditional multi-bit Nyquist-rate beamformers are replaced by simple shift registers [Fre99], [Mas85], [Nou93].

2. Σ–Δ A/D converters need simpler components with lower precision and tolerance rating than multi-bit flash A/D converters, which use high precision analogue components [Can92], [Nor97].

3. Multi-bit A/D beamformers are required to be connected from each beamformer channel to the console, which needs a high cost coaxial cable between the console and transducer. However, Σ–Δ modulators can be easily integrated onto the same chip with the digital processing blocks deploying CMOS VLSI processes [Nor97]. This means that the Σ–Δ

beamformer hardware can be integrated into the ultrasound probe itself rather than the ultrasound console [Rig02]. As a result, the weight and size of the hardware are significantly lower due to the reduced resources used for the interconnection size between the beamformer and the other processing elements [Bru02], [Nor97].

4. Since typical Σ–Δ modulator structures have several operational amplifiers and one comparator, whereas 10-bit A/D converters have 1024 comparators; the A/D structure is significantly simplified [Can85], [Can92].

5. The hardware complexity is reduced due to the simplified signal processing and lower number of bits from 10 bits to 1 bit. For 1-bit Σ–Δ beamformers, the delays are performed via CMOS FIFO's and the beam sum is done via standard adders across the array [Can92], [Gur08], [Fre99], [Nor97]. Thus, pipeline adders can be used for the beam summation, which require an overall number of S-channels $(S/2+1)\times\log_2 S/2$ adders [Che09a], e.g. for a 128 channel system, 390 adders are required by pipeline adders.

In addition, the actual dynamic ranges of A/D converters are always below the theoretical values. For example, a 14-bit A/D converter Analog Devices' AD6644 has a SNR of 74 dB, which is about 12 dB below the theoretical SNR of a 14-bit A/D converter [Bru02], [San08]. Current state-of-the-art beamformers use 10-12 bits per channel. However, the usage of 14 or 16-bits A/D converters will significantly increase the complexity and memory requirements of the beamformer circuitry. Power consumption and circuit size are the two main design issues, since most state-of-the-art ultrasound imaging systems have 128 to 512 channel beamformers, which require 512 to 16,384 parallel processing channels [Tex10], [Tex13]. There is a trade-off between the required power and the image resolution of the ultrasound system. 12-bit A/D converters such as Analog Devices AD9271 or Intersil HI5746 consume several hundred mW [Ana09], [Int10]. On the other hand, 1-bit second-order Σ–Δ modulators with an average power consumption of 20 mW and a circuit area of 0. 24 mm² can be implemented in a standard digital CMOS process [Tov04]. In addition, 16-bit delta-sigma A/D converter such as ADS1115 has the size of 2.0 x 1.5 x .04 mm of a parallel interface with direct connection to DSPs [Tex10].

In Table 4-1, a comparison of A/D converters used in ultrasound systems is given [Tex10], [Tex13], [Tex15].

Product	ADS1605 ADS1610	ADS5281 ADS5282 ADS5287	ADS5292 ADS5294
Bit-Resolution	16	12	14
Sampling Rate	5 MSPS	65 MSPS	80 MSPS
SNR	88	70	78.2
Power Consumption	550 mW	77mW/channel	54mW/channel
Architecture	Delta-Sigma (selectable on chip reference)	Pipeline (8-channel)	Pipeline (8-channel)

Table 4-1 A/D converter product examples used in ultrasound systems

The SNR and power consumption are the most important issues, followed by the implementation of the interface between the A/D converter and the beamformer. Therefore, reducing the power consumption only is not enough to simplify the front-end hardware. As a result, Σ–Δ modulators are widely used to reduce the hardware complexity resulting in significant savings in the size, power consumption and cost [Bil10], [Chi15], [Fre99], [Hem15], [Jun13], [Kar00], [Koz01], [Lie06], [Nil08], [Nou93], [Rig02], [Syn07], [Tom13], [Tov04]. Therefore, the hardware simplicity of the Σ–Δ beamformers is particularly suitable for low-power 3D scanners with large channel count beamformers as well as portable and lightweight ultrasound scanners and intravascular imaging systems [Che09a], [Che13], [Chi00], [Fen96], [Loc98], [Kar95], [Hwa98], [Ste01], [Tom05], [Uca96].

4.3 Basic Principles of Digital Ultrasound Imaging

Ultrasound imaging uses high-frequency sound waves to produce images of the exposed part of the body including the heart, vessels, kidney, liver, developing fetuses and other soft tissues [Wel69], [Wel75], [Hav79]. The ultrasound waves are generated by a transducer

which is held against the body. The piezoelectric crystal elements in the transducer start to vibrate and produce high-frequency sound waves when a high voltage is applied across the transducer. The ultrasound waves can be presented as damped sinusoidal signals with an operating frequency in the range of 2 - 15 MHz. Above this range, sound waves are significantly attenuated by human tissue. And below this range, the wavelength of the sound waves is so long that the resolution for small structures is significantly low [Wel07]. In addition, the acoustic attenuation is proportional to the propagation distance (depth) and the operating frequency. Therefore, there is a trade-off between the operating frequency and image depth, which limits the image quality. A typical attenuation for soft tissues is 1 dB/cm/MHz, which corresponds to 70 dB attenuation for a 3.5 MHz ultrasound wave for a round trip of 20 cm [Kar00].

Different from sound waves, ultrasound waves with high frequencies tend to move more in straight lines, and will be reflected by much smaller objects like light beams and do not propagate easily in gaseous media [Wel69], [Hav79]. The speed of sound varies for different transmission media but the average transmission velocity is assumed to be nearly uniform at 1,540 m/sec for most soft tissues [Hav79]. Through their propagation, sound-waves are partially reflected and refracted depending on the tissue they are exposed to. When two mediums with different densities are located next to each other, an acoustic impedance mismatch is created and sound waves are reflected by this mismatch. Therefore, the ultrasound imaging technique is based on processing the echo signals [Sho88]. The greater the acoustic mismatch, the bigger is the intensity of the echo signal. This is generally seen as brighter areas on the image. Therefore, intensities of the echo signals, (*I*), are relative quantities so that in ultrasound there is no absolute or inherent tissue property. The unit for I is *energy/time/unit area*, which is $J/(m^2\ s)$ [Sho88]. The physical principles of medical ultrasound imaging, the physics of sound waves and their interaction with exposed tissue are extensively covered in [Ald07], [Chi78], [Kin62], [Kin87], [Wel07], [Wel69], [Wel75]. Ultrasound systems and the effects of circuit components at the front-end part on diagnostic performance are explored in [Bru02]. The ultrasound system is summarized in Figure 4-2.

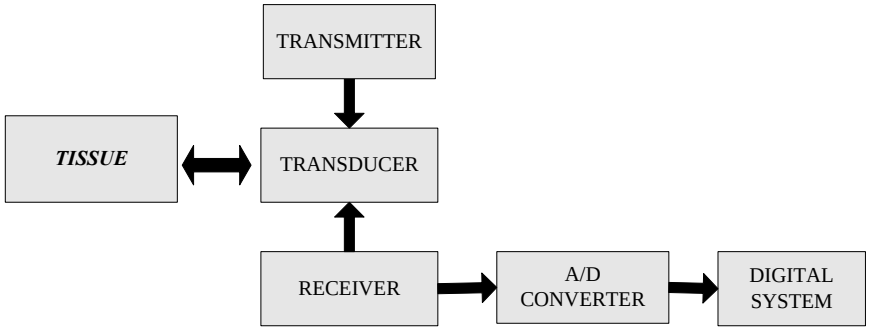

Figure 4-2 Simplified block diagram of the ultrasound system

The transmitter excites the transducer with a series of pulses. The transducer converts electrical energy from the transmitter into ultrasound waves sent to the target tissue. The reflected echoes from the tissue are converted back to the electrical signals by the same transducer. The amplitude of the received echo defines the tissue properties in terms of image brightness, where the strong reflections due to the high tissue impedance (e.g. bone, gallstone) are represented as white and the no-reflections due to the weak tissue impedance (blood, urine) as black. Also, the total time for waiting for the echo is determined by the depth of the tissue. The system calculates how long it takes for the echo to return to the transducer using the relation: $depth_{echo} = \frac{time_{echo} \times velocity}{2}$ [Kin62].

The commonest process is beam focusing electronically using phased arrays [Tho96], as presented in this study. Transducer arrays are composed of S-transducer elements, and each element transmits and receives ultrasound pulses individually. The characteristics of the transducer (aperture size, bandwidth, operating frequency, array spacing, and number of elements) limit the axial- and angular-resolution of the image. The effects of the transducer parameters on the image quality are well detailed in [Sea02]. If S is chosen to be too small, array elements get too far apart. As a result, more than one beam might be produced, and this makes it impossible to determine the direction of the echo signal. Therefore, in order to eliminate the additional lobes, for a transducer of size $2w$, the space between the array elements, d, needs to be less than half of the ultrasound wavelength, λ [Sea02]: $d = \frac{2w}{S} < \frac{\lambda}{2}$. Therefore, the typical number of phase array elements is 128 or more.

In principle, the ultrasound system focuses sound waves along a given scan line so that the waves constructively add together at the desired focal point [Sho88]. Fixed focus

beamforming is achieved by fixing the output position to a focus point (mostly to the middle range) whose indexes are calculated from the required inter-channel delays relative to the channel that has the shortest flight path to the receive focal point. Once all of the sound waves along the given scan line have been completed, the output positions are switched for each new emission in order to accommodate the new receive focal point, corresponding to a new image line. The transducer focuses along a new scan line until the entire scan lines in the desired region of interest have been measured [Sho88], [Joh93], [Tho96]. This process of using multiple sound waves to steer and focus a beam electronically is referred to as digital beamforming. The scanning format for ultrasound phased array systems performing electronic focusing is illustrated in Figure 4-3.

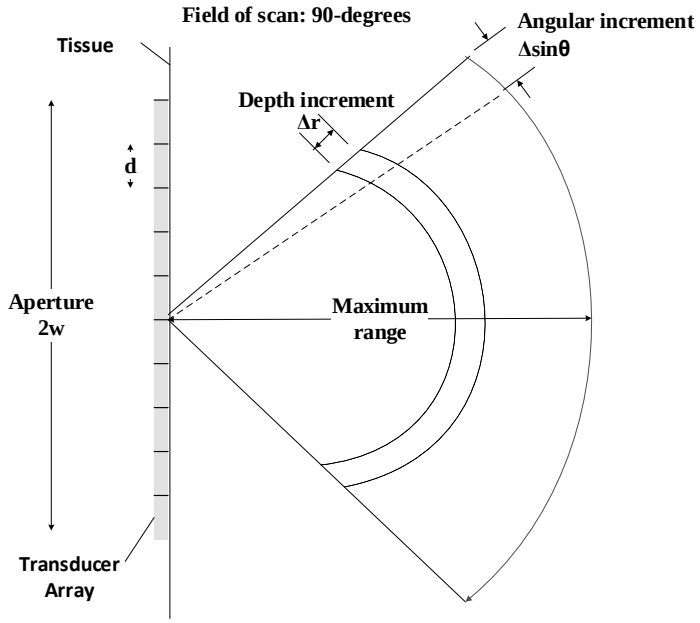

Figure 4-3 Schematic diagram of ultrasound scanning format

Once the beamforming process is completed, envelope detection is required to obtain the peaks in the echo signal to obtain B-mode images. In B-mode, the transmitted sound wave is swept over the plane to produce a 2D image, where brightness is used to represent the amplitude of the echo signal. [Wel69].

4.4 Front-end Signal Processing

4.4.1 Beamforming

In the transmit mode of operation, multiple piezo-electric elements are excited with properly time-delayed pulses and then they become sensors to record the reflected sound waves. Figure 4-4 shows how the time-delay values for each array element are calculated. The location of the focal point (*P*) in this figure is referenced using polar coordinates (*r*-*θ*).

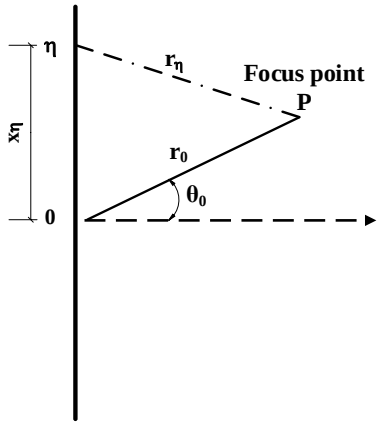

Figure 4-4 Focus point geometry in polar coordinates

Each transducer element is driven with the same pulse waveform. The propagation time, τ_η for the η^{th} element to the focal point (*P*) can be written by the geometry given in Figure 4-4.

$$\tau_\eta = \frac{\sqrt{r_0^2 + x_\eta^2 - 2x_\eta r_0 \sin(\theta_0)}}{c} \tag{4.1}$$

where x_η is the x coordinate of the η^{th} element, (0 is at the center of the array), θ_0 is the angle to the horizontal axis and r_O is the depth of the focal point to the center of the array system. The beams always intersect the array at the center. The conventional approximation of this equation with a Taylor series expansion is given in Appendix A. As a result (4.1) yields [Fre97]:

$$\tau'_\eta = \tau'(x_\eta, r_0, \theta_0) = \tau_\eta - \tau_0 = -\frac{x_\eta \sin\theta_0}{c} + \frac{x_\eta^2 \cos^2\theta_0}{2cr_0} \tag{4.2}$$

Fixed focusing is usually used in *transmit mode*, where the above expression (4.2) is fixed for a predetermined focusing depth. As shown in Figure 4-5, to ensure that the sound waves from each element arrive at the focal point at the same time, the pulse waveform to each element must be delayed by this amount to compensate for the time-delays [Kar95].

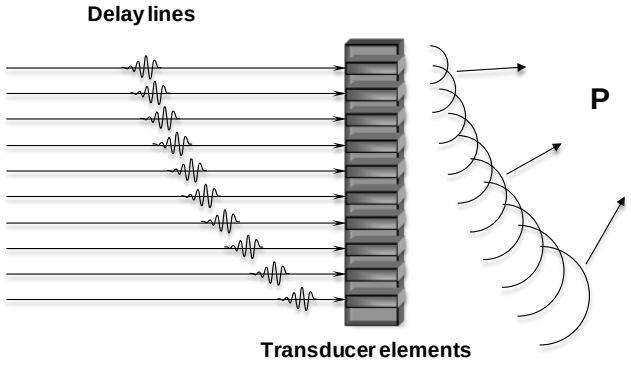

Figure 4-5 Transmit focusing

On the other hand, in the *receive mode*, the scanning is performed line-by-line. The array elements employ dynamic focusing by stimulating each element with different time delays according to the propagation time difference from the focus point, *P*.

As a result, sufficient image detail can be obtained at various depths within the body rather than just one depth as performed at fixed transmit focusing. Figure 4-6 demonstrates how transducer array elements scan dynamically the region of interest.

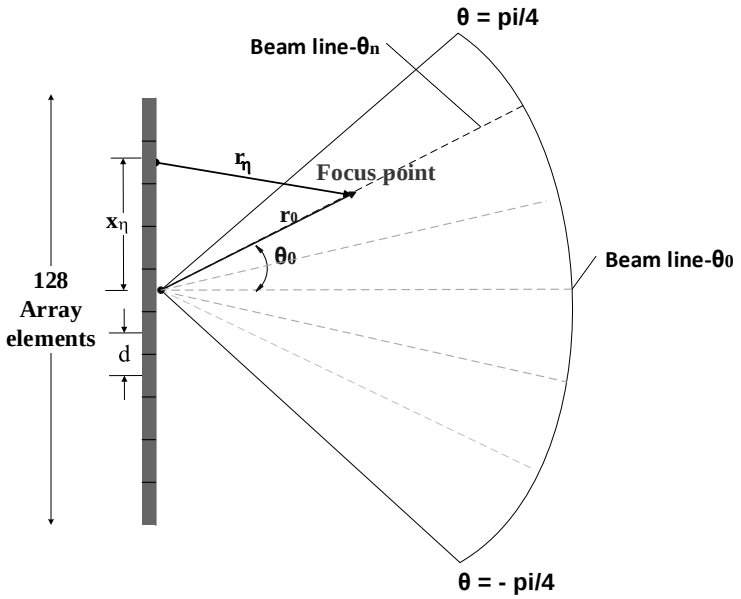

Figure 4-6 Parameters required for ultrasound scanning format

The propagation time difference $\tau_n^{'} = \tau_0 - \tau_\eta$ of the corresponding η^{th} receive element is related to its position to the focus point, P as shown in Figure 4-7.

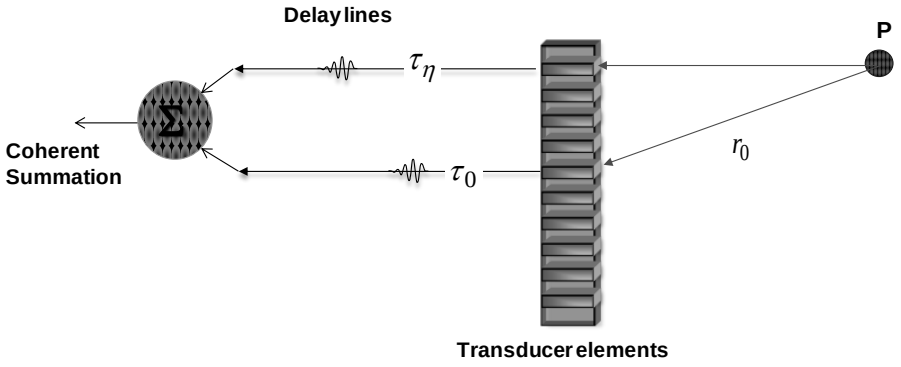

Figure 4-7 Receive Beamforming

The time difference of the arriving echo signals in the dynamic receive beamformation can be performed in two parts: steering and focusing. Using basic geometry, the general term given in (4.2) can be broken down into two parts: steering and focusing as given in (4.3) in order to obtain the propagation time difference to the η^{th} array-element, $\tau_\eta^{'}$ [Odo90]:

$$\tau'_\eta = \tau'(x_\eta, r_0, \theta_0) = \underbrace{-\frac{x_\eta \sin\theta_0}{c}}_{steer-delay} + \underbrace{\frac{x_\eta^2 \cos^2\theta_0}{2cr_0}}_{focus-delay} \tag{4.3}$$

The first term focuses the beam to a particular angle and the second term is to focus it to a particular range. By adjusting the time delays across the array, a region of interest can be scanned over predetermined directions and depth. Signals from each array element $p_\eta(t)$ are delayed ($\tau_\eta^{'}$) and summed to produce a beam sum $p(t)$ localized at the focus point:

$$p(t) = \sum_{\eta=1}^{128} p_\eta(t + \tau_\eta^{'}) \tag{4.4}$$

In dynamic receive beamforming; delays are changed dynamically for the various depths within the sector. In other words, as given in Figure 4-8, each pulse is delayed appropriately and added coherently, to form the desired beam at a particular direction and depth.

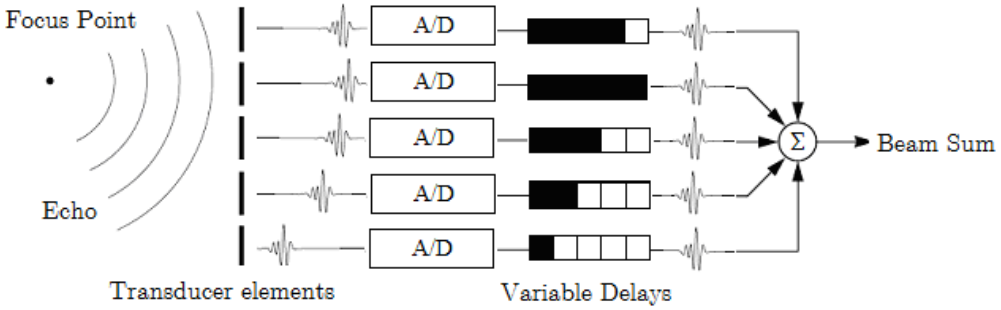

Figure 4-8 Block diagram for the dynamic beamforming in receive mode

As a result of the delay-and-sum process, an image line is produced by continuously focusing along that beam line [Fre99], [Odo90]. In this study, a 90-degree sector is scanned by a B-scan phased array system. To perform a 90-degrees scan, there is an angular sampling constraint where the minimum spatial sampling frequency should be twice the spatial frequency bandwidth in order to avoid any additional main lobes [Moo94], [Sea02]:

$$\Delta \sin\theta \le \frac{\lambda}{4w} = \frac{1}{2 \cdot NA} \tag{4.5}$$

The array size and numerical aperture are represented by $2w$ and NA ($2w/\lambda$) respectively, where $NA = 2w/\lambda$. Since the sampling is uniform in $\sin\theta$, a sufficient number of beams for a 90-degree scan should be predefined according to (4.6) [Moo94]:

$$\text{Number of beams} = \frac{max(\sin\theta) - min(\sin\theta)}{\Delta \sin\theta} \tag{4.6}$$

For a conventional 128-element transducer array, the number of beams must be greater than or equal to 182. In this study, the number of beams is chosen as 182; so that each beam is steered in increments of $\Delta \sin\theta \approx 0.0071$. Once all the 182-scan lines are completed, the mid-end processing stage can be performed.

4.5 Experimental Data-Set

The experimental data acquired from the Ultrasonic Research Laboratory of the University of Michigan is used to demonstrate the performance of the Σ–Δ beamformer and 10-bit A/D beamformer [Kri97]. The data sets include two different phantoms: a wire target phantom,

consisting of six wires in a water tank, and a cyst phantom, containing tissue mimicking gel. The 10-bit data was recorded using a commercial 128-element, 3.5-MHz transducer array with an element pitch of 0.22 mm (Acuson, Model # V328) [Kri97]. The same data sets were used in [Fre97], [Fre98], [Fre99], [Kar98], [Kar99], [Kar00], [Koz01], [Che08a], [Che08b], [Nil08], [Uca96]. All the wire target images are displayed over a 70 dB dynamic range, whereas all the cyst images are displayed over a 50 dB dynamic range following logarithmic compression. Transmit focus is fixed at 65mm and dynamic focusing is performed in the receive mode.

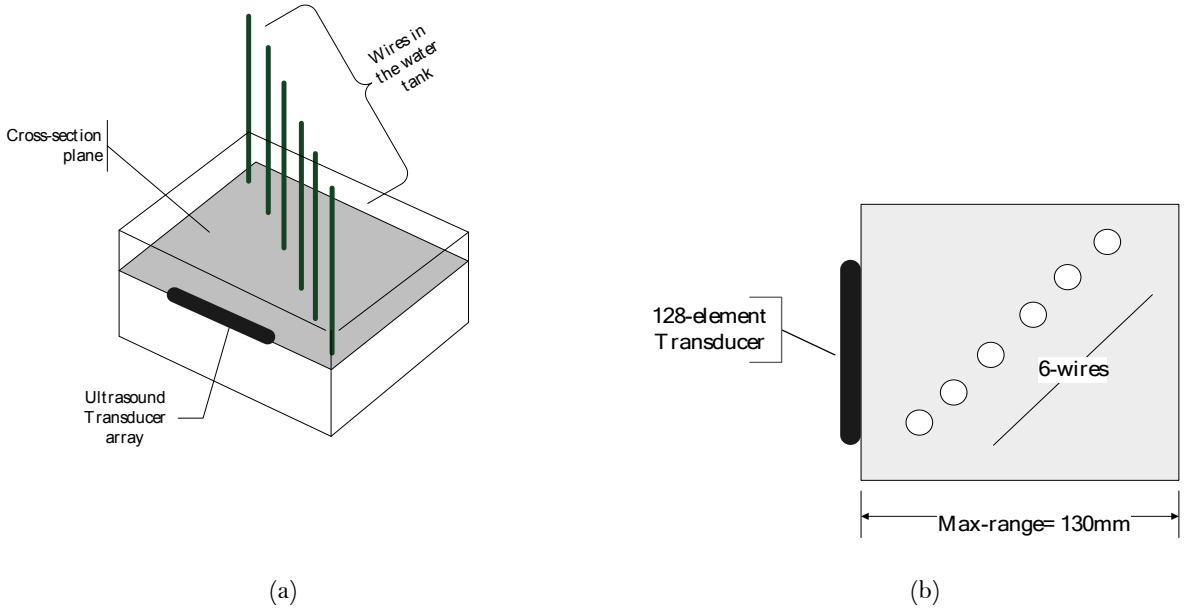

Figure 4-9 Wire phantom, (a) schematic setup, (b) cross-section [Bil03]

The experiment setup for the wire-phantom is given in Figure 4-9. The wires are placed slightly away from each other in order to prevent shadowing. The corresponding simulation parameters are given in Table 4-2.

DESIGN PARAMETER	Value
Transducer operating frequency	3.5 MHz
Sampling Frequency	13.8889 MHz
Number of Channels	128
Transducer Spacing	0.22 mm
Image Depth	130 mm
Transmit Focusing	Fixed Focusing
Receive Focusing	Dymamic focusing
Image Sector	90-degree
Number of Beam Lines	182
Offset Time	29.448 μsec
Speed of Sound	1.48 mm/ μsec

Table 4-2 Simulation Parameters

During transmission, some portions of the transmitted waves are reflected back to the transducer element. To eliminate these echoes during the transmission, a short offset-time for the receive mode is given. The data-set has been obtained as follows: the first transmitter element sends a pulse to the target and after the offset-time all the receivers start to record the echo signals reflected from the targets in the scanning area. After the receive-mode, a second transmitter sends an ultrasound pulse and waits for the receivers to record. This procedure continues until the last transmitter sends the pulse and all the echoes are received [Bil03]. At the end, a data set of a size of [2048 x 128 x 128] is obtained. For example, an echo signal transmitted by the 2nd element and received by the 1st element is presented as a matrix of size [2048x 1 x 1] and is shown in Figure 4-10.

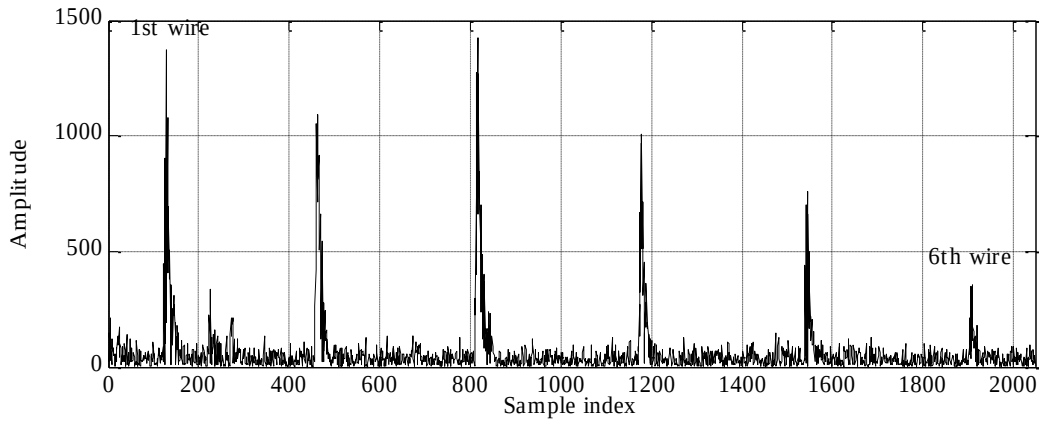

Figure 4-10 Echo signal in time-domain

Since the fixed transmit focal range is chosen as 65mm, the biggest amplitude is obtained from the 3rd wire reflection. In addition, since the signal amplitude attenuation is proportional to the imaging depth, the amplitude of the echo signal decreases with the range. Thus the 6th wire has the smallest echo signal amplitude.

4.6 Mid-end Processing

Mid-end processing can be defined as any signal processing that is performed on each scan line of the beamformed data. The main mid-end processing functions for conventional ultrasound imaging systems include: demodulation (filtering), envelope detection and logarithmic compression [Ali08].

Envelope Detection: Ultrasound systems use band-pass pulse, $p(t)$ to excite the transducer elements, which can be represented as a Gaussian envelope, $a_0(t)$, modulating a carrier center frequency, f_0. The complex presentation is given as an analytic signal:

$$p(t) = a_0(t)e^{i\omega_0 t} \tag{4.7}$$

where $\omega_0 = 2\pi f_0$. Therefore, the real part of the echo signal at the receiver for a focus point at a distance r_0 in the time-domain yields:

$$p(t - 2r_0/c) = A_p \cdot a_0(t - 2r_0/c)\cos(\omega_0(t - 2r_0/c)) \tag{4.8}$$

where A_p is the attenuation term as a function of frequency and the propagation distance.

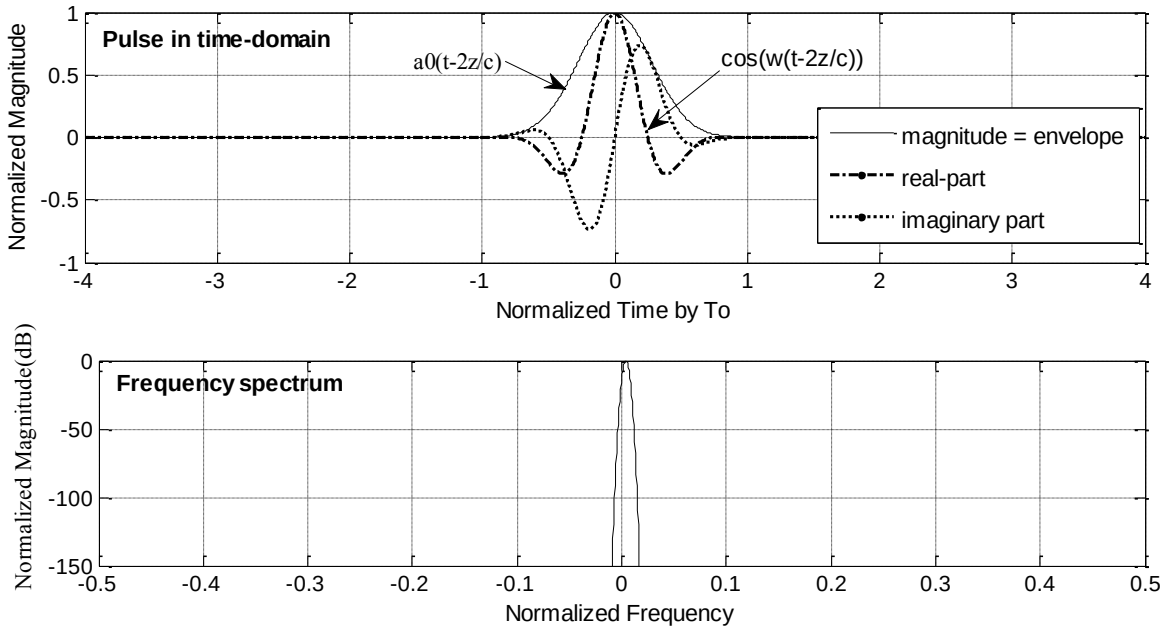

Figure 4-11 Ultrasound pulse signal (a) time domain, (b) frequency-domain

The first stage to extract the envelope of the signal, $a_0(t-2z/c)$ is to create a complex representation of the signal. In order to obtain the analytical signal, two methods can be used: the Hilbert transform or baseband demodulation. Although the Hilbert transform is independent of the operating frequency and imaging mode, the baseband demodulation method is less complex. The signal of a centre frequency can be demodulated in baseband using a complex rotator followed by a low-pass filter to suppress the side lobes. As given in Figure 4-11, the envelope of the signal is obtained as the magnitude of the sum of its in-phase and quadrature components.

Log Compression: Since the maximum dynamic range of the human eye is in the order of 30 dB [Sza04], a log compressor is used to compress the actual dynamic range of the envelope. The actual dynamic range of the envelope signal depends on the A/D converter resolution. Usually, an image resolution of 7-8 bits is used for the display [Ali08].

4.7 Back-end Processing

Scan conversion: The final process of the ultrasound system is scan conversion. In B-mode, a two-dimensional diagnostic ultrasound presentation of echo is displayed. The intensity of the echo is represented by modulation of the brightness of the spot, and the position of the echo is determined from the angular position of the transducer and the transit time of the

acoustical pulse and its echo. As discussed above, reconstruction of the ultrasound data is inherently done in polar coordinates in a sector scanner. However, polar coordinates are not appropriate for the monitor display, therefore a method of converting this data is required. This involves presenting the data as a meaningful image by transforming the data from polar coordinates (r-$sin\theta$), to Cartesian coordinates (x-y). Therefore, equally spaced data in polar space need to be interpolated to a physical space. The most commonly used technique for scan conversion is bilinear interpolation.

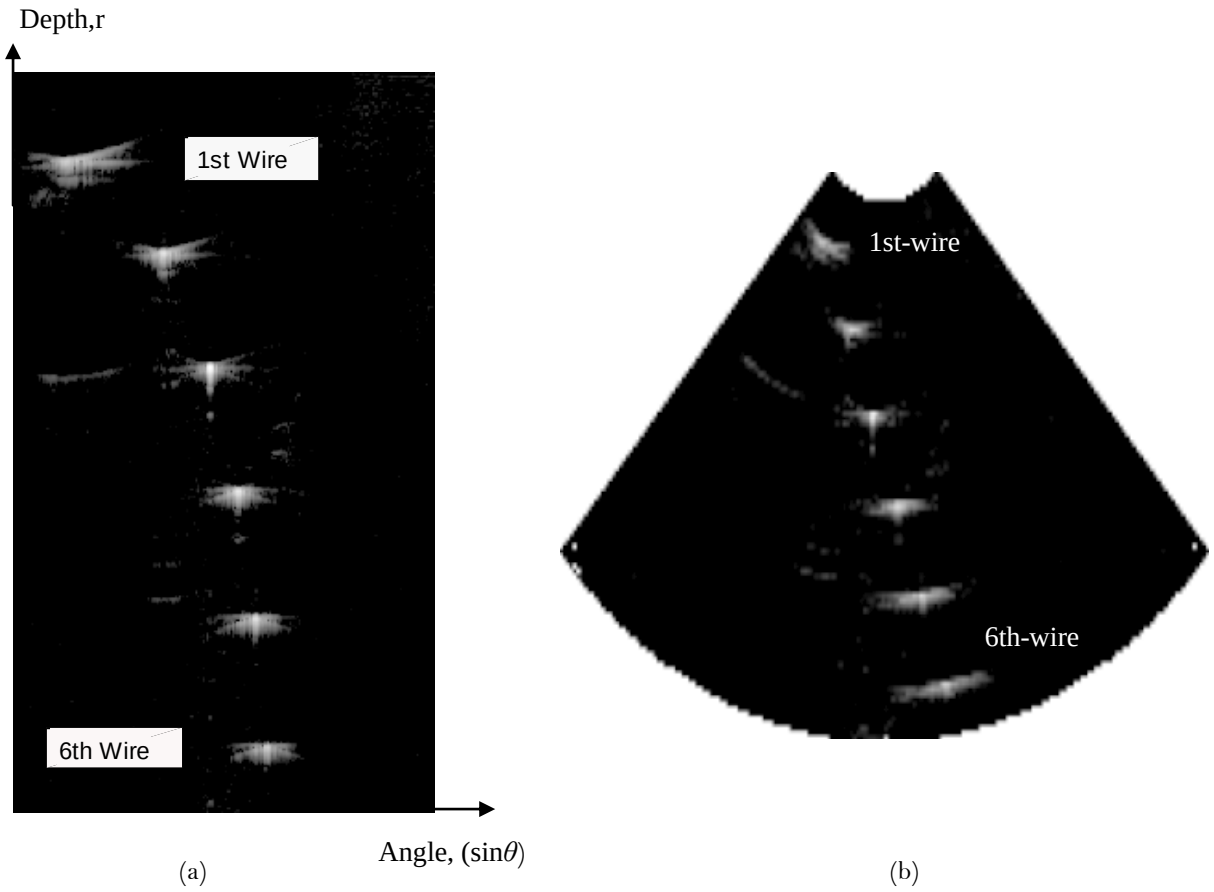

Figure 4-12 Final B-scan images in, (a) Polar coordinates(r-sinθ), (b) Cartesian coordinates(x-y)

The constructed image after scan conversion can be seen in Figure 4-12. The brightness of each pixel in the image is adjusted as a function of the amplitude of the reflected signals [Sho88].

4.8 Beamformer Performance Analysis

Besides the quality of the final B-scan images, the performances of the beamformers can be evaluated quantitatively in terms of the SQNR, CNR values and PSF. Due to the fixed transmit focusing at half the maximum imaging distance, the strongest reflector is the third wire.

For focus points away from the transmit focus, the beamwidth enlarges and the side lobes increase [Rib02]. Therefore, the frequency spectrums of a single beam line lying at the centre of the main lobe of the third wire and the corresponding PSF will be used [Kar95], [Koz01].

4.8.1 Wire Phantom

The noise level can be compared in terms of the SQNR values, which are calculated using the envelope signal before the logarithmic compression. As shown in Figure 4-13, the signal power at each wire is calculated within a small kernel (approximately 6 pixels) over the wire including the main lobe and the noise power is calculated as the root mean square within a larger kernel (approximately 24 pixels) near that wire excluding the acoustic artefacts, reflectors and the side lobes.

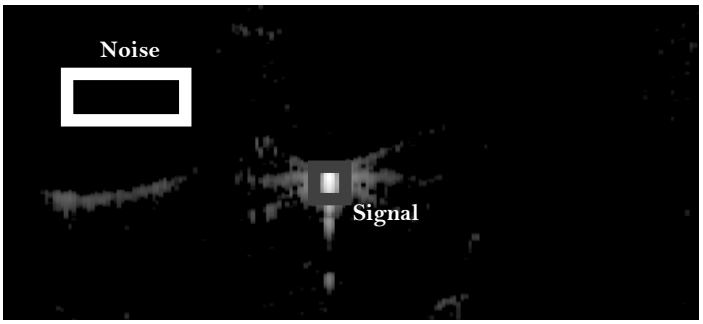

Figure 4-13 Representing noise- and signal pixels in the one wire image

For the signal power; the mean square root of the main lobe is calculated. However, as shown in Figure 4-14b, the envelope signal is a sinc function. Therefore, the signal power is calculated for varying depth- and angle indices and the average value is calculated. For the signal power, the range of samples within ± 6 of the centre index is used in the calculation. On the other hand, for the noise power, a wider range of samples, i.e.± 20 samples from the centre index is used. For each of the wire images, the mean SQNR is calculated over six

wires as given in Figure 4-14a [Che08a], [Che08b], [Fre97], [Fre99], [Kar00], [Kar95], [Koz01].

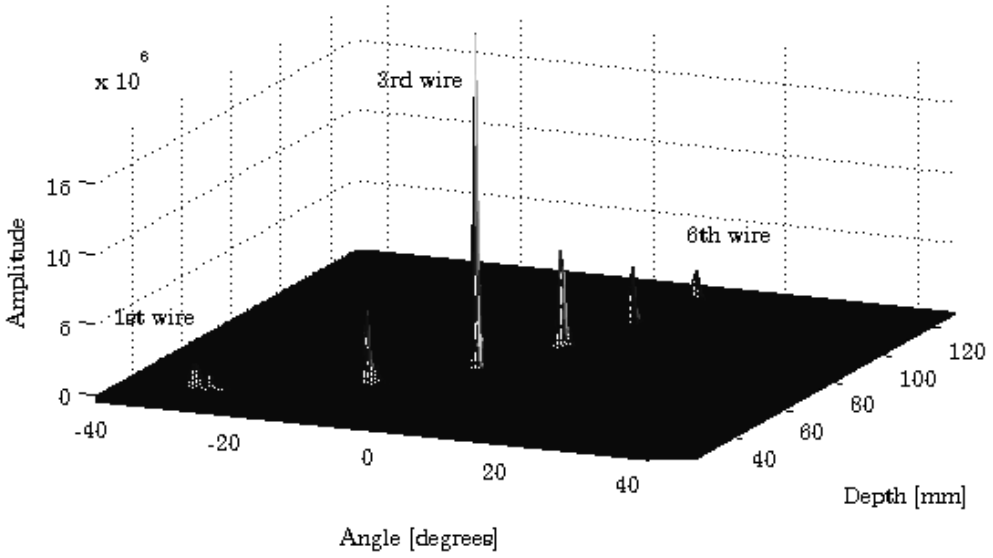

(a)

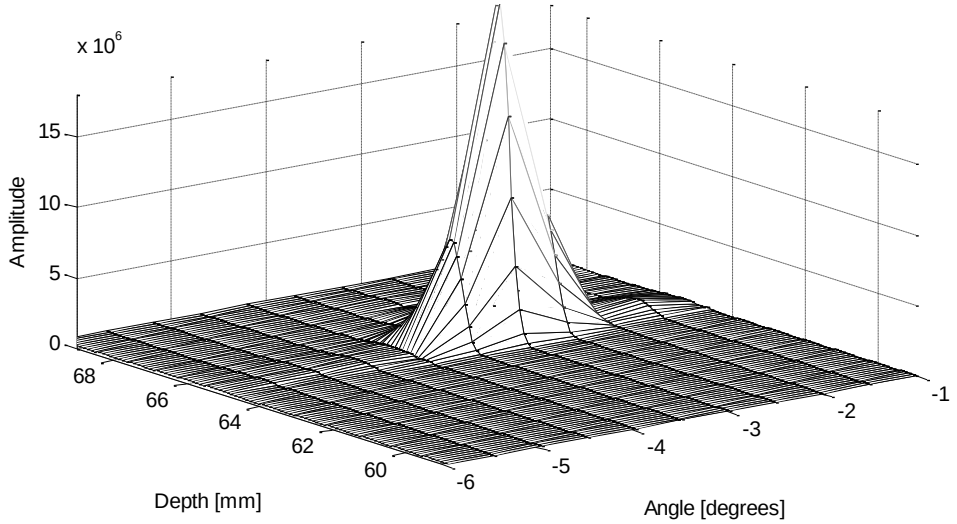

(b)

Figure 4-14 3D plot of the envelope, (a) all 6 wires, (b) zoomed at 3rd wire

It is important to take into account that the kernel sizes used to calculate the signal- and noise- power are chosen specifically for this wire-phantom-data.

4.8.2 **PSF**

The spatial resolution in the image refers to the ability to distinguish two separate but closely positioned structures accurately in space, which can be separated as axial and lateral resolution as given in Figure 4-15.

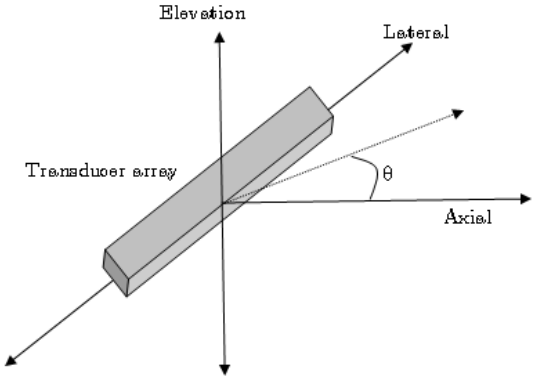

Figure 4-15 Coordinates for the scanning area

Axial resolution refers to the ability to resolve two adjacent objects situated one above the other, which are parallel to the propagation axis of the ultrasound beam. Axial resolution is dependent on the sound wave pulse length and inversely proportional to the frequency. Also the size of the object for which the pulse is propagated through affects the axial resolution. If the pulse length is longer than the distance between the objects, only a single reflection will be detected and the image will show only one structure. [Coa01], [Sho88].

Lateral resolution is the ability to resolve two structures, which are located separately side by side and perpendicularly to the axis of the sound wave beam. Lateral resolution is directly proportional to the beam frequency, whereas the higher the frequency and the narrower the beam width the greater is the lateral resolution [Coa01, [Sh088]. [Wel69],

Axial resolution only depends on the transducer. However, lateral resolution depends on the transducer as well as the beamforming quality. Therefore, the lateral resolution can be increased also when the ultrasound beam width is minimized by focusing the ultrasound pulses as they are generated by the transducer. This can be performed using phased arrays. Each array element behaves like a circular wavefront. Therefore, according to the superposition principle, ultrasound beams generated by rectangular transducer arrays have the form of a sinc function with one main lobe and multi-side lobes of decreasing

amplitudes [Sea02]. Therefore, the performance of different beamformer structures can be also tested in terms of lateral resolution in the time-domain by using PSF plots that include the beam pattern side lobe levels. Figure 4-15 shows the key terms for the coordination of a focused beam. The noise behaviour for different angles and ranges can be analysed in detail by using PSF plots.

4.8.3 Cyst Phantom

To quantify the contrast in the final image, the Contrast-to-Noise (CNR) values can be used, where the contrast is defined as the logarithmic difference between the mean values of the image kernels fully within and outside the cysts, as shown in Figure 4-16.

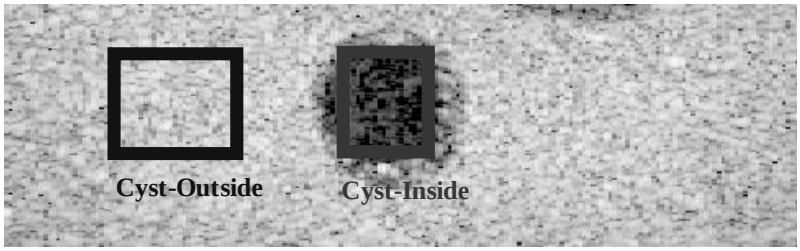

Figure 4-16 B-scan images of one cyst

The CNR is defined in [Fre99] and [Kar95] and is given by:

$$CNR = \frac{\left|\mu_{out} - \mu_{in}\right|}{\sigma_{out}} \tag{4.9}$$

where μ_{out} and μ_{in} denote the mean values outside and inside the cyst regions, and σ_{out} is the standard deviation outside the cysts. The mean value inside the cyst is calculated within a kernel including most of each anechoic region and the mean value outside the cyst is calculated including a kernel outside the cyst at the same ranges at each cyst [Fre99], [Kar95].

Similar to the SQNR calculations, the mean values for the cyst are calculated directly from the envelope signal.

4.9 10-bit A/D Beamformers

Since the phantom data sets were acquired by a 10-bit transducer, the incoming echo signals are digitized using 10-bit A/D converters, delayed and summed coherently to form the focus of interest (Figure 4-14). However, the sampling rate of traditional multi-bit A/D converters is not adequate for accurate delays to properly form a focus (1/32 of the wavelength) [Pet84].

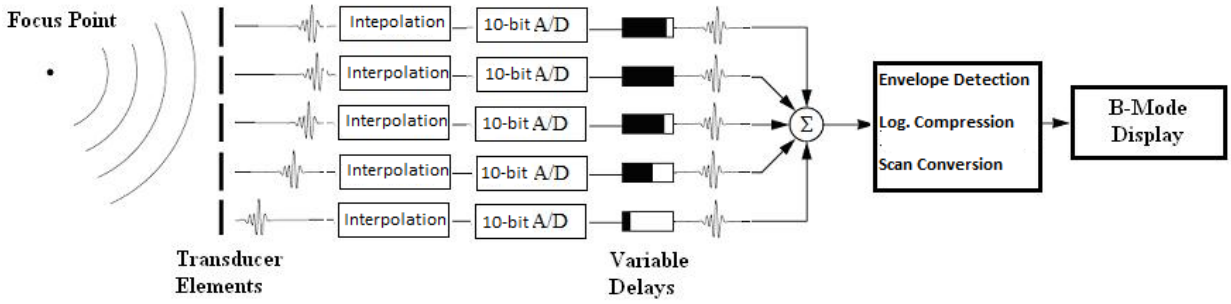

Figure 4-17 Block Diagram of the 10-bit A/D Beamformer System

In order to achieve effective time delay accuracy, the digitized echo signals are interpolated to 16 times the Nyquist-rate through padding 15-zeros between each sample. The spectrum of the upsampled signal is shown in Figure 4-18. The 16 times-reduced intersampling period provides delay accuracy for sufficient focusing.

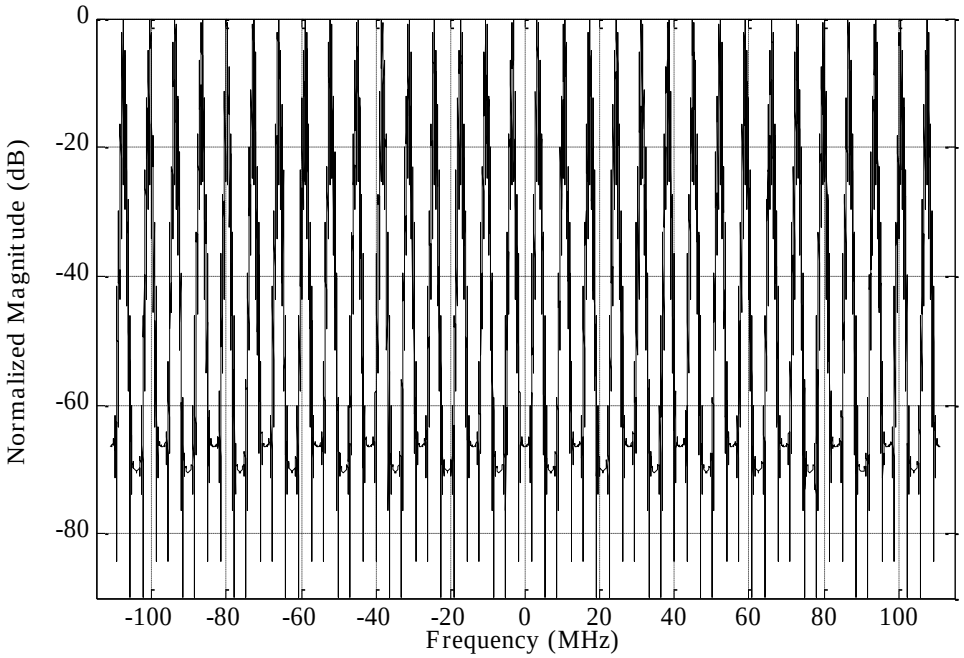

Figure 4-18 Upsampled Echo signal via zero padding

Upsampled signals are then interpolated using interpolation filters as seen in Figure 4-19. Beamforming parameters are designed to suppress the quantization grating lobe lower than 60dB. As a result, after the beam summation, an image with a dynamic range of 70 dB can be reconstructed.

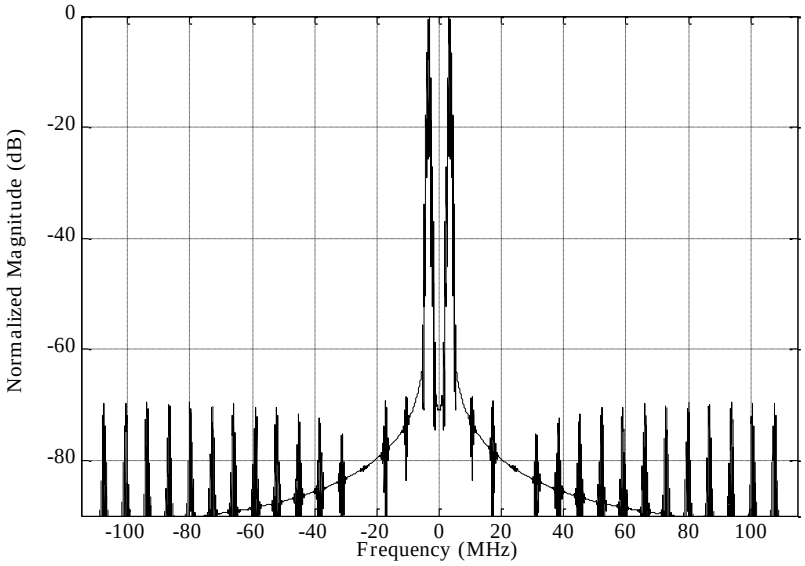

Figure 4-19 Frequency spectrum of the echo signal after interpolation filter

Since the beam summation is performed at the high sampling rate, the sampling rate is reduced to the Nyquist sampling rate. As expected, the envelope of the third wire looks like a sinc-function (after the mid-end and back-end processes described in Sections 4.6 and 4.7 The brightness of each pixel in the image is adjusted as a function of the amplitude of the reflected signals.

4.10 1-Bit Σ–Δ Beamformers

In order to preserve the hardware simplicity of the Σ–Δ beamformer, a conventional second-order Σ–Δ modulator at 222 MHz was used to digitize the incoming signals centered at 3.5 MHz. As a result, the Σ–Δ beamformer can select the delay without interpolation. The noise-shaping function of the oversampled Σ–Δ modulators attenuates the quantization noise in the signal band, thereby pushing most of the noise components to

out-of-band frequencies. This can be removed by using a digital low-pass filter. The suppressed noise in the signal band, which depends on the OSR, causes the in-band SNR value to increase by 2.5 equivalent bits for every doubling of the OSR value [Azi96]. Therefore, to obtain a 10-bit equivalent resolution using a single-bit second-order Σ–Δ modulator, the OSR is taken as 16. Due to the high sampling rate of Σ–Δ modulators, accurate delays can be achieved directly with the summation of phased shifted signals.

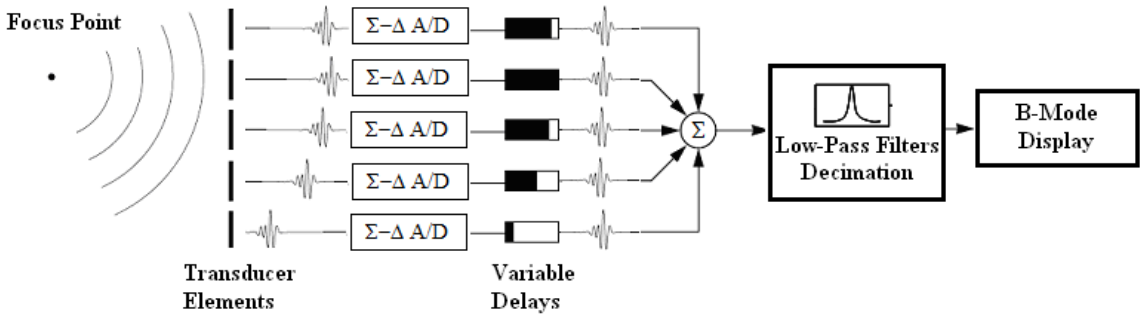

Figure 4-20 Block diagram of the Σ–Δ based beamformer system

As seen in Figure 4-20, once the echo signals are modulated, digital beamforming can be performed as the delay-and-sum process as detailed in Section 4.4.1 As given in Figure 4-21, since dynamic focusing is performed at the oversampling rate and the quantization noise is shaped to the higher frequencies, the beam sum output is then demodulated with a LP decimation filter and downsampled to the Nyquist sampling rate [Nou93]. After the high frequency quantization noise is filtered out, the envelope detection and scan conversion processes are performed.

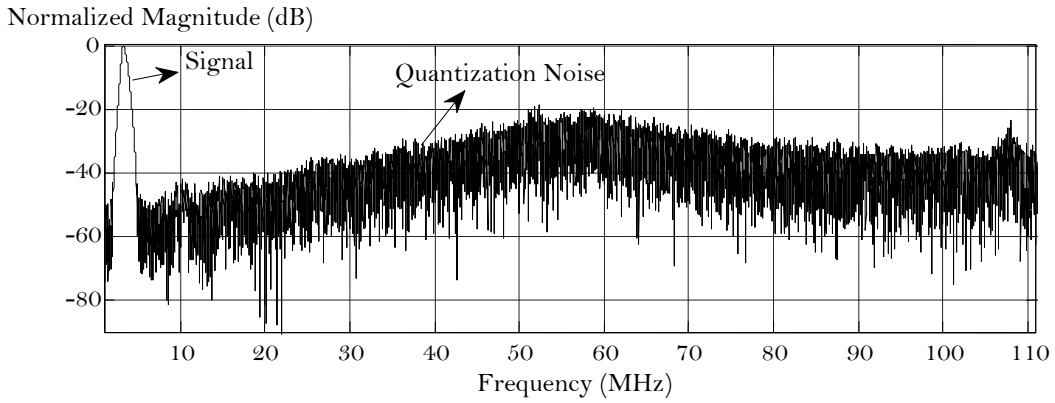

Figure 4-21 Frequency spectrum of the one beam line modulated with second-order Σ–Δ modulator

During each clock cycle of the dynamic focusing delay-and-sum process, a sample is selected from each channel according to the predetermined time delay to compensate for the echo time difference. However, as shown in Figure 4-22, the delay updates to focus the beam at closely spaced focus points cause some samples to be repeated and some of those to be skipped. These repeated/omitted samples during the dynamic focusing cause the demodulator filter to interpret an extra sample, which actually does not exist [Fre97], [Fre99], [Koz01].

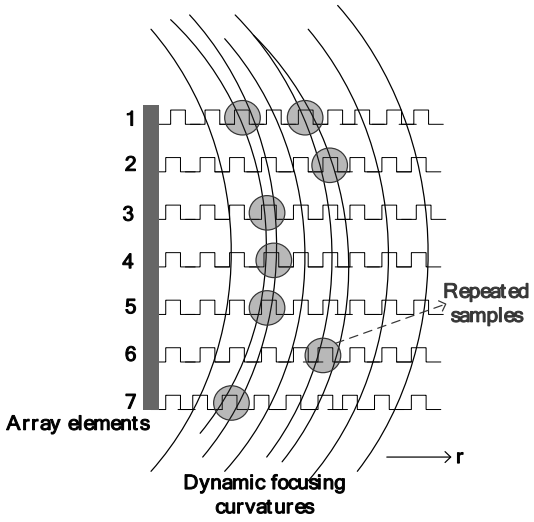

Figure 4-22 Illustration of sample repetition in dynamic focusing [Koz01]

Therefore, repeating/dropping samples degrade the synchronization between the modulator and demodulator so that the noise-shaping feature of Σ–Δ modulators is disrupted and some of the quantization noise folds back to the signal band. As a result, the background noise level is increased and severe image artefacts are exhibited in the image as a snowy background as shown Figure 4-24 and Figure 4-25.

4.11 Simulation Results

4.11.1 Wire Phantom

In order to investigate the performance of the beamformers quantitatively, the frequency spectrum of a single beam line lying at the centre of the main lobe of the third wire is plotted. As seen in Figure 4-23, due to the extra energy introduced into the output signal, the noise-shaping responses of the Σ–Δ modulators are degraded and some parts of the quantization noise are folded back to the signal band. The main lobe widths are

approximately the same. However, compared to the noise level in the 10-bit A/D beamformers, the in-band noise level in the conventional Σ–Δ beamformer is elevated by almost 12 dB. These elevated low-frequency noise components of the Σ–Δ beamformers will degrade the final image quality as the low-pass decimation filters just suppress the quantization noise components, which are shaped to the higher frequencies. The low-frequency noise level can be observed as snowy background in the final image (Fig 4-21)

The noise elevation may vary according to the data type. This noise level is not always 12 dB and is calculated specifically for the 6-wire data set.

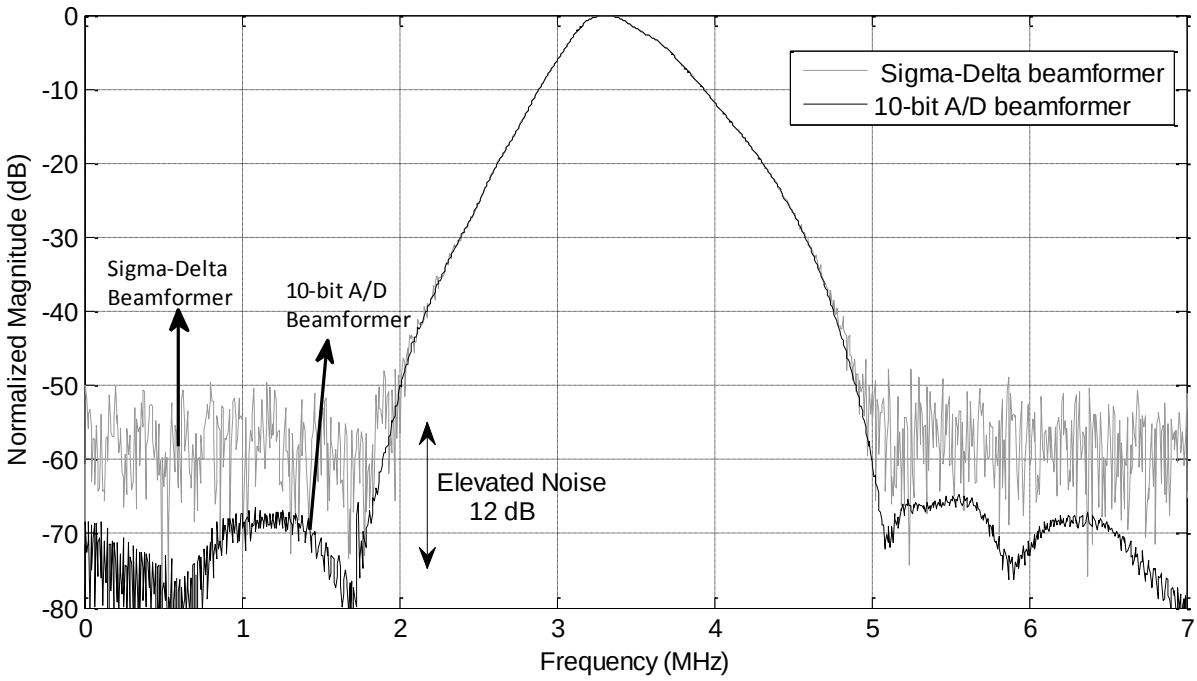

Figure 4-23 Frequency spectrum of a single beam-line, 10-bit A/D beamformer (black line) and 1-bit Σ–Δ beamformer (grey line).

The comparison of the B-scan sector images reconstructed by the 10-bit A/D beamformer and conventional Σ–Δ beamformer is given in Figure 4-24. The snowy background in the image reconstructed by the conventional Σ–Δ beamformer is significantly noticeable compared to the one obtained by the 10-bit A/D beamformer, due to the elevated noise floor at low frequencies shown in Figure 4-23. As seen in Figure 4-24 in the B-scan image of the Σ–Δ beamformer. The contrast resolution is dramatically reduced. This degradation can be quantified in terms of the SQNR values. The calculated SQNR of

the conventional one-bit Σ–Δ beamformer relative to the 10-bit A/D beamformer is – 11.53dB.

(a) (b)

Figure 4-24 Wire phantom B-scan images, (a) 10-bit A/D beamformer, (b) 1-bit Σ–Δ beamformer.

The brightest zone, i.e. the most contrast zone is the third wire, since the fixed transmit focus is performed. Therefore the frequency spectrum comparisons in this study are performed using the main lobe of the third wire.

4.11.2 Cyst Phantom

The cyst phantom data was used to test the performance of the Σ–Δ beamformer against the 10-bit A/D beamformer. In Figure 4-25, the B-scan sector image produced by the Σ–Δ beamformer is compared with the images obtained by the 10-bit A/D beamformer. As shown in Figure 4-25, the elevated background noise in the conventional Σ–Δ beamformer degrades the image contrast resulting in less visible cysts compared to the 10-bit A/D beamformer.

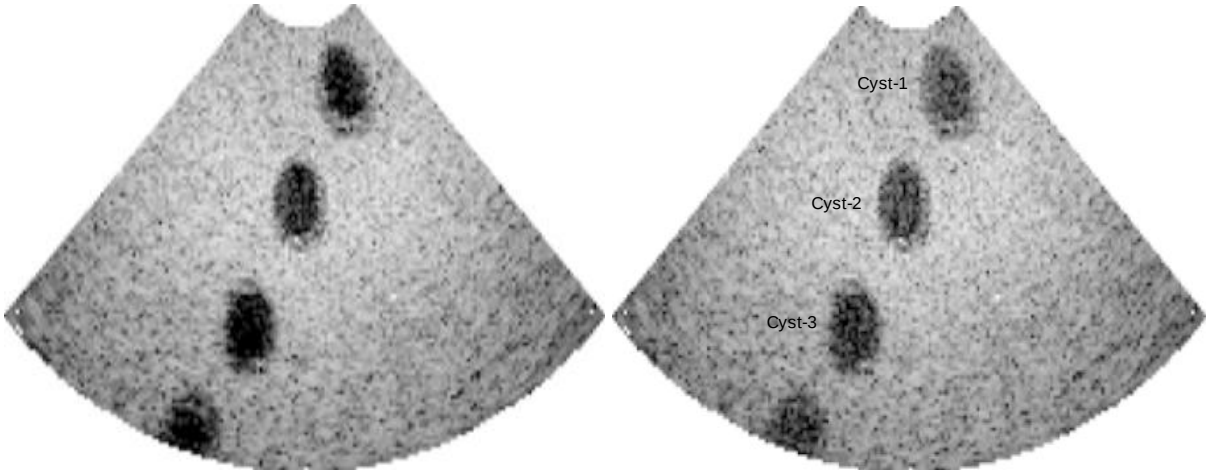

(a) (b)

Figure 4-25 Cyst phantom B-scan images, (a) 10-bit A/D beamformer, (b) 1-bit Σ–Δ beamformer.

	10-bit A/D Beamformer	1-bit Σ–Δ Beamformer	Difference
Cyst-1	5.49	3.90	1.59
Cyst-2	4.81	4.17	0.64
Cyst-3	4.11	3.09	1.02

Table 4-3 CNR values in anechoic region in phantom cyst images

The CNR results shown in Table 4-3 indicate that the Σ–Δ beamformers substantially decrease the contrast resolution resulting in reduced cyst detectability compared to the 10-bit A/D beamformers. The difference between the 10-bit A/D beamformer and 1-bit Σ–Δ beamformer varies as a function of the depth. Since the rate of delay changes decreases as a function of range, as depth decreases, the contrast resolution degrades. Therefore, near the top of the image, close to the transducer, the sample repetition rate is high, resulting in increased background noise. Thus, the difference between the CNR values obtained from the Σ–Δ beamformer and 10-bit A/D beamformer is the biggest for cyst-1.

4.12 Concluding Remarks

The major challenge in ultrasound imaging systems is to simplify the front-end hardware of the phased array system. Due to the simplified signal processing, the hardware complexity, size and power consumption of traditional phased array front-end components using 10-bit A/D beamformers at each array element can be substantially reduced by using single-bit Σ–Δ beamformers. When a Σ–Δ modulator is operated with a sampling frequency of 32 times the center frequency of the ultrasound signal, the number of bits involved in the signal processing is greatly reduced, and the need to interpolate between samples is eliminated. It then becomes feasible to achieve parallel beam formation via the duplication of hardware, which has been drastically simplified compared to the conventional case. The price of this simplicity is the need for a high speed Σ-Δ modulator. Although such high speed operation of the Σ-Δ modulator might appear to be wasteful of power, Σ-Δ modulators use significantly less power than Nyquist-rate A/Ds operating at the same speed, because they supply only a single bit of resolution at that speed. That single bit of resolution, however, is enough to provide the required delay accuracy, saving the conversion to high resolution until after the complex beamformer hardware, where it is needed at a much lower rate. Most importantly, the speed and size of the digital hardware is reduced because of the simplified signal processing and reduced number of bits being processed.

However, the repeated samples during dynamic focusing degrade the synchronization between the modulator and demodulator, which leads to an elevated noise floor in the reconstructed signal. It was concluded through software simulations using the wire-data sets that the conventional 1-bit Σ–Δ beamformers cause the noise components to be elevated at low-frequencies by almost 12 dB compared to the one obtained by 10-bit A/D beamformers. In addition, the simulation results using the cyst phantom data showed that the CNR values of the images produced by the Σ–Δ beamformers were significantly decreased as given in Table 4-3. The reduced resolution and contrast in the B-scan images reconstructed by Σ–Δ beamformers were the direct result of dynamic focusing. Therefore, in the next chapter, novel resolution and contrast improvement techniques to reduce the image artefacts caused by 1-bit Σ–Δ beamformers will be presented

Chapter 5

Improved Digital Ultrasound Σ–Δ Beamformers

Besides the reduced size, cost and the simplified signal processing as well as the discussion in Section 4.2 Σ–Δ beamformers were shown to exhibit significant image artefacts because of the disrupted synchronization between the modulator and the demodulator due to the repeated/omitted samples in dynamic focusing. Therefore, in this chapter post-processing techniques are introduced to reduce the resulting image artefacts. First of all, the analysis of image artefacts and a detailed literature survey on resolution improving techniques are given in 5.1 In Section 5.2 band-pass reconstruction filters including IIR- (Butterworth, Chebyshev Type-II- and elliptic-filters) are applied to reduce the quantization noise at low frequencies [Alt11b]. Polyphase filters are introduced to simplify the IIR BP filter structure by involving the design issues of LP-to-BP transformed all-pass cascaded structures. For further improvements in resolution, adaptive RO filters are introduced in Section 5.3 In Section 5.4 a novel combination of the RO filters with IIR, slink- and polyphase low-pass filters are detailed [Alt11c]. Finally, adaptive band-pass reconstruction filters including BP IIR filters and hardware efficient BP polyphase filters are presented in Section 5.5 In Section 5.6 the performances of the proposed reconstruction structures are verified through simulations using the same phantom data sets as detailed in Section 4.5 The resulting B-scan images are compared with the images reconstructed by conventional

10-bit A/D beamformers. The noise analyses in the frequency- as well as in the time-domains will show the effectiveness of the proposed reconstruction method in improving the noise performance.

5.1 Artefacts due to the Ultrasound Σ–Δ Beamformers

Besides the simplified signal processing and the hardware complexity of the phased array front-end components; the use of single-bit Σ–Δ beamformers introduces significant artefacts in the final image. The repeated/omitted samples in the dynamic focusing degrade the synchronization between the modulator and demodulator. This disrupts the Σ–Δ modulation sequence and causes distortion when recovering the signal. As a result, significant artefacts are introduced in the final image as elevated background noise level. In order to minimize the image artefacts, different correction techniques have been reported in the open literature as summarized in Table 5-1.

Summary of publications on artefact-reduction techniques of Σ–Δ beamformers	Limitations	Ref
Insert Zero Technique: For each repeated sample, a null sample is inserted into the sample sequence	Increased signal processing complexity due to the bit growth during the beam summation	[Fre97] [Fre98] [Fre99]
Divide-by-two technique: The repeated sample is halved to compensate for repeated samples		
Modified Σ–Δ modulator: The repeated samples are manipulated by an analogue feedback gain within the Σ–Δ modulator	Increased hardware complexity	[Fre99] [Odo90]
Non-uniform oversampling beamformers: employing different clocks at each array channel to provide exact synchronization	Large memory requirements	[Bil10] [Kar00] [Koz01] [Lie06] [Tov04]

Insert a pair of samples +1 and -1 when delay is required	Increased signal processing complexity	[Rig02]
Multiplier-less pre-delay reconstruction by applying the dynamic focusing delays to the partially reconstructed Σ–Δ modulator output signals	Increased hardware complexity due to multiple multi-bit accumulators and a filter coefficient look-up- table in each channel	[Han02] [Han04] [Han06]
Non-lienear beamformer model is developed using pre-modulation sequence (1,1,-1,-1) for a constant input	Increased signal processing complexity	[Ine02]
The FIR sub-filtering using the sparse sample processing concept: only the necessary amount of samples for display is reconstructed.	Long FIR filter requirements-large area for high-speed adders	[Tom05]
Sparse sample processing with Sinc reconstruction filters	Limited to Sinc reconstruction	[Han02]
Using Mathematical sample processing model for any type of reconstruction filters	Computationally complex	[Nil06] [Nil08]
Sparse sample processing with IIR reconstruction filters		[Che09a]
Cascaded reconstruction using box-car filters to reduce the pre-delay quantization noise level	Increased hardware complexity due to the required multi-bit shift registers or FIFO memory for the temporary storage of the intermediate multi-bit data, increased signal processing complexity	[Che08a]
Prior to the beam summation, a partial reconstruction is used, i.e. a sampling rate less than the oversampling rate, but greater than the Nyquist rate is employed		[Jeo07] [Liu09]
Σ–Δ beamformers with multi-bit outputs	Increased word length	[Che08b]
Improved spatial resolution of Σ–Δ phased arrays	Increased number or array elements	[Kri13]
Input-feedforward multi-bit adder-less Σ–Δ modulators	Increased word length Lack of dynamic beamforming application	[Jun13]
Utilizing sequential synthetic aperture beamforming, where the first beamforming stage is a fixed-focus beamformer.	Integrated apodization needed. Increased signal processing complexity	[Tom13]

Increased resolution via continious-time Σ–Δ beamformer	Increased signal processing as 3rd order modulator is employed	[Zha15]
Applying apodization to the recived signals in the ultrasound probe	Increased DSP complexity due to the variable control apodization control	[Hem15]

Table 5-1 Summary of artefact correction techniques for Σ–Δ beamformers

As shown in Table 5-1, a number of studies have worked on incorporating dynamic receive focusing in Σ–Δ beamformers. Despite the reduced artefacts and high image resolution, the improvements are achieved at the expense of either increased hardware or signal processing complexity. The main problem is to reduce the image artefacts by preserving the hardware and signal processing simplicity of conventional Σ–Δ beamformers. Due to the dynamic focusing, the quantization noise is folded back at low frequencies. Therefore, conventional low-pass decimators are deemed to be insufficient to achieve an output that is equivalent to 10-bits of resolution. Therefore, compared to the existing beamformers reported in the open literature (Table 5-1), which employ conventional low-pass reconstruction filters; the image artefacts are effectively reduced in the decimation stage by employing different types of reconstruction filters. It has been shown that, adaptive rank-ordered (RO) filters following the decimation filters ensure effective in-band noise level reduction resulting in a significantly improved SQNR in the final image. Therefore, different from the existing approaches, the proposed methods do not need any modification in the conventional single-bit dynamic focusing stages or the align-and-sum processes. Significant improvements in the resolution are achieved after the dynamic focusing stage without compromising the hardware simplicity of conventional Σ–Δ beamformers.

As seen in Figure 5-1, reconstruction structures are proposed to reduce the demodulation artefacts without losing the advantages of Σ–Δ modulators [Alt11b], [Alt11c]. Since the noise level occurred at low-frequencies, the performance of different band-pass reconstruction filters is tested. Chebyshev-II-, Butterworth- and elliptic decimation filters are used. Furthermore, the structure of BP decimation filters is simplified by utilising polyphase BP decimation filters. Secondly, novel adaptive rank-ordered filter algorithms are introduced following the conventional slink and polyphase low-pass decimation filters. Since the rank-ordered filter algorithms are adaptive to the noise components, it is proposed to use the rank-ordered filters following the decimators to reduce the demodulation error at

low-frequencies. Finally, it is proposed to employ the rank-ordered filters after the BP IIR- and polyphase decimation filters.

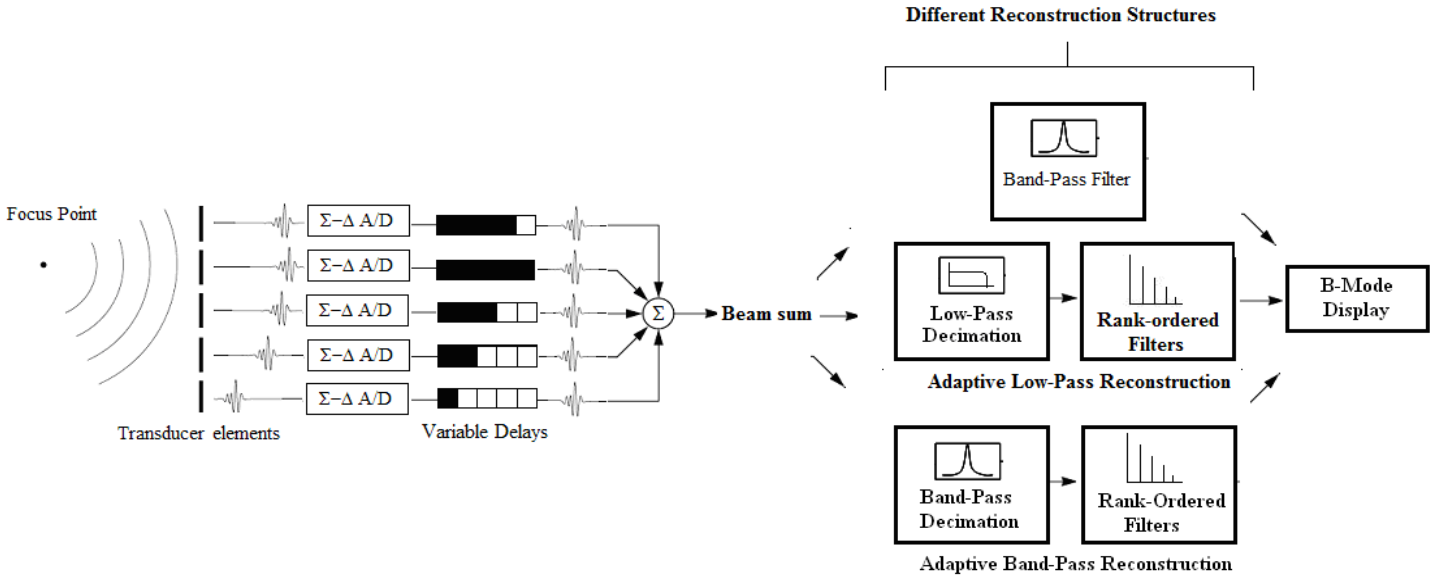

Figure 5-1 Proposed reconstruction structures for Σ–Δ modulator based beamformers.

5.2 Band-Pass Reconstruction Filters

After the delay-and-sum process, different types of band-pass decimators are used in the proposed structure to suppress the quantization noise elevated at the low-frequencies. Since the decimation filters operate at high sampling rates, the sampling rate is then decreased by 16.

5.2.1 IIR Band-Pass Reconstruction Filters

IIR BP decimation filters with a bandwidth close to the signal bandwidth (~3 MHz) are applied to reconstruct the multi-bit data for the back-end processing, as shown in Figure 5-1. As seen in Figure 4-21, in order to suppress the shaped noise at high frequencies the minimum stop-band attenuation should be 50 dB. Therefore, three different computationally inexpensive filters are used to demodulate the output signals: Elliptic, Chebyshev-Type-II and Butterworth filters, whose magnitude responses are given in Figure 5-2. The first decimation filter is an eighth-order elliptic filter with a normalized transition band of 0.019, a pass-band ripple of 0.01 dB, and stop-band attenuation of 50 dB. The second filter is an eighth-order Chebyshev Type-II filter with a normalized transition band of 0.064, and a

stop-band attenuation of 50 dB. The third filter is a tenth-order Butterworth filter with a normalized transition band of 0.025.

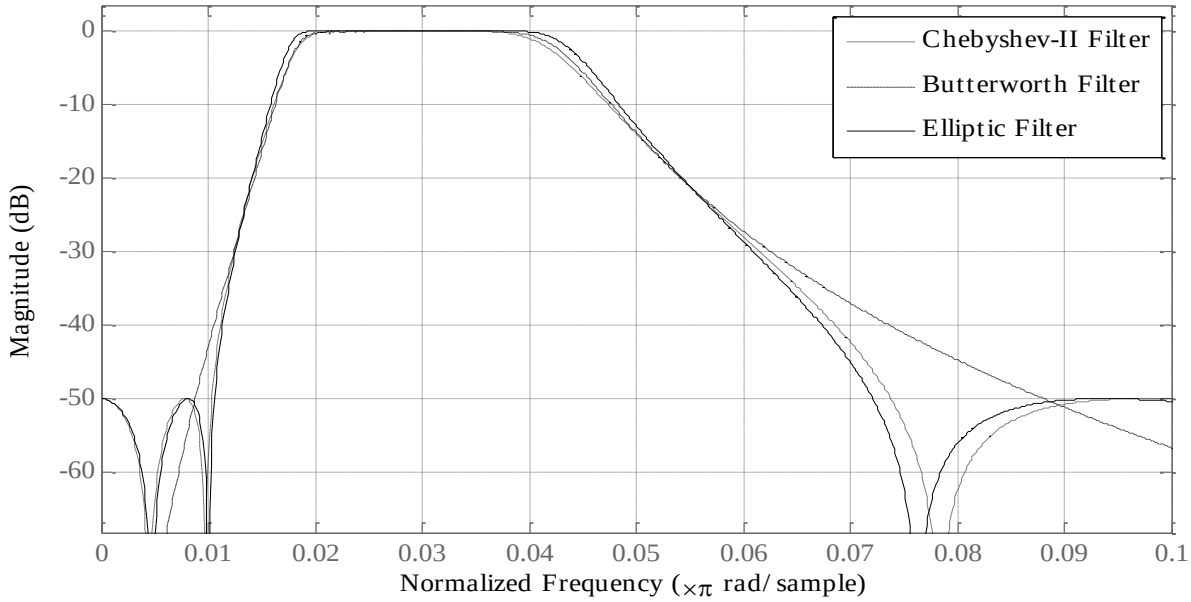

Figure 5-2 Magnitude responses of the band-pass filters used in the decimation stage.

The corresponding band-pass decimation filters may be implemented using conventional structures, but can be further simplified by using band-pass polyphase filters.

5.2.2 Polyphase Band-Pass Reconstruction Filters

In order to simplify the hardware complexity of the IIR band-pass reconstruction filters, computationally efficient all-pass sub-filters operating in the polyphase structure are used. The Polyphase filters can simplify the Σ–Δ beamformer structure greatly so that slower and fewer multipliers and adders are needed. The sub-filters exhibit unity magnitude responses, but have differently designed phase responses [Kal94], [Kal96], [Val83]. The cut-off frequency of the overall polyphase filter is adjusted by shifting the phase of each sub-filter between consecutive branches, which add constructively in the pass-band and destructively in the stop-band. A second-order one-coefficient all-pass filter $A(z^{-2})$ that is used in polyphase structures can be designed as given in Figure 5-3 [Kal94].

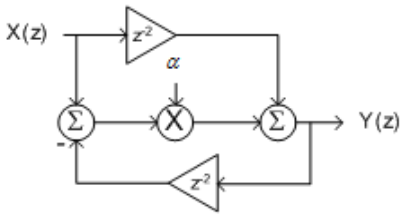

Figure 5-3 One coefficient all-pass filter structure

The corresponding transfer function of the one-coefficient (α) all-pass filter is:

$$A(z) = \frac{\alpha + z^{-2}}{1 + \alpha z^{-2}} \tag{5.1}$$

As seen in Figure 5-3, the one coefficient all-pass structure needs one multiplier, two adders and a small memory. Therefore, the all-pass subsections greatly reduce the hardware complexity of the overall decimation filter structure. A two-path polyphase filter is formed as a sum of two parallel all-pass sub-sections with the appropriate delay in the lower branch as shown in Figure 5-4.

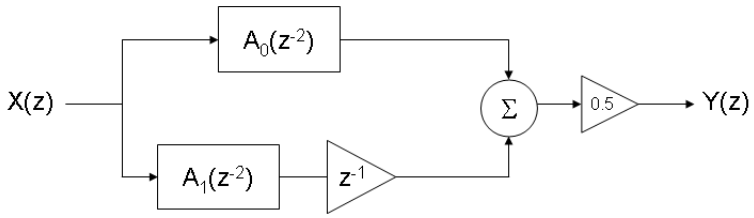

Figure 5-4 Half-band low-pass polyphase filter structure

The resulting transfer function of the two-path half-band low-pass polyphase filter given in Figure 5-4 is [Con70]:

$$H_{HB}(z) = \frac{1}{2}\left(A_0(z^{-2}) + z^{-1}A_1(z^{-2})\right) \tag{5.2}$$

where $A_0(z^{-2})$ and $A_1(z^{-2})$ are composed of cascaded one-coefficient second-order all-pass sub-filters [Kru99], [Kru03]:

$$A_{in}(z^{-2}) = \prod_{u=1}^{U_{in}} A_{in,u}(z^{-2}) = \prod_{u=1}^{U_{in}} \frac{\alpha_{in,u} + z^{-2}}{1 + \alpha_{in,u} z^{-2}} \tag{5.3}$$

Each all-pass sub-filter $A_{in,u}(z^{-2})$ has 2 poles at $z=(-\alpha_{in,u})^{1/2}$ and 2 zeros at $z=(-a_{in,u})^{-1/2}$. Thus, the overall transfer function of the half-band low-pass filter presented in Figure 5-4 becomes:

$$H_{HP}(z)=\frac{1}{2}\left(\prod_{u=1}^{U_0}\frac{\alpha_{0,u}+z^{-2}}{1+\alpha_{0,u}z^{-2}}+z^{-1}\prod_{u=1}^{U_1}\frac{\alpha_{1,u}+z^{-2}}{1+\alpha_{1,u}z^{-2}}\right) \quad (5.4)$$

The order of the filter is $in=2(U_0+U_1)+1$, where U_0 and U_1 are the number of cascaded all-pass sub-filters in the upper and lower branches respectively. By proper choice of the sub-filter coefficients *(α's)*, the phase shift of each branch of the two-path polyphase structure can be designed to match or to differ by multiples of π at certain regions [Kru99]. The transfer function of a two-coefficient half-band low-pass polyphase filter becomes:

$$H_{HP}(z)=\frac{1}{2}\left(\frac{\alpha_0+z^{-2}}{1+\alpha_0 z^{-2}}+z^{-1}\frac{\alpha_1+z^{-2}}{1+\alpha_1 z^{-2}}\right) \quad (5.5)$$

Design techniques of two-path half-band polyphase filters with a single coefficient per second-order stage are detailed in the studies [Val83], [Har91]. According to the straightforward algorithm reported in [Val83], the filter coefficients α_0 and α_1 can be computed according to the parameters: stop-band attenuation d_s and transition band ω_t. For the required ω_t, the following parameters should be computed first [Val83].

$$p=\tan^2\left(\frac{\pi}{2}(0.5-\omega_t)\right) \quad (5.6)$$

$$e_p=\frac{1}{2}\frac{1-\sqrt[4]{1-p^2}}{1+\sqrt[4]{1-p^2}} \quad (5.7)$$

$$q_p=e_p+2e_p^{\,5}+15e_p^{\,9}+150e_p^{\,13} \quad (5.8)$$

The filter order *in* is related to the number of filter coefficients U by: $i = 2U + 1$. Using the parameters computed in (4.15), (4.16) and (4.17), the required number of filter coefficients is determined for the specified stop-band attenuation [Val83].

$$U = 2\log_{q_p}\left(\frac{1}{4}\frac{d_s^2}{1-d_s^2}\right) - 1 \tag{5.9}$$

Using the parameters q_p and *in*, the analogue frequencies ω_i and the analogue filter coefficients α_i are computed as:

$$\omega_i = \frac{2q^{1/4}\sum_{o=0}^{\infty}(-1)q^{o(o+1)}\sin[(2o+1)\pi i/in]}{1+2\sum_{o=1}^{\infty}(-1)^o q^{o^2}\cos[2o\pi i/in]} \tag{5.10}$$

$$\alpha_i = \frac{\left[(1-\omega_i^2 p)(1-\omega_i^2/p)\right]^{1/2}}{1+\omega_i^2} \tag{5.11}$$

The digital filter coefficients are computed using:

$$\alpha_{in} = \frac{1-\alpha_i}{1+\alpha_i} \tag{5.12}$$

The odd-indexed coefficients are used in the all-pass filters in the upper branch and the even-indexed coefficients are used in the all-pass filters in the lower branch. Using the coefficients computed by (4.21), a half-band low-pass polyphase prototype filter can be designed. For a stop-band attenuation of 50 dB and a normalized transition band of 0.25, the filter coefficients are calculated as:

$$\alpha_0 = 0.138024994073021,\ \alpha_1 = 0.584683257487319.$$

The filter structure is shown in Figure 3-24.

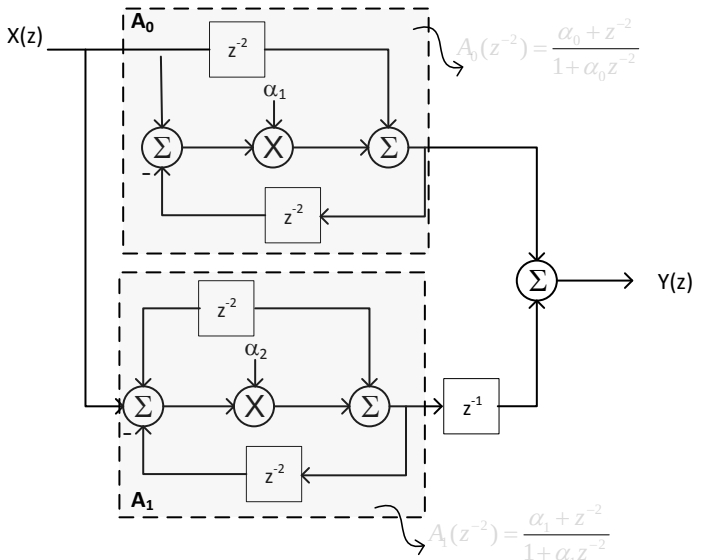

Figure 5-5 Two-coefficient half-band low-pass polyphase prototype filter

As seen in Figure 5-6a, the phase responses of $A_0(z^{-2})$ and $A_1(z^{-2})z^{-1}$ overlap (in-phase) at low frequencies and are displaced by π (out-of-phase) for high frequencies [Kru99]. Therefore, the phase difference of the upper- and lower-branches becomes π/2 at the half-band frequency. As a result, the half-band prototype filter having the magnitude response given in Figure 5-6b is obtained.

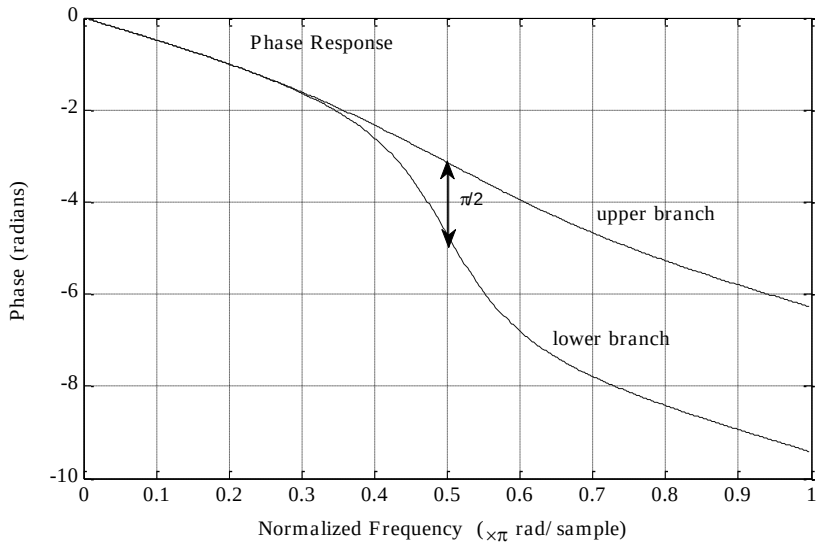

(a)

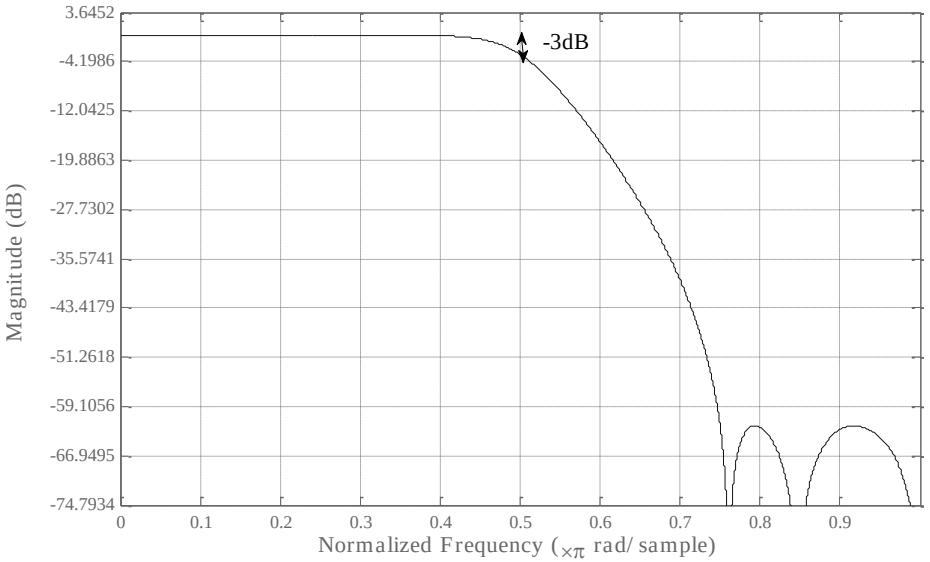

(b)

Figure 5-6 Half-band LP polyphase prototype filter, (a) phase responses of upper- and lower branch, (b) magnitude response

As seen in Figure 5-5, the two-path polyphase structure has a five-to-one savings in multiplications in comparison to the equivalent elliptic filter. As a result, a fifth-order half bandwidth two-path polyphase filter requires only two coefficients as opposed to the direct implementation which requires ten [Har91], [Kru99].

In order to design a hardware efficient band-pass filter, the prototype low-pass polyphase filter given in Figure 5-5 is transformed to a band-pass filter using the LP-to-BP frequency transformation [Con70], [Kru99], [Kru03]. Therefore, an all-pass mapping filter is computed which changes the prototype low-pass filter with a cutoff frequency at $\omega_0 = 0.5$ to the band-pass filter with cut-off frequencies at $\omega_1 = 0.017$ and $\omega_2 = 0.045$. Using the mapping filter, the low-pass prototype filter coefficients are mapped to the desired band-pass filter coefficients. The resulting tenth-order band-pass filter can be designed as transformed cascaded all-pass sections with the transfer functions given in (4.22) and (4.23).

$$A(z^{-4}) = \frac{\alpha_0 + \alpha_1 z^{-1} + \alpha_2 z^{-2} + \alpha_3 z^{-3} + z^{-4}}{1 + \alpha_3 z^{-1} + \alpha_2 z^{-2} + \alpha_1 z^{-3} + \alpha_0 z^{-4}} \tag{5.13}$$

$$A(z^{-2}) = \frac{\alpha_0 + \alpha_1 z^{-1} + z^{-2}}{1 + \alpha_1 z^{-1} + \alpha_0 z^{-2}} \tag{5.14}$$

The transformed filter structure is composed of cascaded all-pass filters as shown in Figure 5-7 and Figure 5-8.

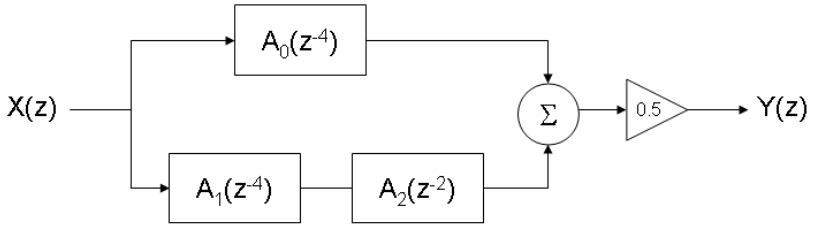

Figure 5-7 LP-to-BP transformed polyphase filter structure

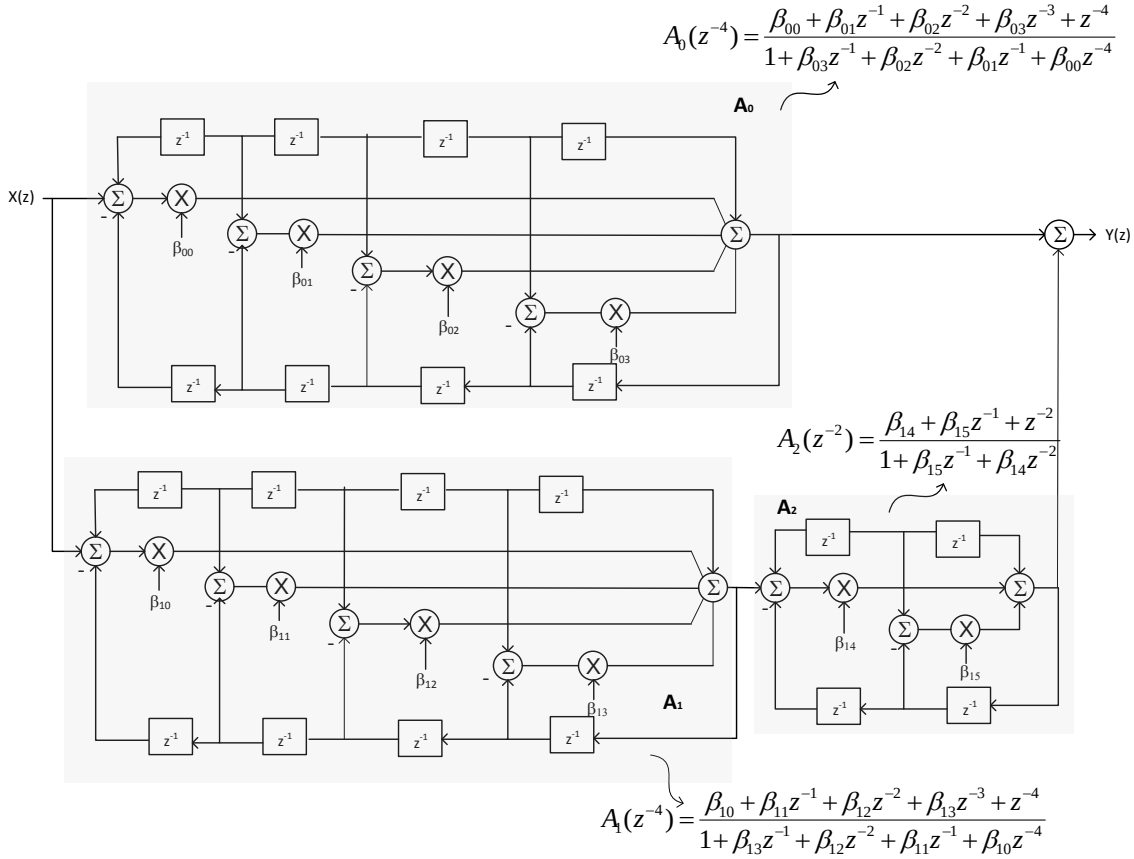

Figure 5-8 All-pass filter implementation for tenth-order LP-to-BP transformed polyphase filter

The corresponding filter coefficients β's are given in Table 5-2.

$A_0(z^{-4})$	$A_1(z^{-4})$	$A_2(z^{-2})$
β_{00} = 0.876096221155215	β_{10} = 0.955317161716164	β_{14} = -0.916295855648072
β_{01} = -3.607536678270576	β_{11} = -3.844005881224662	β_{15} = 1.909095296171167
β_{02} = 5.585906422853115	β_{12} = 5.821779591677784	
β_{03} = -3.854413089001439	β_{13} = -3.933035762634492	

Table 5-2 Coefficients of allpass sections

The resulting magnitude response of the tenth-order IIR band-pass filter with the filter coefficients given in Table 5-2 of cascaded all-pass sections with a normalized bandwidth of 0.0280 is given in Figure 5-9.

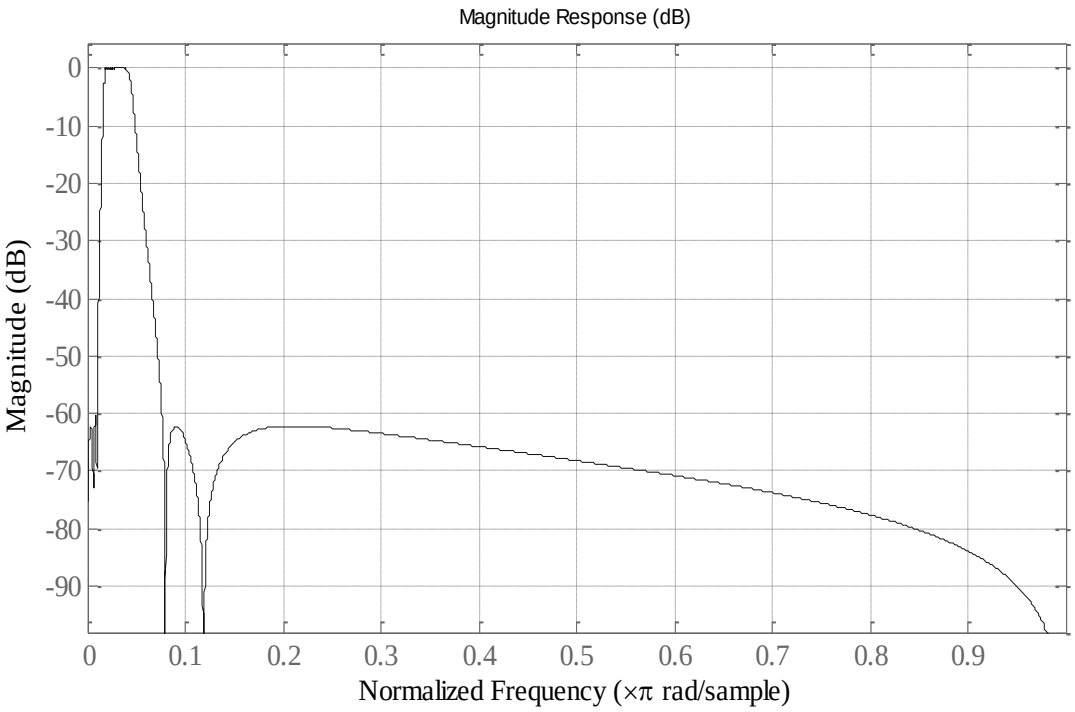

Figure 5-9 Magnitude response of the band-pass filter used in the decimation stage

As seen in Figure 5-9, the magnitude response of the resulting BP polyphase filter has a normalized bandwidth of 0.028. This very narrow pass-band with an stop-band attenuation of 70dB is designed to assure sufficiently suppression of the out-of band noises of the ultrasound signal with an operating frequency of 3.5MHz at a sampling rate of 222MHz.

Implementation of IIR filters as cascaded all-pass filters have important advantages over conventional IIR filter implementations. As seen in Figure 5-8, the use of all-pass filter sections will halve the number of coefficients, thus greatly reducing the hardware complexity of the reconstruction filter compared to the standard implementation of the IIR filters. Due to the two-to-one savings in multiplications; a tenth order two-path band-pass polyphase filter requires only ten coefficients as opposed to the direct implementation which requires ten coefficients for the numerator and 9 coefficients for the denominator. The second is that all-pass structures exhibit unity gain to all internal states hence do not require extended precision registers to store intermediate results as do cascade second-order IIR implementations [Har91].

5.2.3 Simulation Results

The performance of the proposed IIR- and polyphase-BP reconstruction filters can be evaluated quantitatively by comparing the frequency spectrums of a single beam line lying at the centre of the main lobe of the third wire as discussed in Section 4.8

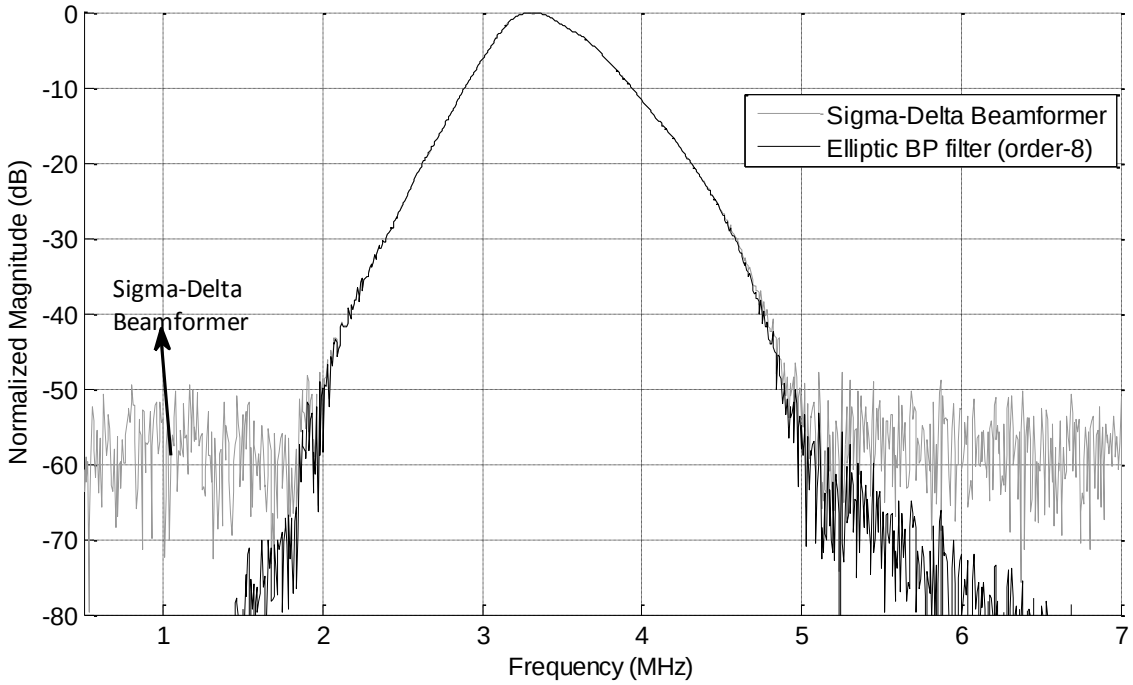

(a)

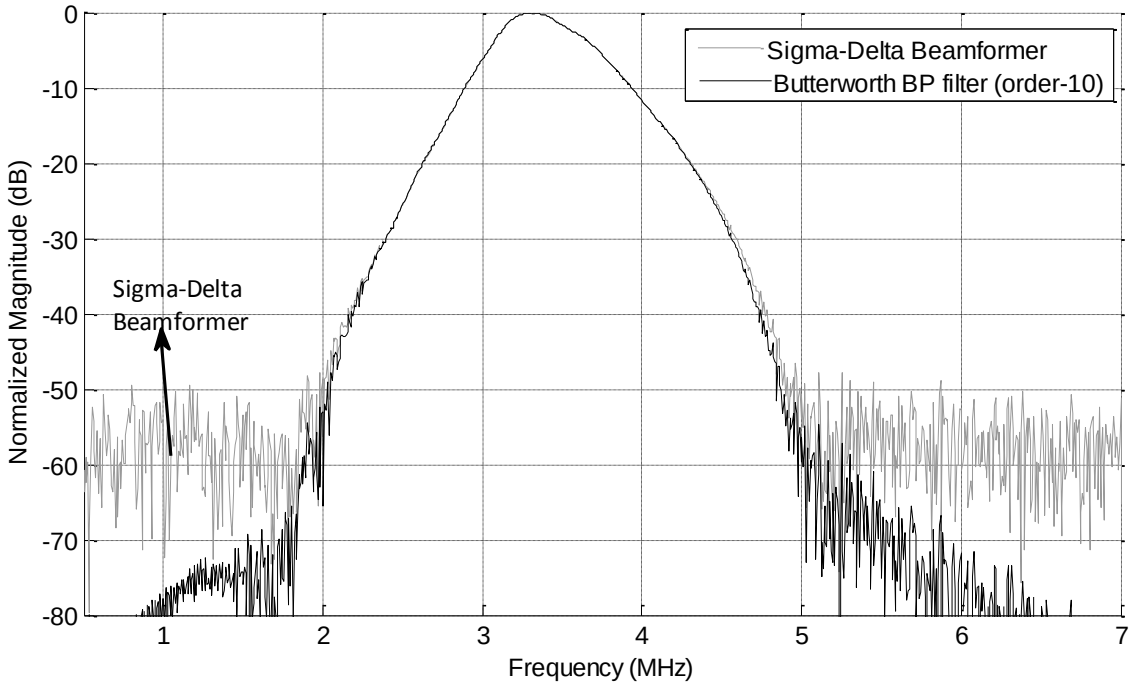

(b)

Figure 5-10 Frequency spectrum of a single beam-line of the third wire produced Σ–Δ beamformer (grey line) with, (a) elliptic-(b) Butterworth-, BP reconstruction filters (black line)

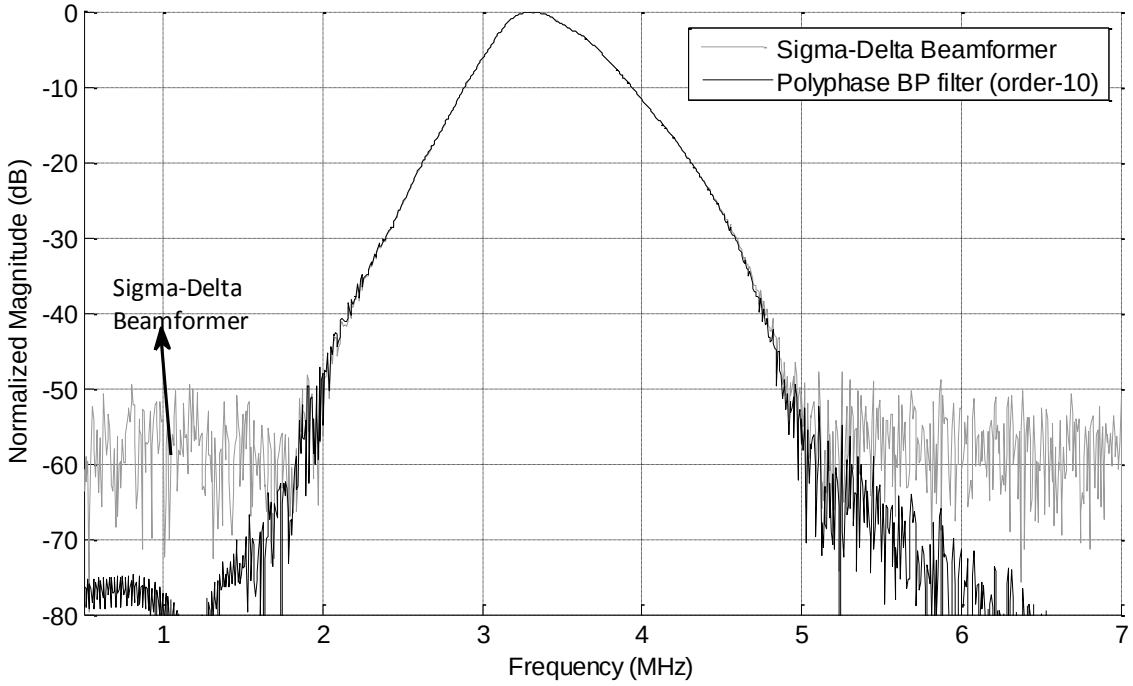

Figure 5-11 Frequency spectrum of a single beam-line of the third wire produced by Σ–Δ beamformer (grey line) reconstructed by polyphase BP reconstruction filters (black line)

As seen in Figure 5-10 and Figure 5-11, using band-pass IIR and band-pass polyphase reconstruction filters reduce the increased noise floor at the low frequencies level in the conventional Σ–Δ beamformer to more than -70 dB. The BP reconsruction filters significantly suppress the in-band as well as out-of-band noise components as obtained by 10-bit A/D beamformers as given in Figure 4-23.

5.3 Adaptive Reconstruction Filters

Due to the $1/r$ dependency (4.3), the sample delays are changing rapidly in order to focus the beams to a short-range distance. Therefore, as the focusing depth decreases, more quantization noise is introduced at the lower frequencies. As seen in Figure 5-12, for conventional Σ–Δ beamformers; the noise floor around the 1st wire (35mm) is almost 10 dB higher than that of the 2nd wire (49mm) and 20 dB higher than that of the 3rd wire (65mm). As a result, more image artefacts are observed in the final image close to the transducer (Figure 5-27).

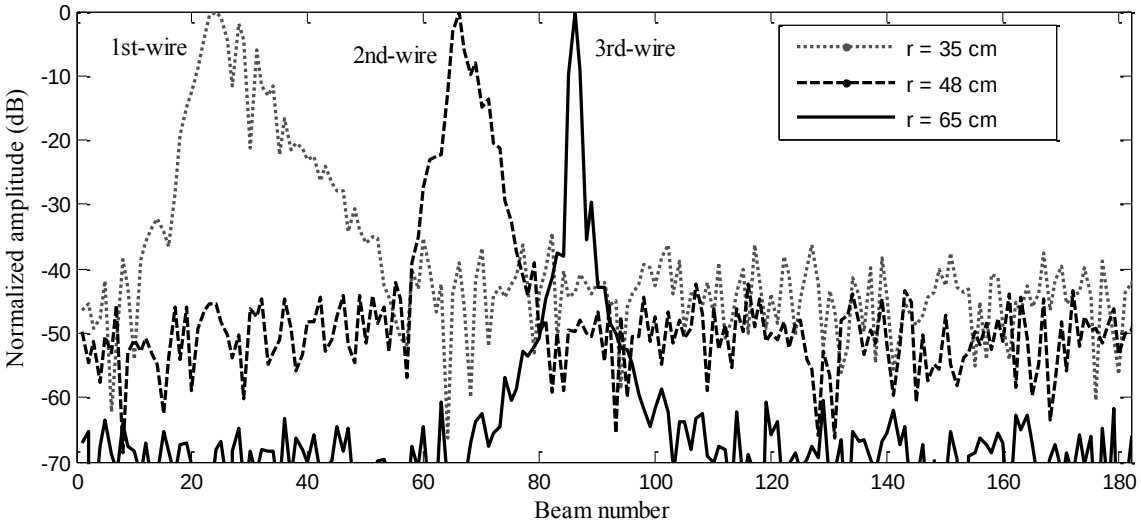

Figure 5-12 Lateral PSF of conventional Σ–Δ beamformers at different depths

Since the SQNR of the final image is directly related to the sample repetition rate, which is dynamically changing along the imaging depth, an adaptive rank-order filter is required following the decimation filters in order to suppress the in-band noise level significantly. Thus, after the delay-and-sum process, the novel combinations of decimation filters with adaptive rank-ordered filters are applied to reconstruct the multi-bit data for the back-end processing.

Since the proposed rank-ordered filter is employed after the decimation filter, the filter algorithm is performed at the reduced sampling rate (Nyquist sampling rate), thereby reducing the processor and processing demands put on the overall processing budget. Hence, the memory and processing requirement for sorting the data will be greatly reduced.

5.3.1 **Rank-Ordered Filters**

In the rank-ordered filter algorithm, a digital signal is represented as successive sets of data, *s*. For each data set, a change of gradient is used to determine the threshold value to differentiate between the signal and noise components. Samples in each data set are considered as a composite signal containing both the signal and the noise, where the elements having the lower gradient than the threshold values are considered as noise. As shown in Figure 5-13, the original signal therefore can be processed to suppress these elements which have been identified as noise [Che09b], [Sum92]. The algorithm process can be summarized as given in the block diagram in Figure 5-14.

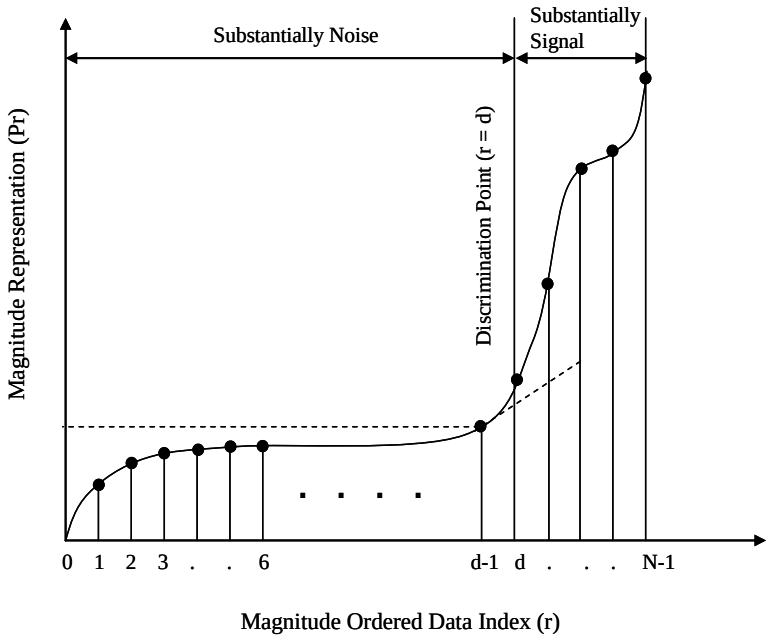

Figure 5-13 Rank ordered algorithm [Sum92]

In order to determine the optimum size of *s*, the maximum repetition rate in the whole scanning area can be used. As given in (4.2), the maximum sample repetition rate can be obtained using the time difference between two consecutive times of arrivals, $\tau'_{\eta 1}$ and $\tau'_{\eta 2}$. Since at each sampling period the beam line is focused to a new focus point, $\Delta r / 2c = T$. Therefore, (4.2) becomes [Che08a]:

$$\tau'_{\eta 1} = -\frac{x_\eta \sin\theta_0}{c} + \frac{x_\eta^2 \cos^2\theta_0}{2cr_0} \tag{5.15}$$

$$\tau'_{\eta 2} = \frac{\Delta r}{c} - \frac{x_\eta \sin\theta_0}{c} + \frac{x_\eta^2 \cos^2\theta_0}{2c(r_0 + \Delta r)} \tag{5.16}$$

$$\Delta\tau'_\eta = \frac{\Delta r}{c}\left(2 - \frac{x_\eta^2 \cos^2\theta_0}{2r_0(r_0 + \Delta r)}\right) \tag{5.17}$$

$$\Delta\tau'_\eta = T\left(1 - \frac{x_{\eta\max}^2}{4r_0^2}\right) = T(1 - \frac{1}{16 f_{num}^2}) \tag{5.18}$$

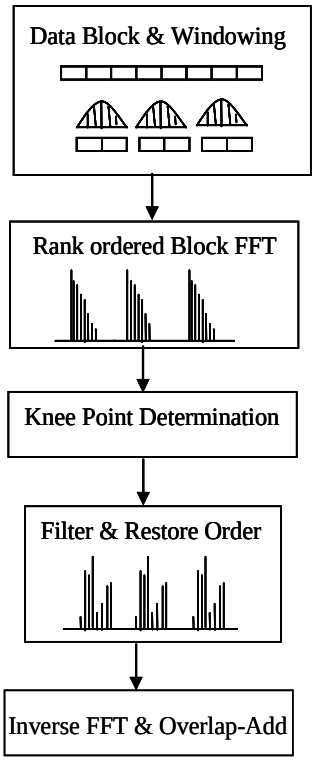

Figure 5-14 Rank-ordered algoritm process

where f_{num} is equal to $R/2x_{\eta max}$. As a result, the minimum sample number between the two sample repetitions can be obtained as [Che08a]:

$$s = \frac{T}{T - \Delta\tau} = 16 f_{num}^2 \tag{5.19}$$

For f_{num} = 2, the maximum repetition rate is 64, i.e. samples will be repeated every 64 samples. Therefore, in order to suppress the noise contributed by the sample repetition, the size of the block data is taken as 64. For best performance, each data block of size 64 is windowed by a Hanning window and overlapped in an attempt to prevent any spectral leakage. The power spectrum of each data block is ordered in an ascending sequence by simultaneously keeping the initial order of the spectrum. The points are determined where there is a significant change in the gradient in order to discard or suppress any frequency content which has a magnitude less than the knee point values. The knee point is determined by a novel technique which looks at the spectrum's gradient change [Che09b]. After the noise components are filtered from the signal, the filtered spectrum is put back into its original order by overlapping the data blocks to retain the continuity of the signal. The algorithm is adaptive because each block of data might have a different threshold value due to the beam line spectrum.

5.4 Adaptive Low-Pass Reconstruction Filters

5.4.1 Adaptive LP IIR Reconstruction Filters

The IIR reconstruction filters can simplify the Σ–Δ beamformer structure by 8 times compared to the Σ–Δ beamformers that utilise the FIR reconstruction filters [Che09a]. Because the signal band is very narrow compared to the sampling frequency, the phase within the signal band can be mostly linear even for IIR filters. Therefore, the shaped noise at the high-frequencies due to the noise-shaping function of the Σ–Δ modulators can be suppressed using IIR low-pass decimation filters after the beam sum. Since the rank-ordered filters suppress the high frequency noise as well, low-order low-pass filters are adequate in the decimation stage, which further simplifies the hardware complexity. Therefore, in this study, a fourth-order low-pass elliptic filter with a normalized bandwidth of 0.045 is used as shown in Figure 5-15. After the decimation filter, the low-frequency components are suppressed using adaptive the RO technique.

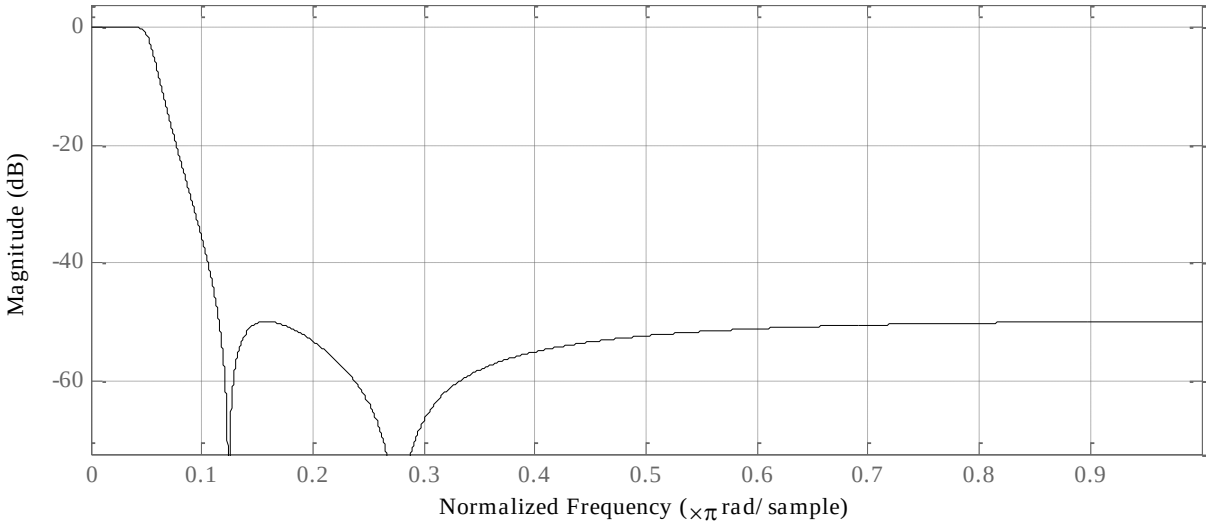

Figure 5-15 Magnitude response of the LP elliptic filter used in decimation stage

5.4.2 Adaptive Low-Pass Slink Reconstruction Filters

The quantization noise at the high-frequencies can be also suppressed using hardware efficient slink filters, whose block diagram is given in Figure 5-16 [Hog81]. A slink-filter of length R is a FIR filter with all R coefficients equal to one [Par98].

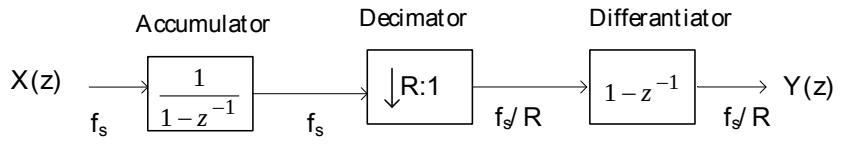

Figure 5-16 Block diagram of one-stage slink filter

The general transfer function of a slink-filter is [Hog81]:

$$H(z) = H_A(z)H_D(z) = \frac{(1-z^{-R})^N}{(1-z^{-1})^N} \tag{5.20}$$

A single slink-filter stage usually does not have enough stop-band attenuation in the region of interest to prevent aliasing after decimation. However, cascaded slink-filters can be used to give enough stop-band attenuation. Therefore, in the reconstruction filter, a three-stage cascaded slink filter with the transfer function of $H(z) = \frac{(1-z^{-16})^3}{(1-z^{-1})^3}$ is used.

The corresponding low-pass slink decimation filter can be implemented using a conventional three-stage structure as shown in Figure 5-17 [Hog81].

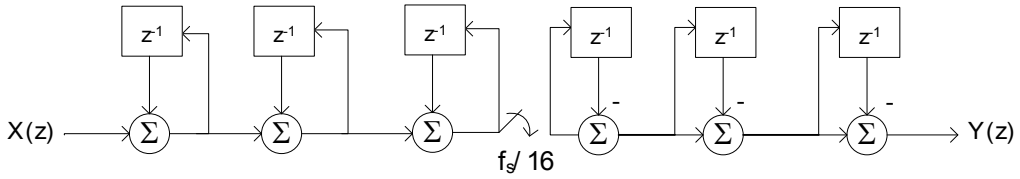

Figure 5-17 Three-stage structure slink-filter

This realization needs six registers, six adders and no multipliers. The resulting spectrum is given in Figure 5-18.

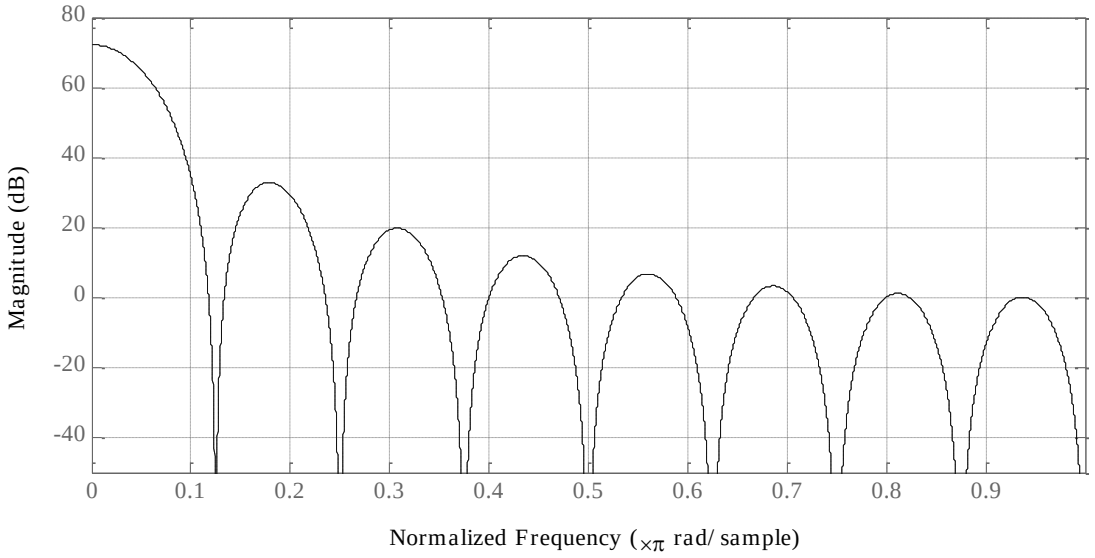

Figure 5-18 Magnitude response of the slink filter used in the decimation stage.

Since no multipliers and no storage for filter coefficients are required, using slink filters greatly reduce the hardware complexity of the reconstruction filters. In addition, compared to the equivalent implementation using cascaded uniform FIR filters, the intermediate storage is also reduced by using integrators at the high sampling rate and differentiators at the low sampling rate [Par98].

5.4.3 Adaptive Low-Pass Polyphase Reconstruction Filters

As detailed in Section 5.2.2 polyphase filter structures can be used in order to simplify the hardware implementation of IIR filters. Using the LP-to-LP frequency transformation, the cut-off frequency of a half-band low-pass prototype filter can be moved to the desired

frequency [Con70], [Kru99]. The transformation is performed by substituting every first-order delayor of the prototype filter with the first-order all-pass filter [Kru99]. Therefore, the transformation does not increase the order of the overall filter, but now the second-order sub-filter sections are composed of two coefficients instead of one. The coefficients of the resulting frequency transformed filter can be computed using the parameter β [Kru99]:

$$\beta_0 = \frac{\alpha + \gamma^2}{1 + \gamma^2} \tag{5.21}$$

$$\beta_1 = -\frac{2\gamma(\alpha + 1)}{1 + \gamma^2} \tag{5.22}$$

where,

$$\gamma = \frac{\sin \pi(\nu_{old} - \nu_{new})}{\sin \pi(\nu_{old} + \nu_{new})} \tag{5.23}$$

The corresponding transfer function of the second-order all-pass filter, $A(z)$ can be written as:

$$A(z^{-2}) = \frac{\beta_0 + \beta_1 z^{-1} + \beta_2 z^{-2}}{1 + \beta_1 z^{-1} + \beta_0 z^{-2}} \tag{5.24}$$

The half-band low-pass polyphase filter having a stop-band attenuation of 50 dB and a normalized transition band of 0.25 as designed in Section 5.2.2 is used as a prototype filter. Using the LP-to-LP frequency transformation, the cut-off frequency of the prototype filter is moved to 0.055 [Con70], [Kru03]. The resulting 5th-order IIR LP filter can be designed as cascaded all-pass sections as shown in Figure 4-41. The coefficients of the LP-to-LP transformed second-order all-pass sections are given in Table 4-6.

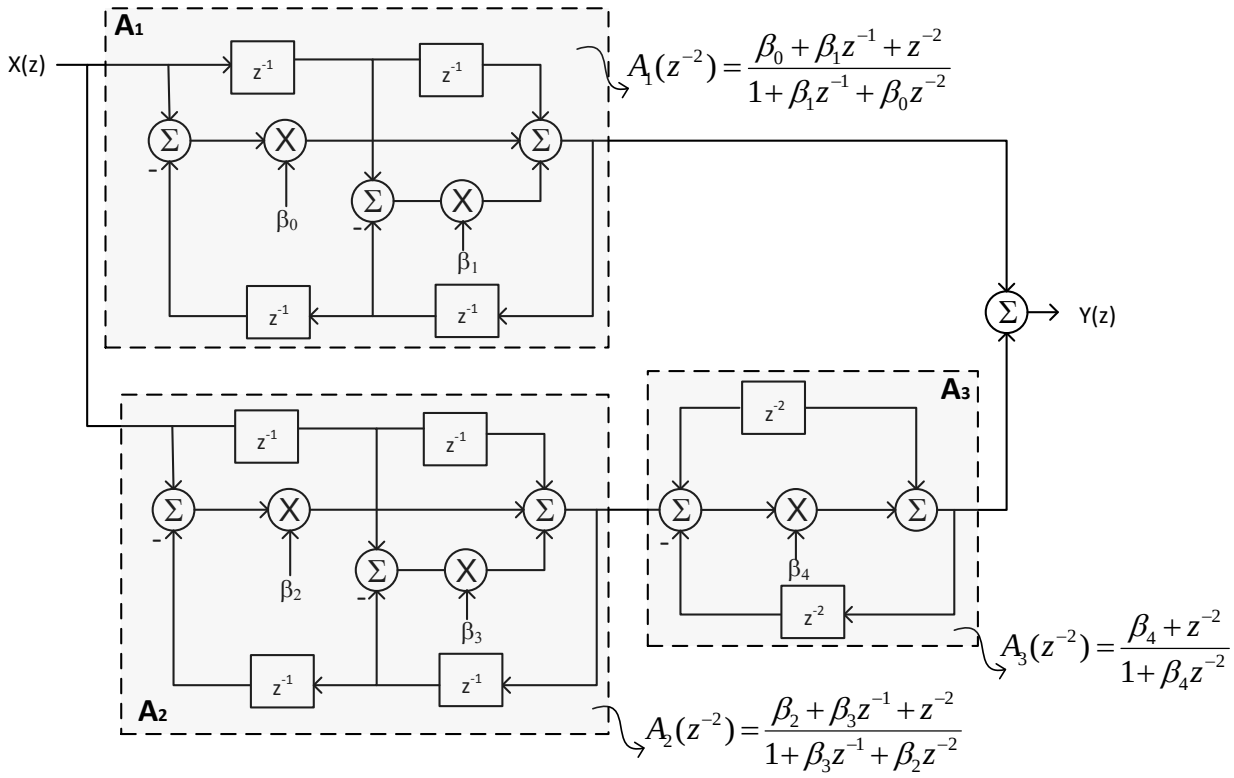

Figure 5-19 LP-to-LP transformation filter implemented by second-order all-pass filters

$A_1(z^{-2})$	$A_2(z^{-2})$	$A_3(z^{-1})$
β_0 = 0.773238877297939	β_2 = 0.915253510356223	β_4 = -0.843272067211630
β_1 = -1.747783315316791	β_3 = -1.887759270822757	

Table 5-3 Coefficients of all-pass sections

The magnitude responses of the prototype filter and the resulting fifth-order IIR low-pass filter are shown in Figure 5-20.

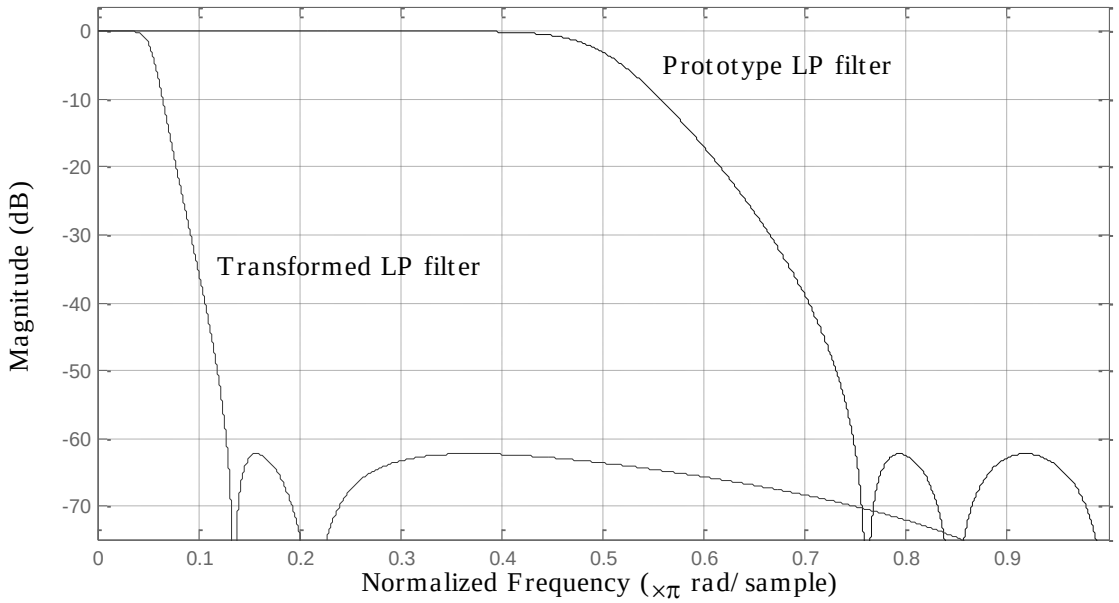

Figure 5-20 Filter responses of the (a) LP prototype filter, (b) frequency transformed LP filter

Compared to the equivalent elliptic filter implementation, the use of all-pass filters sections $A(z)$, will halve the number of coefficients, thus reducing the hardware complexity.

However, regardless of the decimation filter type, the elevated noise level at low-frequencies cannot be suppressed completely using non-adaptive filters. Therefore, in order to reconstruct the Σ–Δ modulator outputs properly, after the proposed low-pass decimation filters, the proposed adaptive rank-ordered filters are applied to suppress the undesirable low-frequency noise components.

5.4.4 **Simulation Results:**

Since the sample repetition rate during the dynamic focusing is dependent on the focusing depth, especially for focus ranges close to the transducer, the in-band noise level can not be suppressed efficiently by employing conventional LP reconstruction filters. The PSF produced by Σ–Δ beamformers utilizing Slink low-pass reconstruction filters and the proposed adaptive Slink low-pass reconstruction filters are shown in Figure 5-21.

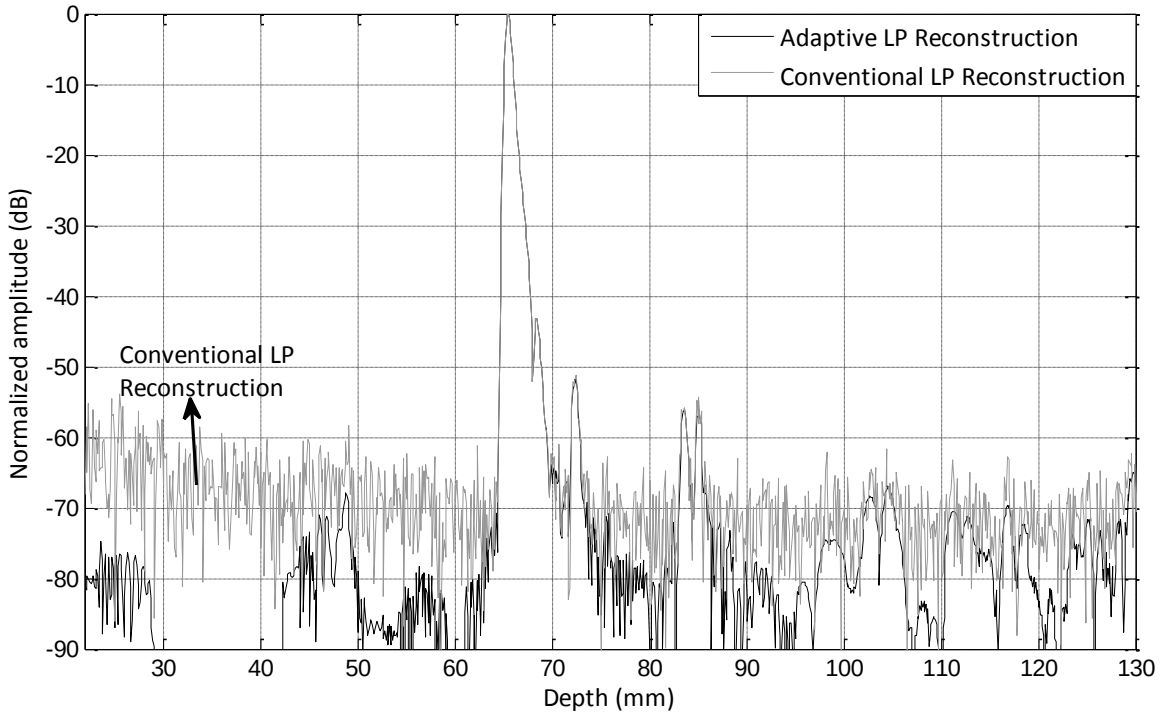

Figure 5-21 Axial PSF of the 3rd wire

As seen from Figure 5-21, the rapidly changing delay samples to focus the beams to short ranges cause the background noise level to increase more when it is close to the transducer compared to when it is far away from the transducer, especially for depth ranges shorter than 50mm. Therefore, as seen in Figure 5-21, for the shorter ranges, the reconstruction error as elevated noise floor, is greatly reduced by using the proposed adaptive rank-order filters. In addition, the frequency spectrum after the reconstruction filters at the Nyquist rate (13.89 MHz) is given in Figure 5-22. Conventional sigma-delta beamformers employing slink filters are compared with adaptive slink filter in the reconstruction stage. The frequency spectrum of the single beam line of the third wire reconstructed by adaptive elliptic filters and adaptive polyphaser filters are given in Figure 5-23 a and b, respectively.

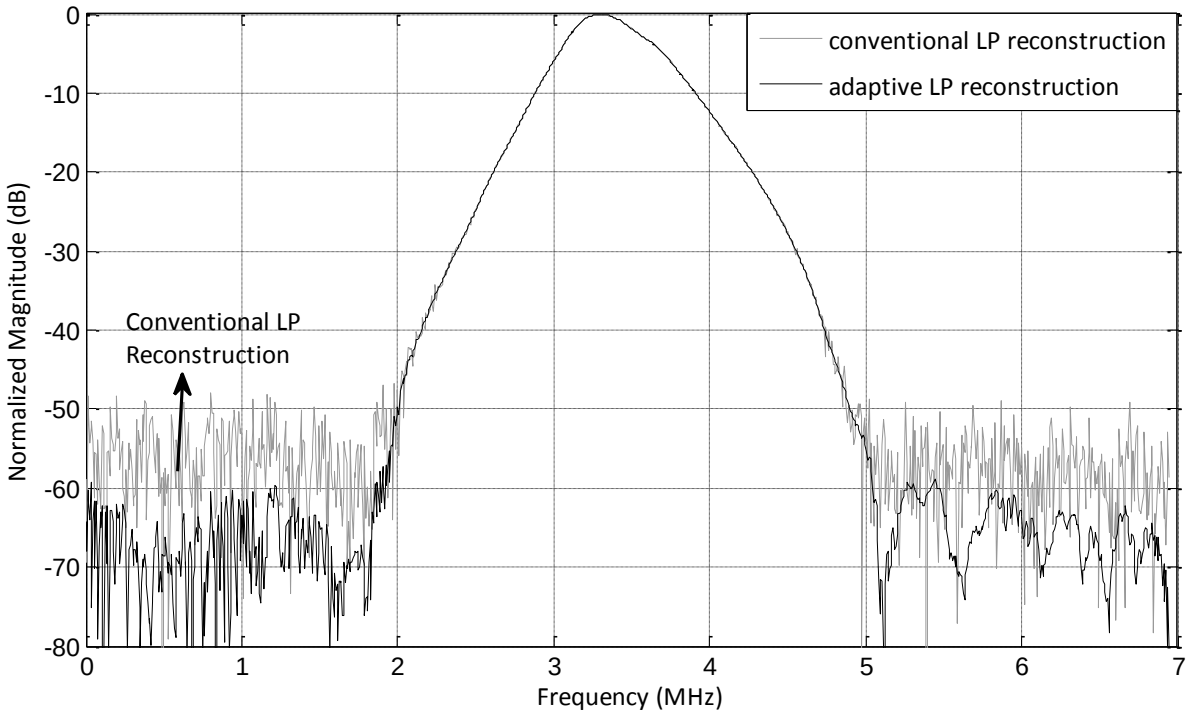

Figure 5-22 Frequency spectrum of a single beam-line, conventional Σ–Δ beamformer with LP-slink-reconstruction filters, and with adaptive LP-slink-reconstruction filters.

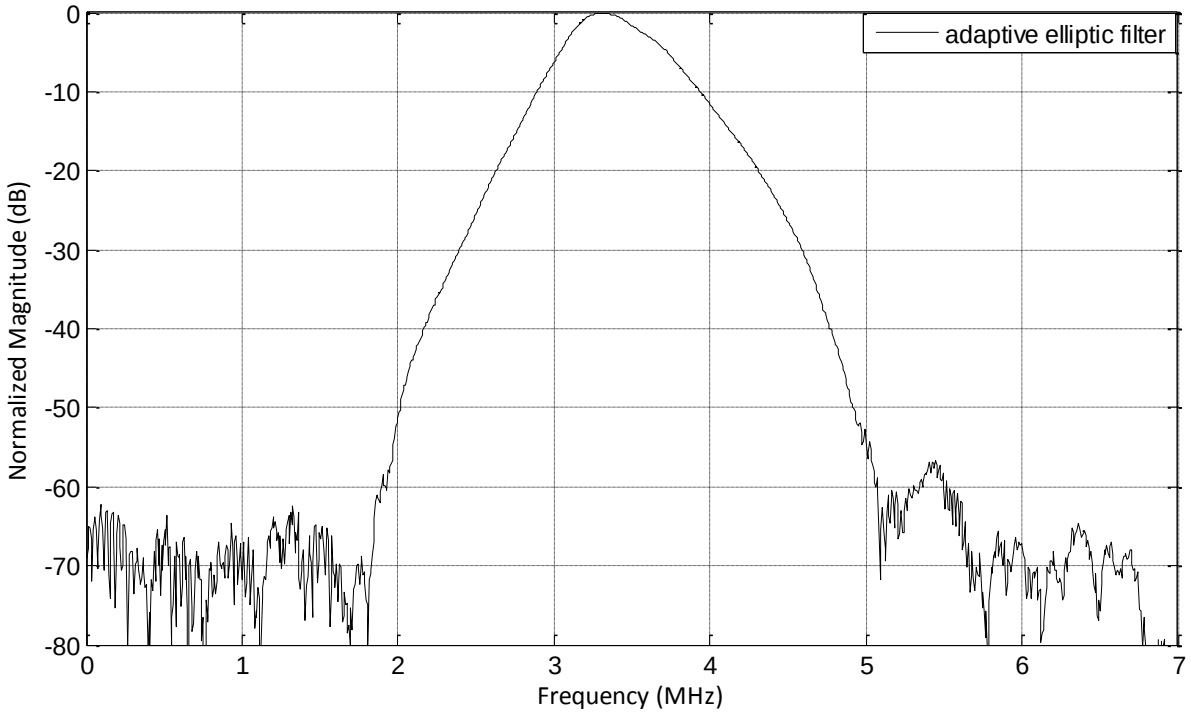

(a)

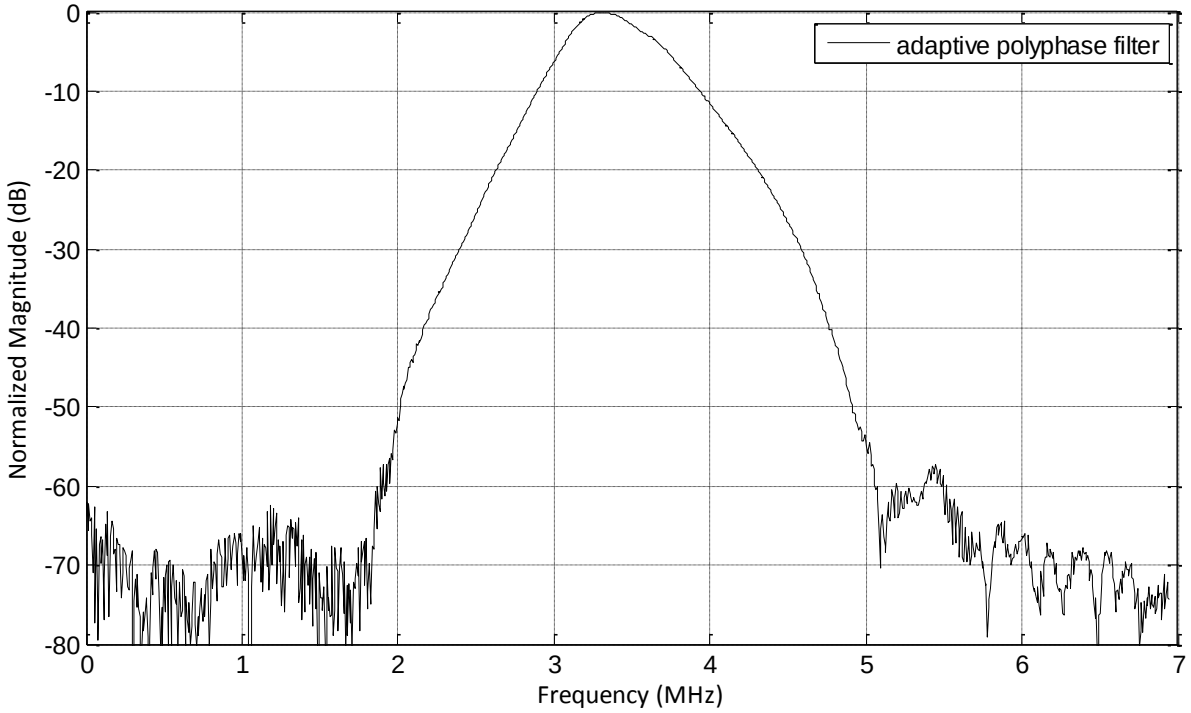

(b)

Figure 5-23 Frequency spectrum of a single beam-line, beamformer with (a) adaptive LP-elliptic- and (b) polyphase-reconstruction filters.

As seen, the increased noise floor at the low frequencies cannot be sufficiently suppressed using low-pass reconstruction filters. However, Figure 5-22 and Figure 5-23 demonstrate that the in-band noise level by a single-bit Σ–Δ beamformer utilizing an adaptive reconstruction filter is greatly suppressed to -70 dB, which is nearly equivalent to that achieved by a 10-bit A/D beamformer.

5.5 Adaptive Band-Pass Reconstruction Filters

Adaptive rank-ordered filters following the band-pass decimators given in Section 5.2 are employed to provide sufficient suppression of the low-frequency quantization noise level. The noise analyses in the time-domain have shown the effectiveness of the proposed reconstruction method in improving the noise performance.

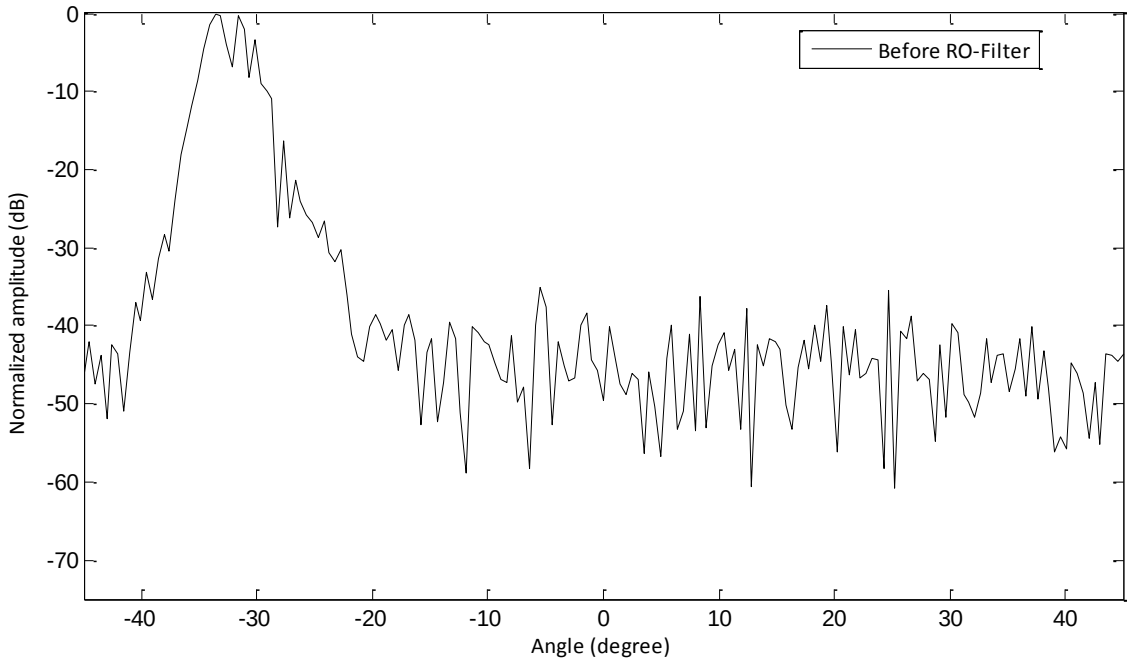

(a)

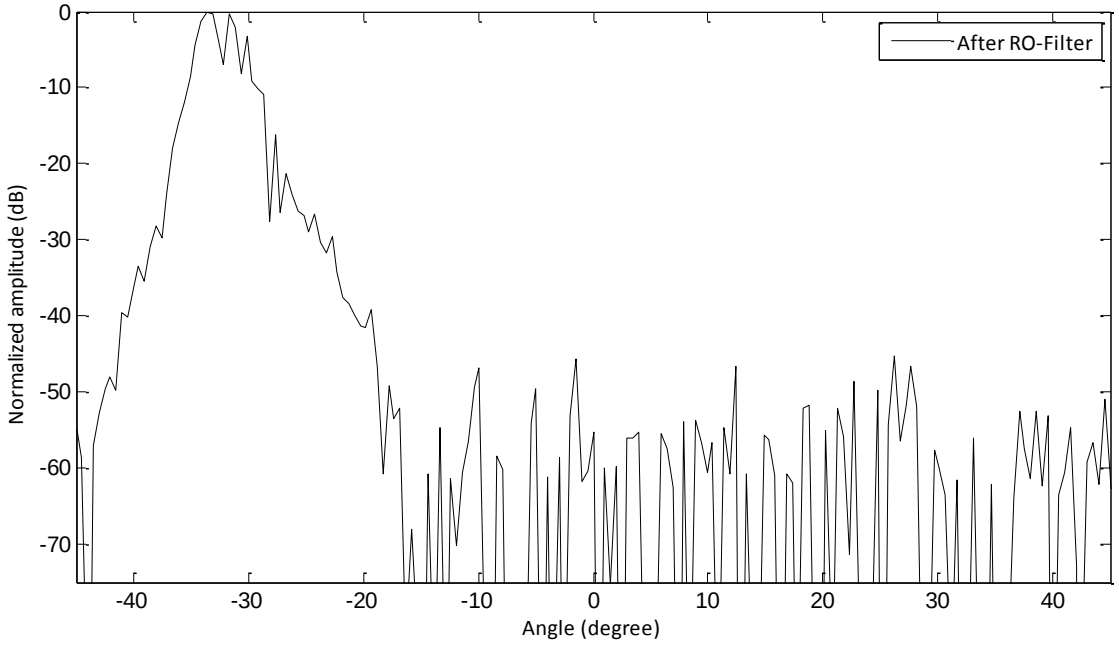

(b)

Figure 5-24 Lateral PSF of BP polyphase reconstruction filters for depth 35mm (1th wire), (a) before RO filter, (b) after RO filter (adaptive)

The PSF produced by Σ–Δ beamformers utilizing band-pass polyphase reconstruction filters with and without adaptive rank-ordered filters are given in Figure 5-24. As seen from the figures, using band-pass decimation filters, the increased noise floor at the low

frequencies is suppressed sufficiently but not completely for the short focusing ranges (Figure 5-24b). However, as indicated in Figure 5-24 b, the in-band noise level is further suppressed by utilizing the rank-ordered filters after the band-pass decimator.

Figure 5-25 shows the comparison of the frequency spectrum of the main lobe of the single beam line for the first-, third- and sixth-wire produced by Σ–Δ beamformers with conventional (LP slink filters) and adaptive BP elliptic reconstruction filters.

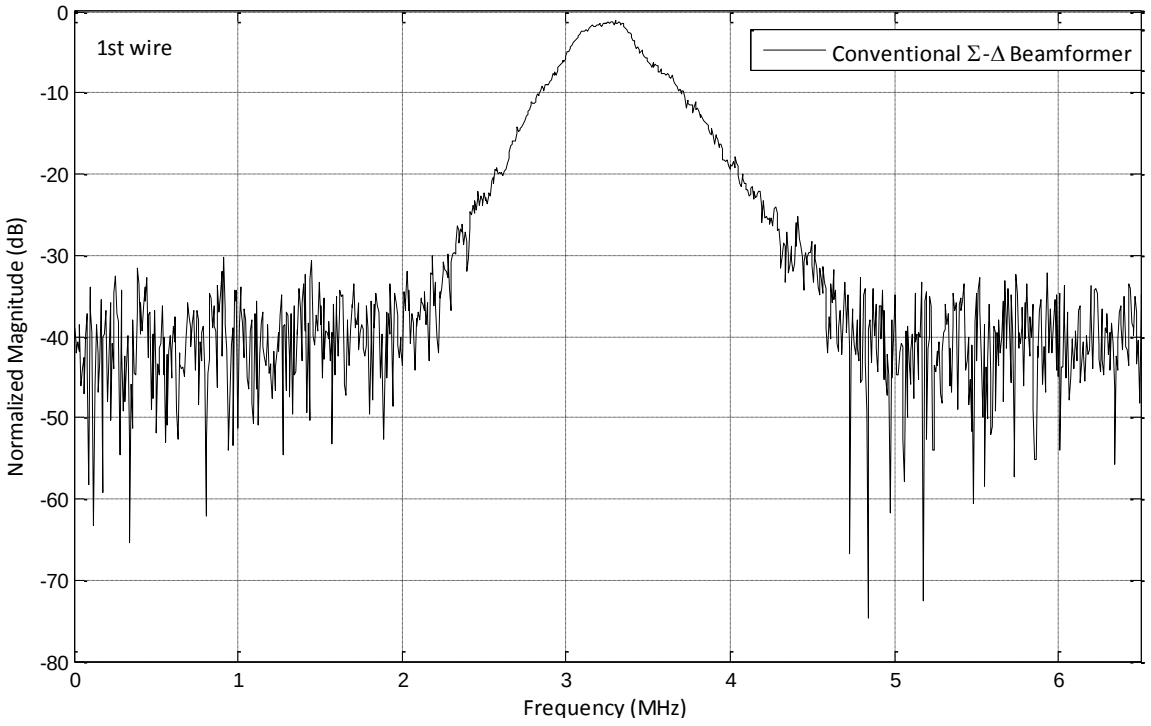

(a)

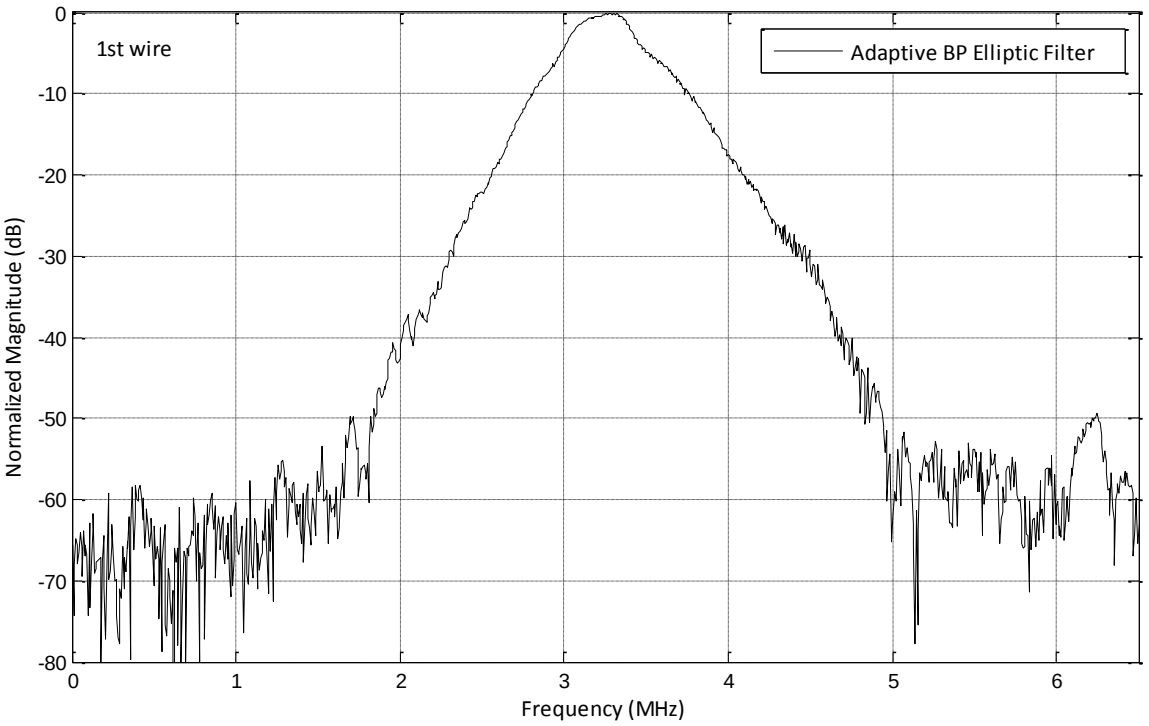
1st wire
Adaptive BP Elliptic Filter
Normalized Magnitude (dB)
Frequency (MHz)
0
-10
-20
-30
-40
-50
-60
-70
-80
0
1
2
3
4
5
6

(b)

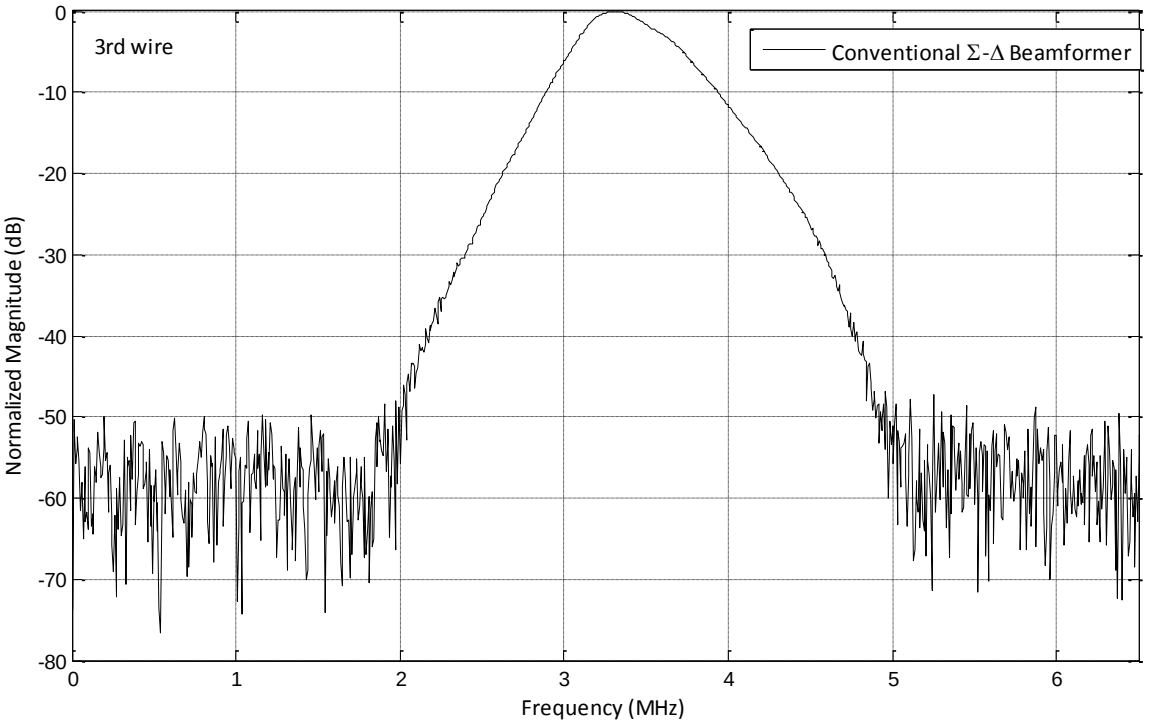
3rd wire
Conventional Σ-Δ Beamformer
Normalized Magnitude (dB)
Frequency (MHz)
0
-10
-20
-30
-40
-50
-60
-70
-80
0
1
2
3
4
5
6

(c)

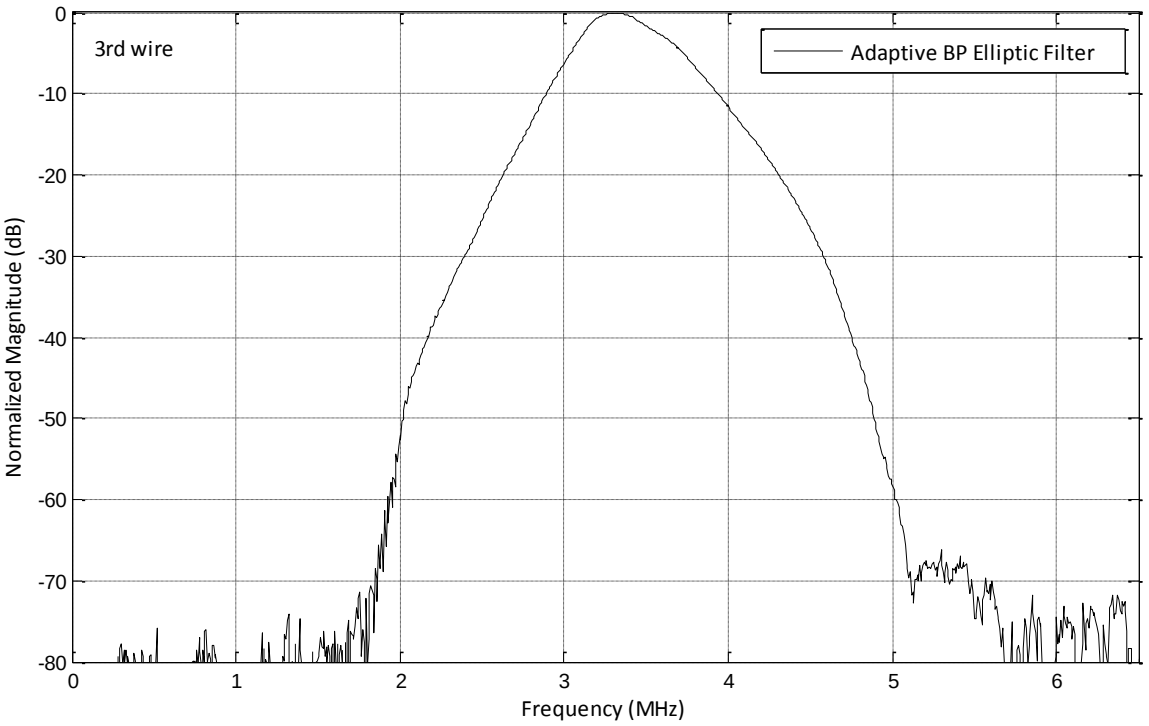
3rd wire
Adaptive BP Elliptic Filter
Normalized Magnitude (dB)
Frequency (MHz)
0
-10
-20
-30
-40
-50
-60
-70
-80
0
1
2
3
4
5
6

(d)

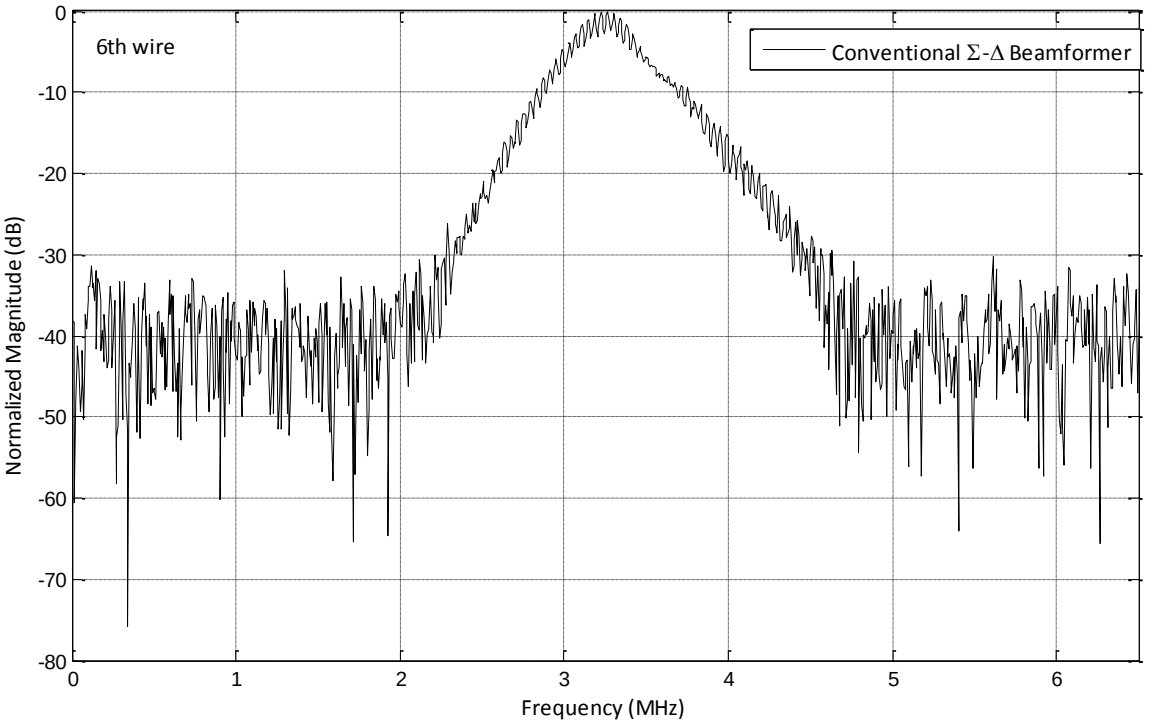
6th wire
Conventional Σ-Δ Beamformer
Normalized Magnitude (dB)
Frequency (MHz)
0
-10
-20
-30
-40
-50
-60
-70
-80
0
1
2
3
4
5
6

(e)

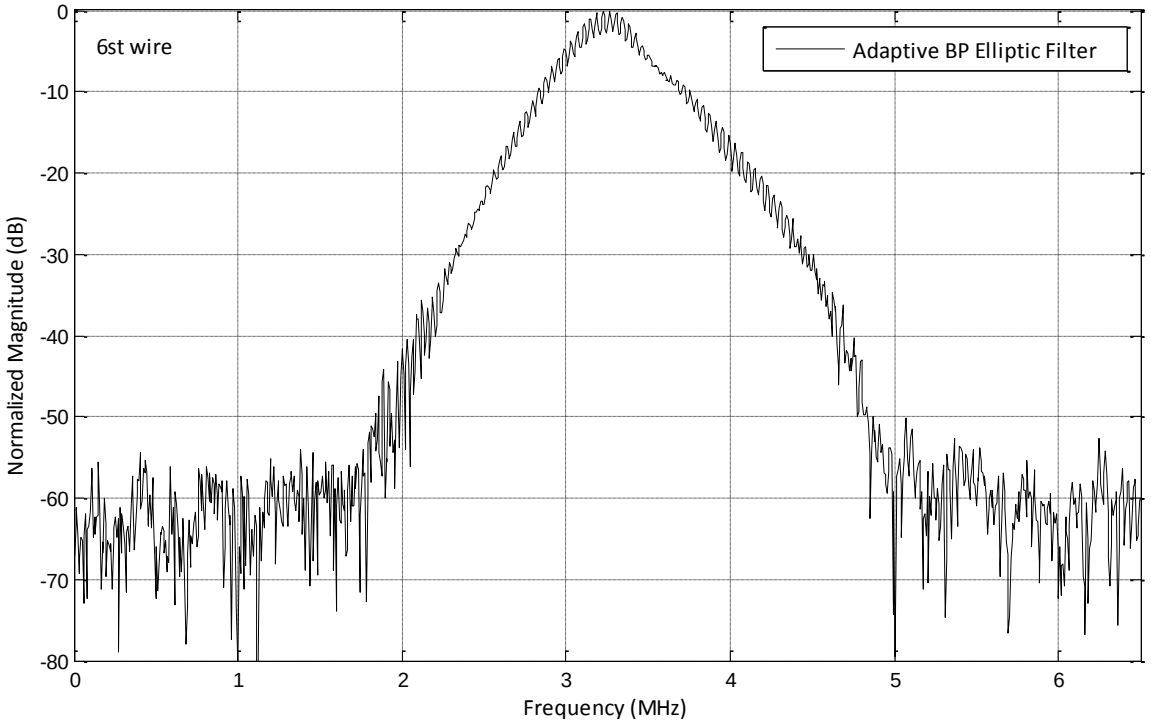

(f)

Figure 5-25 Frequency spectrum of a single beam-line for first-, third- and sixth-wire reconstructed by (a), (c), (e) conventional reconstruction filters and (b), (d), (f) adaptive BP elliptic filters

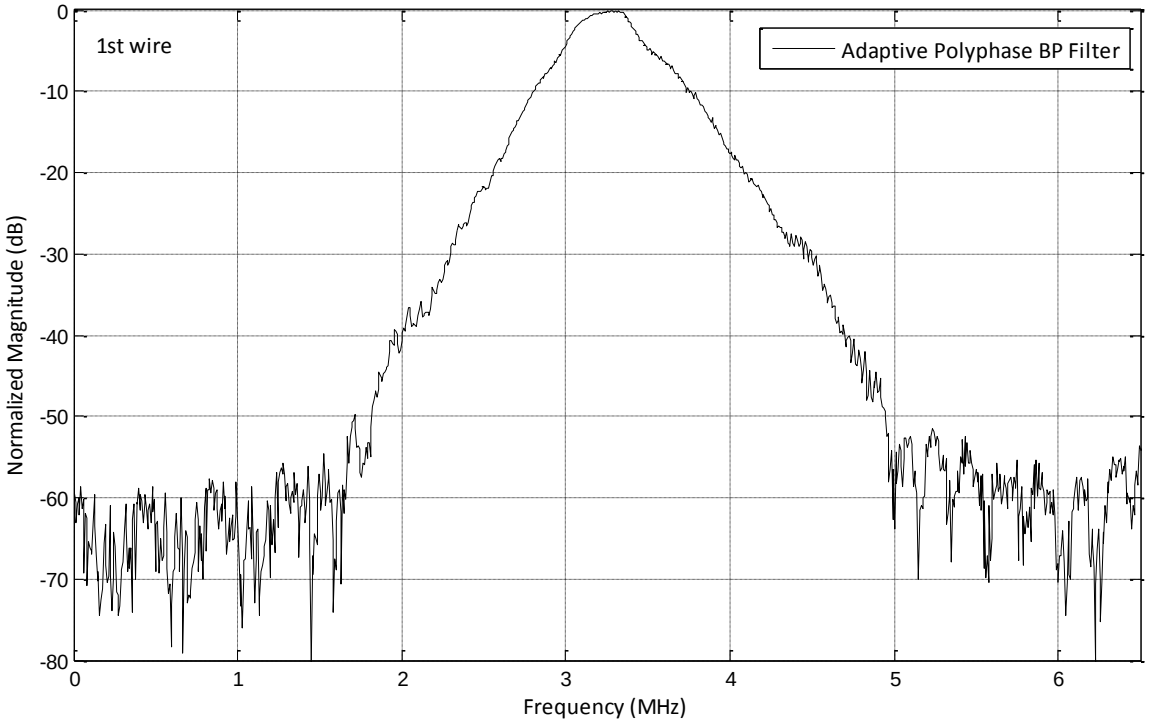

Figure 5-26 Frequency spectrum of a single beam-line reconstructed by adaptive BP polyphase filter, for the first-wire

As seen in Figure 5-25 and Figure 5-26, BP Elliptic Filters and BP polyphase filters in combination with adaptive RO filters suppress the demodulation error for all the three wires successfully. However as seen in Figure 5-25a, Figure 5-25e, as the focusing range is close to the transducer or far away from the transducer, the quantization noise level increase to -40dB, which is reduced to -60dB by adaptive BP elliptic- and polyphase filters In addition, as given in Figure 5-25c the noise level of the third wire is at -55dB, which is suppressed to -80dB by adaptive BP elliptic filters.

5.6 B-Scan Images and Simulation Results

The performances of the proposed reconstruction techniques detailed in Sections 5.2 5.4 and 5.5 are compared using the B-scan images using wire- and cyst-phantom data sets. The simulation results have illustrated that the proposed methods achieve significant improvement in resolution and thus provide similar high quality B-scan images as the ones obtained by conventional 10-bit A/D beamformers.

5.6.1 Wire Phantom

The B-scan images obtained by the 10-bit A/D beamformer, conventional single-bit Σ–Δ beamformer and the proposed adaptive LP- and BP-reconstruction filters are given in Figure 5-27.

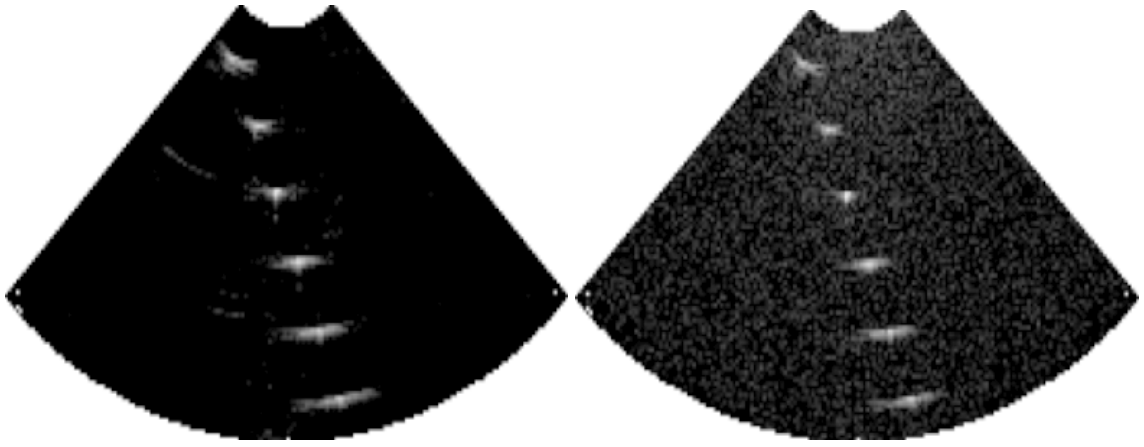

(a) (b)

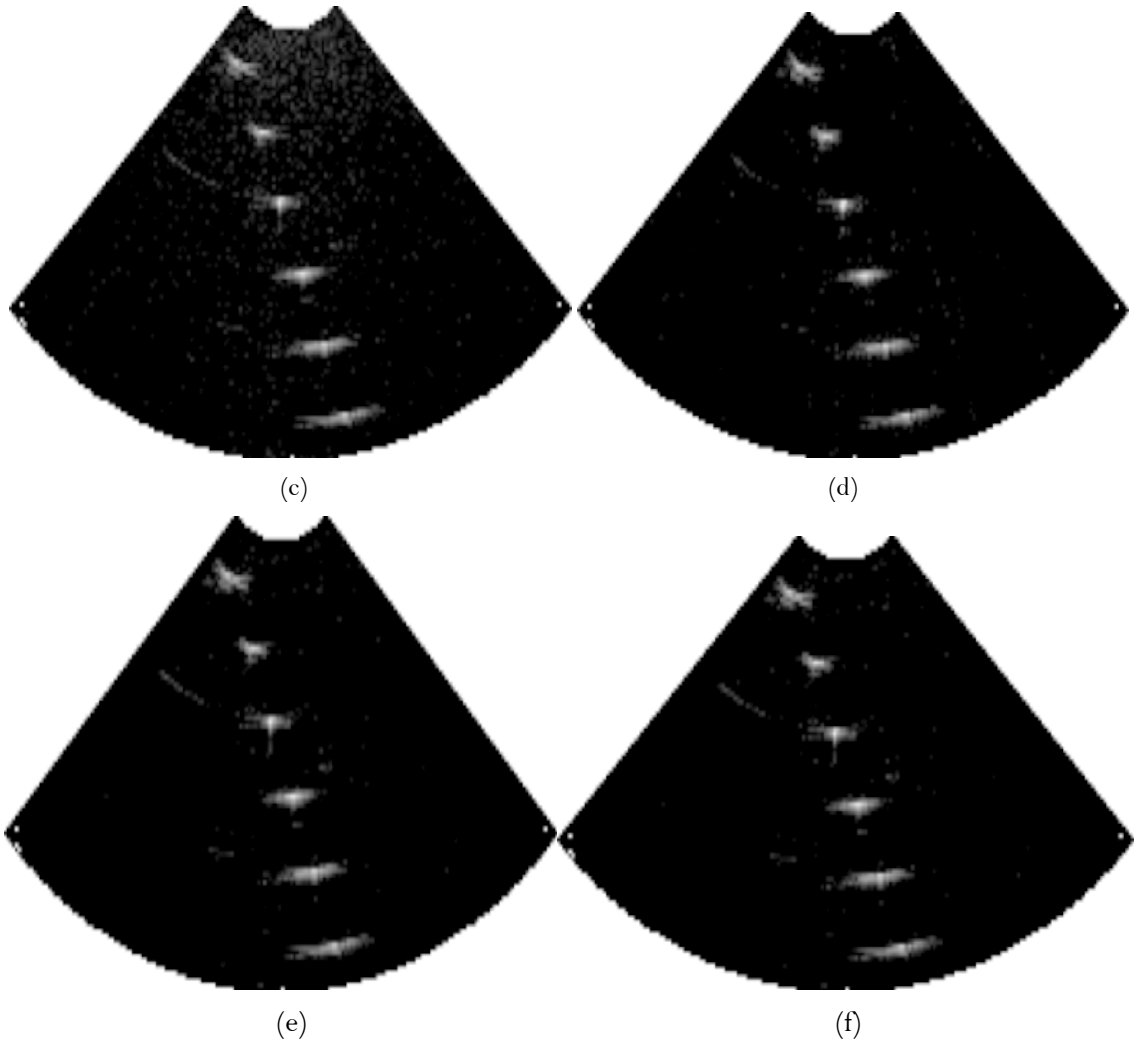

Figure 5-27 Wire phantom B-scan images, (a) 10-bit A/D beamformer, (b) conventional Σ–Δ beamformer, (c) Σ–Δ beamformer with BP polyphase-reconstruction filters, (d) Σ–Δ beamformer with adaptive LP slink-reconstruction filters, (e) Σ–Δ beamformer with adaptive BP polyphase- (f) Σ–Δ beamformer with adaptive BP elliptic- reconstruction filters.

As given in Figure 5-27-b, the reconstruction error causes the background noise to be elevated resulting in significant degradation in the image quality. The noisy background is greatly improved by using BP decimation filters (Figure 5-27-c). However, the rapidly changing delay samples to focus the beams to short ranges cause the background noise level to increase more when it is close to the transducer (top of the image) compared to when it is far away from the transducer (bottom of the image). Therefore, as seen in Figure 5-27-d-f, the resolution is further improved by the combination with the adaptive rank-order filters. The RO algorithm following the decimation filters achieve high quality B-scan images as obtained by 10-bit A/D beamformers.

The SQNR values are used in order to compare quantatively the performances of the corresponding beamformer structures. These are calculated before the logarithmic compression stage as detailed in Section 4.8.

BEAMFORMER STRUCTURES	SQNR (dB)
Conventional Σ–Δ Beamformer LP-reconstruction	
Elliptic filters	-10.0382
Polyphase filters	-9.9119
Slink filters	-11.5194
Σ–Δ Beamformer Adaptive LP-reconstruction	
Adaptive elliptic filters	-1.2758
Adaptive polyphase filters	-1.8481
Adaptive slink filters	-2.4450
Σ–Δ Beamformer BP-reconstruction	
Butterworth filters	-7.9919
Chebyshev filters	-7.7119
Elliptic filters	-7.9227
Polyphase filters	-7.9443
Σ–Δ Beamformer Adaptive BP- reconstruction	
Adaptive Butterworth filters	-2.5745
Adaptive Chebyshev filters	-1.7234
Adaptive elliptic filters	-0.9574
Adaptive polyphase filters	-1.1816

Table 5-4 Relative SQNR values for proposed reconstruction structures

The simulation results have shown that the proposed reconstruction filters effectively reduce the image artefacts and provide high quality B-scan images comparable to the ones obtained by 10-bit A/D beamformers. Since the rank-ordered filters manage to sufficiently suppress the quantization noise at the low as well as at the high frequencies, the hardware complexity of the decimation filters is greatly reduced. The calculated SQNR values of the conventional Σ–Δ beamformer relative to the 10-bit A/D are given in Table 5-4. Σ–Δ beamformers employing LP reconstruction filters have an increased noise power by almost 10 dB less than the one produced by 10-bit A/D beamformers. When the adaptive RO filters are applied to conventional LP reconstruction filters, nearly 1.5 bit improvement is achieved, so that an almost -1.2 dB relative SQNR is obtained. As seen in Table 5-4, compared to slink LP filters, elliptic- and polyphase filters achieve more than 1 dB improvement. As seen in Figure 5-27c, BP reconstruction filter without RO filters can greatly suppress the background noise for the image depths far from the transducer. However, the quantization noise level at the top of the image could not be suppressed sufficiently using the BP reconstruction filters. Therefore, the overall relative SQNR values of conventional Σ–Δ beamformers are improved by almost 2 dB by employing BP reconstruction filters. When RO filters are applied to the BP reconstruction filter output, the noise elevation for close ranges is sufficiently reduced so that an additional 7 dB SQNR improvement is achieved. BP decimators followed by adaptive RO filters achieve the high quality images as obtained by 10-bit A/D beamformers. Compared to Chebyshev- and Butterworth BP filters, BP elliptic- and polyphase filters achieve almost 1 dB better resolution. The adaptive BP-elliptic filters achieve the best result among the proposed reconstruction filters so that there is less than 1 dB difference to the 10-bit A/D beamformers.

5.6.2 Cyst Phantom

The cyst-phantom B-scan images reconstructed by the conventional Σ–Δ beamformer are compared with the images generated by the Σ–Δ beamformer employing the proposed filters. As shown in Figure 5-28a, the increased background noise in the conventional Σ–Δ beamformer degrades significantly the contrast of the image, and hence masks the fine details of the cyst regions. The images obtained by the proposed structure are consistent with those obtained using wire data sets. As indicated in Figure 5-28, the proposed adaptive

LP and BP reconstruction filters significantly reduce the background noise resulting in a high quality image with significantly improved contrast resolution.

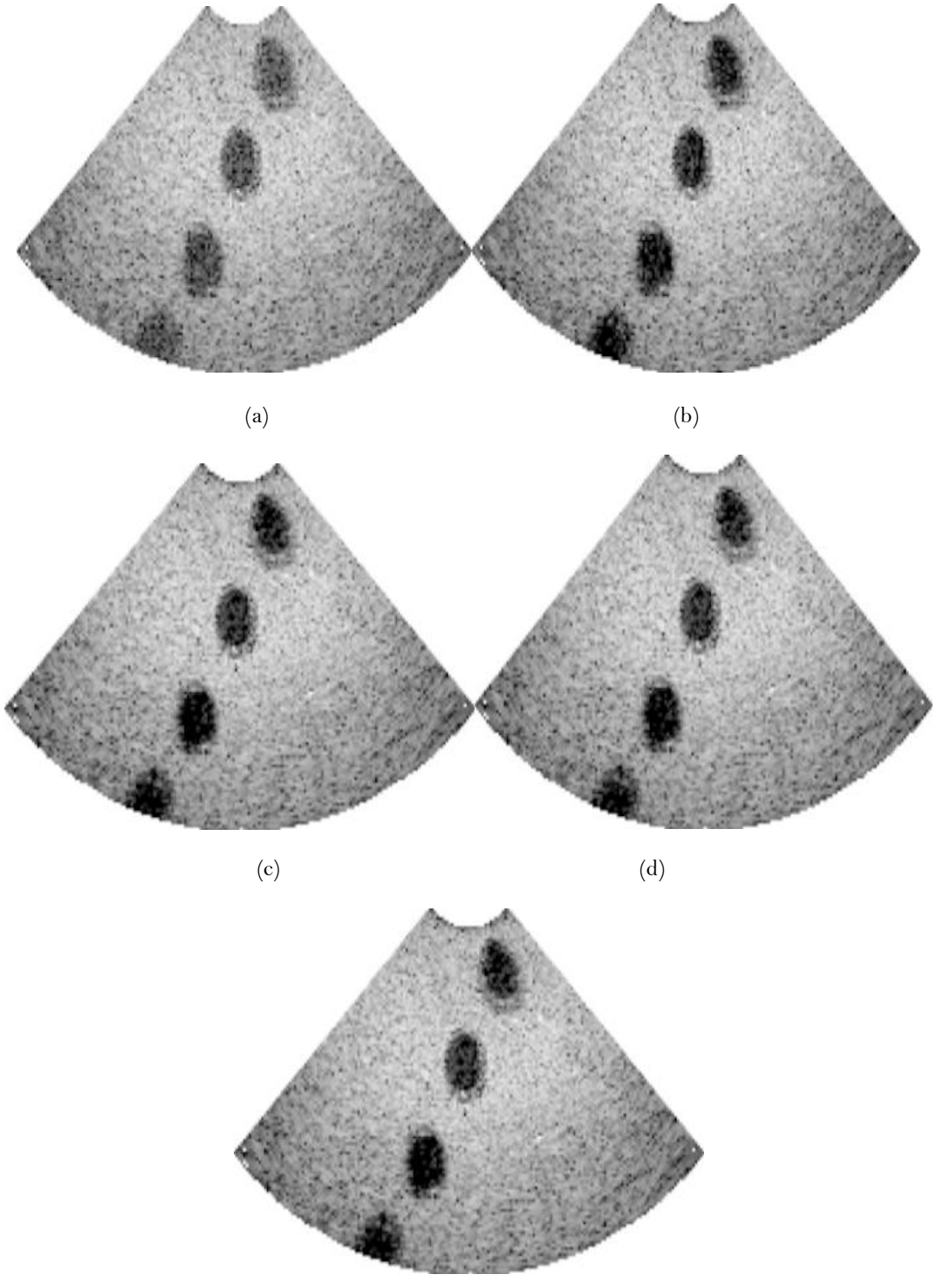

(a) (b)

(c) (d)

(e)

Figure 5-28 Cyst phantom B-scan images, (a) conventional LP-,(b) adaptive LP-, (c) BP-polyphase-, (d) adaptive-BP-polyphase-, (e) adaptive BP-elliptic reconstruction filter.

BEAMFORMER STRUCTURE	Cyst-1	Cyst-2	Cyst-3
10-bit A/D Beamformer	5.50	4.81	4.11
Conventional Σ–Δ Beamformer LP-reconstruction			
Elliptic filters	4.09	4.37	3.30
Polyphase filters	4.12	4.40	3.37
Slink filters	3.09	4.18	3.09
Σ–Δ Beamformer Adaptive LP-reconstruction			
Adaptive elliptic filters	5.26	4.81	3.92
Adaptive polyphase filters	5.25	4.81	4.09
Adaptive slink filters	5.17	4.81	4.11
Σ–Δ Beamformer BP-reconstruction			
Butterworth filters	4.57	4.55	3.56
Chebyshev filters	4.65	4.56	3.52
Elliptic filters	4.59	4.56	3.49
Polyphase filters	4.56	4.58	3.52
Σ–Δ Beamformer Adaptive BP-decimation			
Adaptive Butterworth filters	5.37	4.81	4.08
Adaptive Chebyshev filters	5.47	4.79	4.11
Adaptive Elliptic filters	5.50	4.81	4.11
Adaptive Polyphase filters	5.31	4.81	4.11

Table 5-5 CNR values of cyst images obtained by different reconstruction structures

The CNR results for various reconstruction structures are given in Table 5-5. The CNR results show that the band-pass decimation filters significantly reduce the background noise level resulting in improved contrast resolution compared with the conventional Σ–Δ beamformers with low-pass non-adaptive reconstruction filters. The contrast resolutions are further improved by applying the adaptive rank-ordered technique following the band-pass decimation filters. The simulation results have shown that the proposed adaptive low-

pass and band-pass reconstruction structures provide effectively improved cyst contrast resulting in high quality B-scan images comparable to those attained by 10-bit A/D beamformers. BP reconstruction filters significantly increase the cyst detectability compared to conventional LP reconstruction filters. As concluded with wire-data results, using adaptive RO filters following the LP- and BP-reconstruction filters significantly improve the contrast resolution.

The proposed beamformer performance can be compared with the existing beamformers using the same experimental data sets [Fre97], [Fre99], [Kar99], [Koz01]. The B-scan images obtained by two different digital beamforming approaches: one-bit Σ–Δ beamformer with 2X compensation [Fre97], [Fre99] and the non-uniform one-bit oversampling Σ–Δ beamformer [Kar99], [Koz01] are compared with those obtained by the proposed beamformer. The comparisons have shown that the proposed Σ–Δ beamformer methods provide increased SQNR values resulting in improved image quality with significantly reduced noise levels. The relative SQNR for the one-bit Σ–Δ beamformers employing 2X compensation is −2.4 dB and for the non-uniform oversampling structure is −1.5 dB. On the other hand, the SQNR of the proposed beamformer employing adaptive BP polyphase, adaptive LP elliptic and adaptive BP elliptic-reconstruction filters achieve -1.18 dB, -1.27 dB and -0.95 dB respectively. Besides the increased image quality, in the proposed structure the hardware simplicity of the conventional Σ–Δ beamformers are completely preserved. In the Σ–Δ beamformer with 2X compensation the improvements are achieved at the expense of increased hardware complexity via additional feedback control in the Σ–Δ modulator circuitry in each of the 128-channels [Fre97], [Fre99]. In addition, in the non-uniform one-bit oversampling Σ–Δ beamformer, signal processing is dramatically increased via non-uniform control requirements at different clocks in each of the 128-channels [Kar99], [Koz01]. In the proposed method, the Σ–Δ modulator structure and align-and-sum phase do not need to be modified, as the noise components are suppressed in the reconstruction stage via proposed reconstruction filters after the beam summation. The conventional Σ–Δ modulators employed in each of the 128-channels remain unchanged, resulting dramatically in simplified hardware- and signal processing complexity compared to existing methods.

The hardware complexity of the proposed reconstruction filters are given in Table 5-6.

RECONSTRUCTION FILTERS	Number of adders	Number of multipliers
LP-reconstruction		
Elliptic filters (fourth-order)	8	9
Polyphase filters (fifth-order)	9	5
Slink filters (three-stages)	6	0
BP-reconstruction		
Butterworth filters (tenth-order)	20	21
Chebyshev filters (eighth-order)	16	17
Elliptic filters (eighth-order)	16	17
Polyphase filters (tenth-order)	14	10

Table 5-6 Number of adders and multipliers used in the reconstruction filter implementations

A polyphase filter architecture designed as a cascaded all-pass filter structure reduces the hardware complexity by requiring fewer adders and multipliers as shown in Table 5 6. Slink and polyphase filter structures ensure high quality images as obtained by IIR filters. They also have less hardware requirements in terms of the number of adders and multipliers.

5.7 Concluding Remarks

The repeated samples during dynamic focusing degrade the synchronization between the modulator and demodulator, which leads to an elevated noise floor in the reconstructed signal. As a result, the increased in-band noise level causes severe image artefacts as a snowy background. Therefore, recent interest in ultrasound image formation has focused on suppressing the background noise level caused by Σ–Δ beamformers. Many different techniques have been reported in the open literature to reduce the reconstruction error and improve the image quality (Table 5-1). However, the improvements are achieved at the expense of either increased hardware- or signal processing complexity. In this chapter,

novel reconstruction methods to reduce the image artefacts produced by Σ–Δ beamformers by completely preserving the hardware simplicity of single-bit Σ–Δ modulators were presented. Since, the noise level is elevated at low-frequencies, the conventional low-pass reconstruction filters are deemed to be insufficient to suppress the in-band noise level. Therefore, different from the existing methods in the open literature, the improvements in resolution are achieved in the demodulation stage after the delay-and-sum process. As a result, the conventional structure of the second-order Σ–Δ modulator was completely preserved and the dynamic delays were applied via the traditional delay-and-sum approach. The performance of the proposed methods had been evaluated by means of simulations using experimental data acquired from two different phantoms. Firstly, BP reconstruction filters were proposed to reduce the in-band noise level. The simulation results demonstrated that the BP decimation filters provided improved image quality compared to the one constructed by conventional LP reconstruction filters. However, due to the sample repetition rate during the delay-and-sum process, the noise components at the low-frequencies are dynamically changing along the scan depth. Therefore, the image resolution was further improved by combining the LP decimation filters with adaptive rank-ordered filters. It was verified that the proposed rank-ordered filters following the LP reconstruction filters significantly reduce the noise level and achieve high quality image as generated by a 10-bit A/D beamformer. Moreover, further resolution improvements were obtained by employing rank-ordered filters in combination with BP decimation filters. As seen in Table 5-4 and Table 5-5, the best results in terms of the SNR and CNR values were obtained by adaptive BP elliptic filters. Therefore, finally, the hardware complexity of the BP reconstruction filters were greatly simplified by using polyphase filters as cascaded all-pass filter structures as shown in Table 5-6.

Since the image artefacts are reduced at the reconstruction stage, a Σ–Δ beamformer structure does not require any hardware modification in the modulator structure or in the delay-and-sum process. As a result, the advantages of the conventional single-bit Σ–Δ beamformers are completely preserved. In addition, only a single adaptive reconstruction filter is required per beam sum to achieve high quality B-scan images as the ones obtained by 10-bit A/D beamformers. Therefore, the simplicity of the proposed hardware efficient reconstruction methods makes it suitable for cost-efficient, portable, lightweight ultrasound scanners as well as 3D scanners with large channel counts. .

Chapter 6

A GUI Driven Σ–Δ Modulator Design Tool

In this chapter, a user-friendly design, evaluation and measurement tool that includes a practical ultrasound reconstruction analyses created in the MATLAB/Simulink environment is given. In Section 6.1 the methodology of the design tool including the input parameters and measurement setups is detailed. The GUI covers a variety of Simulink-based design topologies of single- and multi-stage LP, BP and HP Σ–Δ modulators. The design and evaluation methodologies are detailed step-by-step via several example cases. In Section 6.3 the design tool is further extended to include a practical ultrasound reconstruction process by covering the entire ultrasound Σ–Δ beamformer reconstruction steps including the noise analyses and the resulting final B-scan images.

6.1 Σ–Δ Modulator Design Tool

The design procedures can be optimized based on performance analyses, since there is not a unique methodology to guarantee the stability and proper operation of high-order Σ–Δ modulators, Thus, several design automation tools for LP and BP modulators at the system level were reported in the literature [Chu07], [Fra00], [Jan94], [Ken88], [Kuo99], [Med93], [Med99], [Nor97], [Rui04], [Tal09]. The commonest approach to automate the design procedure was based on iterative performance optimization via a performance evaluation loop using statistical methods or behavioral simulations for the desired modulator parameters [Chu07], [Ken88], [Med93], [Med99], [Fra00], [Rui04], [Tal09]. The other common approach is the automation of the modulator coefficients by optimizing the Noise Transfer Functions (NTF) or Signal Transfer Functions (STF) for the desired design specifications. Inverse Chebyshev or Butterworth approximations were used for the NTF designs in order to obtain acceptable quantization noise reduction in the signal band [Nor97], [Kuo99], [Jan94].

In contrast to many of the Σ–Δ design automation tools in the literature, which mostly employ specific design structures, this tool enables the user to design and analyze a variety of LP, HP and BP based Σ–Δ modulator topologies such as the single-stage, multi-stage, chain of accumulators with weighted feedforward summation and chain of accumulators with feedforward summation with local resonator feedbacks. Moreover, the tool allows the user to design the NTFs of Butterworth and Inverse Chebyshev approximations based on input specifications such as the cut-off frequency, bandwidth and modulator order. Butterworth and Inverse Chebyshev based Σ–Δ modulators have the advantage of offering improved stability and tonality performance particularly for higher-order structures. This tool gives designers the ability to use easy-to-implement Σ–Δ modulator topologies and display their corresponding simulation results including the output spectrums, the NTFs and the power spectral densities (PSD) of the modulator outputs as well as their in-band SNR values. The MATLAB routines embedded in the GUI simulate the desired topologies according to the input parameters defined by the user. The implementation of the Σ–Δ modulator structures on the MATLAB/SIMULINK platform provides advantages such as the relative ease of data manipulation as well as flexibility. Furthermore, this tool has been developed to design HP based Σ–Δ modulators

for the applications reported in [Ral07]. The creation of a Graphical User Interface (GUI) driven design, evaluation and measurement tool for HP Σ–Δ modulators has not been previously reported in the open literature to the best knowledge of the author. Finally, the tool is easily extendible to other Σ–Δ modulators structures and can be also used to design Σ–Δ modulators for digital-to-analogue converter applications.

A GUI was created using MATLAB and the simulation models were designed in the Simulink environment given in Appendix B. The models could be easily developed in Simulink using block formats which can be controlled by MATLAB routines so that they could be used in conjunction with the GUI. The models are navigated by the parameters defined by the user through the GUI and the simulation results are displayed on the GUI panes. The user has the option to open, modify and obtain the simulation results from a menu which contains a selection of Σ–Δ modulator structures.

6.2 Σ–Δ Modulator Design Tool in Operation

In the first part, the user can select low-pass, band-pass or high-pass Σ–Δ modulators as shown in Figure 6-1.

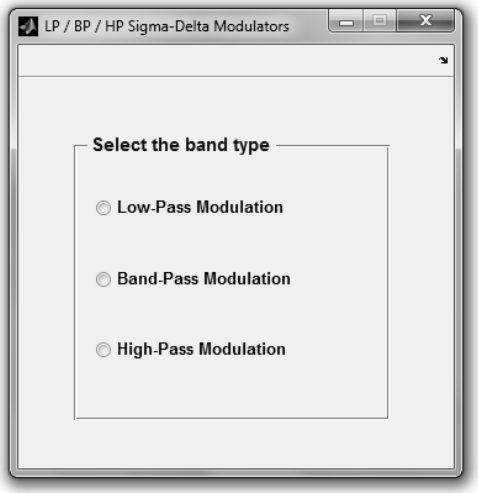

Figure 6-1 First step of the GUI for the options of the LP, BP or HP Σ–Δ modulators (screenshot)

In the second part of the GUI, for the chosen type of Σ–Δ modulator, the desired specifications can be defined in the parameters section.

Input Parameters: The desired specifications can be defined by the user such as: the number of samples, the amplitude, frequency and type of the input signal as well as the amplitude of the dither signal where appropriate. The GUI also allows the user to choose the order and the structure of the Σ–Δ modulator from a variety of design topologies such as single-stage, an assortment of MASH topologies, the chain of accumulators with weighted feedforward summation and chain of accumulators with feedforward summation with local resonator feedbacks. The MATLAB routines set the user-defined parameters to the Simulink models, run the simulation, analyze and display the simulation results and the corresponding modulator model.

Measurement Setup: The plots of the Σ–Δ modulator output spectrums, the corresponding NTFs, the PSDs and the histograms of the modulator outputs as well as the in-band SNR values are computed. The frequency spectrums are computed using the FFT of the corresponding signals, which are windowed with a Hanning window of the same length as the signal length. The FFT sample number is specified by the user in the parameter section, which is defined as 'the number of samples'. The SNR values are calculated for oversampling ratios (OSR) of 32, 64, 128, and 256, as well as other user defined ones. Moreover, for the power spectrum densities, the Welch averaging method is used. The associated overlap number is chosen as 2048 as default but can be modified as and when needed.

As shown in the flowchart of the GUI given in Figure 6-2, the user can define the specifications in order to design a variety of single-stage or multi-stage LP, BP and HP Σ–Δ modulators. Once the user determines the bandwidth of the modulator as LP, BP or HP, the simulation parameters can be chosen, which will be mapped to the corresponding simulink block parameters. The structures that can be obtained from the GUI are given in Appendix B. The simulation resulting from the chosen paramaters and Σ–Δ modulator are given in terms of SNR values and graphical plots. The GUI updates the frequency response of the output signal, the NTF and the input to the quantizer, as well as the in-band SNR values for each alteration that the user makes to the input parameters. Thus, the effects of small input changes can be easily observed at the output.

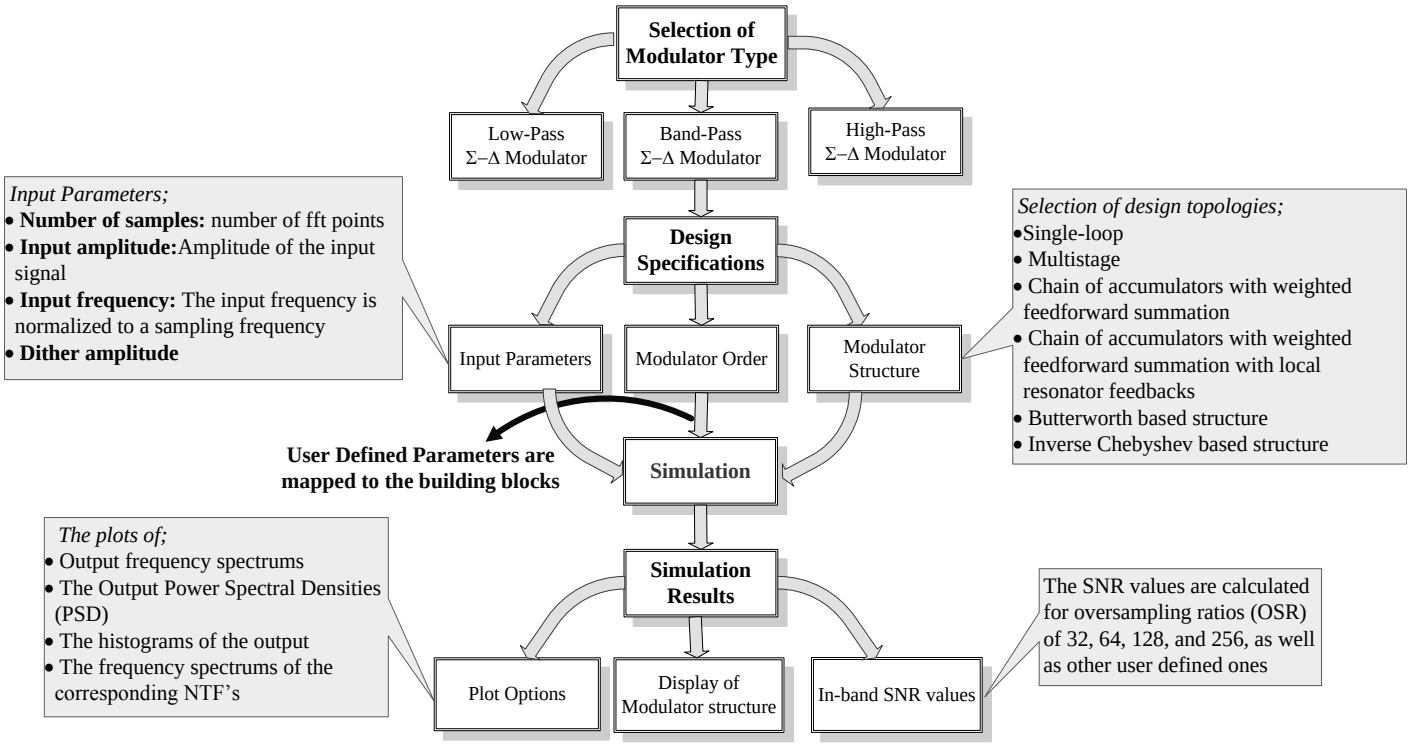

Figure 6-2 GUI flowchart

6.2.3 **Case-1: LP Σ–Δ Modulator**

In this section, the tool is explained through an example for a third-order low-pass Σ–Δ modulator using a multistage structure. The specified Σ–Δ modulator is simulated for an input amplitude signal of 0.5, a normalized frequency of 0.01 and a dither amplitude signal of 0.3. The mentioned parameters are directly set in the text-boxes in the Parameters section. In the Structure & Order Selection Section, the third-order cascaded (MASH) option is chosen.

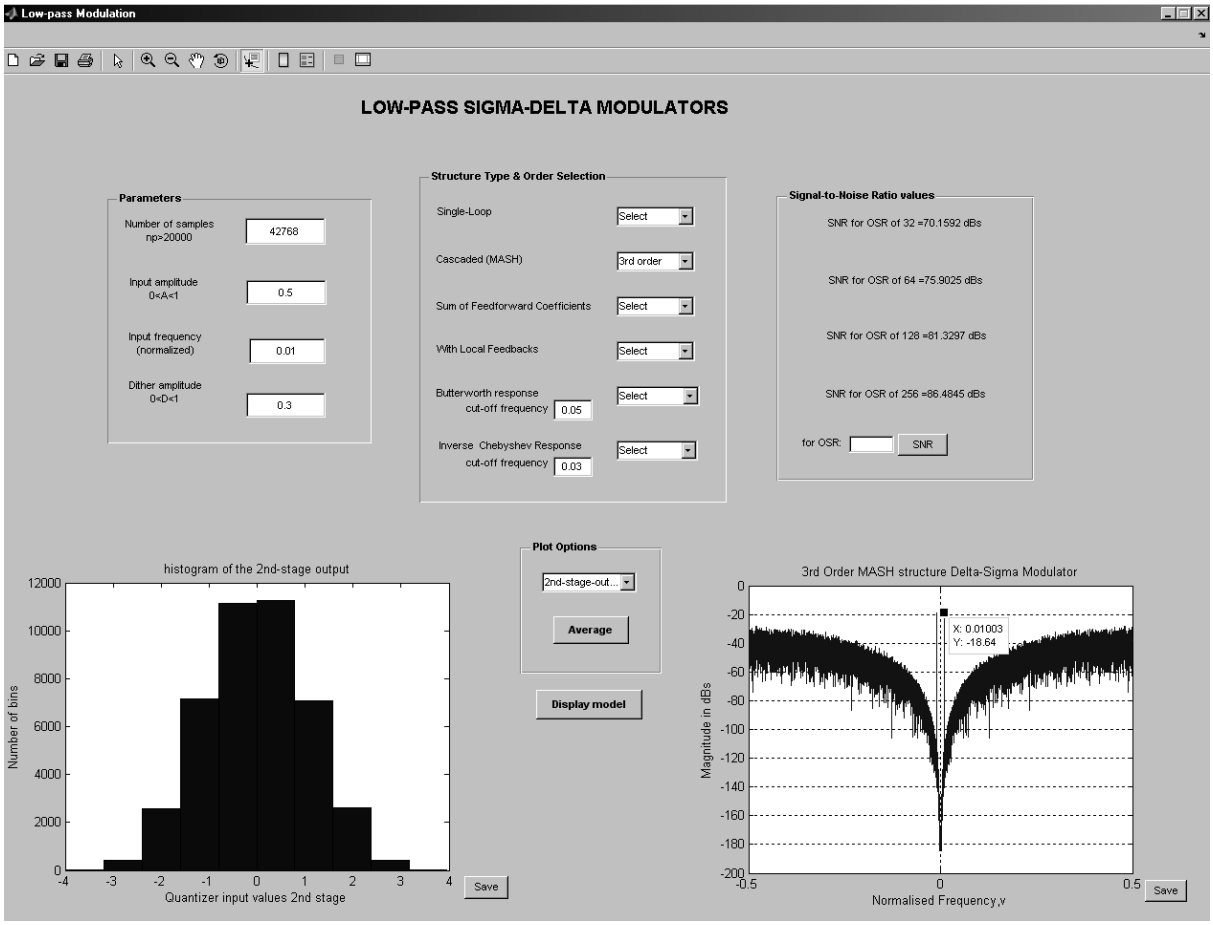

Figure 6-3 LP third-order MASH structure design and simulation

When in the 'Order and Structure Selection' section, the 3rd order Multistage (MASH) option is chosen as seen in Figure 6-3, the third-order cascaded LP Σ–Δ modulator is called via the MATLAB routines and the user-defined parameters are assigned to the SIMULINK model parameters given in Figure B-5 in Appendix B. The simulations of the histogram of the second-stage output, the Σ–Δ modulator output spectrum and the corresponding SNR values are all shown in Figure 6-3. The output spectrum in Figure 6-3 shows the input signal occurring at the correct frequency (0.01) and also shows spectral tones at lower frequencies. The Simulink model for the third-order modulator with variable parameters as shown in Figure B-5 is already created in the workspace, which is controlled by the GUI specifications. Using the option Display model, the corresponding structure can be displayed.

6.2.4 **Case-2: BP Σ–Δ Modulator**

As soon as the user selects the band-pass modulation option in the main window, the parameter-specification-window for BP Σ–Δ modulators will be displayed. A sixth-order mid-band band-pass Σ–Δ modulator using the chain of accumulators structure with weighted feedforward summation was also simulated for an input amplitude of 0.55, a normalized input frequency of 0.2 (mid-band), and a dither amplitude signal of 0.2. The NTF and the output spectrum are plotted. The corresponding simulation results are shown in Figure 6-4.

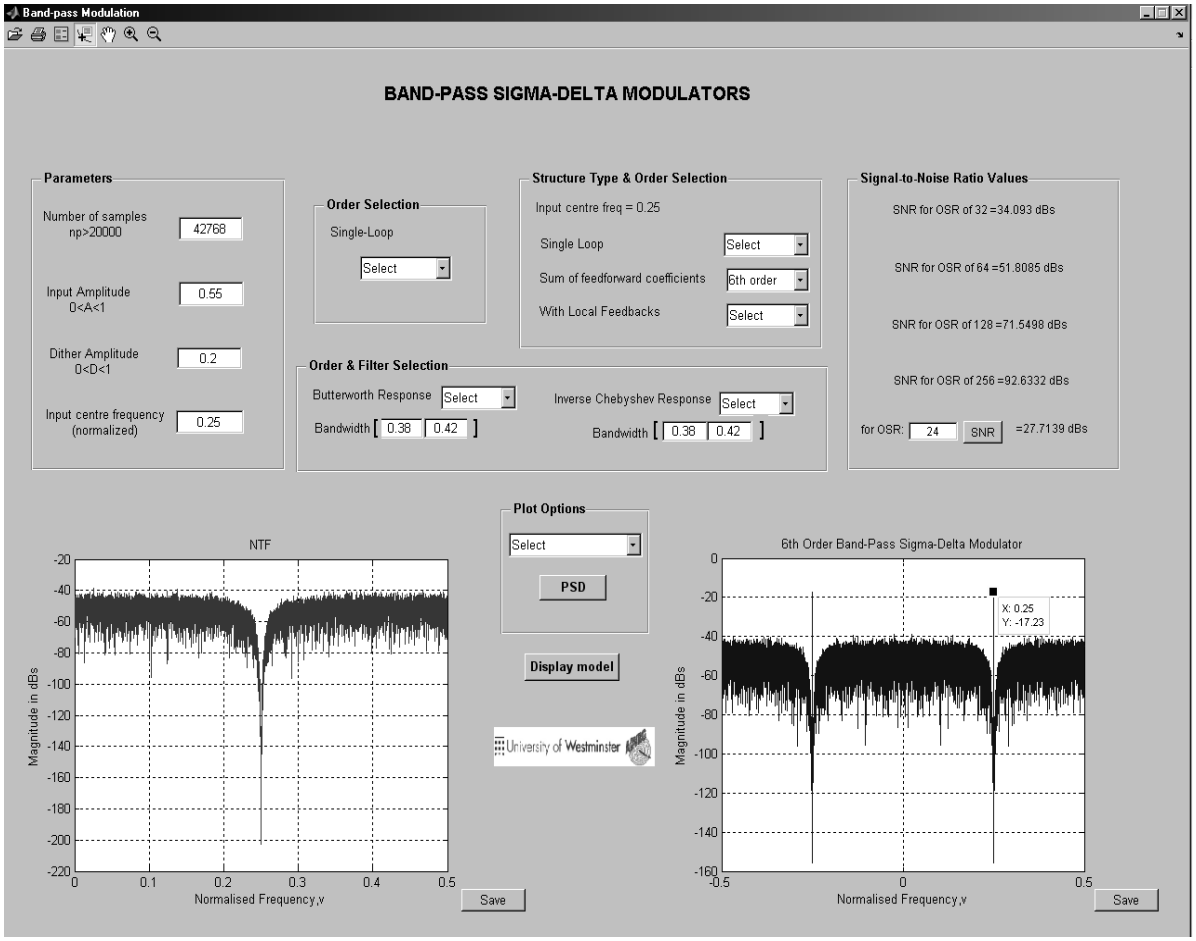

Figure 6-4 Screenshot of the GUI consisting of the input parameters and simulation results for sixth-order BP Σ–Δ Modulator

The corresponding structure of a sixth-order BP Σ–Δ modulator is given in Figure 6-5. Using the Butterworth approximation, the coefficients $a1$, $a2$ and $a3$ are calculated as -0.2512, 0.0306 and -0.0018 respectively.

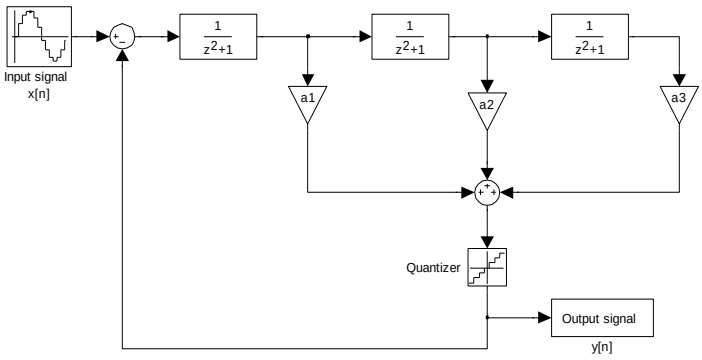

Figure 6-5 A sixth order mid-band BP Σ–Δ Modulator using chain of accumulators with weighted feedforward

Moreover, the tool allows the user to design the NTFs of Butterworth and Inverse Chebyshev filters based on input specifications such as the cut-off frequency, bandwidth and modulator order using the generic structure given in . The Butterworth filter or Inverse Chebyshev filter responses can be used to design higher-order BP Σ–Δ modulators, by adjusting the bandwidth of the filter according to the desired input signal frequency. The lower and upper frequencies of the NTF of the filters are selected so as to ensure that the input signal is positioned at the centre of the signal bandwidth. Figure 6-6 gives the simulation results for a 6th-order BP Σ–Δ modulator designed using the Butterworth filter. Since the input normalized frequency is 0.3, the bandwidth is chosen as [0.58-0.62]. The center of the bandwidth is twice as the input frequency (0.6), because of MATLABs routines for the NTF calculations. Furthermore, the upper and lower cut-off frequencies of the bandwidth should be symmetrical in relation to the centre frequency.

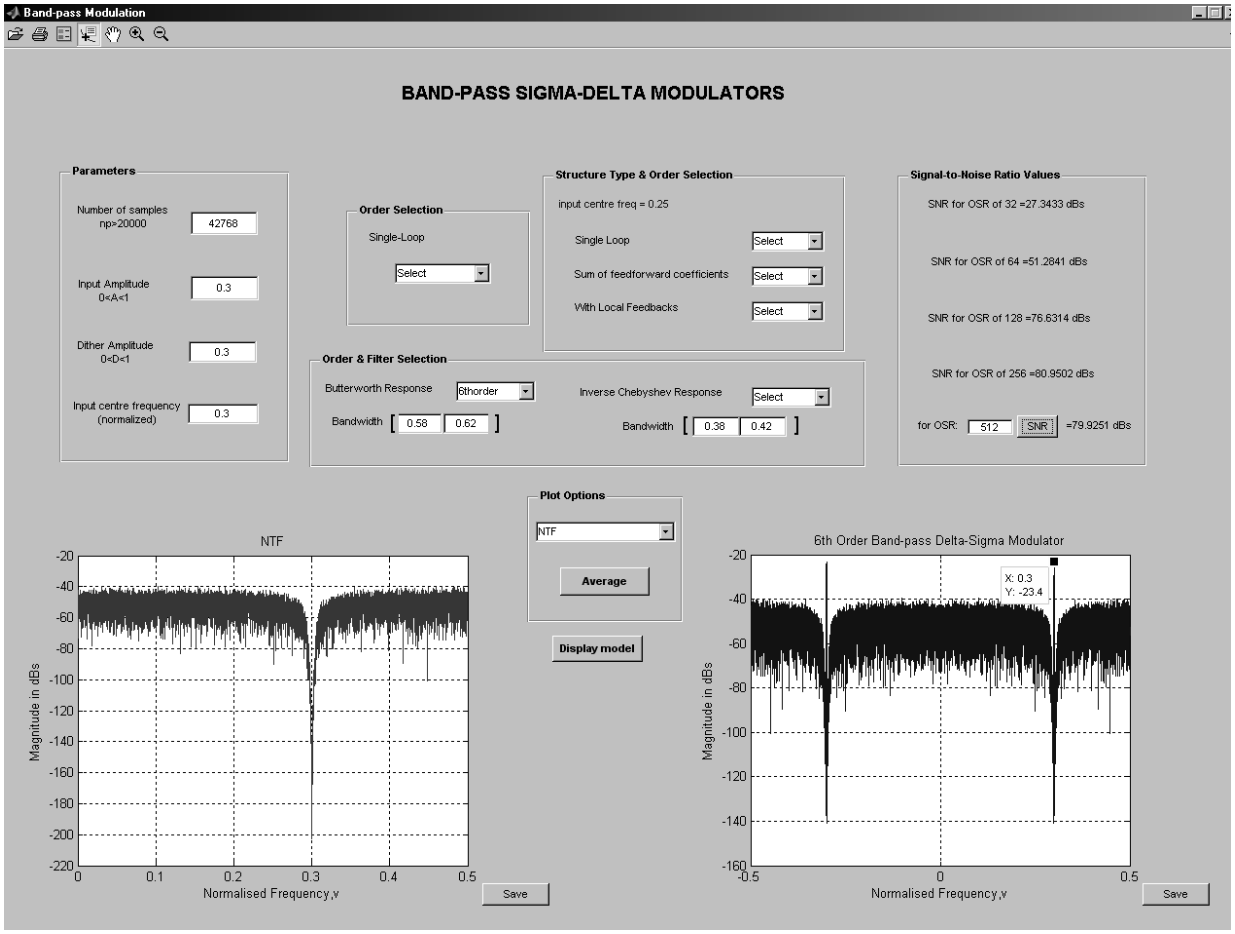

Figure 6-6 A sixth order BP Σ–Δ modulator simulation results displayed in GUI with a normalized of frequency 0.3

As seen in the examples, users can choose among different modulator structures and sinusoidal input signals. The GUI updates the frequency response of the output signal, the NTF and the output responses of different stages, as well as the SNR values for each alteration that the user makes to the input parameters. Thus, the effects of small input changes can be easily observed in the output.

6.2.5 **Case-3: HP Σ–Δ Modulator**

In the 'Σ–Δ Modulator Design Tool in Operation' section, the tool is explained through an example for a third-order HP Σ–Δ modulator using a 1-1-1 MASH structure. The specified Σ–Δ modulator is simulated for an input amplitude signal of 0.4, a normalized frequency of 0.499 and a dither amplitude signal of 0.3. All the simulations assume 10000

points for the transients. Thus, the total number of points chosen is 42768, which refers to 2^{15}+10000. The mentioned parameters are directly set in the Parameters section. In the 'Structure & Order Selection' section, the third-order 1-1-1 MASH option is chosen. The third-order HP Σ–Δ modulator is called via the MATLAB routines and the user-defined parameters are assigned to the already created Simulink model blocks. The simulations of the histogram of the Σ–Δ modulator output, the output spectrum and the corresponding SNR values are all shown in Figure 6-7.

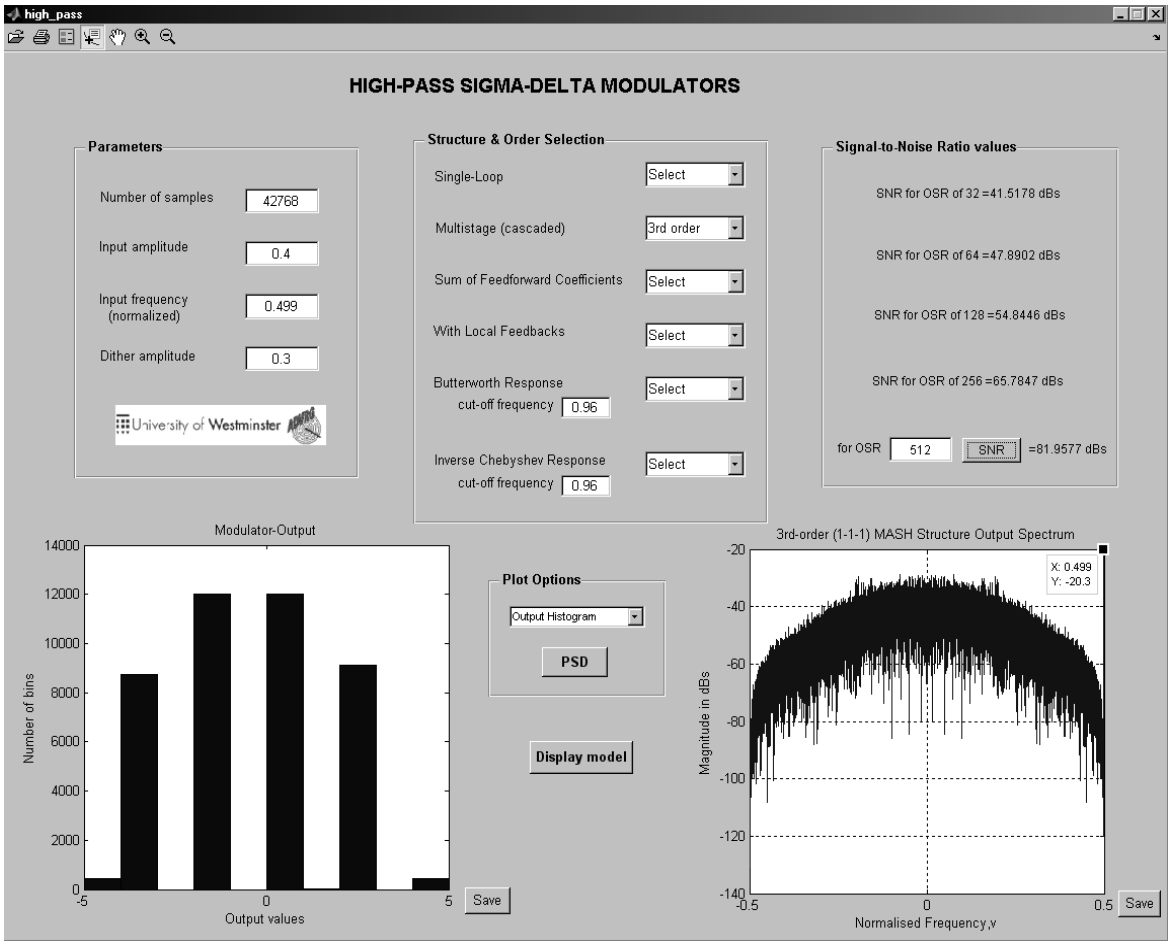

Figure 6-7 Screenshot of the GUI consisting of the input parameters and simulation results for a third order HP Σ–Δ Modulator

The output spectrum from Figure 6-7 shows the input signal at the correct frequency as well as the spectral tones at the lower frequencies. The resulting SNR values for OSRs of 32 and 256 are 41 dB and 65dB respectively. These show good agreement with the reported results in the open literature [Ral07], [Nyg06].

The Simulink model for a third-order HP Σ–Δ modulator using a 1-1-1 MASH structure is shown in Figure 6-8.

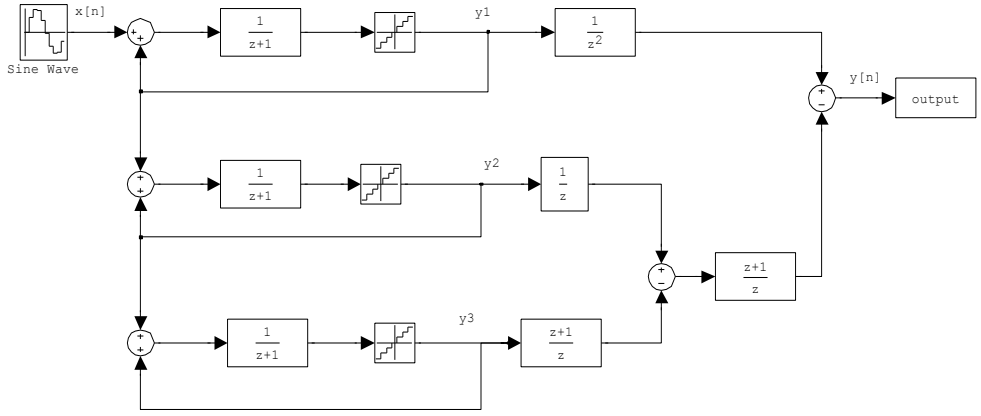

Figure 6-8 A Third order HP Σ–Δ Modulator using 1-1-1 MASH structure

The power spectral density of the output signal is computed using the Welch's averaged modified periodogram method of spectral estimation with 2048 overlaps. By averaging the output spectrum, the tones can be distinguished so that the Σ–Δ modulators performance can be analyzed more effectively. The averaged PSD of the output of the corresponding HP Σ–Δ modulator is plotted using the 'PSD' options in the GUI pane, as shown in Figure 6-9. The user can zoom in/out the plots and also save them to the desired file locations. The data cursor option provides the user simulation analyses and a comparison of the different output stages.

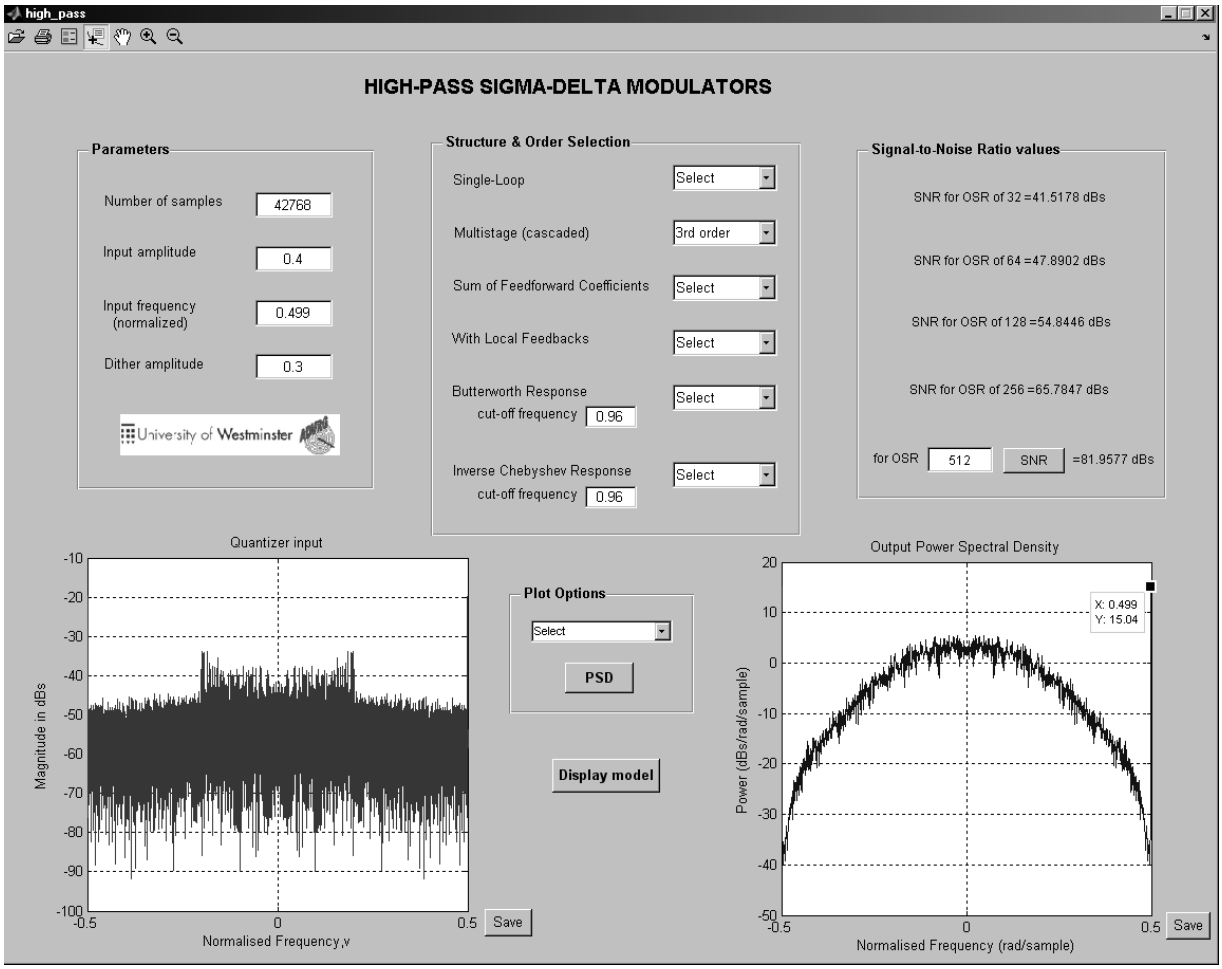

Figure 6-9 quantizer input (left) and the output PSD (right) plots of a third-order HP Σ–Δ Modulator

When the user changes the input signal parameters or the Σ–Δ modulator specifications according to the desired design structure, the simulation results are updated simultaneously.

As in the example above, the user can define the specifications in order to design a variety of single-loop or multi-stage LP, and BP Σ–Δ modulators.

6.3 Ultrasound Reconstruction Filters Analysis Tool

The GUI is extended to include the reconstruction stages of the ultrasound beamformers including a variety of decimation filters. Such a design and measurement tool for digital Σ–Δ beamformers has not been previously reported in the open literature to the best knowledge of the author. The MATLAB routines embedded in the GUI simulate the

desired reconstruction filters according to the input filter specifications defined by the user. The easy-to-implement tool of the Σ–Δ beamformer structures could be navigated by the user, which provides the user to analyse the reconstruction filter variations easily and fast. The reconstruction filter structures are given in Appendix C. The flowchart of the toolbox is shown in Figure 6-10.

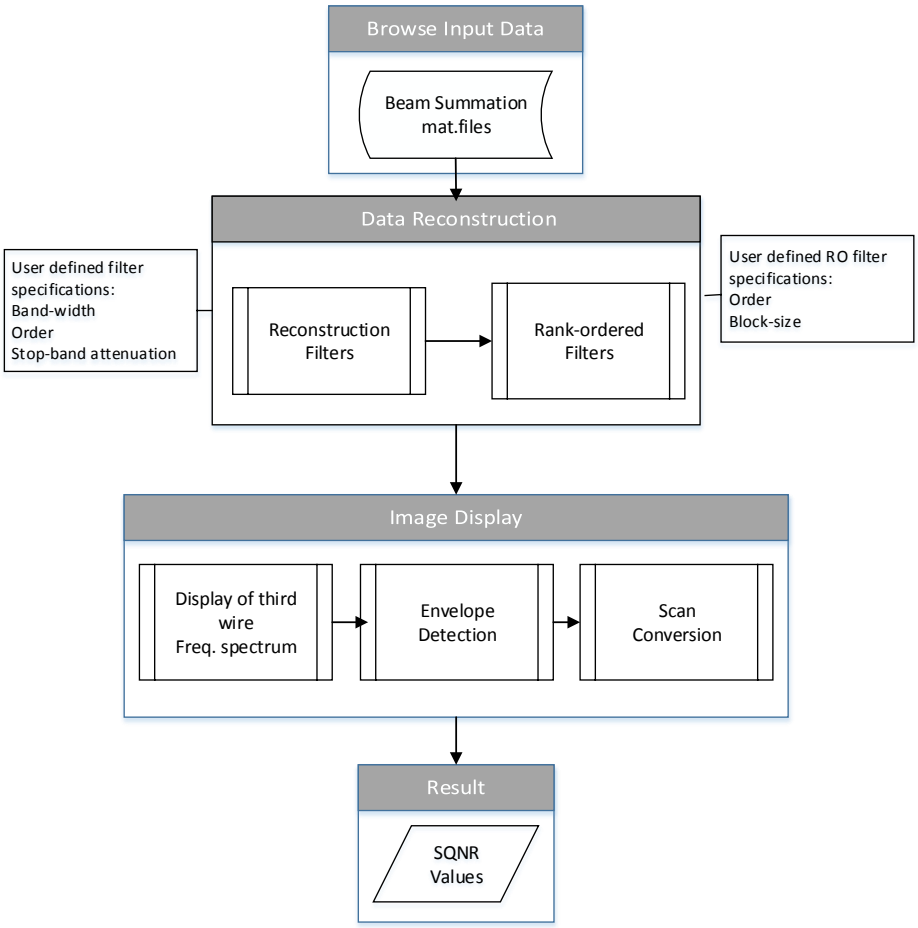

Figure 6-10 GUI for ultrasound reconstruction filters flowchart

As shown in the flowchart, in the first stage of the tool, the user needs to browse the wire- or cyst-phantom data corresponding to the beam summation, which is the echo signals modulated by the Σ–Δ beamformers, delayed-and-summed. The reconstruction toolbox is not working on raw-data sets. The six-wire raw data should be processed according to align-and sum process, and should be saved in an external file, which needs to be accessible via ultrasound toolbox. The desired reconstruction filter specifications can be then defined by the user such as the type of the decimation filter, the size and order of the rank-ordered filters.

The GUI allows also the user to choose the order and the structure of the decimation filters from a variety of design topologies such as the: LP and BP elliptic, Butterworth, Chebyshev Type-II, IIR filters, LP slink filters, LP and BP polyphase filters. The MATLAB routines set the user-defined parameters to the embedded codes, run the simulations, analyze and display the simulations.

The filter functions are written in MATLAB codes. The coefficients of the numerator and denominator (*a*'s and *b*'s) of IIR filters are obtained using [a b] = ellip(N,Rp,Rs,Wn); [a b] = cheby2(N, Rs, Wn); [a b] = butter(N, Wn), for elliptical- , Chebyshev-type-II and Butterworth-filter respectively, where *N* is the filter order, *Rs* is the stopband attenuation *Rp* is pass-band attenuation and *Wn* is the filter bandwidth. The user needs to enter the specifications for *N*, *Rs* and *Wn* (*Rp* for elliptical) in order to design the desired LP or BP decimation filter. Each 182 beam-line need to be filtered in a loop using the filtered_signal = filter(a,b,unfiltered_signal(:,beamline)')' before the envelope detection function. In order to apply adaptive filters, the order and the block-size of the rank-ordered filter need to be defined by the user. As described in Section 5.3.1 the block-size is optimum when it is equal to the maximum sample repetition rate during the dynamic focusing, which is 64. The polyphase filters are designed as explained in Sections 5.2.2 and 5.4.3

The plots of the response of the third wire output spectrums are shown in the same panel as soon as the user defines all the filter specifications and confirms by pressing 'OK'. The corresponding SQNR's, and the final B-scan images were computed. The tool is explained through an example for a Σ–Δ beamformer using an adaptive BP elliptic reconstruction filter. The simulations of the third wire and the resulting SQNR values are all shown in Figure 6-11. As soon as the user choose the 'display', the envelope detection function is called, the reconstructed image in the x-y coordinate before the scan conversion is displayed as shown in Figure 6-12. The 'display sector image' button calls the scan-conversion function and displays the final sector B-scan images in sector format.

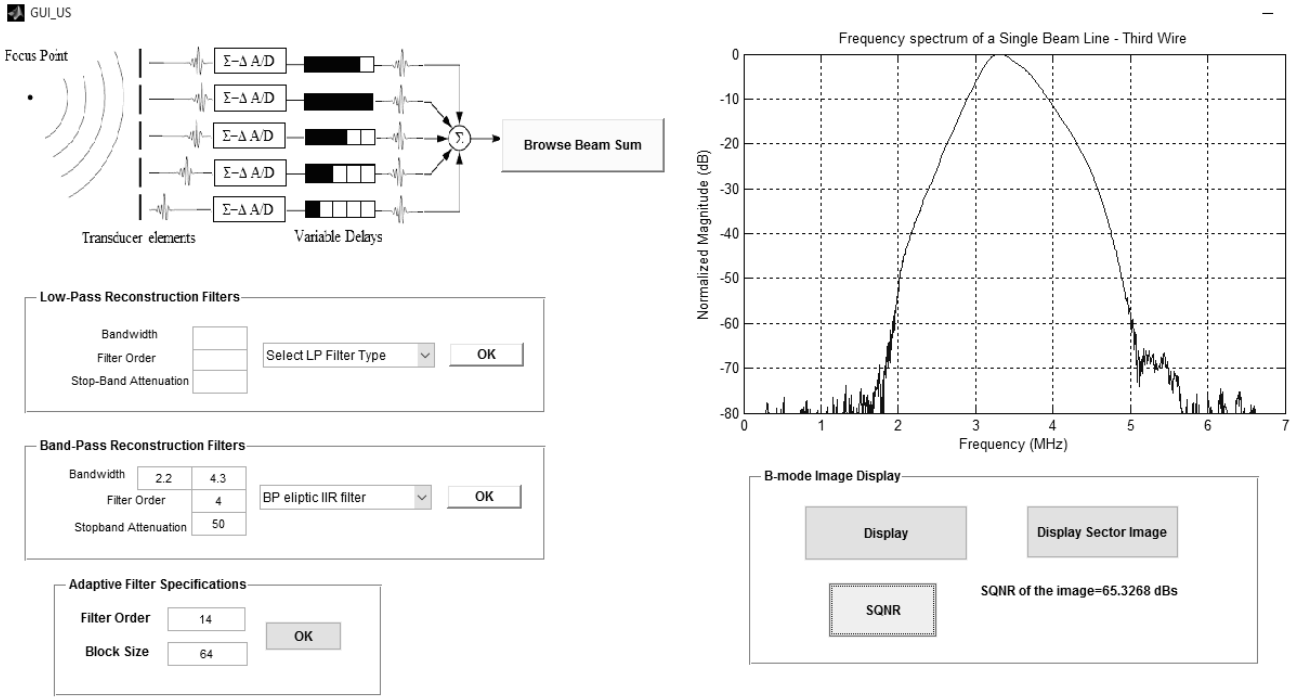

Figure 6-11 A Σ–Δ Beamformer employing adaptive Adaptive BP elliptic reconstruction filter

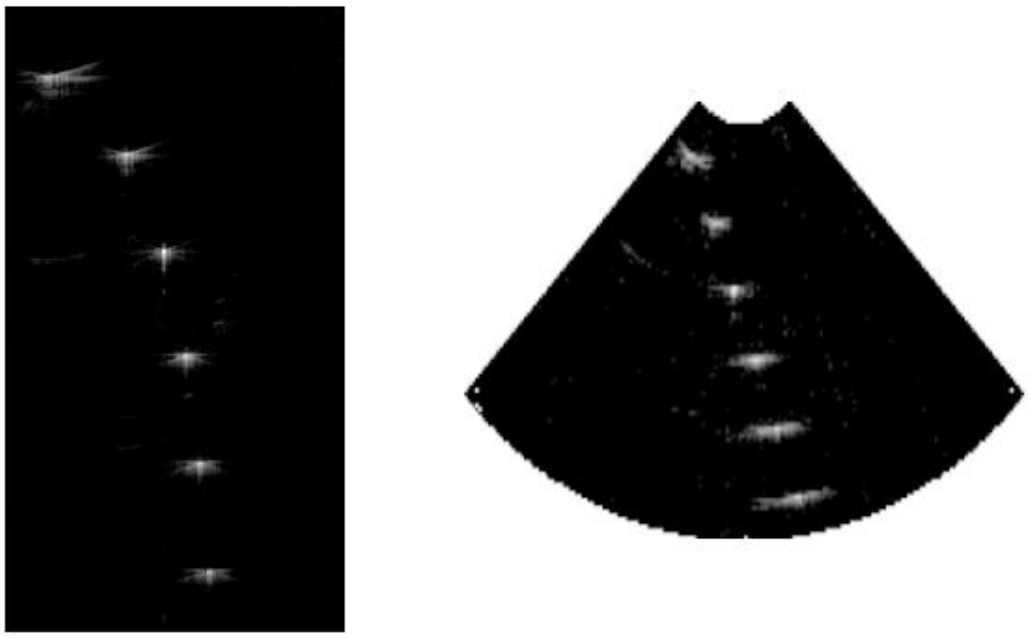

(a) (b)

Figure 6-12 (a) envelope detection, in cartesian coordinate (b) scan conversion in polar coordinates

The user can design a variety of decimation filters and compare their results using the frequency response of the third-wire or final B-scan images. The most-time consuming part is the rank-ordered filter section as it separates each beam line into blocks of size *s*. The RO filter algorithms are then applied to each block separately. However, the total time required for the whole reconstruction stage and the display of the images are less than 120sec depending on the order of the rank-ordered filter.

6.4 Concluding Remarks

A software design, evaluation and measurement tool in a MATLAB environment in conjunction with SIMULINK is developed to speed up the design, analysis and evaluation at the system-level of various easy-to-implement LP, BP and HP Σ–Δ modulators. The proposed modulator structural diagrams are given in Appendix B. The design and evaluation tool for HP Σ–Δ modulators is novel and has not been previously reported in the open literature. This tool is easy to use as it allows designers and practitioners to perform detailed simulations very easily. The MATLAB routines embedded in the GUI map the user-defined parameters into the building block specifications and display the simulation results in terms of the SNR values, histograms and power spectral densities. In addition, this practical, user friendly tool is further extended to evaluate and analyze ultrasound Σ–Δ beamformers in conjunction with a variety of reconstruction filters. The flexibility and relative ease of using MATLAB routines for the front-end, mid-end and the back-end stages of the ultrasound image acquisition stages will allow researchers and practitioners to design and verify the feasibility of Σ–Δ beamformer reconstruction filters at a much earlier stage of the design process, thus saving considerable time, effort and cost. This tool can be also used as a valuable teaching tool for advanced courses on data converters or digital ultrasound imaging.

Chapter 7

Conclusions

7.1 Thesis Summary:

Chapter 1 commenced with a brief history of the developments of Σ–Δ modulators and their diverse applications with an emphasis on biomedical imaging applications. A discussion addressing the advantages but also some of the problems associated with the design of ultrasound imaging systems that employ Σ–Δ modulators in their front-end-circuitries was presented. An extensive literature survey at the time showed that there was a considerable gap in digital ultrasound image reconstruction techniques that used relatively simple hardware circuits. This in conjunction with the continued demand for Σ–Δ modulators in state-of-art ultrasound imaging systems represented the prime motivation behind this work.

Chapter 2 started by reviewing the fundamental principles of Σ–Δ modulation and comparing their characteristics with those of Nyquist rate and conventional oversampling A/D converters. A detailed explanation of the operation of first- and higher-order single-stage and multi-stage LP Σ–Δ modulators, including the popular distributed feedback topologies was provided. This was followed by a system-level description as well as the

design and analysis of BP and HP Σ–Δ modulators. The LP-to-BP $(LP \rightarrow BP)$ frequency transformation was explained and analysed in order to design BP loop-filters for arbitrary normalised centre frequencies and bandwidths. In order to achieve simpler hardware, Σ–Δ modulators which employed special centre frequencies were designed and verified. Mid-band resonator based Σ–Δ modulators that utilized the $z^{-1} \rightarrow -z^{-2}$ transformation were designed and evaluated at the behavioural-level. This was followed by the design of easy-to-implement HP sigma-delta modulators·

Chapter 3 started by reviewing and analysing the stability problems of higher-order Σ–Δ modulators. An extensive literature survey has revealed a gap for the stability analysis of higher-order BP and HP Σ–Δ modulators. Based on the findings in chapter 2, the main source of the non-linearity was the one-bit quantizer in the feedback-loop. Therefore, this chapter presented the detailed non-linear analysis of higher-order HP- and BP Σ–Δ modulators using the describing function method in conjunction with quasi-linear modelling of the one-bit quantizer. The stability boundaries for single- and dual-sinusoidal inputs were determined.

In the quasilinear-model, the quantizer in a conventional Σ–Δ modulator is modelled by a gain factor *K*, followed by an additive white noise source. Since the quantization noise was found to depend on the value of *K*, this proposed model reflected the non-linear behaviour of Σ–Δ modulators. This quasilinear analysis was extended to HP- and BP-Σ–Δ modulators, by employing Butterworth- and Chebyshev Type-II filters with specified stopband attenuation and bandwidth for the desired NTF prototypes. The Σ–Δ modulator loop-filters were directly designed from these NTF prototypes by using MATLAB routines that were developed by the author. The closed-form mathematical expressions were derived for the stability curves for different quantizer gain values. According to the desired quantization noise attenuation, a variety of Butterworth and Chebyshev Type-II HP- and BP-filters and their resulting noise amplification curves that incorporated the variable K-values were investigated throughout this chapter. However, this quasi-linear model did not fully reflect the effect of the input signals on the Σ–Δ modulator outputs. Thus the quasi-linear model was further extended to a non-linear quabtizer by separating the Σ–Δ modulator as a signal model and a noise model using the describing function method.

The stability analysis for higher-order HP and BP Σ–Δ modulators for single- and dual-tone sinusoidal inputs was established using describing functions combined with the quasi-linear model. The quantization noise variances and the theoretical noise amplification curves for different input amplitudes, stop-band bandwidths, and stop-band attenuations were derived. Using these noise amplification curves, the maximum stable amplitude (MSA) limits for higher-order Butterworth- and Type-II Chebyshev-based HP and BP Σ–Δ modulators for different quantizer gain values, depending on the input amplitudes (for dual-sinusoidal inputs) were established. The theoretical results employing various BP and HP Σ–Δ modulators were discussed and presented in detail. These included the effects of varying the stop-band attenuation, bandwidth as well as the order of the modulator on the maximum stable amplitude limits of HP and BP Σ–Δ modulators. Furthermore, the comparison of Chebyshev-Type-II based Σ–Δ modulators with the Butterworth-based Σ–Δ modulators were examined in terms of the stability boundary limits. The theoretical results were verified via behaviour-level simulation results computed by specially designed routines in MATLAB in order to facilitate the computation of the coefficients for all the above designs. The theoretical results were shown to be in good agreement with the simulation results for a variety of input amplitudes, bandwidths, and modulator orders. Moreover, the reasons for the differences between the theoretical- and the simulated results were also analysed and provided in detail including the limitations of the quantization noise model, the tonality concept and the signal model for the dual sinusoidal inputs.

In Chapter 4, a detailed explanation of the operation of single-bit Σ–Δ modulators in the digital ultrasound beamformer systems together with the underlining advantages over multi-bit A/D converters was provided. A discussion addressing the hardware problems and image artefacts caused by Σ–Δ beamformers associated with the dynamic focusing concept was presented. This was followed by a chronological survey of reported publications, an up-to-date review of potential image artefacts suppression techniques and implementations of modified Σ–Δ beamformers. A detailed literature survey at the time showed that there was a considerable lack of artefact-free Σ–Δ beamformers with simple signal processing circuitries. These limitations coupled with the accelerating demand for easy-to-design, compact ultrasound systems provided ample justification for further development of conventional Σ–Δ beamformers. The search for alternative image reconstruction approaches that could deliver reduced image artefacts and therefore improved image quality was urgently needed.

The fundamental principles of digital ultrasound image acquisition employing digital phased arrays were provided and mathematically analysed. Guidelines to facilitate the design and behavioural-level simulations of the entire front-end, mid-end and back-end processes of the ultrasound system were given. These included dynamic beam focusing (beamforming), delay-and-sum, envelope detection, logarithmic compression and scan conversion. Routines in MATLAB were written in order to facilitate the computation of the entire image acquisition steps using the raw experimental ultrasound data acquired from the Ultrasonic Research Laboratory of the University of Michigan. The simulation approach and the performance criteria that were used for the evaluation of all beamformer structures were presented and explained in detail. These included the SQNR, CNR, lateral PSF and frequency spectrums especially for the third wire that corresponded to the fixed-focus point for the transmitted signals.

The image artefacts caused by conventional Σ–Δ beamformers were analysed. The B-scan sector images of the 6-wire phantom reconstructed by conventional single-bit Σ–Δ beamformers exposed SQNR values that were 11.53 dB lower compared to those obtained by 10-bit A/D beamformers. On the other hand, for the cyst phantom, the cyst detectability in the B-scan images reconstructed by Σ–Δ beamformers was reduced dramatically in comparison to the images obtained by 10-bit A/D beamformers. The simulation results demonstrated that the CNR values for the 1st-, 2nd-, and 3rd- cysts were 1.59, 0.61 and 1.02 different between the cyst images produced by the Σ–Δ beamformers and the 10-bit A/D beamformers. As in this work, the fixed transmit focal range was chosen to be 60 mm (the middle range of the scan area), the strongest reflector was the third wire (from the top) and 2nd cyst had the highest detectability as expected. Depending on the beamformer type, the incoming echo signals were digitized using either 10-bit A/D converters or single-bit Σ–Δ modulators, delayed and summed coherently to form the focus of interest. During this delay-and-sum process, a sample was selected from each array according to the predetermined time delay to compensate for the echo time difference. However, the delay updates to focus at closely spaced focus points caused some samples to be repeated and some of those to be omitted. For 10-bit A/D beamformers, these facts did not have any effects on the final reconstructed images. However, for the Σ–Δ modulators the repeated/skipped samples during the dynamic focusing caused the demodulator filter to interpret an extra sample, which actually did not exist. As a result of the degraded noise-shaping function of the Σ–Δ modulators, the quantization noise folded back to the signal band at the low-

frequencies. Therefore the main reason for these artefacts in the images obtained by conventional Σ–Δ beamformers directly related to the synchronization problem between the Σ–Δ modulator and the low-pass demodulator (decimation filter). It was verified that the conventional low-pass reconstruction filters were deemed to be insufficient to suppress the in-band noise level.

Based upon the above comments, a starting-point involved developing Band-Pass (BP) reconstruction filters for Σ–Δ beamformers in order to suppress the in-band noise level. IIR BP decimation filters including eighth-order Chebyshev Type-II, tenth-order Butterworth- and eighth-order elliptic filters with bandwidths close to the signal bandwidth were developed. The corresponding filter specifications and magnitude responses were provided. The IIR BP reconstruction stage was further developed and simplified by proposing polyphase BP reconstruction filters. The one-coefficient all-pass structure needed one multiplier, two adders and a small memory. Therefore all-pass sub-sections operating in polyphase structures provided greatly reduced hardware complexity of the overall IIR decimation filter structure. A practical step-by-step method for the design of the BP polyphase filters according to the desired filter specifications involving the prototype LP polyphase filter design and its LP-to-BP frequency transformation was presented in detail. The computed filter coefficients of the all-pass sections were given as well. The polyphase implementation of IIR filters as cascaded all-pass filters provided simplified hardware complexity of the standard implementation of IIR filters by halving the number of coefficients. The simulation results obtained by the proposed IIR- and polyphase BP filters were compared and analysed with those obtained by conventional Σ–Δ beamformers and 10-bit A/D beamformers. The frequency spectrum analyses of a single beam-line of the third wire produced by 10-bit A/D beamformers and Σ–Δ beamformers employing the proposed BP IIR filters as well as the BP polyphase filters showed at least 10dB noise suppression at the low-frequencies. On the other hand, the final B-scan images demonstrated that this BP reconstruction approach provided a 3.5dB increase for the entire image resolution of conventional Σ–Δ beamformers. In addition, the cyst phantom evaluations showed that the differences in the CNR values for the 1st-, 2nd-, and 3rd- cysts were reduced to 0.93, 0.23 and 0,59 compared to cysts images produced by the 10-bit A/D beamformers. The image artefacts were directly related to the sample delays, which were changing dynamically in order to focus the beams to a short-range distance. Therefore, as the focusing depth decreased, more samples were repeated which resulted in more quantization noise

accumulation at the low frequencies, which were also demonstrated via lateral PSF at different depths. Therefore, the noise levels for the focus points closer to the transducer (1st-wire, 1st cyst) were higher compared to the focus points away from the array system. Thus the BP reconstruction filters improved the overall image quality but were not dramatically sufficient to suppress the dynamically changing noise components in the signal-band.

A novel reconstruction technique which proposed the use of adaptive rank-ordered filters was developed to provide significant suppression of the dynamically changing, low-frequency noise components. In the rank ordered filter algorithm, the signal after the decimation filter was separated as sets of data, for which a change in the gradient was used to determine the threshold value to differentiate the signal from the noise components. As the threshold value for each set of data was varying dynamically, the cut-off frequency was adaptive for each signal beam line depending on the noise level. Therefore, the adaptive in-band noise level caused by dynamic focusing was eliminated successfully. The adaptive rank-ordered filters were applied at the output of the LP decimation filters, including a fourth-order elliptic IIR filter, three-stage slink filters and fifth-order polyphase filters. As the rank-ordered filters suppressed the noise at the low- as well as at the high-frequencies, the LP decimation filters did not need to be at high orders, which significantly provided simpler hardware complexity compared to conventional LP reconstruction filters. The simulation results showed that the adaptive LP slink-, polyphase- and elliptic reconstruction filters achieved SQNR improvements of 8.8 dB, 8.1 dB and 9.1dB, respectively. Compared to the equivalent elliptic filter implementation, the use of the polyphase structured all-pass sections halved the number of coefficients, thus significantly reducing the hardware complexity. On the other hand, slink filters further reduced the hardware complexity, while no multipliers and no storage for the filter coefficients were required.

This chapter culminated by establishing further novel improvements in the reconstruction stage by employing adaptive rank-ordered filters following the BP decimation filters. The rank-ordered filters eliminated the dynamically changing noise level in the signal-band especially for close ranges to the transducer, which were not totally filtered out by solely applying the BP decimation filters. The proposed BP IIR filters including Butterworth, Chebyshev Type-II and elliptic filters were examined. In addition, the hardware of the IIR reconstruction filters was further simplified by using polyphase structures. The B-scan wire and cyst phantom images verified that the Σ–Δ beamformers with the proposed adaptive BP elliptic- and polyphase reconstruction filters achieved almost

the same image quality compared with that produced by a 10-bit A/D beamformer (less than 1dB difference). The cyst detactability in terms of CNR values had no differences between the Σ–Δ beamformers employing adaptive BP elliptic reconstruction filters and the 10-bit A/D beamformers. On the other hand, Σ–Δ beamformers with the adaptive BP polyphase reconstruction filters exposed 0.1 less cyst detactability just for the 1st cyst. Detailed guidelines for the choice of decimation filters, coefficients as well as the hardware complexity were obtained and in combination with the simulation results presented in tabular form. The graphs and final B-scan images were provided which depicted the reconstruction filters performances including the signal-to-quantization-noise ratios, point-spread-functions, and dynamic ranges as well as the contrast-to-noise ratios.

Since the Σ–Δ beamformers did not require any hardware modifications in the modulator structure or in the delay-and-sum process, the advantages of the conventional Σ–Δ beamformers were completely persevered. In addition, since the image artefacts eliminated in the reconstruction stage and only a single adaptive reconstruction filter was required per beam sum, high quality B-scan images as the ones obtained by 10 bit A/D beamformers could be achieved with greatly reduced hardware complexity via polyphase structured reconstruction filters. Therefore, the proposed hardware efficient adaptive BP polyphase reconstruction filters would be suitable for use in Σ–Δ based beamformers for low-power 3-D scanners with a large channel count as well as portable, compact and lightweight ultrasound scanners and point-of-care applications and intravascular imaging systems.

In Chapter 5, a user-friendly design and performance evaluation tool for LP, BP and HP Σ–Δ modulators was developed in MATLAB by using an assortment of design methodologies and Σ–Δ modulator topologies. The toolbox was further modified by including the ultrasound image reconstruction steps, which included the reconstruction filter design, performance analysis in terms of the SQNR measurements and envelope detection as well as the image display in sector format. This user-friendly tool was designed to allow the user to design and verify a variety of reconstruction filters by analysing the results directly on the B-scan ultrasound images, thus saving considerable time and effort.

7.2 Novel Contributions:

- Novel ultrasound post-processing techniques for 1-bit Σ–Δ beamformers were developed. High quality images were obtained similar to the ones produced by 10-bit A/D beamformers, but with much simplifier hardware and signal processing complexity. The reconstruction methods proposed to reduce the image artefacts produced by Σ–Δ beamformers without any increase in hardware complexity. The novelty of this resolution improvement technique involved removing the noise components with new post-processing techniques in the reconstruction stage after the beam-sum without compromising the inherent advantages of Σ–Δ modulators and also by keeping the structures as simple as possible. This work has not been previously reported in the open literature to best the knowledge of the author.

- Stability boundaries of higher-order LP, BP and HP modulators for single and dual sinusoidal inputs are established by quasi-linear modelling of the quantizer. The maximum stable amplitude limits for higher-order BP and HP Σ–Δ modulators have not been reported in the open literature. In addition, as the ultrasound signals are damped sinusoidal signals, this quantizer model will help to design higher-order Σ–Δ beamformers.

- A novel GUI was created in order to provide a Σ–Δ modulator design and evaluation tool that covers the ultrasound post-processing stages. This tool enables practitioners to carry out performance analysis of B-scan images thus saving considerable time and effort.

7.3 Suggestions for Future Research

Based on the research study carried out and the theoretical and simulated results obtained thus far, the following research can be done as future work.

- To develop the proposed GUI to incorporate the modeling of non-idealities at the system-level as well as the stability and tonality indexes and other relevant metrics.

- To automate the decimation filters with rank-ordered filters according to the characteristics of the ultrasound echo signals.

- To apply non-linear theory in order to model the elevated noise at low frequencies more accurately, which would enable the automation of the rank-order filter parameters.

- To implement variable-band band-pass Σ–Δ beamformers in order to focus the array elements without dynamic focusing distortion.

References

[Ada86] Adams, R.W.; , "Design and Implementation of an Audio 18-Bit Analog-to-Digital Converter Using Oversampling Techniques," J. Audio Eng. Soc., vol. 34, pp. 153-166, Mar 1986

[Ada91] Adams, R.W.; Ferguson, P. F. ; Ganesan, A.; Vincelette, S.; Volpe, A.; Libert, R.; , "Theory and practical implementation of a fifth-order sigma-delta A/D converter" J. Audio Eng. Soc., vol.39, pp. 515-528, Jul 1991.

[Ada94] Adams, R.; ,"Design aspects of high-order delta-sigma A/D converters," IEEE Intemational Sym. on Circuits and Systems Tutorials, pp. 235- 259, 1994

[Ada98] Adams, R.; Nguyen, K.; Sweetland, K.; , "A 113 dB SNR Oversampling DAC with Segmented Noise-Shaped Scrambling, " ISSCC Digest of Technical Papers, vol. 41, pp. 62, 63, 1998

[Adl98] Adler, E.; Clark, J.; Conn, M.; , "Low cost enabling technology for multimode radar requirements", Proc. IEEE Radar Conference, pp. 50-55, May 1998

[Agr83] Agrawal, B.; Shenoi, K.; , "Design Methodology for Σ–Δ," IEEE Trans. on Commun., vol.31, no.3, pp. 360- 370, Mar 1983

[Ald07] Aldrich, J.E.; ,"Basic physics of ultrasound imaging", Crit. Care Med, Vol.35, N0.5, pp 131-137, 2007

[Ali08] Ali, M.; Magee, D.; Dasgupta, U.; , "Signal processing overview of ultrasound systems for medical imaging", Texas Instrument white paper, Nov 2008

[Alt09] Altinok, G.; Al-Janabi, M.; Kale,I.; , "A GUI driven Σ–Δ modulator design, evaluation and measurement tool with a view to practical implementation, IEEE Instrumentation and Measurement Conf., May 2009

[Alt10a] Altinok, G.; Al-Janabi, M.; Kale,I.;, "Stability predictions for higher-order band-pass Σ–Δ modulators for dual sinusoidal input", IEEE Instrumentation and Measurement Con., May 2010

[Alt10b] Altinok, G.; Al-Janabi, M.; Kale,I.; ,"A describing function based method for predicting the stability of higher-order high-pass Σ–Δ modulators", IEEE International Conference on Ph.D. Research in Microelectronics and Electronics, Jul 2010

[Alt11a] Altinok, G.; Al-Janabi, M.; Kale,I.; , "Stability Analysis of Band-Pass Sigma-Delta Modulators for Single and Dual Tone Sinusoidal Inputs", IEEE Trans. Instrumentations and Measurement, vol. 60, no.5, pp. 1546-1554, May 2011.

[Alt11b] Altinok, G.D.; Al-Janabi, M.; Kale, I.; , "Improved Ultrasound Digital Beamforming Using Single-Bit Sigma-Delta Modulators with Band-Pass Decimation Filters", IEEE International Symposium on Circuits and Systems 2011, May

[Alt11c] Altinok, G.D.; Al-Janabi, M.; Kale, I.; , "Improved Sigma-Delta Ultrasound Beamformers with Adaptive Low-Pass Decimation Filters", International Instrumentation and Measurement Conf., May 2011

[Alj00] Al-Janabi, M.; , "Design, analysis and evalution of bandpass sigma-delta modulation", PhD Thesis, University of Westminster, 2000

[Ana09] Analog Devices, AD9271 Data Sheet Rev B, May 2009

[Ard87] Ardalan, S.; Paulos, J.; , "An analysis of nonlinear behavior in delta - sigma modulators," IEEE Trans. on Circuits and Systems, vol.34, no.6, pp. 593- 603, Jun 1987

[Ath82] Atherton, D. P., "Nonlinear Control Engineering: Describing Function Analysis and Design" Van Nostrand Reinhold, pp. 383–388, 1982

[Azi96] Aziz, P.; Sorensen, H.; Spiegel, J.; , "An overview of sigma-delta converters", IEEE Signal Processing Mag., Vol.13, No.1, Jan 1996

[Baz95] Bazarjani, S.; Snelgrove, M.; "A 4th order SC bandpass Σ–Δ modulator designed on a digital CMOS process", 38th Midwest Symposium on Circuits and Systems, vol.2, pp. 1345-1348, Aug 1995.

[Ben48] Bennett, W.; ,"Spectra of quantized signals", Bell System Technical Journal, pp.446-472, July 1948

[Bil02] Bilge, H.S.; Karaman, M.; "Subarray delta-sigma beamforming for ultrasonic imaging," IEEE Ultrasonics Symposium, 2002. Proc., vol.2, no., pp. 1623- 1626 vol.2, 8-11 Oct 2002

[Bil03] Bilge, H.S.; "A Beamforming method based subarray processing with delta-sigma oversampling", PhD Thesis, Baskent University Department of Electrical and Electronics Engineering, 2003

[Bil10] Bilge, H.S.; "Delta-sigma subarray beamforming for ultrasonic imaging," Turk J Electronics eng. and Computer sci., vol.18, no.6, pp. 1003-1018, 2010

[Bry94] Bryant, J.M., "Bandpass sigma-delta ADCs for direct IF conversion", Analog Devices, pp.5.4.1-5.4.10, USA, 1994

[Bru02] Brunner,E.;, "Ultrasound System Considerations and their Impact on Front-End Components," Analog Devices, Inc., 2002

[Can74] Candy, J.C.;, "A Use of Limit Cycle Oscillations to Obtain Robust Analog-to-Digital Converters," IEEE Trans. on Commun., vol. 22, pp.298-305, Dec 1974

[Can81] Candy, J. C. ; Benjamin, O. J. ; , "The structure of quantization noise from sigma-delta modulation", IEEE Trans. on Commun., vol-29, No.9, September 1981

[Can85] Candy, J. C.; "A use of double integration in Sigma-Delta modulation", IEEE Trans. On Commun., vol.33, no.3, pp.249-258,March 1985

[Can92] Candy, J.; Temes, G.; , "Oversampling methods for AID and D/A conversion" in Oversampling Delta-Sigma Data Converters, pp. 1-25, IEEE Press, 1992

[Cha90] Chao, K.; Nadeem, S.; Lee, W.; Sodini, C.;, "A higher order topology for interpolative modulators for oversampling A/D converters," IEEE Trans. on Circuits and Systems, pp. 309-318, Mar, 1990.

[Che98] Cherry, J. A.; Snelgrove, W.M.; "Theory, practice, and fundamental performance limits of high-speed data conversion using continuous time delta-sigma modulators", PhD thesis, Carleton University, Canada, 1998.

[Che08a] Cheong, J.H.; Lam, Y.Y.H.; Kei Tee Tiew; Liang Mong Koh; , "Sigma-delta receive beamformer based on cascaded reconstruction for ultrasound imaging application", Ultrasonics, Ferroelectrics and Frequency Control, IEEE Transactions on , vol.55, no.9, pp.1935-1946, September 2008

[Che08b] Cheong, J.H.; Lam, Y.Y.H.; Liang Mong Koh; Kei Tee Tiew; , "Multi-bit sigma-delta beamformer with minimal dynamic focusing artifacts," IEEE International Conference on Electron Devices and Solid-State Circuits, vol., no., pp.1-4, 8-10 Dec. 2008

[Che09a] Chen, L.; Xu, R.; Yuan,J.; , "Efficient BScan-Sample-Based Σ-Δ Beamformer for Medical Ultrasound Imaging" IEEE Conf. on Biomedical Circuits and Systems, Nov. 2009

[Che09b] Cheraghi, P.; , "DSP based noise reduction system for audio applications", Project Thesis, University of Westminster, May 2009

[Che13] Chernyakova, T.; Eldar, Y.C.; Amit, R., "Fourier domain beamforming for medical ultrasound," Acoustics, Speech and Signal Processing, 2013 IEEE International Conf. pp.924,928, 26-31 May 2013

[Chi15] Chiou, J.; Chang, C.; Lee, s.; "Low-power and wide-dynamic-range sigma-delta modulator for an ECG acquisition system," International Symposium on Bioelectronics and Bioinformatics, Beijing, pp. 95-98, 2015.

[Chi78] Chivers, R. C.; Parry, R. J.;, "Ultrasonic velocity and attenuation in mammalian tissues", Acous. Soc. Am., vol.63, no.3, pp.940-953, Mar 1978

[Chi00] Chiang, A.M.; P. P. Chang, P.P; Broadstone, S. R. "PC-based ultrasound imaging system in a probe," Proc. IEEE Ultrason. Symp., pp. 1255–1260, 2000

[Chi09] Chih-Yuan, C., Rong-Guey, C., Jia-Hua, H., Shuenn-Yuh, L.: 'Stability analysis and system design of sigma–delta-modulators'. Proc. Int. Symp. on Integrated Circuits, pp. 9–12, Dec 2009

[Chu97] Chuang, S.; Yu, X.; Sculley, T., Bamberger, R. "Design and implementation of a sixth-order bandpass delta-sigma A/D converter with single quantiser", International Symposium on Circuits and Systems, vol. I, Hong Kong, pp. 381- 384, Jun 1997

[Chu07] Chung-Ming Hsieh; Hung-Wei Chiu; , "Sigma Delta Modulator Design Automation,"

ICCCAS, pp.1034-1038, July 2007

[Coa01] Coatney, R.W.; , "Ultrasound Imaging: Principles and Applications in Rodent Research" Ilar Journal, 2001

[Con70] Constantinides, A.; "Spectral transformations for digital filters", Proc. IEE,pp. 1585-1590, 1970

[Cut52] Cutler, C.C.; "Differential quantization of communication signals," U.S. Patent 2,605,361, Jul 1952

[Cut60] Cutler, C.C;, "Transmission Systems Employing Quantization," U.S. patent 2,927,962 , Mar 1960

[Deg06] Degertekin, F.L.; Guldiken, R.O.; Karaman, M;, "Annular-ring CMUT arrays for forward-looking IVUS: transducer characterization and imaging," IEEE Trans. Ultrason., Ferroelect., Freq. Contr., vol. 53, pp. 474-482, Feb. 2006

[Del46] Deloraine, E. M.; Van Mierlo, S.; Derjavitch, B. ; , "Methode et systéme de transmission par impulsions," French Patent 932,140, issued Aug, 1946, (British Patent 627,262, issued 1949)

[Del53] Deloraine, E. M.; Van Mierlo, S.; Derjavitch, B. ; , "Communication System Utilizing Constant Amplitude Pulses of Opposite Polarities," U.S. Patent 2,629,857, filed Oct 1947, (issued Feb 1953)

[Eyn91] Eynde, F.; Yin, G.; Sansen, W.; , "A CMOS fourth-order 14b 500k-samples/s sigma-delta ADC converter," Digest of Technical Papers, International Solid State Circuits Conference, pp. 62-63, 1991

[Erg99] Ergelen, J.V.; Plassche, R.; , "Bandpass Sigma Delta Modulators", Kluwer academic Publishers, Boston, 1999

[Far98] Farrell, R.; Feely, O.; , "Bounding the integrator outputs of second-order sigma-delta modulators," IEEE Trans. on Circuits and Systems II: Analog and Digital Signal Processing, vol.45, no.6, pp.691-702, Jun 1998

[Fee95] Feely, O.; ,"Nonlinear dynamics of bandpass sigma-delta modulation", Proc of the Third International workshop on nonlinear dynamics of electronic systems, Jul 1995

[Fee96] Feely, O.; Fitzgerald, D.; , "Bandpass sigma-delta modulation-an analysis from the perspective of nonlinear dynamics," IEEE International Symposium on Circuits and Systems, vol.3, no., pp.146-149 vol.3, May 1996

[Fee97] Feely, O.;, "A tutorial introduction to non-linear dynamics and chaos and their application to sigma–delta modulators," Int. J. Circuit Theory Appl., vol. 25, pp. 347–367, 1997.

[Fen96] Fenster, A.; Downey, D.B.; , "3-D ultrasound imaging: a review," IEEE Engineering in Medicine and Biology Magazine, vol.15, no.6, pp.41-51, Dec 1996

[Fer90] Ferguson, P.F.; Ganesan, A.; Adams, R.W.; , "One bit higher order sigma-delta A/D converters" IEEE International Symposium on Circuits and Systems, vol 2, pp. 890-893,

May 1990

[Fer91] Ferguson, P.; Ganesan, A.; Adams, R.; , "An 18-Bit 20-kHz Dual Sigma-Delta A/D Converter," ISSCC Digest of Technical Papers, Feb 1991

[Fra00] Francken, K.; Vancorenland,P.; Gielen, G.; ,"DAISY: A simulation-based high-level synthesis tool for Σ–Δ modulators," Proc. IEEE Int. Conf. Computer-Aided Design, pp. 188–192, 2000

[Fra02] Fraser, N.A.; Nowrouzian, B.; "A novel technique to estimate the statistical properties of sigma–delta A/D converters for the investigation of DC stability". Proc. IEEE International Symposium on Circuits and Systems, 02, vol. 3, pp. 111-289–111-292, May 2002

[Fre97] Freeman, S.R.; Quick, M.K.; Morin, M.A.; Anderson, R.C.; Desilets, C.S.; Linnenbrink, T.E.; O'Donnell, M.; , "An ultrasound beamformer using oversampling," IEEE Proceedings of Ultrasonics symposium, pp. 1687-,1690,1997

[Fre98] Freeman, S.R.; Quick, M.K.; Morin, M.A.; Anderson, R.C.; Desilets, C.S.; Linnenbrink, T.E.; O'Donnell, M.; , "Efficient, high-performance ultrasound beamforming using oversampling " Proceedings of SPIA: Medical Imaging, 3341: pp. 220-227,1998

[Fre99] Freeman, S.R.; Quick, M.K.; Morin, M.A.; Anderson, R.C.; Desilets, C.S.; Linnenbrink, T.E.; O'Donnell, M.; , "Delta-sigma oversampled ultrasound beamformer with dynamic delays ," IEEE Trans. on Ultrasonics, Ferroelectrics and Frequency Control, vol.46, no.2, pp.320-332, Mar 1999

[Fri88] Friedman, V.; "The structure of the limit cycles in sigma-delta modulation", IEEE Trans. on Commun., vol.36, pp. 972-979. Aug 1988

[Gai89] Gailus, P.H.; Turney, W.J.; Yester, F.R.;, "Method and Arrangement for a Sigma Delta Converter for Bandpass Signals," U.S. Patent 4,857,928, Aug, 1989

[Gou94] Gourgue, F.; Bellanger, M.; "A bandpass subsampled delta-sigma modulator for narrowband cellular mobile communications", International Symposium on Circuits and Systems, vol. 5, pp. 353-356, May 1994.

[Gel68] Gelb, A.; Vander Velde, W.E.; , "Multiple-input Describing functions and non-linear system design", New York McGraw-Hill, 1968

[Ger89] Gerzon, M. ; Craven P.G.; , "Optimal noise shaping and dither of signals", Proc. 87th AES Convention, Oct 1989

[Gil07] Gill, E. A. ; Klas, B.; ,"Three-dimensional echocardiography: an historical perspective," Cardiology Clinics, Vol. 25, No. 2, pp. 221-229, May 2007

[Goo69] Goodman, D.J.; "The Application of Delta Modulation of Analog-to-PCM Encoding," Bell System Technical Journal, Vol. 48, pp. 321-343. Feb 1969

[Goo95] Goodson, M.; Bo Zhang; Schreier, R.; , "Proving stability of delta-sigma modulators using invariant sets ,", IEEE International Symposium on Circuits and Systems, vol.1, no., pp.633-636 vol.1, May 1995

[Gra90] Gray, R.; , "Quantization noise spectra" IEEE Trans. on Information Theory, pp. 1220-1244, Nov, 1990

[Gur08] Gurun, G.; Qureshi, M.S.; Balantekin, M.; Guldiken, R.; Zahorian, J.; Peng, S.Y.; Basu, A.; Karaman, M.; Hasler, P.; Degertekin, F.L.;, "Front-end CMOS electronics for monolithic integration with CMUT arrays: Circuit design and initial experimental results," in IEEE Ultrasonics Symposium, 2008

[Had75] Haddad, A.H., "Nonlinear systems", benchmark papers in electrical engineering and computer science, vol. 10, Dowden, Hutchinson & Ross, Inc and Halsted Press, page 197, 1975.

[Hag02] Haghighat, A. ; "A Review and technical challenges of software defined radio", Proc. MILCOM, vol.1, pp.377-382, Oct 2002

[Han02] Han, H.S. ; Park, H.J., Song, T.K.; , " A new architecture for ultrasound Sigma-Delta Modulation beamformer," IEEE Ultrasonics Symposium , pp. 1631-1634

[Han04] Han, H.S. ; Song, T.K.; , "Multiplierless sigma-delta modulation beam forming for ultrasound nondestructive testing," Key Engineering Materials, vol. 270 - 273, no., pp. 215 - 220, May 2004.

[Han06] Han, H.S.; Song, T.K.; Kim, B.H.; Kim, H.H.; ,"Error-Free Pulse Compression Method for Ultrasound Beamforming Using Sigma-Delta Modulation," in IEEE Ultrasonics Symposium , pp. 2140-2143, 2006

[Har91] Harris, F.J.; D'oreye de Lantremange, M; Constantinides, A.G.;, 'Digital Signal Processing with Efficient polyphase Recursive All-Pass Filters', Int. Conf. on Signal Processing, Florence, Italy, 4-6 Sep 1991.

[Hau91] Hauser, M.W.; , "Principles of Oversampling A/D Conversion," Journal Audio Engineering Society, Vol. 39, No. 1/2, pp. 3-26 „Jan/Feb 1991

[Hav79] Havlice, J.F.; Taenzer J.C.; , "Medical Ultrasonic Imaging: An Overview of Principles and Instrumentation," Proceedings of the IEEE, Vol. 67, No. 4, pp. 620-640, Apr 1979

[Hei92] Hein, S.; Zakhor, A.; , "Stability and scaling of double loop ΣΔ modulators," International Symposium on Circuits and Systems, vol.3, no., pp.1312-1315 vol.3, May 1992

[Hei93] Hein, S.; Zakhor, A.;, "On the stability of sigma delta modulators", IEEE Trans. Int. Sysmp. Circuits Sys., vol.2, pp: 2322-2348, Jul 1993

[Hem15] Hemsenn, M., Stuart, M., M., Tomov, Jensen, J.; "Ultrasound imaging probe with sigma-delta beamformer and apodization therein", Patent US 2015/0340023 A1, Nov 2015

[Hen01] Hendriks, P.; Schreier, R.; DiPilato, J.; "High Performance Narrowband Receiver Design Simplified by IF Digitizing Subsystem in LQFP," Analog Dialogue, Vol. 35-3, Jul 2001.

[Hog81] Hogenauer, E. B.; "An economical class of digital filters for decimation and interpolation." IEEE Transactions on Acoustics, Speech and Signal Processing, ASSP-29(2):155-162, 1981

[Hon92] Hongmo, W.; , "A geometric view of sigma-delta modulation", IEEE transactions on circuits and systems-II, vol. 39, issue 6, pp. 402-405, Jun 1992

[Hou03] Houser, D.; Martin, S.; Bauer, E.; Herrin, T.; Moore, P.; , "Signal processing applied to the dolphin based sonar system", proc. Oceans, vol.1, pp. 292-303, 2003

[Hwa98] Hwang, J.; Quistgaard, J.; Souquet, J.; Crum, L. A.; ,"Portable ultrasound devive for battlefield trauma", Proceedings IEEE Ultrasound symposium, pp. 1663-1667, 1998

[Ine02] Inerfield, M.; Lockwood, G.R.; Garverick, S.L., "A sigma-delta-based sparse synthetic aperture beamformer for real-time Σ–Δ ultrasound," Ultrasonics, Ferroelectrics, and Frequency Control, IEEE Transactions on , vol.49, no.2, pp.243,254, Feb. 2002

[Ino62] Inose, H.; Yasuda, Y.; Murakami, J.;, "A Telemetering System by Code Modulation-Δ–Σ Modulation," IRE Trans. Space Electron. Telem.,vol. 8, pp. 204-209, Sep 1962

[Ino63] Inose, H.; Yasuda, Y.; , "A Unity Bit Coding Method by Negative Feedback," Proc. IEEE, vol.51, pp. 1524-1535, Nov 1963

[Int10] Intersil, HI5746 Data Sheet Rev B Jul 2010

[Ish03] Ishida, K.; Fujishima, M.; , "Chopper-stabilized highpass sigma-delta modulator utilizing a resonator structure", IEEE Trans. on Circuits and Systems–II: Analog and Digital Signal Processing, Sep 2003

[Jan91] Jantzi, S.; Schreier, R.; Snelgrove, M.;, "Bandpass sigma-delta analogto-digital conversion," IEEE Transactions On Circuits and Systems, pp. 1406-1409, Nov, 1991.

[Jan93] Jantzi, S.A.; Snelgrove, M.; Ferguson, P.F.;, "A 4th-Order Bandpass Sigma-Delta Modulator," IEEE Journal of Solid State Circuits, Vol. 38, No. 3, pp. 282-291, Mar 1993

[Jan94] Jantzi, S.; Ouslis, C.; Sedra, A.; "Transfer function design for Σ–Δ converters," IEEE Proc. ISCAS, pp. 433-436, May 1994.

[Jen13] Jensen, J.A.; Holten-Lund, H.; Nilsson, R.T.; Hansen, M.; Larsen, U.D.; Domsten, R.P.; Tomov, B.G.; Stuart, M.B.; Nikolov, S.I.; Pihl, M.J.; Yigang Du; Rasmussen, J.H.; Rasmussen, M.F., "SARUS: A synthetic aperture real-time ultrasound system," IEEE Ultrasonics, Ferroelectrics, and Frequency Control , vol.60, pp.1838-1852, Sep. 2013

[Jeo07] Jeong, C.; Jun-Young L.; Jae-hee, S.,; Younglok, K.; Tai-Kyong S., , "A fractional filter-based beamformer architecture using postfiltering approach to minimize hardware complexity," IEEE Trans. Ultrasonics, Ferroelectrics, and Frequency Control, vol.54, no.5, pp.1076-1079, May 2007

[Joh93] Johnson, D. H.; Dudgeon, D. E.; , " Array signal processing", Prentice-Hall, Newyork, 1993

[Jun13] Jung, Y.; Hyungdong Roh; Jeongjin Roh, "An Input-Feedforward Multibit Adder-Less Delta-Sigma Modulator for Ultrasound Imaging Systems," IEEE Trans. Instrumentation and Measurement, vol.62, no.8, pp.2215,2227, Aug. 2013

[Kal96] Kale, I., "Sigma-delta modulation and polyphase filtering - the key to high-fidelity data conversion and instrumentation", IMEKO TC4 Workshop:ADC Modelling, Smolenice

Castle, Slovak Republic, pp. 183-192, 7-9 May 1996

[Kal94] Kale, I.; Morling, C.S. ; Krukowski, A.; Devine, D.A.; , 'A high fidelity decimation filter for sigma-delta A/D converters', IEE Second international conf. on advance A-D and D-A conversion techniques and their applications, no. 393, pp.30-35, Jul 1994

[Kan14] Kang, K.; Stubberud, P.; ' A comparison of continuous time sigma delta modulator simulation methods', IEEE International Midwest Symposium on Circuits and Systems, 2014

[Kan15] Kang, K.; Stubberud, P.; 'Stability Analysis of Continuous Time Sigma Delta Modulators' , publisher Springer, Progress in Systems Engineering, pp.487-493,2015

[Kar95] Karaman, M.; Pai-Chi Li; O'Donnell, M.; , "Synthetic aperture imaging for small scale systems," IEEE Transactions on Ultrasonics, Ferroelectrics and Frequency Control, vol.42, no.3, pp.429-442, May 1995

[Kar98] Karaman, M.; O'Donnell, M.; , "Subaperture processing for ultrasound imaging," IEEE Transactions on Ultrasonics, Ferroelectrics and Frequency Control, 45(1), pp. 126-135, Jan 1998

[Kar99] Karaman, M.; Kozak, M.; , "Digital beamforming using nonuniform oversampling delta-sigma conversion," IEEE Ultrason. Symp., vol. 2, pp. 1279–1282, Oct. 1999.

[Kar00] Karaman, M. and M. Kozak, "An asynchronous oversampling beamformer", WIPO PCT Patent, WO 0010638, March 2000

[Ken88] Kenney, J.G.; Carley, L.R.; , "CLANS: a high-level synthesis tool for high resolution data converters," IEEE International Conference on Computer-Aided Design, Digest of Technical Papers., vol., no., pp.496-499, Nov 1988

[Kes08a] Kester, W.; , "ADC Architectures III: Sigma-Delta ADC Basics", Analog Devices, Tutorial MT-022, Oct 2008

[Kes08b] Kester, W.; , "ADC Architectures IV: Sigma-Delta ADC Advanced Concepts and Applications", Analog Devices, Tutorial MT-023, Oct 2008

[Kim07] Kim, S., Joeres, S.; Zimmermann, N.; Robbens, M.; Wunderlich, R.; Heinen, S.; "Continuous-Time quadrature bandpass sigma-delta modulator for GPS/Galilelo Low-IF Receiver", IEEE International Workhop on Radio Frequency Integration Technology, Singapore, Dec 2007.

[Kin62] Kinsler, L.E.; Frey, A, R.; , "Fundamentals of Acoustics", New York, Wiley, 1962.

[Kin87] Kino, G.; , "Acoustic waves", Prentice Hall, Newyork, 1987

[Kri97] Krishnan, S., "Ultrasound RF data set wire cbb," University of Michigan, MI., Dec. 1997[Online] http://bul.eecs.umich.edu/research/sriramk/wire_cbb.shtml, last visit May 2008

[Koz01] Kozak, M.; Karaman, M.; , "Digital phased array beamforming using single-bit delta-sigma conversion with non-uniform oversampling," , IEEE Trans. on Ultrasonics, Ferroelectrics and Frequency Control, vol.48, no.4, pp.922-931, Jul 2001

[Koz03] Kozak, M.; Kale, I.; , "Oversampled delta-sigma modulators: analysis, applications and novel topologies", Kluwer Academic Publishers, Boston 2003

[Kri13] Krieger, J. D. ; Yeang, C. P. ; Wornell, G. W. ; "Dense Delta-Sigma Phased Arrays," in IEEE Transactions on Antennas and Propagation, vol. 61, no. 4, pp. 1825-1837, April 2013.

[Kru03] Krukowski,A.; Kale, I.; ," DSP system design: complexity reduced IIR filter implementation for practical applications", Kluwer Academic Publishers, 2003

[Kru99] Krukowski, A.; , "Flexible IIR digital filter design and multipsth realisation", PhD Thesis, University of Westminster, Jan 1999

[Kuo99] Kuo, T.; Chen, K.; Chen, J.; "Automatic coefficients design for high-order sigma–delta modulators", IEEE Trans. on Circuits and Systems-II: Analog and Digital Signal Proc., Vol.46, No. 1, January 1999

[Lai15] Lai, W. C., Huang, J. F., Huang, K. J., & Yang, P. G.,; "The Bandpass Sigma-Delta Modulator with Converter Chip Design for Positron Emission Tomography Front-End Application". In Proceedings of the 4th International Conference on Computer Engineering and Networks (pp. 963-970). Springer International Publishing.

[Lee87] Lee, W.L.; Sodini, C.G.; , "A Topology for Higher-Order Interpolative Coders," International Symposium on Circuits and Systems, 1987

[Lee15] [Lee15] Lee, S.Y.; Hong, J. H. ; Hsieh, C. H. ; Liang, M. C. ; Chang S. Y. ; Lin, K. H. "Low-Power Wireless ECG Acquisition and Classification System for Body Sensor Networks," in IEEE Journal of Biomedical and Health Informatics, vol. 19, no. 1, pp. 236-246, Jan. 2015.

[Leu92] Leung, B.; Sutarja, S.; , "Multibit sigma-delta A/D converter incorporating a novel class of dynamic element matching techniques", IEEE Transactions on Circuits and Systems II, Vol. 39, No. 1, pp.35-51, Jan 1992

[Lie06] Lie, I.; Tanase, M.; Lascu, D.; LAscu, M.; " Ultrasonic Beamforming with Delta-Sigma Modulators, "Proceedings of the 10th WSEAS International Conference on Circuits, Vouliagmeni, Athens, Greece, July 2006

[Lia14] Liang, R.; Zhaohan L. ; Zhao, B. ; Cui, S.; Wang, G. ; Chang, Y.; "A CMOS third-order 2-1 cascade sigma-delta modulator," in Solid-State and Integrated Circuit Technology, vol., no., pp.1-3, 28-31 Oct. 2014

[Lip94] Lipschutz, D.; , "Delay interpolator for digital phased array ultrasound beamformers", U.S. Patent 5,345,426, Sep 1994

[Liu09] Liu, D.; Brueske, D.; Colby, B.; ,"Dynamic receive beamformer with oversampling for medical diagnostic ultrasound", U.S. patent 7,583,214, 2009

[Loc98] Lockwood, G. R. ; Talman, J. R. ; Brunke S. S. ; , " Real-time 3-d ultrasound imaging using sparse synthetic aperture beamforming", IEEE Transactions on Ultrasonics, Ferroelectric and Frequency Control, vol.45, no.4, pp.980-988, Jul 1998

[Lon93] Longo, L.; Horng, B.;"A 15b 30 kHz Bandpass Sigma-Delta Modulator," 1991 IEEE Int. Solid-State Circuits Conf. Dig. Tech. Papers, pp. 226-227, Feb. 1993

[Lot07] Lota, J.; Al-Janabi, M.; Kale, I.; , " Stability Analysis of Higher Order Σ–Δ Modulators for sinusoidal inputs," IEEE Conf. Instrumentation and Measurement, vol.57, no.3, pp.593-596, May 2007

[Lot08] Lota, J.; Al-Janabi, M.; Kale, I.; , "Nonlinear-Stability Analysis of Higher Order Σ–Δ Modulators for DC and Sinusoidal Inputs," IEEE Transactions on Instrumentation and Measurement, vol.57, no.3, pp.530-542, March 2008

[Lot13] Lota, J.; Al-Janabi, M.; Kale, I., "Nonlinear Model-Based Approach for Accurate Stability Prediction of One-Bit Higher-Order Delta–Sigma Modulators," IEEE Trans. Instrumentation and Measurement, vol.62, no.4, pp.686-692, Apr 2013

[Lot14] Lota, J.; Al-Janabi, M.; Kale, I.; "Nonlinear Stability Prediction of Multibit Delta–Sigma Modulators for Sinusoidal Inputs," in IEEE Transactions on Instrumentation and Measurement, vol. 63, no. 1, pp. 18-26, Jan 2014

[Mal07] Maloberti, F.; , "Data converters", Pavia University ,Springer Publisher, Netherland, 2007

[Mat89] Matsuya, Y.; , "A 17-Bit Oversampling D/A Conversion Technology Using Multistage Noise Shaping," IEEE Journal of Solid-State Circuits, Vol. 24, No. 4, pp. 969-975, Aug 1989

[Mas85] Maslak, S.; Wright, J.; ,"Phased array acoustic imaging system," U.S. Patent 4,550,607, November 5, 1985

[Mas51] Massey, F.J.: "The Kolmogorov–Smirnov test for goodness of fit", J. Am. Stat. Assoc., 46, (253), pp. 68–78, 1951

[Med93] Medeiro, F.; PerezVerdu, B.; RodriguezVazquez, A.; Huertas, J.L.; , "A tool for automated design of sigma-delta modulators using statistical optimization," IEEE International Symposium on Circuits and Systems, pp.1373-1376 vol.2, May 1993

[Med99] Medeiro, F.; Perez-Verdu, B.; Rodriguez-Vazquez, A.; "Top-down design of high-performance modulators," Kluwer Academic Publishers, Netherlands, 1999.

[Moo94] Mooney, M.G.; Wilson, M.G.;, "Linear Array Transducers with Improved Image Quality for Vascular Ultrasonic Imaging," Hewlett-Packard Journal, Vol. 45, No. 4, pp. 43-51, Aug 1994

[Mou94] Moussavi, S.; Leung, B.;, "High-order single-stage single-bit oversampling A/D converter stabilized with local feedback loops," IEEE Transactions on Circuits and Systems II, pp. 19-25, Jan, 1994.

[Nak01] Nakajima, N.; Kolino, R.; Kubota, S.;, "Research and development of software defined technologies in Japan", IEEE Commun. Mag., vol. 39, pp. 146-155, Aug 2001

[Nau97] Naus P.J.A.; , "A CMOS Stereo 16-bit D/A Converter for Digital Audio", IEEE Journal Solid-State Circuits, vol. SC-22, pp. 390-394, Jun 1997

[Nel08] Nelson B.P.; K. Chason. "Use of ultrasound by emergency medical services: A review" J. Emerg. Med., 1:253–259, 2008.

[Nil06] Nilsen, C.-IC.; Holm, S., "Distortion-Free Delta-Sigma Beamforming with Dynamic Delays," IEEE Ultrasonics Symposium, vol., no., pp.2136,2139, 2-6 Oct. 2006

[Nil08] Nilsen, C.-I.C.; Holm, S.; , "Distortion-free delta-sigma beamforming," IEEE Transactions on Ultrasonics, Ferroelectrics and Frequency Control, vol.55, no.8, pp.1719-1728, Aug 2008

[Nor96] Norman, O.;, "A band-pass delta-sigma modulator for ultrasonic imaging at 160 MHz clock rate," IEEE J. Solid-State Circuits, vol. 31, no. 12, pp. 2036–2041, 1996.

[Nor92] Norsworthy, S.R.; "Effective dithering of sigma-delta modulators," IEEE International Symposium on Circuits and Systems, vol.3, pp.1304-1307, May 1992.

[Nor97] Norsworthy, S. R.; Schreier, R.; Temes, G. ; , "Delta-Sigma Data Converters: Theory, Design, and Simulation", IEEE press, Piscataway, NJ, 1997.

[Nou93] Noujaim, S.E.; Garverick, S.L.; O'Donaell, M.; , "Phased array ultrasonic beam forming using oversampled A/D converters," US Patent 5203335, Apr 1993

[Nyg06] Nyguyen, V.T.; Loumeau, P.; Naviner, J.F; " High-pass Σ–Δ modulator: from System Analyses to Circuit Design", IEEE International Symposium on Circuits and Systems, 2006

[Odo90] O'Donnell, M.; Engeler, W.E.; Pedicone, J.T.; Itani, A.M.; Noujaim, S.E.; Dunki-Jacobs, R.J.; Leue, W.M.; Chalek, C.L.; Smith, L.S.; Piel, J.E.; Harris, R.L.; Welles, K.B.; Hinrichs, W.L.; , "Real-time phased array imaging using digital beam forming and autonomous channel control," IEEE Ultrasonics Symposium, pp.1499-1502 vol.3, Dec 1990

[Ora03] Oralkan, O.; Ergun, A.S.; Johnson, J.A.; Karaman, M.; Khuri-Yakub, B.T.; , "Volumetric acoustic imaging using two-dimensional capacitive micromachined transducer arrays," IEEE Trans. Ultrason., Ferroelect., Freq. Contr., vol. 50,pp. 1581-1594, Nov. 2003

[Opp89] Oppenheim, A.; Schafer, R.; ,"Discrete Time Signal Processing", Prentice-Hall, 1989

[Par05] Parikh, V.K.; Feygin, G.; Balsara P.T.; Rezeq, R.; Staszeuski, R.B.; Vemulapalli, S.; Eliezer, O.; , "Implementation of a high speed digital band-pass sigma-delta modulator for wireless transmitter", Proc. IEEE Workshop on Architecture, Circuits and Implementation of System-on-Chip, pp. 207-210, Oct 2005

[Par98] Park, S.; ,"Principles of sigma-delta modulation for analog-to-digital converters", Motorola Digital Signal Processors, April 1998

[Par14] Park, C.; Kim;, H.; Hwang, J.; Jang, K.; Yoo, Y. ; Choi, J. ; "Design of analog front end for mobile fuel gauge applications," IEEE SoC Design Conf., vol., no., pp.165-166, 3-6 Nov. 2014

[Pau87] Paulos, J.; Brauns, G.; Steer, M.; Ardalan, S.; , " Improved signal-to-noise ratio using tri-level Delta-Sigma Modulation", IEEE Conference on CAS, pp. 463-466,.1987

[Pet84] Peterson, D.K.; Kino, G.S.; "Real-time digital image reconstruction: A description of

imaging hardware and an analysis of quantization errors," IEEE Trans. Sonics Ultrason., vol. SU-31, pp. 337-351, July 1984.

[Pri79] Pridham, R.G.; Mucci, R.A.; , "Digital interpolation beamforming for low-pass and bandpass signals," Proceedings of the IEEE , vol.67, no.6, pp. 904- 919, Jun 1979

[Pro96] Proakis, J.G.; Manolakis, D.G.; ," Digital signal processing", Pearson Prentice Hall, 1996

[Qia15] Qian, H.; Chen, J.; Yao, S.; Zhang, Z. Y. ; Zhang, H.; Xu,W. "One-Bit Sigma-Delta Modulator for Nonlinear Visible Light Communication Systems," IEEE Photonics Technology Letters, vol.27, no.4, pp.419-422, Feb. 2015

[Qui97] Quistgaard, J.U.; , "Signal acquisition and processing in medical diagnostic ultrasound", IEEE Signal Processing Magazine, vol.14, no.1, pp.67-74, Jan 1997

[Ral07] Ralph, S.; Farrell, R.; "Using high pass sigma-delta modulation for class-S power amplifiers," Circuit Theory and Design 18th European Conf, pp. 707 - 710, Aug 2007.

[Ran04] Ranganathan, K.; Santy, M.K; Blalock, T.N; Hossack, J.A.; Walker, W.F.;, "Direct sampled i/q beamforming for compact and very low-cost ultrasound imaging," IEEE Trans. Ultrason., Ferroelect., Freq. Contr., vol. 51, no.9, pp. 1082–1094, 2004

[Rei05] Reiss, J.: "Towards a procedure for stability analysis of higher-ordersigma–delta modulators", 119th Audio Engineering Society Convention, 2005

[Rei08] Reiss, J.D., "Understanding sigma delta modulation: the solved and unsolved issues," Journal of the Audio Engineering Society, vol. 56, pp. 49-64, 2008

[Rib94] Ribner, D.B.; , "Multistage Bandpass Delta sigma Modulators", IEEE Transactions on Circuits and Systems II: Analog and Digital Signal Processing, Vol. 41, No. 6, pp.402-405, Jun 1994

[Rig02] Rigby, K.W.; "Delta-sigma beamformers with minimal dynamic focusing artifacts", US Patent 6366227, Apr 2002

[Ris94a] Risbo, L., "Stability predictions for higher-order sigma-delta modulators based on quasilinear modelling," IEEE Trans. on Circuits and Systems, vol.5, no.6, pp. 361- 364, 1994

[Ris94b] Risbo, L., "Sigma-Delta Modulators - Stability Analysis and Optimization," PhD Thesis, Electronics Institute. Lyngby: Technical University of Denmark, 1994

[Rit90] Ritoniemi, T.; Karema,T.; Tenhunen, H.; , " The design of stable higher order I-bit sigma-delta modulators," IEEE International Symposium on Circuits and Systems, pp. 3267-3270, May 1990.

[Rui04] Ruiz-Amaya, J.; Rosa, J.M.; Medeiro, F.; Fernandez, F. V.; del Rio, R.; Perez-Verdu, B.; Rodriguez-Vazquez, A.; , "MATLAB/SIMULINK-based high-level sysnthesis of discrete-time and continuous-time Σ–Δ modulators," IEEE Computer society, 2004.

[Rus03] Rusu, A.; Tenhunen, H.; , " A 3rd-order sigma-de;ta modulator for dual mode receiver", Proc. IEEE International Midwest Symposium on Circuits and Systems, vol.1,pp. 68-71, Dec 2003

[Sab14] Sabarinath, P.; Prakash, J.; Jose, B.R.; 'Overloading Prediction in Symmetric Cross Coupled Low-Pass Sigma Delta Modulators' , Proceedings of the International Conf. on Information and Communication Technologies, Dec 2014

[Sal07] Salgo, I.S.;, "Three-dimensional echocardiographic technology," Cardiology Clinics, Vol. 25, No. 2, pp. 231-239, May 2007

[San13] Sanchez, J. R. ; 'An FPGA-based coded excitation system for ultrasonic imaging using a second-order, one-bit sigma-delta modulator', IEEE International Conference on Electro-Information Technology , pp.1-6, 2013

[Sap08] Saputra, N., Pertijis, M., Makinwa, K.; Hujising, "Sigma Delta ADC with a Dynamic Reference for Accurate Temperature and Voltage Sensing", IEEE International Symposium on Circuits and Systems, 2008.

[Sav03] Savord, B.; Solomon, R.; "Fully sampled matrix transducer for real time 3D ultrasonic imaging," IEEE Ultrason. Sympos., pp. 945-953, 2003

[Sea02] Seagar,A.; Liley, D.; "Basic principles of ultrasound imaging system design", Swinburne University of Technology School of Biophysical Sciences and Electrical Engineering, Biomedical imaging lecture notes, Mar 2002

[Sch89] Schreier, R.; Snelgrove, M.; , "Bandpass Sigma-Delta Modulation," Electronics Letters, pp. 1560-1561, Nov. 9, 1989

[Sch91] Schreier, R.; Snelgrove, M.; , "Sigma-Delta Modulation is a Mapping", IEEE International Symposium on Circuits and Systems, vol 5, pp.2415-2418, 1991

[Sch97] Schreier, R.; Goodson, M.V.; Bo Zhang; , "An algorithm for computing convex positively invariant sets for delta-sigma modulators," IEEE Transactions on Circuits and Systems I: Fundamental Theory and Applications, vol.44, no.1, pp.38-44, Jan 1997

[Sch02] Schreier, R.; Lloyd, J.; Singer, L.; Paterson, D.; Timko, M.; Hensley,M.; Patterson, G.; Behel, K.; Zhou, J.; , "A 10-300 MHz IF-Digitizing IC with 90-105 dB Dynamic Range and 15-333 kHz Bandwidth, IEEE Journal of Solid State Circuits, Vol. 37, No. 12, pp. 1636-1644, Dec 2002

[Sch05] Schreier, R.; Temes, G.C.; , "Understanding delta-sigma data converters", IEEE Press-Wiley-Interscience Publication, 2005

[Sha49] Shannon, C.E., "Communication in the presence of noise", in proc. IRE, pp. 37:10-21, 1949.

[Sho88] Shoup, T.A.; Hart, J.; , "Ultrasonic imaging systems," IEEE Ultrasonics Symposium, vol., no., pp.863-871 vol.2, 2-5 Oct 1988

[Shu06] Shuen-Yuh, L.; Chih-Jen, C.; , "A low voltage and low power adaptive switched current sigma-delta A/D converter for Bio-acquisition Microsystems", IEEE International Trans. on Circuits and Systems, vol.53, no. 12, pp. 2628-2636, Dec 2006

[Sir15] Sirdeshpande, N., Desai, R ,"Simulink Based Approach For Modelling Of Third Order Sigma Delta Modulator For Audio Applications", Proc. of The International Conference

on Computer Technology and Information Systems, Oct 2015

[Sno01] Snoeji, M.F.; Bajdechi, O.; Huijising, J.H.; , " A 4th-order switched-capacitor sigma-delta A/D converter using a high-ripple chebyshev loop filter", IEEE International Symposium on Circuits and Systems, vol. 1, Page(s):615 - 618 , 6-9 May 2001

[Ste94] Steiner, P.; Yang, W.; , "Stability analysis of the second order ΣΔ modulator," IEEE International Symposium on Circuits and Systems , vol.5, pp.365-368 vol.5, Jun 1994

[Ste01] Stergiopoulos, S.; "Advanced Signal Processing Handbook: Theory and Implementation for Radar, Sonar and Medical Imaging Real-Time Systems,", CRC Press: Boca Raton, FL, 2001

[Ste96] Stewart, R.W.; Pfann, E.; , "Oversampling and sigma-delta strategies for data conversion", Electronics & Communication Engineering Journal, Feb 1998

[Sti88] Stikwoort, E.F.; "Some remarks on the stability and Performance of the noise shaper or sigma-delta modulator," IEEE Trans. On Communications, vol. 36, no.10, pp. 1157-1162, Oct. 1988

[Sum92] Summers, B. ;, "Signal Processing Apparatus and Method" U.S. patent 92/15150, 1992

[Sun03] Sun-Hong, K.; Ho-Yeon, L.; Seok-Woo, C.; Dong Yong, K.; , "Wideband multi-bit 3rd order sigma-delta A/D converter for wireless transeivers", Proc. 5th International Conference on ASIC, vol.1, pp. 689-692, Oct 2003

[Syn07] Synnevag, Johan F, Austeng, A.; Holm, S.; "Adaptive Beamforming Applied to Medical Ultrasound Imaging." IEEE Transactions on Ultrasonics, Ferroelectrics and Frequency Control 54.8:1606-1613, 2007

[Sza04] Szabo, T. L., "Diagnostic Ultrasound Imaging: Inside Out," Elsevier Academic Press: Hartford, Connecticut, 2004

[Tal09] Talay, S.; Deniz, E.; Dundar, G.; "A Sigma-Delta ADC design automation tool with embedded performance estimator", Elsevier Journal on Integration and VLSI, vol. 42, pp. 181–192, Feb 2009

[Tex10] Texas Instrument, "Medical Applications Guide: Diagnostic, Patient Monitoring and Therapy", 2010

[Tex13] Texas Instrument, "Medical Applications Guide: TI Health Tech", 2013

[Tex15] Texas Instruments, 'Datasheet ADS5294', Analog-to-Digital Converter, Texas Instruments, Sep 2015 http://www.ti.com/lit/ds/symlink/ads5294.pdf, last visited Mar 2016

[Tho96] Thomenius, K.E.; "Evolution of ultrasound beamformers," in Proc. IEEE Ultrason. Symp., pp. 1615–1622, 1996

[Tom05] Tomov, B.; Jensen, J.; , "Compact FPGA-based beamformer using oversampled 1-bit A/D converters", IEEE Trans. Ultrason., Ferroelect., Freq. Contr., vol.52, no. 5, pp. 870-880, May 2005

[Tom13] Tomov B.; , Stuart MB, Hemmsen MC, Jensen JA. "A Delta-Sigma beamformer with integrated apodization", International Society for Optical Engineering. 2013.

[Tov04] Tov, B.; Kozak,M.; Friedman, E.G.; ,"A 250 MHz Delta-sigma Modulator for Low Cost Ultrasound/Sonar Beamforming Applications", IEEE electronics, Circuits and Systems, pp.113-116, Dec 2004

[Tro93] Troster, G.; Drepler, H.; "An interpolative bandpass converter on a 1.2 umBiCMOS analog/digital array," IEEE Journal of Solid State Circuits, pp. 471477, Apr, 1993.

[Uca96] Ucar, F.N.; Kraman M.; , "Beam space processing for low-cost scanners", Proceedings of IEEE Ultrasonics Symposium, pp. 1349-1352, 1996

[Uch88] Uchimura, K.; Hayashi, T. ; Kimura, T.; Iwata, A.; ,"Oversampling A-to-D and D-to-A converters with multistage noise shaping modulators", IEEE Trans. Acoustic., Speech, Signal Proc, vol. 36, pp. 1889- 1905. Dec. 1988

[Val83] Valenzuela, R.A. ; Constantinides, A.G. ; , 'Digital Signal Processing Schemes for Efficient Interpolation and Decimation', IEE Proceedings, Vol. 130, Pt. G. No. 6, pp. 225-235 Dec. 1983

[Vun05] Vun, N.; Premkumar, A.B.; , "Analog-to-digital converter systems for software defined radio for digital front-end", Proceedings 9th International symposium on Consumer Electronics, pp. 359-363, Jun05

[Wag12] Wagner, N.; Eldar, Y.C.; Friedman, Z., "Compressed Beamforming in Ultrasound Imaging," Signal Processing, IEEE Transactions on , vol.60, no.9, pp.4643,4657, Sept. 2012

[Wan93] Wang, H.; "On the stability of third-order sigma-delta modulation", IEEE International Symposium on Circuits and Systems, vol.2, pp.1377-1380, May 1993.

[Wel89] Welland, D.R.; Del Signore, B.P.; Swanson, E.J.; Tanaka, T.; Hamashita, K.; Hara,S.; Takasuka,K.;, "A stereo 16-bit sigma-delta A/D converter for digital audio," J. Audio Eng. Soc., vol37, pp. 476-486, Jun 1989

[Wel69] Wells, P. N.; , "Physical principles of ultrasoundic diagnosis", Academic Press, London, 1969

[Wel75] Wells, P. N.; ,"Absorption and dispersion of ultrasound in biological tissue", Ultrasound in medicine and biology, vol.63 no.3, pp.369-376, 1975

[Wel87] Wells, P. N.; "The prudent use of diagnostic ultrasound," Ultrasound Med. Biol., vol. 13, no. 7, pp. 391–400, 1987.

[Wel07] Wells, P. N.; "Ultrasound imaging". Phys. Med. Biol., 51:R83–R98, 2007.

[Wil94] Williams, L.; Wooley, B.; , "Third-order sigma-delta modulator with extended dynamic range," IEEE Journal of Solid State Circuits, pp. 193-202, Mar, 1994

[Wol88] Wolff, C. ; Carley, L.R.; , "Modeling the quantizer in higher-order delta-sigma modulators", IEEE International Symposium on Circuits and Systems, pp.2335-2338, Jun 1988

[Won03] Wong, N., Tung-Sang, N.G.: 'DC stability analysis of higher-order, lowpass sigma–delta modulators with distinct unit circle NTF zeroes', IEEE Trans. Circuits Syst. II, Analog Digit. Signal Process., 50,(1), pp. 12–30, 2003

[Yan14] Yang, Y. ; Gu, C. ; L, Y.; Gale, R.; Changzhi Li, "Doppler Radar Motion Sensor With CMOS Digital DC-Tuning VGA and Inverter-Based Sigma-Delta Modulator," IEEE Trans. Instrumentation and Measurement, vol.63, no.11, pp.2666-2674, Nov. 2014

[Yin93] Yin, G.; Stubbe, F.; Sansen, W.; , "A 164 320-kHz CMOS A/D converter using two-stage third-order sigma-delta noise shaping," IEEE Journal of Solid State Circuits, pp. 640-647, Jun, 1993

[Zha00] Zhang, Y.; Hayahara, E.; , "Correction of transfer function implementation on delta-sigma modulator stability analysis", Institue of electronics, Information and communication engineering transactions on fundamentals, vol. E83-A, no. 4, Apr 2000

[Zha03] Zhang, J., Brennan, P.V., Juang, D., Vinogradova, E., Smith, P.D.:"Stable analysis of a sigma–delta modulator", International Symposium on Circuits and Systems, vol. 1, p. 1-961–1-964, May 2003

[Zha15] Zhang, Y. ; Chia-Hung, C.; Tao He; Temes, G.C., "A Continuous-Time Delta-Sigma Modulator for Biomedical Ultrasound Beamformer Using Digital ELD Compensation and FIR Feedback," IEEE Trans. on Circuits and Systems, I: Regular Papers, vol.62, no.7, pp.1689-1698, Jul 2015

[Zho14] Zhou, J.; Hoyos, S.; Sadler, B.M., "Asynchronous compressed beamformer for portable diagnostic ultrasound systems," in Ultrasonics, Ferroelectrics, and Frequency Control, IEEE Transactions on , vol.61, no.11, pp.1791-1801, Nov 2014

[Zie98] Ziemer, R. E.; Tranter, W. H.; Fannin, R. D. ; , "Signals & Systems, continuous and discrete", Prentice Hall Press, USA, 1998

[Zri05] Zrilic, D.G.; , "Circuits and Systems Based on Delta Modulation", Linear, Nonlinear and Mixed Mode Processing, Springer-Verlag Berlin Heidelberg Published, 2005

Appendix A

Beamforming Time-Delays:

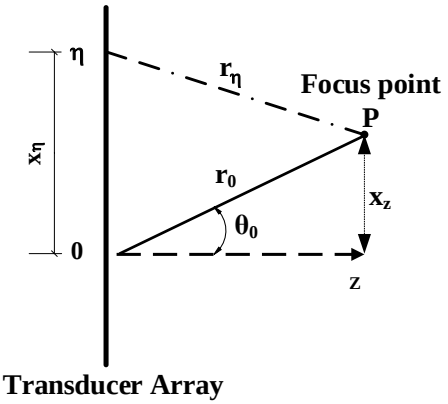

Figure A-1 Focus point geometry in polar coordinates

x_η is the distance of the η-th element of the transducer array to the center of the transducer (0). r_η is the distance of the η-th element of the transducer array to the focus point, *P*. r_0 is the distance of the the focus point to the center of the transducer array. x_z is the vertical distance of the focus point to the center of the transducer array, where θ_0 is the angle of P to the center of the transducer array. Using the geometry in Figure A-1:

$$r_\eta = \sqrt{\left(x_\eta - x_z\right)^2 + z^2} \tag{A.1}$$

$$r_\eta = \sqrt{\left(x_\eta - r_0 \cdot \sin\theta_0\right)^2 + \left(r_0 \cdot \cos\theta_0\right)^2} \tag{A.2}$$

$$r_\eta = \sqrt{x_\eta^2 - 2 \cdot x_\eta \cdot r_0 \cdot \sin\theta_0 + r_0^2} \qquad \text{(A. 3)}$$

$$r_\eta = r_0 \sqrt{1 - 2\frac{x_\eta}{r_0}\sin\theta_0 + \left(\frac{x_\eta}{r_0}\right)^2} \qquad \text{(A.4)}$$

Using the Taylor series expansion of *f(x)* expanded around *x*, the first 3-terms:

$$f(x) = \sqrt{1+x} \cong 1 + \frac{1}{2}x - \frac{1}{8}x^2 \qquad \text{(A.5)}$$

where;

$$x = -2\frac{x_\eta}{r_0}\sin\theta_0 + \left(\frac{x_\eta}{r_0}\right)^2 \qquad \text{(A.6)}$$

Therefore (A.5) becomes:

$$f(x) \cong 1 + \frac{1}{2}\left(-2\frac{x_\eta}{r_0}\sin\theta_0 + \left(\frac{x_\eta}{r_0}\right)^2\right) - \frac{1}{8}\left(4\left(\frac{x_\eta}{r_0}\right)^2 \sin^2\theta_0 + O\left(\left(\frac{x_\eta}{r_0}\right)^3\right)\right) \qquad \text{(A.7)}$$

Assuming that $r_0^2 >> x_\eta^2$; thus the term $\frac{1}{8}O\left(\frac{x_\eta}{r_0}\right)^3$ is negligible. Therefore (A.7) yields:

$$f(x) \cong 1 - \frac{x_\eta}{r_0}\sin\theta_0 + \frac{1}{2}\left(\frac{x_\eta}{r_0}\right)^2 - \frac{1}{2}\left(\frac{x_\eta}{r_0}\right)^2 \sin^2\theta_0 \qquad \text{(A.8)}$$

$$f(x) \cong 1 - \frac{x_\eta}{r_0}\sin\theta_0 + \frac{1}{2}\left(\frac{x_\eta}{r_0}\right)^2 \left(1 - \sin^2\theta_0\right) \qquad \text{(A.9)}$$

$$f(x) \cong 1 - \frac{x_\eta}{r_0}\sin\theta_0 + \frac{1}{2}\left(\frac{x_\eta}{r_0}\right)^2 \cos^2\theta_0 \tag{A.10}$$

$$r_\eta = r_0\sqrt{1 - 2\frac{x_\eta}{r_0}\sin\theta_0 + \left(\frac{x_\eta}{r_0}\right)^2} = r_0 \cdot f(x) \tag{A.11}$$

$$r_\eta \cong r_0 - x_\eta \sin\theta_0 + \frac{x_\eta^2}{2r_0}\cos^2\theta_0 \tag{A.12}$$

Since the time-delay ($\tau_\eta^{'}$) for the η-th array element is related to its position to the focus point:

$$\tau_\eta^{'} = \frac{r_\eta - r_0}{c} \tag{A.13}$$

The time-delay is obtained as:

$$\tau'_\eta = \tau'(x_n, r_0, \theta_0) = \frac{r_\eta - r_0}{c} = -\frac{x_\eta \sin\theta_0}{c} + \frac{x_\eta^2 \cos^2\theta_0}{2cr_0} \tag{A.14}$$

Appendix B

Σ–Δ Modulator Design Tool Simulink Models:

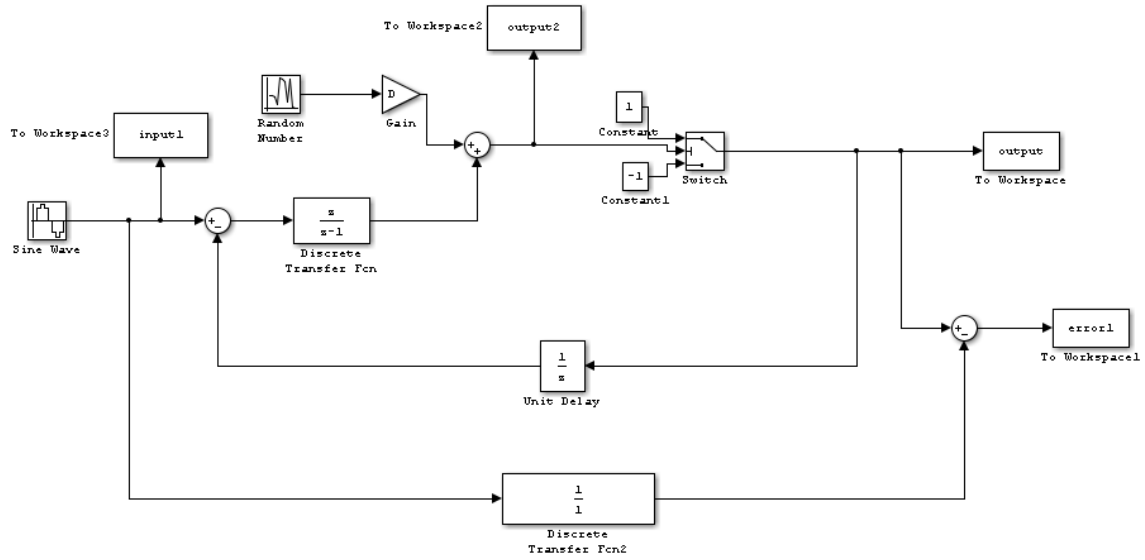

Figure B-1 LP First-order single-stage structure

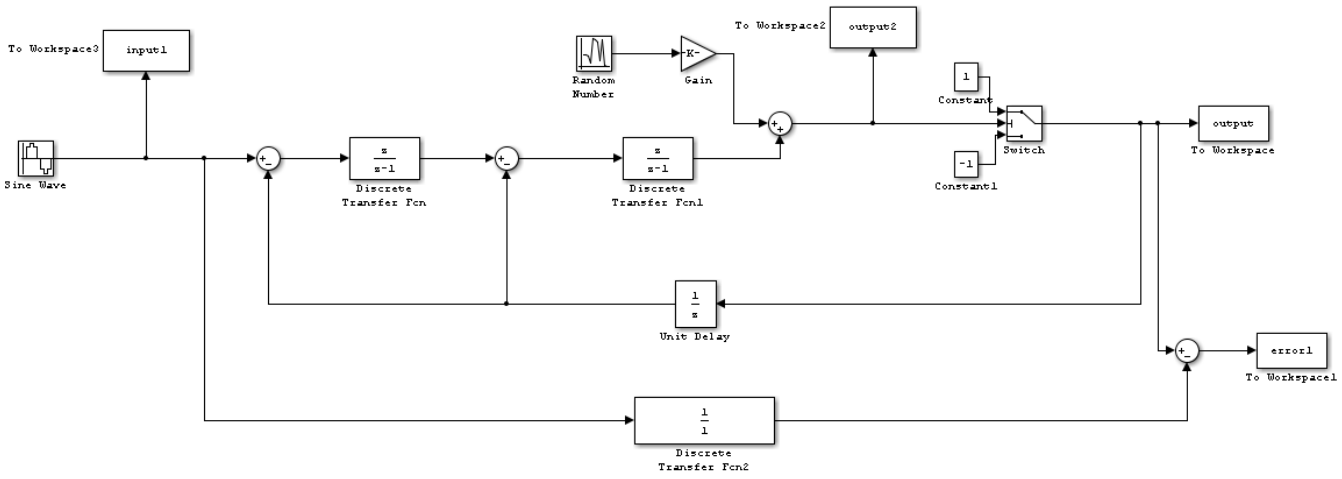

Figure B-2 LP Second-order single-stage structure

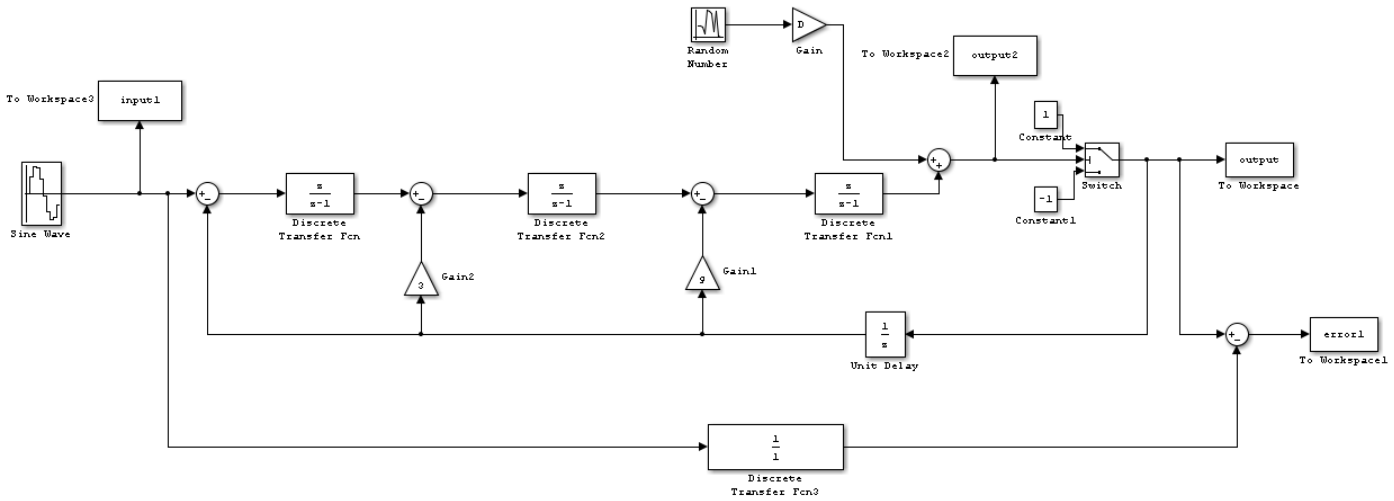

Figure B-3 LP Third-order single-stage structure

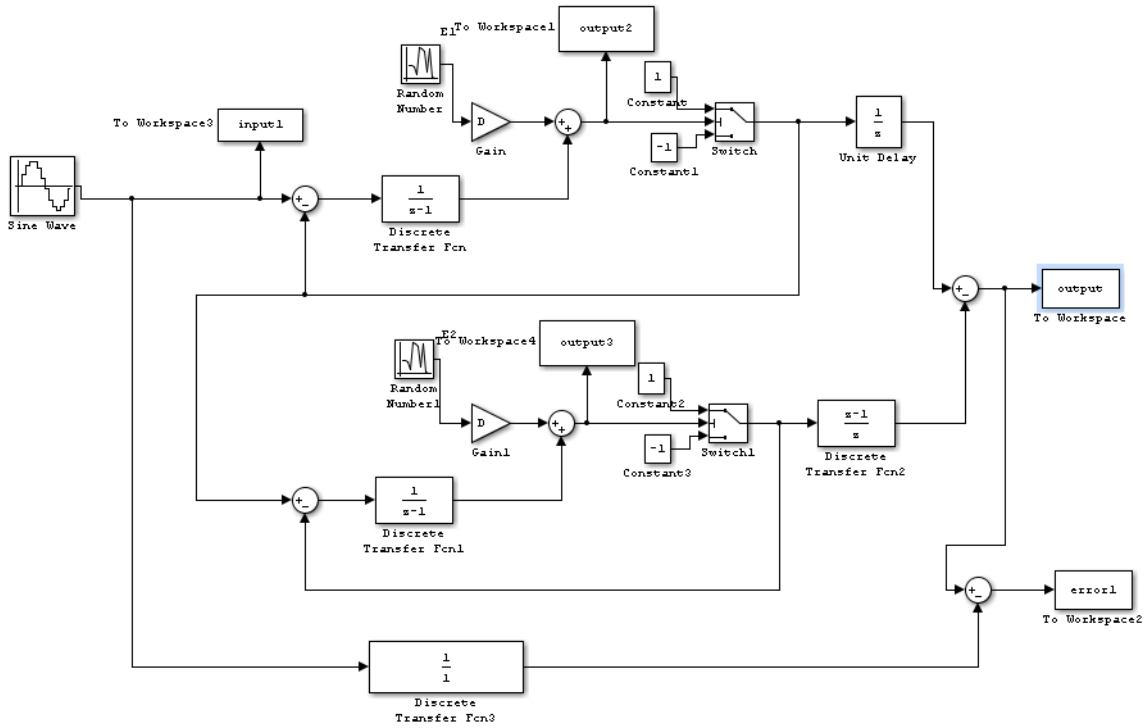

Figure B-4 LP Second-order multi-stage structure

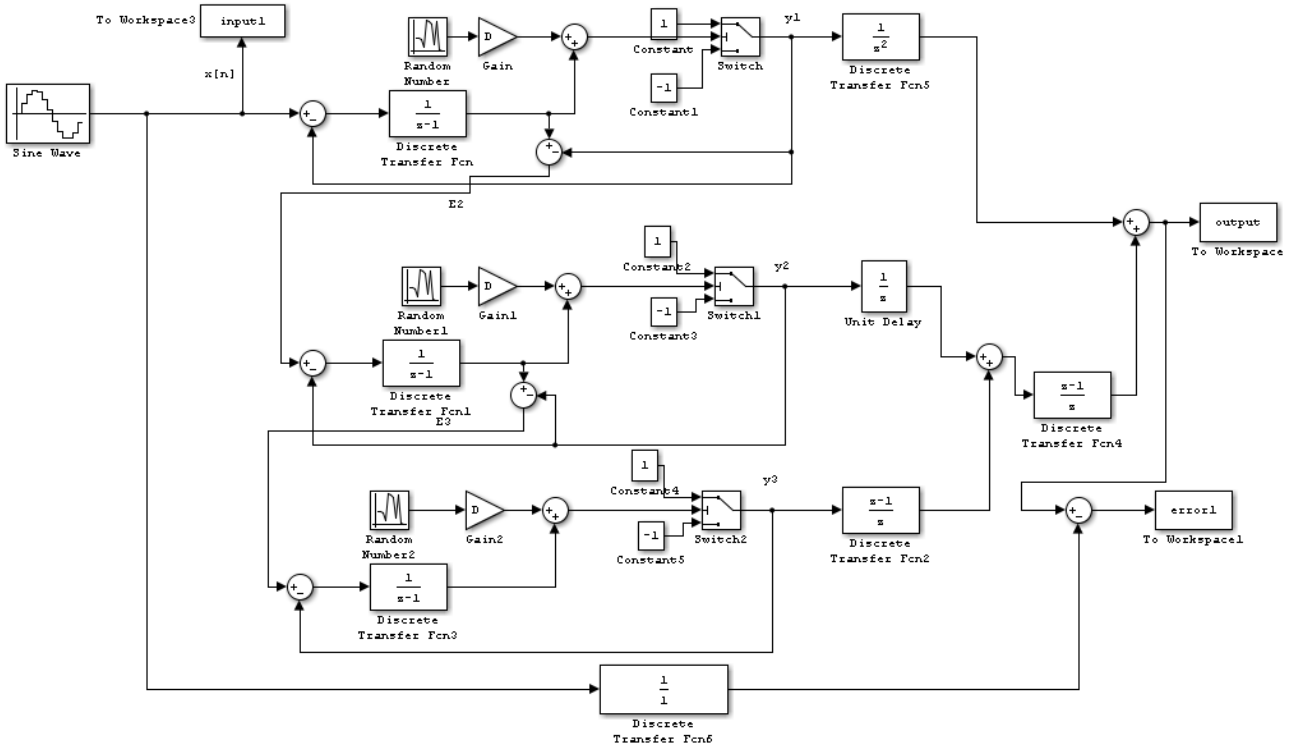

Figure B-5 LP Third-order multi-stage structure

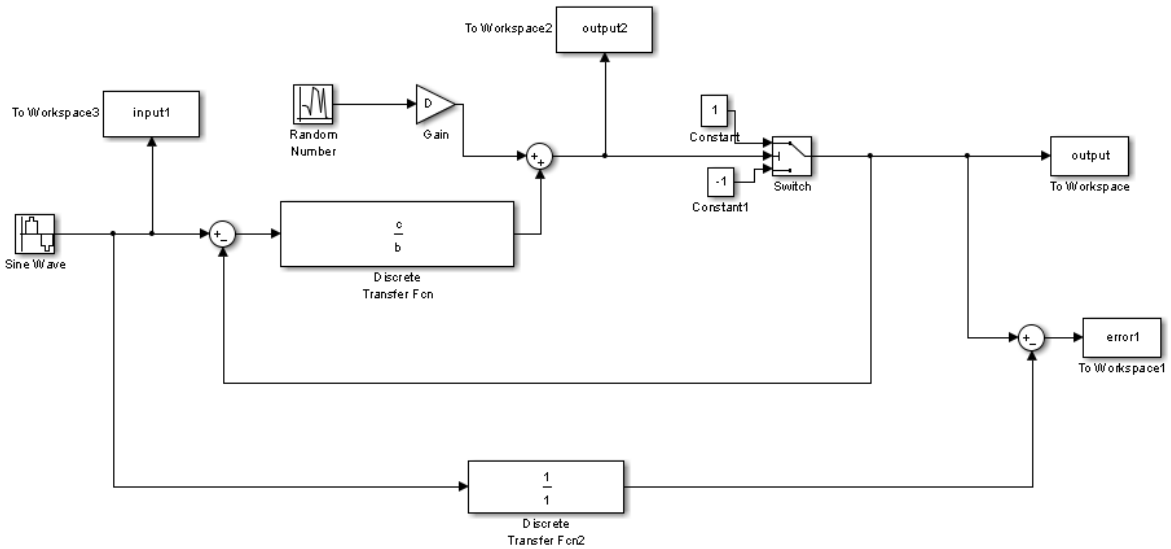

Figure B-6 LP Generic structure based on LP,BP,HP Butterworth/Chebyshev Type-II Filter response

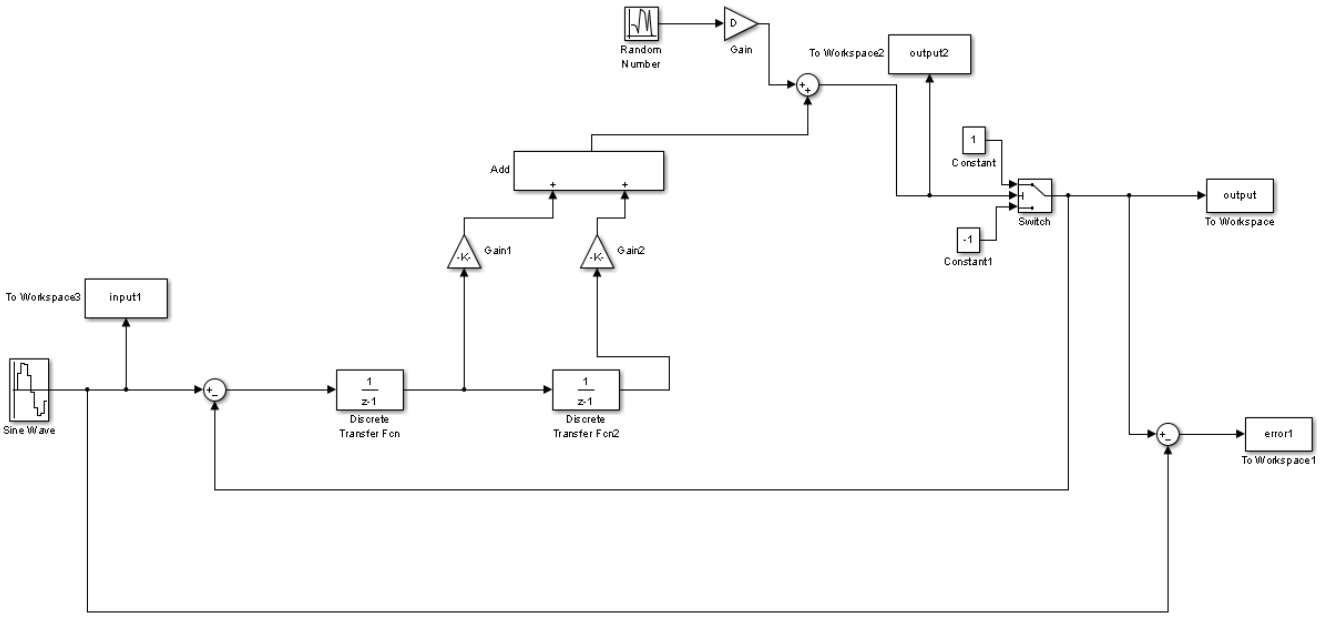

Figure B-7 LP second-order summation of weighted feedforward coefficients structure

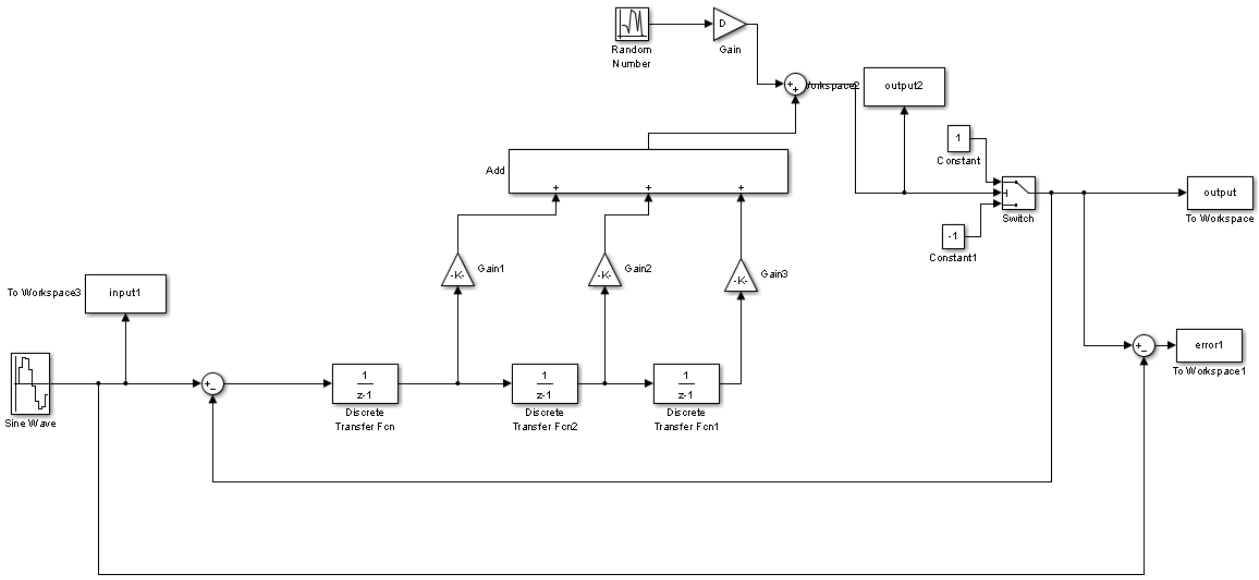

Figure B-8 LP third-order summation of weighted feedforward coefficients structure

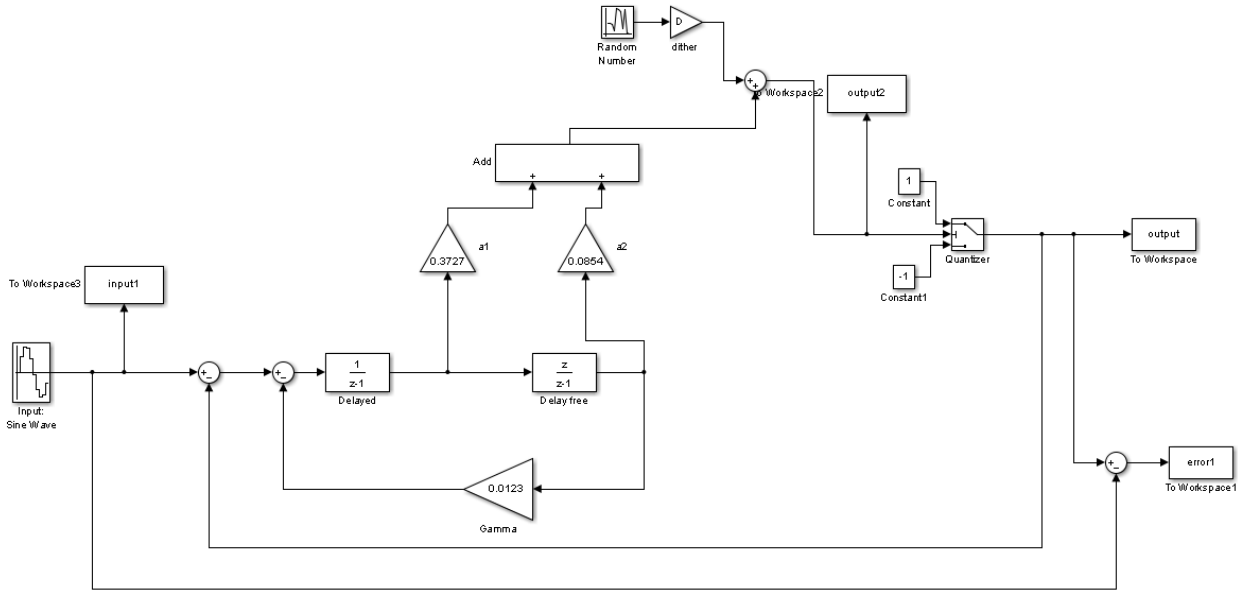

Figure B-9 LP second-order summation of weighted feedforward coefficients with local feedbacks structure

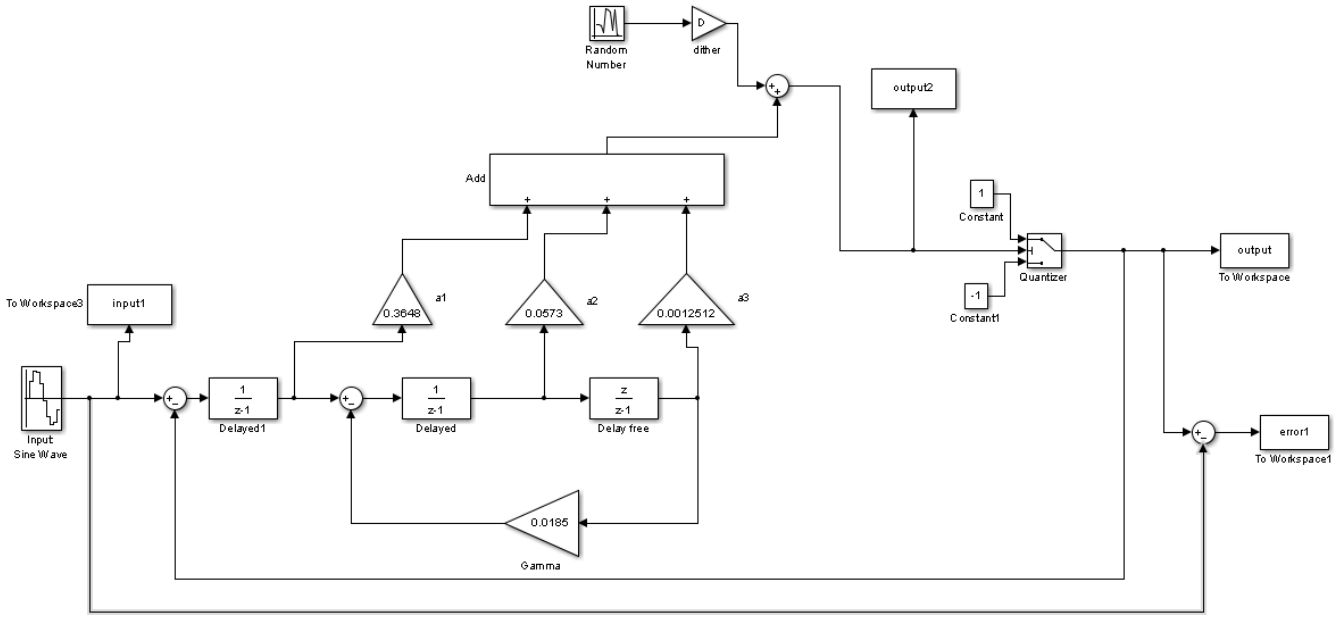

Figure B-10 LP third-order summation of weighted feedforward coefficients with local feedbacks structure

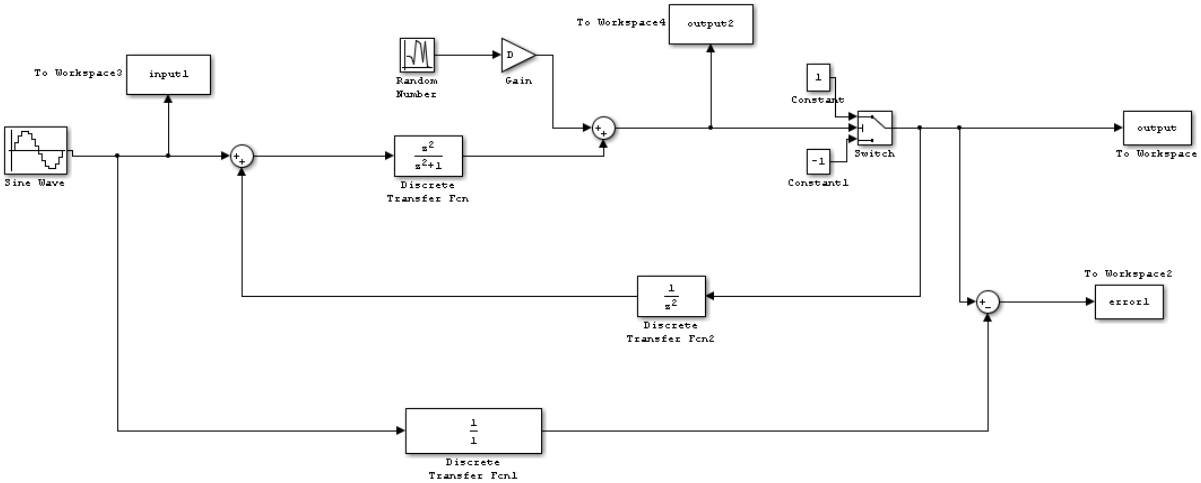

Figure B-11 BP mid-band second-order single-stage structure

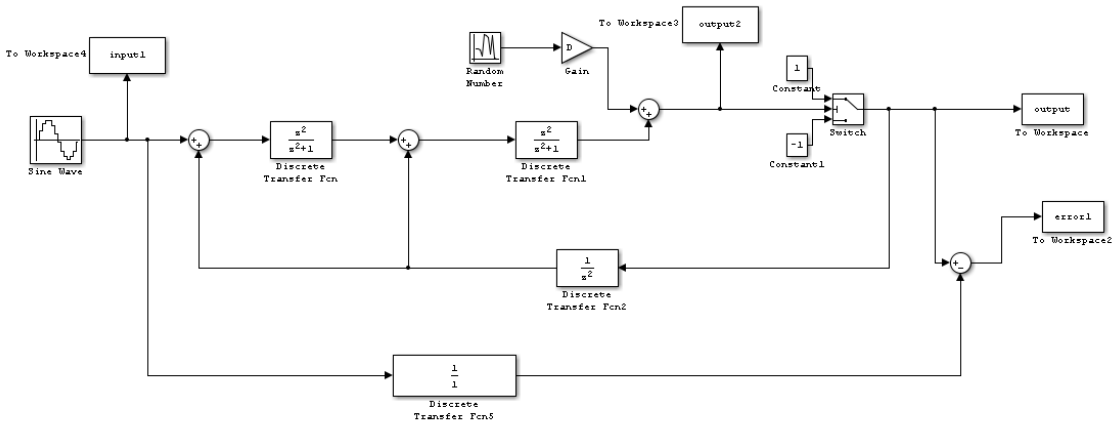

Figure B-12 BP mid-band fourth-order single-stage structure

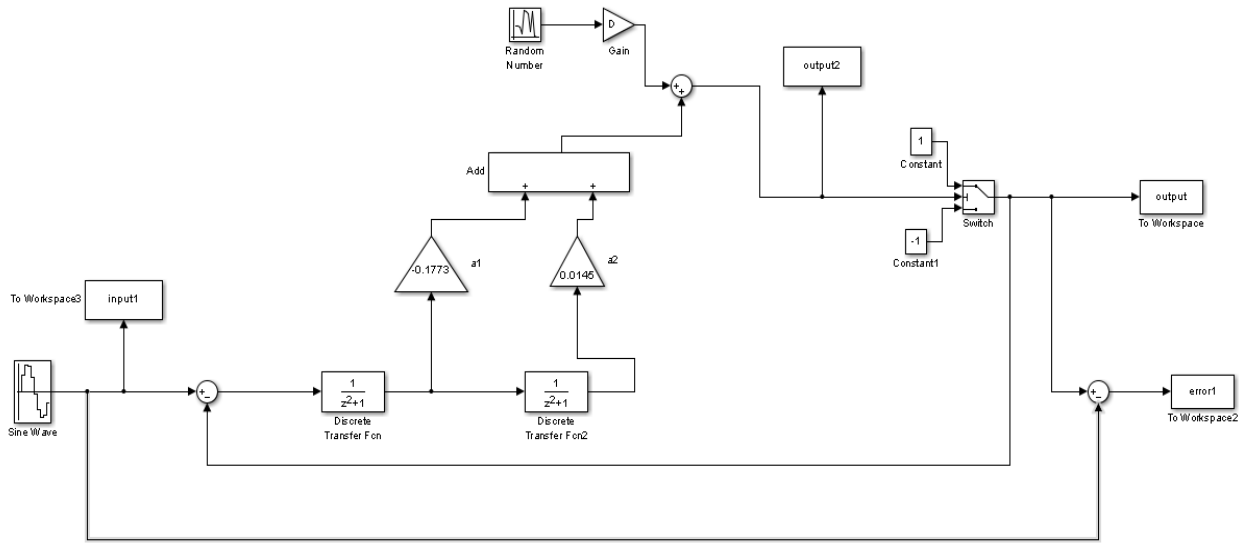

Figure B-13 BP mid-band fourth-order summation of weighted feedforward coefficients structure

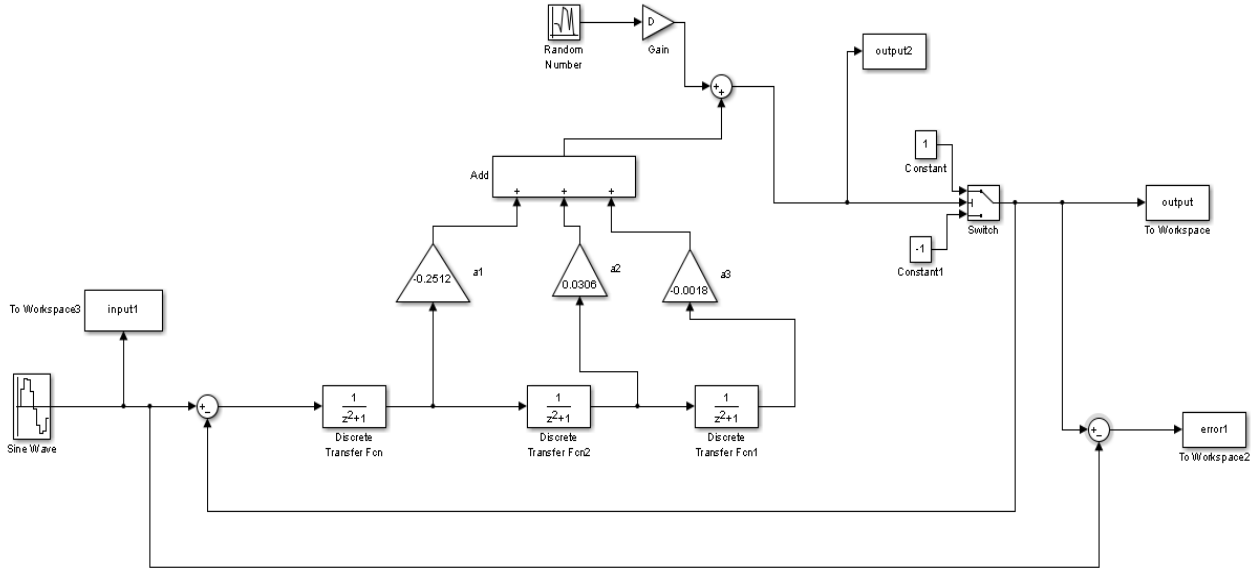

Figure B-14 BP mid-band sixth-order summation of weighted feedforward coefficients structure

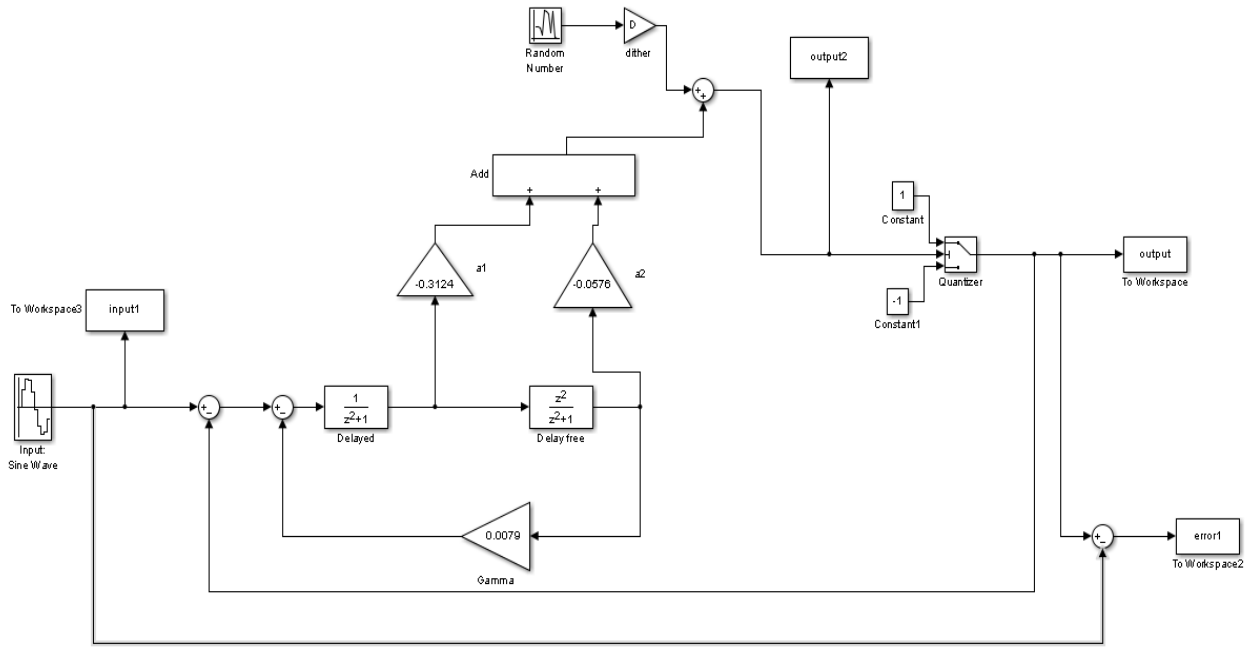

Figure B-15 BP mid-band fourth-order summation of weighted feedforward coefficients with local feedbacks structure

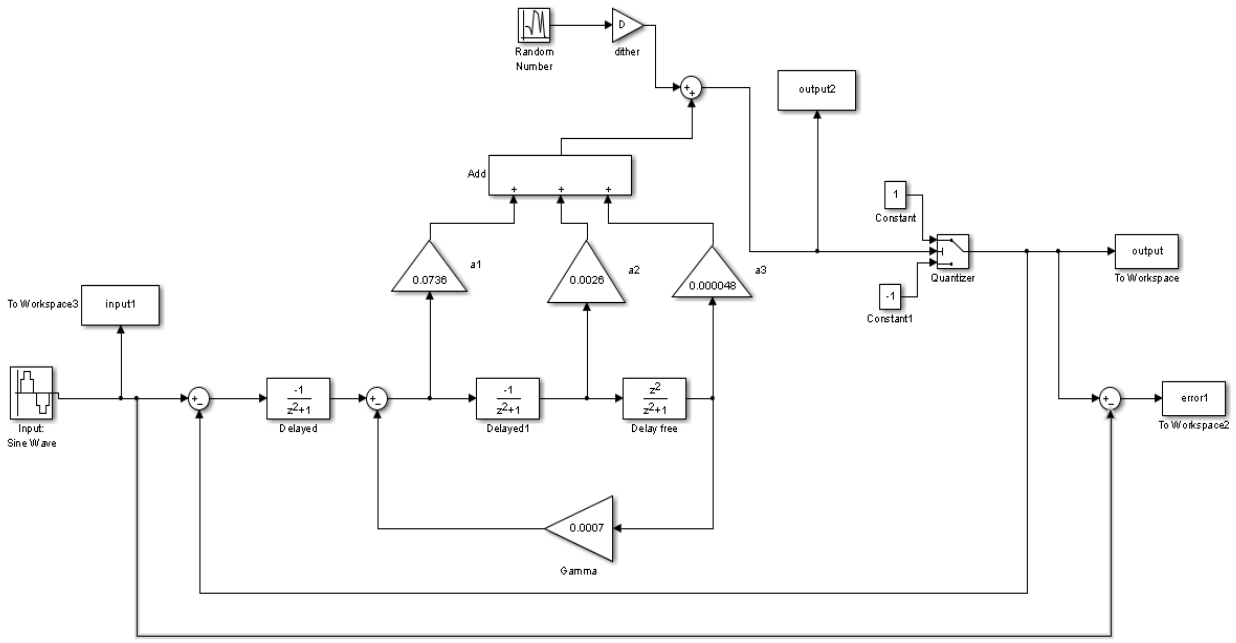

Figure B-16 BP mid-band sixth-order summation of weighted feedforward coefficients with local feedbacks structure

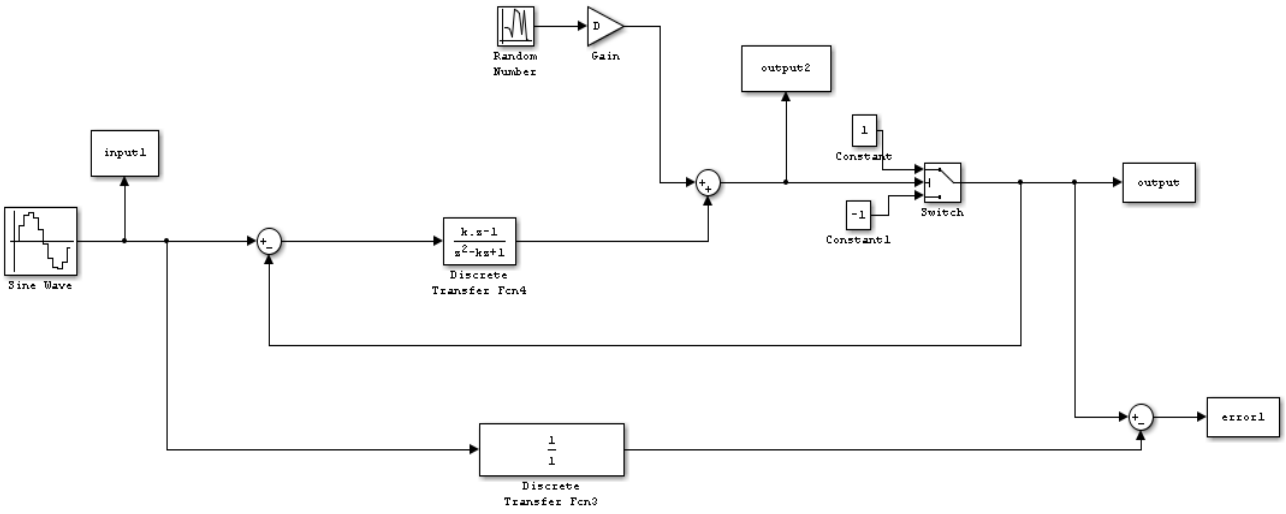

Figure B-17 BP second-order modulator structure for variable frequencies

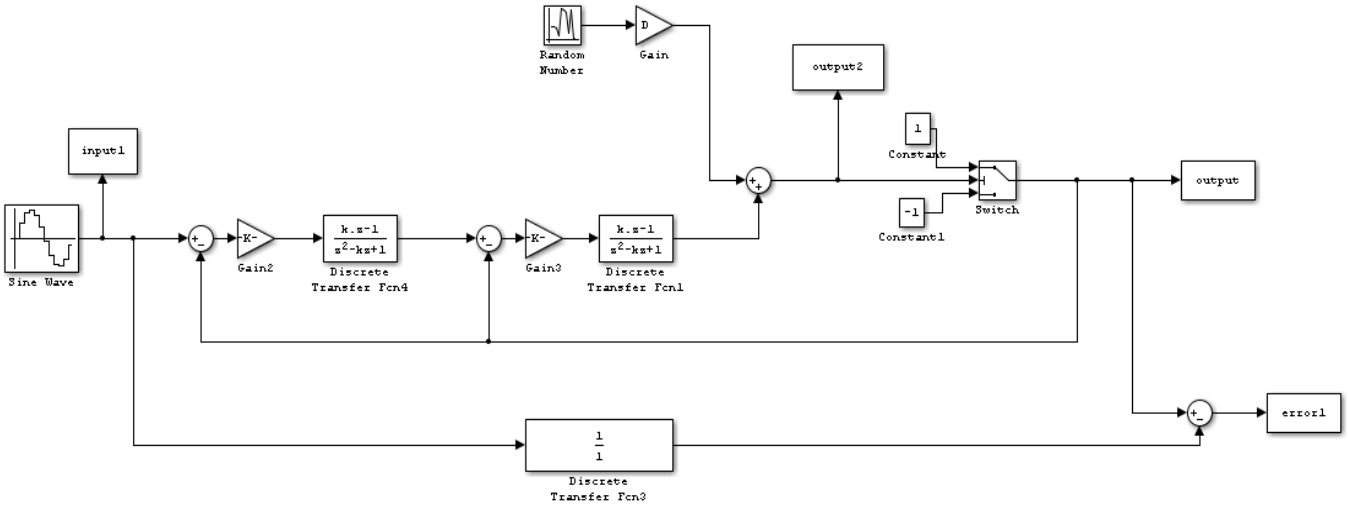

Figure B-18 BP fourth-order modulator structure for variable frequencies

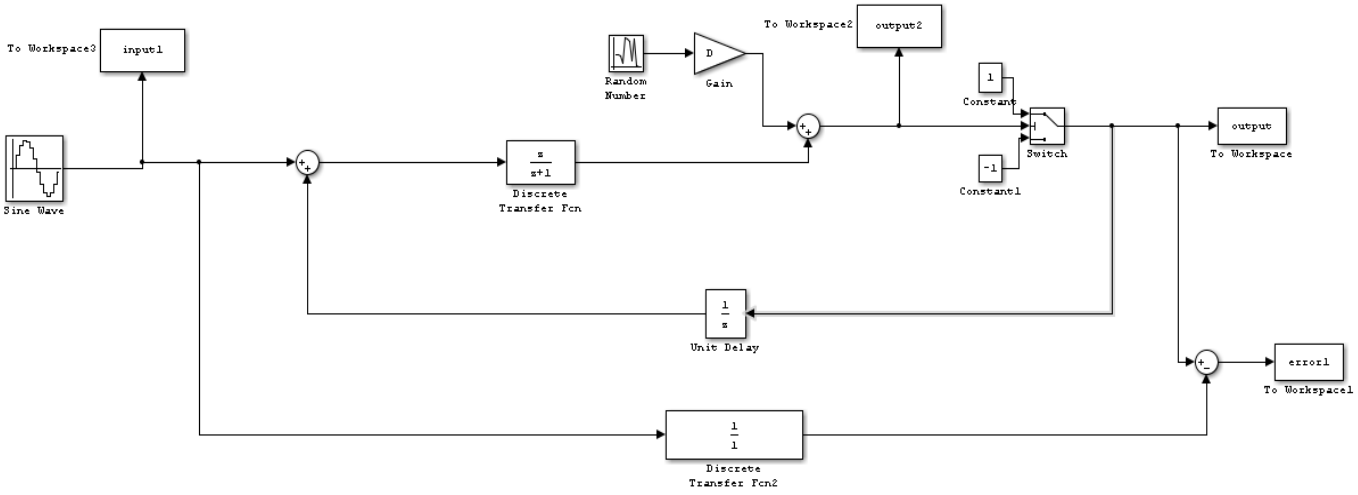

Figure B-19 HP first-order single-stage structure

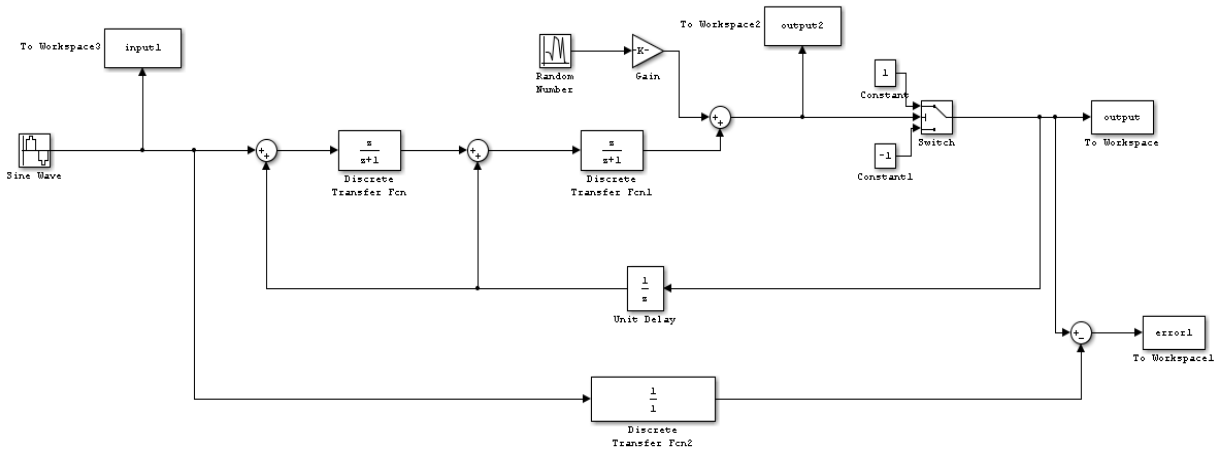

Figure B-20 HP second-order single-stage structure

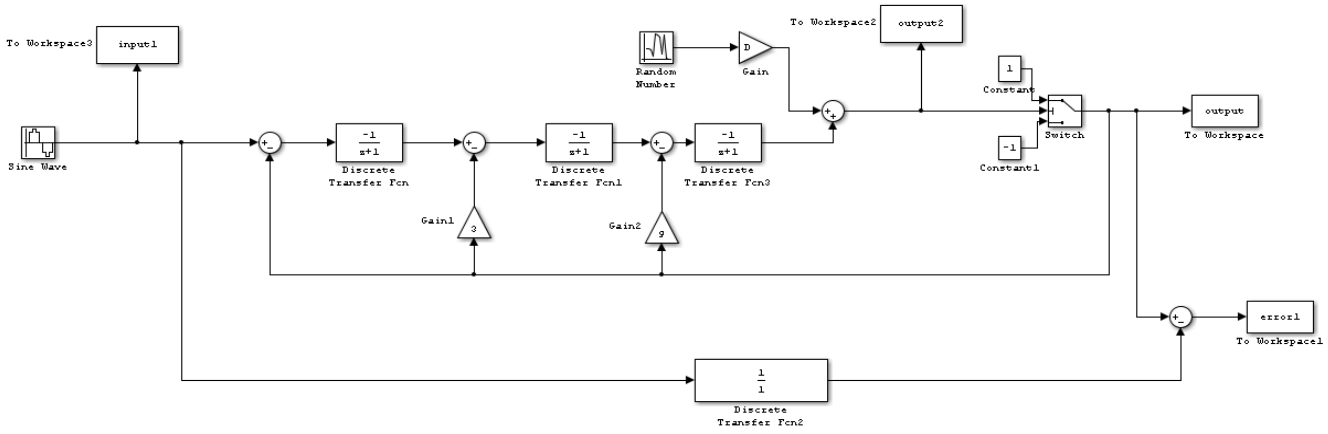

Figure B-21 HP third-order single-stage structure

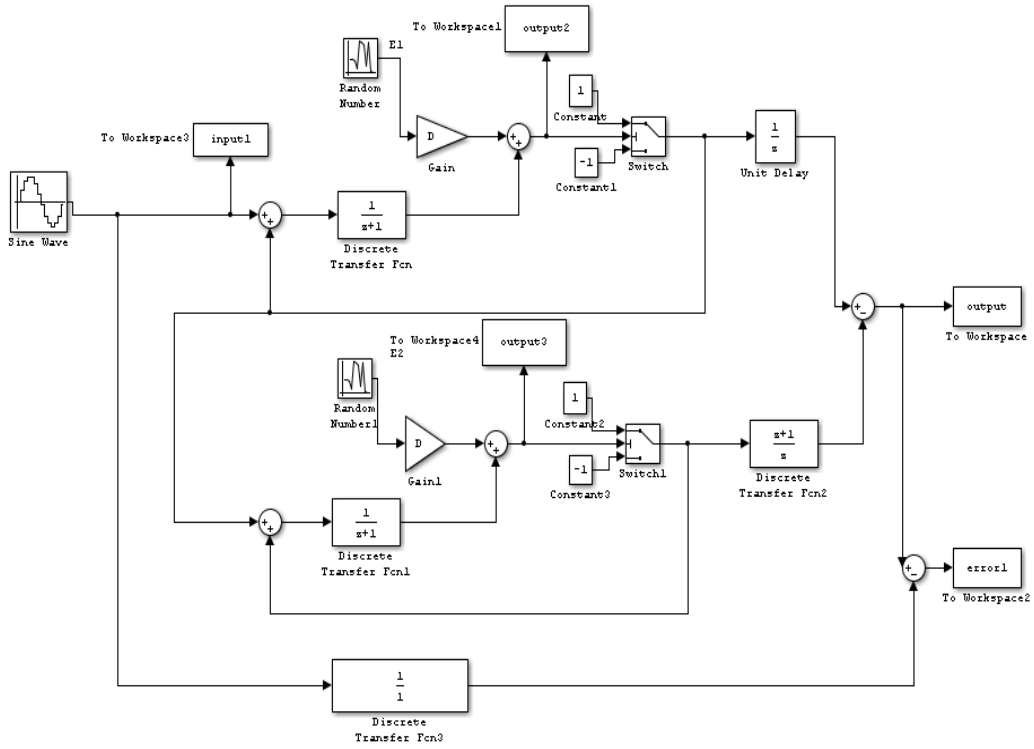

Figure B-22 HP second-order multi-stage structure

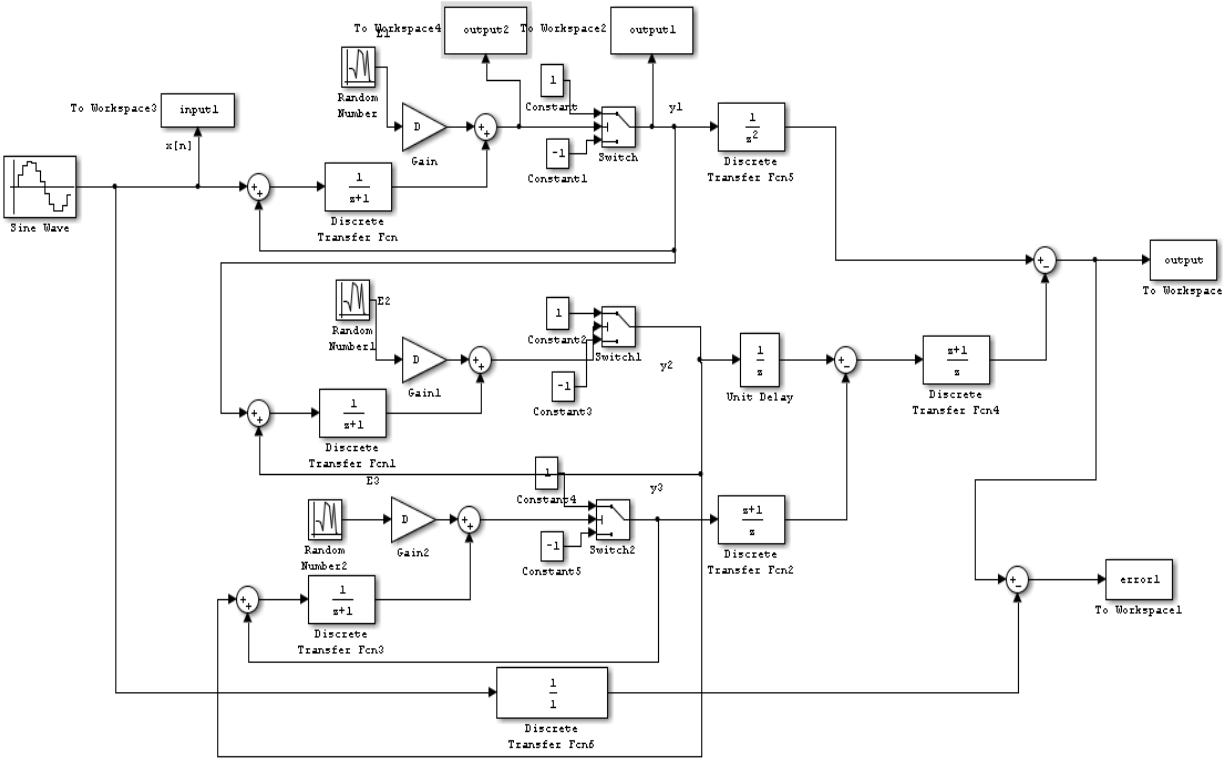

Figure B-23 HP third-order multi-stage structure

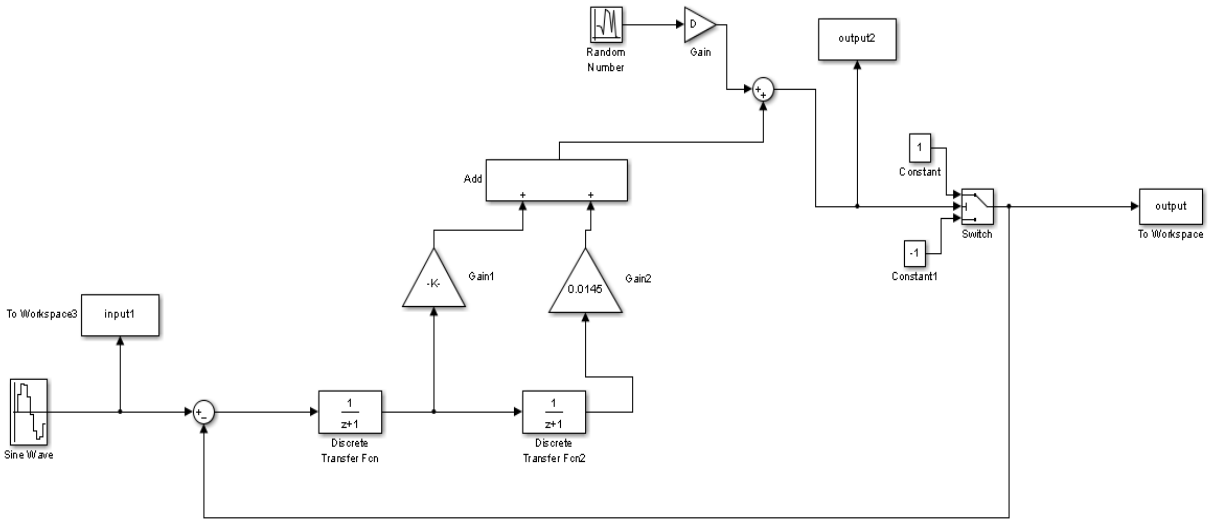

Figure B-24 HP second-order summation of weighted feedforward coefficients structure

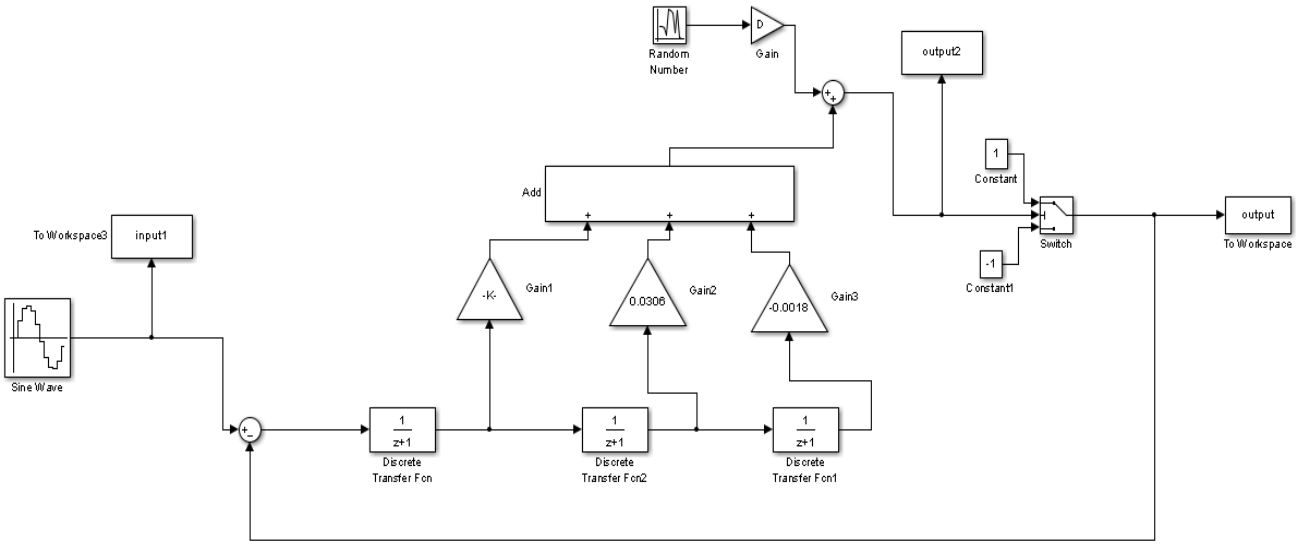

Figure B-25 HP third-order summation of weighted feedforward coefficients structure

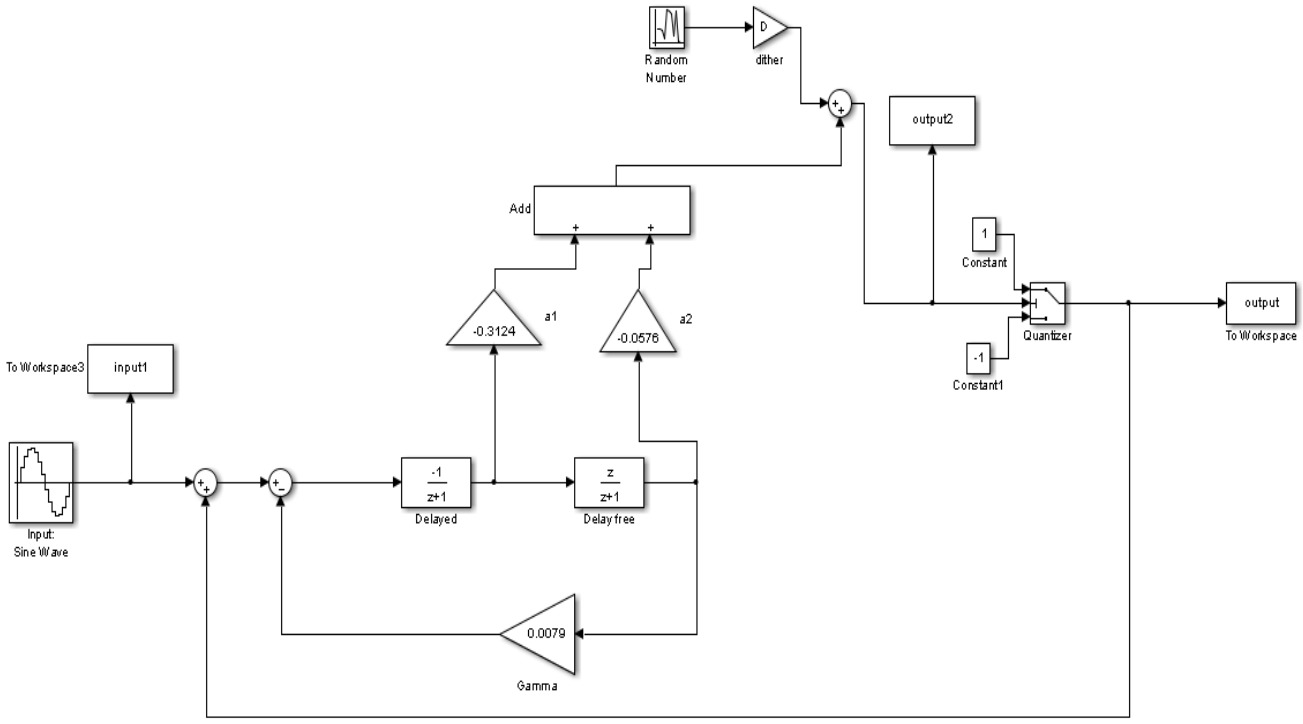

Figure B-26 HP second-order summation of weighted feedforward coefficients with local feedbacks structure

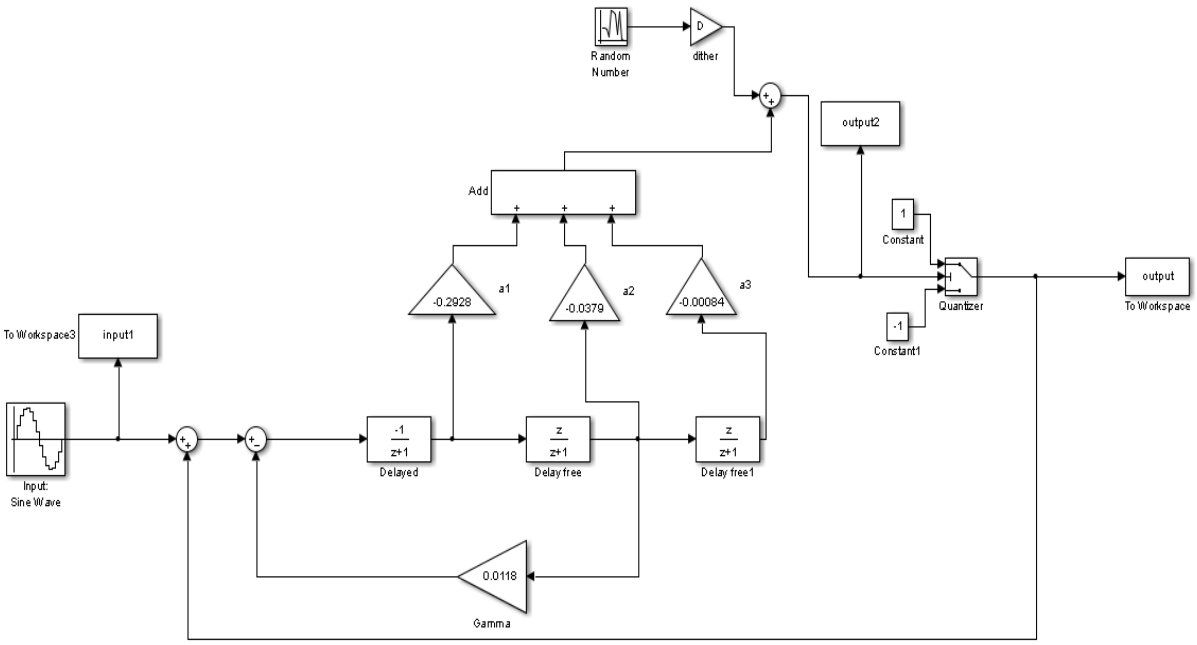

Figure B-27 HP third-order summation of weighted feedforward coefficients with local feedbacks structure